Skoltech

Skolkovo Institute of Science and Technology

Skolkovo Institute of Science and Technology

ASYMPTOTIC MODELS OF COUPLED GEOMECHANICS/FLUID MECHANICS PHENOMENA OF HYDRAULIC FRACTURE GROWTH

Doctoral Thesis

by

EVGENII KANIN

DOCTORAL PROGRAM IN PETROLEUM ENGINEERING

Supervisor
Professor Andrei Osiptsov,
Project Center for Energy Transition and ESG, Skoltech, Russia

Co-supervisor
Professor Dmitry Garagash,
Department of Civil and Resource Engineering, Dalhousie University,
Canada

Moscow - 2022

I hereby declare that the work presented in this thesis was carried out by myself at Skolkovo Institute of Science and Technology, Moscow, except where due acknowledgement is made, and has not been submitted for any other degree.

Candidate: Evgenii Kanin.

Supervisor: Prof. Andrei Osiptsov.

Co-supervisor: Prof. Dmitry Garagash.

Abstract

The present thesis considers a fluid-driven fracture propagating in permeable rock. The main aim of the work is to investigate the impact of various hydrodynamical phenomena on hydraulic fracture growth. We utilise two crack models for the analysis: semi-infinite and penny-shaped. The former describes the near-tip region of a finite crack controlling its propagation and accurately resolving the coupling between the physical processes realised in the vicinity of the moving front. The latter model is an example of a finite fracture occurring in nature which allows obtaining demonstrable results linked with the phenomena under consideration.

Firstly, we look at the pressure-dependent fluid exchange between the crack and ambient porous media. The pressure-independent Carter's law governs the leak-off process in most existing models. We modify this mechanism by including the dependence of the fluid-exchange rate on the fluid pressure inside the fracture channel. The proposed approach allows the liquid to flow out along the bulk part of the fracture and leak in along the region adjacent to the moving front forming a pore fluid circulation cell, i.e., the fracture domain along which the total volume of the pore fluid crossing the fracture surface equals zero. We obtain the general numerical solution for the aperture and pressure for the semi-infinite fracture, assuming that the fracturing and pore fluids are the same; moreover, the solution is fully characterised within the parameter space of the problem. We assess the impact of the pore fluid leak-in on the crack properties and explore the limitations of the near-tip region model with Carter's leak-off. Afterwards, the developed fracture tip model is embedded into a radial crack model as a propagation condition. The main aspect of the analysis of a penny-shaped fracture is a comparison of different crack properties computed by the proposed model with that provided by a radial fracture model in which the pressure-independent mechanism governs the fluid exchange. Based on the comparison, we identify the parameter ranges for which the effect of the pressure-dependent fluid exchange mechanism is essential and, on the other hand, outline zones for which Carter's leak-off model provides accurate results.

Secondly, we build the models for semi-infinite and radial cracks driven by slickwater, i.e., water solution with polymeric additives reducing the fluid flow friction in the wellbore and fracture in reservoir field applications. This part of the thesis focuses on the flow regime transformation inside the fracture channel from laminar to turbulent with distance from the moving front. We assume that the turbulent friction of slickwater is described by the maximum drag reduction asymptote. The main objectives of the examination are to analyse the influence of the leak-off process on the laminar-to-turbulent transition and investigate turbulent flow effects during hydraulic fracture evolution. The numerical solution for a semi-infinite fracture reveals that leak-off enhances the turbulent flow impact by shifting the transition between laminar and turbulent flow regimes closer to the fracture front compared to the impermeable rock case. The numerical solution for a radial fracture corresponding to the typical field cases demonstrates a significant impact of the turbulent flow regime during the initial few minutes of propagation, leading to the shorter radius and broader maximum aperture than the laminar model provides. In addition, fluid pressure has higher values at the wellbore within tens of minutes of the start of the

injection leading to a more significant hydraulic pumping power requirement than the laminar model predicts. We analyse the parameter spaces for both semi-infinite and radial cracks in which the limiting propagation regimes are identified, and their applicability domains are highlighted. We also mark the regions where the turbulent flow affects fracture growth significantly.

Finally, we analyse the influence of fluid yield stress on the propagation of a penny-shaped fracture. Herschel–Bulkley rheological model describes the fracturing fluid properties since it includes yield stress and non-linearity of the shear stress. We implement two numerical approaches to compute the problem solution, accurate and approximate. We present examples corresponding to typical field applications and demonstrate that the yield stress can lead to a shorter radius and wider opening than the corresponding case with simpler power-law fluid rheology. Further, we quantify the limiting propagation regimes and investigate the parametric space of the problem, in which the applicability domains of the limiting solutions are framed. The regime maps allow one to quickly determine the cases in which yield stress provides a strong influence.

The near-tip region models developed in the present thesis can be utilised within the finite fracture models, e.g., radial, KGD, EPKN, Planar3D, EP3D as a tip module. The latter plays the role of a propagation criterion, i.e., determines the front location at each time moment. Moreover, the fracture tip solution accurately describes the finite fracture properties near its front. All physical processes implemented in the tip model must be accounted for along the bulk part of the finite fracture. In turn, proposed radial crack models can be used as a benchmark solution for the numerical simulators of more realistic (complex) fracturing problems, e.g., Planar3D, including the same set of the physical processes as a penny-shaped model possesses.

Publications

1. Evgenii A Kanin, Dmitry I Garagash, and Andrei A Osiptsov. The near-tip region of a hydraulic fracture with pressure-dependent leak-off and leak-in. *Journal of Fluid Mechanics*, 892, 2020d

2. Evgenii A Kanin, Egor V Dontsov, Dmitry I Garagash, and Andrei A Osiptsov. A radial hydraulic fracture with pressure-dependent leak-off. *Journal of the Mechanics and Physics of Solids*, 143:104062, 2020c

3. EA Kanin, EV Dontsov, DI Garagash, and AA Osiptsov. A radial hydraulic fracture driven by a herschel–bulkley fluid. *Journal of Non-Newtonian Fluid Mechanics*, 295:104620, 2021b

4. Evgenii Kanin, Dmitry Garagash, and Andrei Osiptsov. Turbulent flow effects in hydraulic fracture propagation in permeable rock. 2021c

Conference proceedings

1. Evgenii Kanin, Dmitry Garagash, and Andrei Osiptsov. The near-tip region of a hydraulic fracture with pressure-dependent fluid exchange between the fracture and permeable rock. In *AGU Fall Meeting 2019*. AGU, 2019

2. Evgenii Kanin, Dmitry Garagash, and Andrei Osiptsov. Turbulent flow effects in a slickwater fracture propagation in permeable rock. In *ECMOR XVII*, volume 2020, pages 1–18. European Association of Geoscientists & Engineers, 2020b

3. Evgenii Kanin, Dmitry Garagash, and Andrei Osiptsov. Radial fracture in permeable rock driven by turbulent-laminar flow. In *AGU Fall Meeting 2020*. AGU, 2020a

4. E Kanin, E Dontsov, D Garagash, and A Osiptsov. The impact of fluid yield stress on hydraulic fracture propagation. In *82nd EAGE Annual Conference*

& Exhibition, volume 2021, pages 1–5. European Association of Geoscientists & Engineers, 2021a

Acknowledgments

Table of Contents

9

List of Figures

13

17

List of Tables

Chapter 1

Introduction

1.1 Literature review

Hydraulic fractures are fluid-filled tensile cracks propagating in a solid material, such as Earth's crust, and their dynamics is driven by the high-pressure fluid injection. Hydraulic fractures exist in nature in the form of magma-filled dykes [Spence and Turcotte, 1985, Lister, 1990, Rubin, 1995, Rivalta et al., 2015, Dontsov, 2016b], fluid-filled cracks in glacier beds [Tsai and Rice, 2010, van der Veen, 2007], and they also form during the maturation of organic shales (and others) [Engelder et al., 1990, Carter et al., 2000b]. However, most often they are human-made and are utilised in the oil and gas fields to enhance production of hydrocarbons [Economides et al., 1989, 2002] by increasing the contact between wellbore and reservoir. Application of horizontal wells with multistage hydraulic fracturing is popular in low permeability formations [Vishkai and Gates, 2019].

From the petroleum industry perspective, hydraulic fracturing is a complicated technique. It requires a large amount of water, multiple pump trucks, different proppants, and polymeric additives, ensuring the required fluid rheology [Osiptsov, 2017]. For this reason, there is a value in constructing numerical models that aim to optimise treatment design and increase the efficiency of operations. The hydraulic fracturing cycle consists of several phases: crack growth [Detournay, 2016], proppant placement [Isah et al., 2021], flowback period [Osiptsov et al., 2019], and production [Economides, 2013]. The current thesis deals with the first phase, namely, the

dynamics of fracture growth.

Various numerical models have been developed over time to simulate hydraulic fracture growth, and their geometric complexity increases gradually. The first models have simple two dimensional geometries: Perkins-Kern-Nordgren (PKN) [Perkins et al., 1961, Nordgren et al., 1972], Khristianovich-Zheltov-Geertsma-De Klerk (KGD) [Khristianovic and Zheltov, 1955, Geertsma et al., 1969] and penny-shaped (or radial) [Geertsma et al., 1969, Abe et al., 1976]. Recent two decades saw both analytical and numerical development of the KGD and radial models to correctly account for the multiphysical processes and their non-trivial coupling (see review of Detournay [2016] and discussion later) and provide blueprints and benchmarks for physically sound numerical three dimensional models of more realistic hydraulic fractures: pseudo-3D [Settari et al., 1986, Adachi et al., 2010, Dontsov and Peirce, 2015a], planar-3D [Ben Naceur et al., 1990, Lee and Lee, 1990, Peirce and Detournay, 2008, Peirce, 2015, Dontsov and Peirce, 2017c], fully-3D [Vandamme and Curran, 1989, Carter et al., 2000a, Sousa et al., 1993]. Further, numerical models for simultaneous growth of multiple hydraulic fractures were proposed [Lecampion and Desroches, 2015, Suarez-Rivera et al., 2019, Dontsov et al., 2019a]. A more extended overview of hydraulic fracture propagation models and insights about the utilised numerical techniques are given in the following review papers [Adachi et al., 2007, Detournay, 2016, Lecampion et al., 2018, Nguyen et al., 2020].

Generally, linear elastic fracture mechanics (LEFM) theory is assumed to govern hydraulic fracture propagation in the numerical models, although its limitations have been recently highlighted in Garagash [2019], Liu and Lecampion [2021]. According to its basics, the crack advances when the stress intensity factor exceeds the critical value known as the rock toughness [Irvin, 1957]. An alternative formulation of this criterion is the square-root behaviour of the crack opening profile near the moving front (known as the toughness asymptote). In the general case, it describes the opening profile along the limited region adjacent to the front [Bunger and Detournay, 2008] because of the realisation of other physical phenomena during propagation besides the brittle rock failure in the vicinity of the fracture tip, e.g., viscous fluid flow in the crack channel and fluid exchange between the ambient reser-

voir and fracture. Typical mesh in the numerical hydraulic fracturing simulators is relatively coarse in order to save computation time; as a result, in the general case, it is impossible to resolve LEFM asymptote. That is why the specialised near-tip region models is preferred over the LEFM asymptote to increase the accuracy of the numerical calculations. The fracture tip model determines the fracture front location for each time instance, describes the fracture characteristic profiles (opening, pressure) near the tip, and resolves the impact of all physical processes on the crack propagation (multiscale model). The tip region is investigated via a semi-infinite fracture model, in which the fracture is moving with a constant velocity that corresponds to an instantaneous local velocity of the finite (parent) fracture front. The viscosity and leak-off tip asymptotic solutions for a hydraulic fracture driven by a power-law fluid were obtained by Desroches et al. [1994] and Lenoach [1995], respectively. The effects of the vapour lag presence at the fracture tip are investigated in works [Rubin, 1993, Garagash and Detournay, 2000]. The multiscale tip solution incorporating toughness, viscosity and leak-off limiting regimes is investigated in Garagash et al. [2011], and, afterwards, Dontsov and Peirce [2015b] proposed its approximate version which can be easily integrated into planar-3D models, e.g., as it is done in [Dontsov and Peirce, 2017c]. In the majority of the models, the fluid exchange process between the fracture and permeable reservoir is governed by Carter's leak-off law [Carter, 1957]. However, the tip model can also be considered with a more complex pressure-dependent formulation as in [Detournay and Garagash, 2003, Kovalyshen, 2010]. In the aforementioned near-tip region models, the fluid flow in the fracture channel is assumed to be laminar. The impact of the laminar-to-turbulent flow regime transition inside the fracture channel is analysed by Dontsov [2016c], Lecampion and Zia [2019]. The generalised asymptotic solutions for a hydraulic fracture driven by a non-Newtonian fluid are developed in the following works: [Dontsov and Kresse, 2018, Bessmertnykh et al., 2021] for the power-law rheology, [Moukhtari and Lecampion, 2018] for the Carreau model and [Bessmertnykh and Dontsov, 2019] for the Herschel-Bulkley model. The influence of cohesive zone and analysis of the LEFM usage constraints in the hydraulic fracture tip problem are examined by Garagash [2019]. The near-tip region of a hydraulic

fracture with proppant particles is studied in the paper [Bessmertnykh et al., 2020].

The near-tip region models have also been applied for the development of approximate solutions for a finite crack. The following idea is the basis of the approximate approaches: the fracture width profile is a continuation of the corresponding characteristic near the moving front. Further, given the width solution, the dynamics of the finite fracture is retrieved from the global fluid balance. This concept is applied for a radial and plane-strain fracture models [Dontsov, 2016a, 2017, Garagash, 2019], as well as for a more general case of an elliptic fracture Dontsov et al. [2019b].

The current work considers two types of models for hydraulic fracture propagation. The first is a semi-infinite fracture model, and we have already discussed its variety. The second one is a penny-shaped model for a fluid-driven fracture, and now, we review its development over time. In a radial hydraulic fracture model, the crack is formed in a pre-defined plane, and its geometry is axisymmetric relative to the injection point. The numerical model for a penny-shaped fracture in an impermeable rock driven by laminar flow of a Newtonian fluid is investigated by Savitski and Detournay [2002]. The toughness dominated regime, i.e. when the fluid viscosity can be neglected, of a radial fracture in a permeable rock is analysed by Bunger et al. [2005] based on the earlier studies for the plane-strain fracture [Garagash, 2000, 2006b]. The early-time solution for a plane-stain fracture with a vapour lag is constructed by Garagash [2006c], and, further, extended to the radial fracture geometry by Bunger and Detournay [2007]. The numerical model for a radial fracture taking into account the rock toughness, fluid viscosity and leak-off is presented in [Madyarova, 2004] for Newtonian fluid. The limiting cases of a penny-shaped fracture model with three dimensional pore pressure diffusion and poroelastic effects are considered by [Kovalyshen, 2010, Kovalyshen et al., 2013]. The occurrence of turbulent flow regime inside the radial fracture channel is explored by Dontsov and Peirce [2017a], Zolfaghari and Bunger [2019] for pure water and by Lecampion and Zia [2019] for slickwater cases. The impact of the power-law fluid rheology on the fracture propagation is firstly studied by Adachi and Detournay [2002], Garagash [2006a] for the plane-strain geometry, and, afterwards, for the penny-shaped fracture in works [Peck et al., 2018a,b]. The same problem is addressed from scaling point

of view in [Dontsov, 2019]. The power-law dependence of fracture toughness with fracture length is embedded into a radial fracture model by Liu et al. [2019]. It is important to highlight that Liu et al. [2019] utilise a numerical algorithms based on Gauss-Chebyshev quadrature and Barycentric Lagrange interpolation techniques discussed earlier by Viesca and Garagash [2018], which allows one to construct an accurate numerical solution of the multi-scale problem without explicit implementation of the near-tip asymptotic solutions.

1.2 Objectives, novelty and significance of the work.

The main aim of the present thesis is to investigate the impact of various hydrodynamical phenomena on the propagation of a hydraulic fracture. We rely on the models for semi-infinite and penny-shaped cracks for the analysis. Chapter 2 outlines their classical problem formulations supplemented by the governing equations. In the subsequent chapters, we describe how the assumptions and equations of each model are modified adjusting them to the particular study.

The first fluid mechanics phenomenon examined in Chapter 3 is the pressure-dependent fluid exchange between the crack and ambient permeable reservoir. Pressure-independent Carter's leak-off law [Carter, 1957] is used in the majority of hydraulic fracture models. However, Section 3.1 explains why its assumptions can be invalid in the vicinity of the fracture tip and in the bulk of the crack meaning that the refinement of the fluid exchange mechanism is required by accounting for the dependence of fluid exchange rate on pressure inside the fracture channel. Numerical studies of hydraulic fracture propagation in permeable rock with pore pressure diffusion, [Carrier and Granet, 2012, Sarris and Papanastasiou, 2011, Golovin and Baykin, 2018], do not pay attention to the physical features linked with the pressure-dependent fluid exchange, e.g., pore fluid influx into the fracture, and possible consequences of the spatially under-resolved fracture tip region during the simulations. In the works [Detournay and Garagash, 2003, Kovalyshen, 2010, Kovalyshen et al., 2013], the authors constructed numerical models for a fluid-driven fracture with semi-infinite geometry propagating in a permeable rock accounting for the pressure-dependent leak-off.

These studies do not include the detailed investigation of the problem parametric and do not answer to highly relevant question in what cases the pressure-dependent fluid-exchange is essential or, in other words, Carter's leak-off law provides inaccurate results. Section 3.2 considers the near-tip region of a fluid-driven fracture propagating in a permeable rock allowing for the pressure-dependent leak-off and leak-in. We discuss the limiting propagation regimes focusing on the cases when the pressure-dependent solution reduces to the outcome of the semi-infinite fracture model with Carter's leak-off [Garagash et al., 2011] allowing us to frame the general structure of the sought solution and its parametric dependence. We perform analytical and numerical exploration of the solution in the parametric space, including an analysis of the relative importance of the pressure-dependent effects in the fluid exchange process between the fracture and the reservoir. Further, in Section 3.3, we build a numerical model for the radial crack involving the pressure-dependent leak-off mechanism. In this model, we use the fracture tip model developed in Section 3.2. The main objective of Section 3.3 is to compare the radial fracture properties obtained via the developed model with the results calculated by the radial fracture model with Carter's leak-off Madyarova [2004] in order to specify cases, in which the pressure-dependent effects are essential and could not be neglected. In addition to the numerical calculations, we also present the analytical analysis demonstrating for which cases the influence of the pressure-dependent leak-off on the fracture propagation is significant. Consequently, using the obtained results, a potential reader can estimate the importance of the pressure-dependent fluid exchange for the required values of input parameters both qualitatively and quantitatively.

Further, Chapter 4 looks at the turbulent-laminar flow inside the fracture channel which can be realised during fracturing conducting via low viscosity fluid injected with high rate. The fracture part adjacent to the wellbore is occupied by the turbulent flow regime, while flow is laminar in the remaining part of the fracture. During the examination, we take slickwater as a fracturing fluid, i.e., water with specific polymers reducing friction significantly. We also assume that the maximum drag reduction or Virk's asymptote [Virk, 1971, 1975] governs slickwater frictional behaviour during the turbulent flow regime. The analyses of turbulent-laminar pure-

water flow affect on the crack propagation carried out in the works [Nilson, 1981, Zolfaghari et al., 2018, Dontsov and Peirce, 2017b, Dontsov, 2016c]. However, frictional behaviour of pure water is different from slickwater. Moreover, these papers do not provide the in depth investigation of the problem parametric space including the derivation of the limiting propagation regimes, determination of their applicability domains and the dependence of the position of the transition boundary between flow regimes on the model input parameters. Such analysis is particularly useful to frame the general solution inside the parameter space resulting in better understanding of the propagation conditions as a function of time. Lecampion and Zia [2019] investigate the propagation of a semi-infinite and radial cracks in an impermeable reservoir due to turbulent-laminar slickwater flow. In turn, in Chapter 4, we consider a permeable formation case, and leak-off process is described by Carter's law. Section 4.2 is devoted to the near-tip region of a hydraulic fracture driven by turbulent-laminar slickwater flow in a permeable reservoir. We would like to analyse how the presence of the leak-off process affects the transition to the turbulent flow regime. We present particular solution profiles, derive limiting propagation regimes and analyse the problem parametric space by constructing the regime maps and exploring the behaviour of the transition boundary between the flow regimes. Section 4.3 considers a radial hydraulic fracture with turbulent-laminar slickwater flow inside the crack channel propagating in a permeable reservoir. The main aim of the examination is to analyse the combined effects of the turbulent-laminar flow of the fracturing fluid with drag reduction agents and the fluid leak-off into the ambient rock on the propagation of a finite hydraulic fracture. We compute the solution examples corresponding to typical field cases, investigate the limiting propagation regimes, namely, revisit the existing limiting solutions and derive new ones, and study the problem parameter space. Moreover, we highlight the domains of the parameter space where the problem solution can be interpreted as a fully-turbulent and fully-laminar. Using the obtained results, a potential reader can estimate how long turbulent flow influences on the crack growth for certain values of the input parameters. If the considered case is located out of the domain of the parameter space where the solution is fully-laminar, hydraulic fracture design should be per-

formed accounting for the turbulent flow inside the fracture and its transformation to laminar flow in the vicinity of the front.

Finally, Chapter 5 presents how a non-zero fracturing fluid yield stress influences the radial crack evolution, and in our model, Herschel–Bulkley model governs the fracturing fluid rheology. Typical fracturing fluid exhibits non-Newtonian shear-thinning behaviour within a specific range of the shear rate values. However, fracturing foams [Gu and Mohanty, 2015, Faroughi et al., 2018, Fu and Liu, 2019], emulsions, suspensions with proppant and fibers [Stickel and Powell, 2005, Osiptsov, 2017] tend to exhibit a shear-thinning rheology with yield stress. Majority of hydraulic fracture models accounting for non-Newtonian rheology of the fracturing fluid do not consider the impact of fluid yield stress on propagation of a finite hydraulic fracture, so we would like to fill the gap and investigate this issue. The main aims of Chapter 5 include the implementation of accurate and approximate solvers, derivation of the limiting propagation regimes, detailed exploration of the problem parametric space, examination on the variations of the fracture properties depending on the yield stress and leak-off intensity for different values of the flow index.

The developed fracture tip models (Section 3.2, Section 4.2) accurately describe the near-tip region of a finite fracture. Using the fracture tip model, one can determine a finite fracture front location for each time instance, i.e., it can be applied as a propagation criterion. For that purpose, the near-tip region model should be numerically implemented into a module for the growth of a finite fracture in the form of a so-called tip element. In literature, the approach based on "tip logic" has been applied inside numerical models of hydraulic fractures with different geometries. In Section 3.3, we embed the fracture tip model with the pressure-dependent leak-off (Section 3.2) into a radial hydraulic fracture model. The constructed penny-shaped hydraulic fracture models (Section 3.3, Section 4.3, Chapter 5) can be used for the verification of the numerical simulators of complex fracturing problems.

Chapter 2

Models for hydraulic fracture propagation

The present chapter revisits the model formulations, i.e., problem definitions and governing equations, for the near-tip region of a fluid-driven fracture and penny-shaped hydraulic fracture. One can call the formulations below as classic since they contain the most common assumptions faced in the literature. The subsequent chapters (3 − 5) will outline the main alterations in the considered formulations compared to the classic ones allowing us to describe the analysed fluid mechanics phenomenon.

2.1 Semi-infinite fluid-driven fracture

2.1.1 Problem definition

The near-tip region of a fluid-driven fracture is considered as the problem of a semi-infinite plane strain fracture (Figure 2-1) propagating with constant velocity V, which is understood as the instantaneous local tip velocity of the parent hydraulic fracture. Since the propagation velocity is constant, it is possible to introduce moving coordinate x denoting distance from the moving fracture front, and in this coordinate system, the problem is steady-state.

The host permeable linear-elastic rock is characterised by Young's modulus E
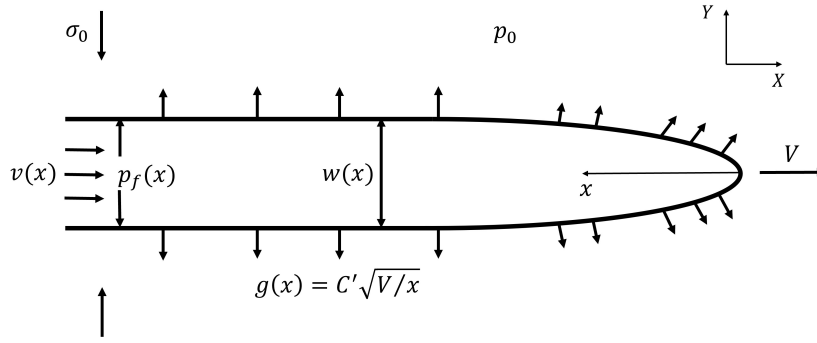
Figure 2-1: Schematic picture of the fracture tip model with the classical set of assumptions.

and Poisson's ratio ν. Small scale yielding [Rice et al., 1968], i.e., the rock damage/yielding zone at the advancing fracture front small compared to the lengthscales of other physical processes active near the tip (e.g., dissipation in the viscous fluid flow inside the fracture channel, fluid exchange between the crack and ambient formation) is assumed. Linear elastic fracture mechanics (LEFM) theory is therefore utilised for the modelling of the quasi-static propagation of the fracture in the rock characterised by the fracture toughness K_{Ic}.

The fracture faces are loaded internally by the fluid pressure $p_f(x)$ while the rock is subjected to the far-field confining stress σ_o. The net pressure function $p(x) = p_f(x) - \sigma_o$ and the aperture profile $w(x)$ completely characterise a semi-infinite fracture solution. The fracturing fluid is a Newtonian liquid of viscosity μ. The fluid flow inside the fracture channel is laminar, and it is described by the lubrication theory [Batchelor, 1967]. Fluid lag is absent in the classic problem formulation since one can assume that its maximum length $\sim \mu V E^2 \sigma_o^{-3}$ is small compared to the near-tip length scales of the fluid-driven fracture [Garagash and Detournay, 2000, Detournay and Garagash, 2003]. In other words, the crack and fracturing fluid fronts coincide in the model.

The fluid exchange between the host rock with porosity ϕ_r and permeability k, and the fracture is taken in the form of Carter's law [Carter, 1957] implying the fluid exchange rate to be proportional to the inverted square root of the 'exposure' time (the interval between the current time and the moment when the fracture front reaches the considered point of the fracture plane). The proportionality

coefficient C_L, or Carter's leak-off coefficient, can be expressed as [Collins, 1976]: $C_L = k(\sigma_o - p_o)/(\mu\sqrt{\pi c})$, where $c = k/(\phi_r c_t \mu)$ is the diffusivity coefficient (c_t is total compressibility) and p_o is the far-field pore pressure, when the cake-building (deposition of the polymer additives onto the fracture walls) is neglected, and formation fluid has similar properties to that of the fracturing fluid in the context of the flow through the porous rock. One can find the expressions for C_L coefficient in more complex cases, e.g., piston-like displacement of pore fluid by fracturing fluid, in [Economides et al., 1989].

2.1.2 Governing equations

Let us introduce the moving coordinate system (x, y) linked with the fixed coordinates (X, Y) by the relations: $x = Vt - X$, $y = Y$; the problem is stationary in the coordinates (x, y). The system of governing equations is formulated for unknown opening $w(x)$ and net fluid pressure $p(x)$ profiles with distance $x \in (0, +\infty)$ from the moving tip, and the set of material parameters:

$$E' = \frac{E}{1 - \nu^2}, \quad K' = 4\sqrt{\frac{2}{\pi}}K_{Ic}, \quad M' = 12\mu, \quad C' = 2C_L, \qquad (2.1)$$

where E' is the plane strain elastic modulus, K' and M' are the toughness and viscosity parameters, and C' is the leak-off parameter.

2.1.2.1 Fracture propagation

LEFM fracture propagation criteria under quasi-static conditions states that the stress intensity factor at the crack tip matches the rock toughness: $K_I = K_{Ic}$, e.g., [Kanninen and Popelar, 1985]. This condition prescribes the asymptotic behaviour of the fracture opening near its front [Irvin, 1957]:

$$w(x) = \frac{K'}{E'}\sqrt{x}. \qquad (2.2)$$

2.1.2.2 Crack elasticity

The net pressure $p(x)$ in the fracture could be expressed as the crack line integral of the opening $w(x)$ using the elasticity equation [Bilby and Eshelby, 1968]:

$$p(x) = \frac{E'}{4\pi} \int_0^\infty \frac{dw(s)}{ds} \frac{ds}{x - s}. \tag{2.3}$$

Equation (2.3) can be inverted [Garagash and Detournay, 2000] to aid in the numerical implementation of the problem solution:

$$w(x) = \frac{K'}{E'}\sqrt{x} + \frac{4}{\pi E'} \int_0^\infty K(x, s)p(s)ds, \tag{2.4}$$

where the integral kernel is: $K(x, s) = \ln\left|\frac{\sqrt{x}+\sqrt{s}}{\sqrt{x}-\sqrt{s}}\right| - 2\sqrt{\frac{x}{s}}.$

2.1.2.3 Fluid flow

The flow of incompressible fluid in the crack channel is described by the continuity equation averaged across the fracture aperture:

$$\frac{\partial w}{\partial t} + \frac{\partial(wv)}{\partial X} + g = 0,$$

which, upon transforming to the moving coordinate system ($\partial/\partial t = V d/dx, \partial/\partial X = -d/dx$), is given by:

$$V\frac{dw}{dx} - \frac{d(wv)}{dx} + g = 0, \tag{2.5}$$

where g is the leak-off rate governed by Carter's law [Carter, 1957]:

$$g(x) = \frac{C'}{\sqrt{t - t_0}} = C'\sqrt{\frac{V}{x}}, \tag{2.6}$$

where t_0 is the time moment at which the fracture tip is at distance X, and we apply the relation $t_0 = X/V$.

Substituting equation (2.6) into (2.5) and integrating from the tip ($x = 0$) to

some coordinate x, we obtain

$$wv = wV + q_\perp. \tag{2.7}$$

Here, we take into account the boundary conditions: $w(0) = 0$ and $(wv)|_{x=0} = 0$. Equation (2.7) signifies that the local fluid volumetric flow rate at distance x from the fracture tip $w(x)v(x)$ is partitioned between the fluid stored in the fracture $w(x)V$ and in the rock via the cumulative rate of fluid leak-off $q_\perp(x)$. In the Carter's leak-off case, the latter term has the following form:

$$q_\perp = 2C'\sqrt{Vx}. \tag{2.8}$$

Finally, Poiseuille's law for laminar flow of Newtonian fluid along the crack channel

$$v = \frac{w^2}{M'}\frac{dp}{dx}, \tag{2.9}$$

completes the fluid flow description.

2.2 Radial fluid-driven fracture

2.2.1 Problem definition

The second model of a fluid-driven fracture examined in the present thesis describes the evolution of a crack with a radial (penny-shaped) geometry, and its sketch is shown in Figure 2-2. The crack grows along the plane perpendicular to the far-field confining stress due to fluid injection through a point source. The fracture is axisymmetric, i.e. there is a symmetry relative to the axis passing through the source and perpendicular to the fracture plane. Therefore, all fracture characteristics are the functions of the distance to the source r and time t.

The volumetric rate of fluid injection is constant and is denoted by Q_0, so that the injected volume equals: $V_{\text{inj}}(t) = Q_0 t$. The ambient rock is taken as linear elastic with Young's modulus E and Poisson's ratio ν. We assume that the size of the zone, where the dissipation processes associated with the rock failure happen, is small
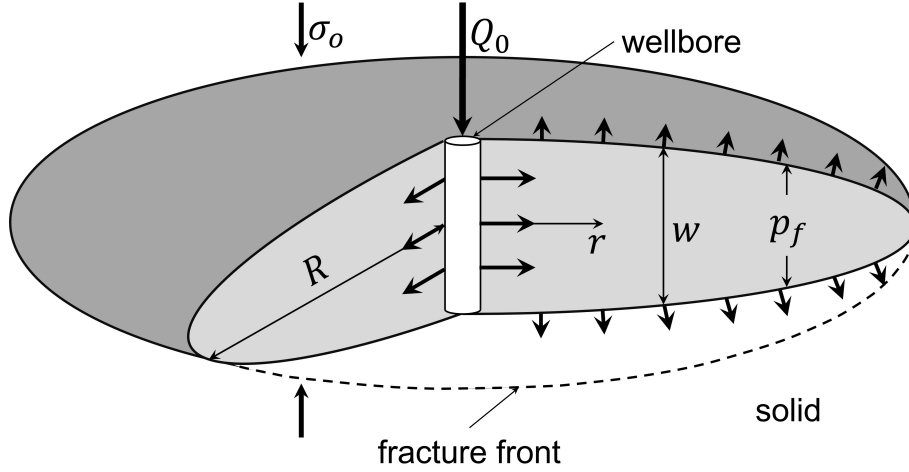
Figure 2-2: A radial fracture model with the classical set of assumptions.

compared to other length scales realised in the model, e.g., linked with the viscous fluid flow and fluid exchange, which is generally true when the in situ confining stress σ_o is much smaller than the rock tensile strength [Garagash, 2019]. Consequently, the linear elastic fracture mechanics (LEFM) theory can be applied to model quasi-static fracture propagation in a solid medium with toughness K_{Ic}. The fracture surface is exerted by the fluid pressure $p_f(r, t)$ from the internal side. The radial fracture model is fully characterised by the opening profile $w(r, t)$, radius $R(t)$, net pressure profile $p(r, t) = p_f(r, t) - \sigma_o$ and efficiency parameter $\eta(t) = V_{\text{crack}}(t)/V_{\text{inj}}(t)$, where $V_{\text{crack}}(t)$ is the fracture volume. The latter allows evaluating the partition of the injected fluid volume $V_{\text{inj}}(t)$ between that of the crack $V_{\text{crack}}(t)$ and the fluid volume leaked into the rock $V_{\text{fluid−exchange}}(t)$.

The injected fracturing fluid is taken as a Newtonian liquid with viscosity μ. The fluid flow inside the fracture channel is controlled by lubrication theory [Batchelor, 1967], and its velocity and the flow rate are denoted by $v(r, t)$ and $q(r, t) = w(r, t)v(r, t)$, respectively. The fracture and fluid fronts are assumed to coincide in classic formulation of a radial hydraulic fracture model meaning that the lag filled by the vapour [Garagash and Detournay, 2000] or pore fluid [Detournay and Garagash, 2003] adjacent to the fracture front is negligibly small compared to the fracture radius.

The ambient reservoir is characterised by porosity ϕ_r and permeability k. Carter's

leak-off law [Carter, 1957] governs the fluid exchange process between the crack channel and formation. According to this law, the leak-off rate $g(r, t)$ is proportional to the inverted square root of the 'exposure' time, i.e., the period between the current time moment and when the crack tip passes the considered point on the fracture plane. In the case of the identical properties of the pore and fracturing fluids, i.e., they have the same viscosity μ and total compressibility c_t, the proportionality (or Carter's) coefficient has the following form [Collins, 1976]: $C_L = k(\sigma_o - p_o)/(\mu\sqrt{\pi c})$, where p_o is the far-field pore pressure, and $c = k/(\phi_r c_t \mu)$ is the diffusivity coefficient. When it is required to take into account the filter-cake building or (and) the different properties of the HF and pore fluids in the pressure-independent approximation of the fluid exchange process, one can find the appropriate expressions for Carter's coefficient in [Economides et al., 1989].

2.2.2 Governing equations

Let us discuss the system of governing equations. It is formulated for the unknown crack radius $R(t)$, opening $w(r, t)$ and net fluid pressure $p(r, t)$ profiles. The fracture characteristics depend on time t, distance from the point source r, the set of material parameters:

$$E' = \frac{E}{1 - \nu^2}, \quad K' = 4\sqrt{\frac{2}{\pi}}K_{Ic}, \quad M' = 12\mu, \quad C' = 2C_L, \qquad (2.10)$$

and the injection rate Q_0. In equation (2.10), E' is the plane strain elastic modulus, K' and M' are toughness and viscosity parameters, and C' is the leak-off parameter.

2.2.2.1 Crack elasticity

The elasticity equation expresses the net fluid pressure $p(r, t)$ in terms of the crack aperture $w(r, t)$ and radius $R(t)$ [Arin and Erdogan, 1971, Cleary and Wong, 1985, Savitski and Detournay, 2002]:

$$p(r, t) = -\frac{E'}{2\pi R(t)} \int_0^{R(t)} G\left(\frac{r}{R(t)}, \frac{s}{R(t)}\right) \frac{\partial w(s, t)}{\partial s} ds, \qquad (2.11)$$

The integral kernel $G(\rho, s)$ in equation (2.11) has the following form:

$$G(\rho, s) = \begin{cases} \frac{1}{\rho}\mathrm{K}\left(\frac{s^2}{\rho^2}\right) + \frac{\rho}{s^2-\rho^2}\mathrm{E}\left(\frac{s^2}{\rho^2}\right), & \rho > s, \\ \frac{s}{s^2-\rho^2}\mathrm{E}\left(\frac{\rho^2}{s^2}\right), & \rho < s, \end{cases} \tag{2.12}$$

where $\mathrm{K}(x)$ and $\mathrm{E}(x)$ are the complete elliptic integrals of the first and the second kind, respectively.

2.2.2.2 Fluid flow

Based on lubrication theory [Batchelor, 1967], we write out the width-averaged mass conservation equation for the fluid flow inside the crack channel:

$$\frac{\partial w}{\partial t} + \frac{1}{r}\frac{\partial(rq)}{\partial r} + g(r, t) = 0, \quad q(r, t) = w(r, t)v(r, t). \tag{2.13}$$

The equation for the leak-off rate $g(r, t)$ is provided by Carter's law:

$$g(r, t) = \frac{C'}{\sqrt{t - t_0(r)}}, \tag{2.14}$$

where $t_0(r)$ is the inverse fracture radius function: $t_0(r) = R^{-1}(t)$ or $R(t_0(r)) = r$, i.e., it indicates the time moment at which the fracture front is at the distance r from the source.

The expression for the fluid velocity inside the crack channel is given by Poiseuille's law for Newtonian fluid:

$$v = -\frac{w^2}{M'}\frac{\partial p}{\partial r}. \tag{2.15}$$

By combining the continuity equation (2.13), Poiseuille's law (2.15) and the formula for the leak-off rate (2.14), we obtain the Reynolds equation:

$$\frac{\partial w}{\partial t} = \frac{1}{M'}\frac{1}{r}\frac{\partial}{\partial r}\left(rw^3\frac{\partial p}{\partial r}\right) - \frac{C'}{\sqrt{t - t_0(r)}}, \tag{2.16}$$

which is one of the key equations determining behaviour of hydraulic fracture growth dynamics.

2.2.2.3   Fracture propagation

The LEFM theory states that for quasi-static propagation of a hydraulic fracture, the stress intensity factor matches rock toughness: $K_I = K_{Ic}$. The alternative form to this condition can be expressed in terms of the near-tip asymptotic behaviour of the fracture opening $w(r, t)$ [Irvin, 1957]:

$$w = \frac{K'}{E'}\sqrt{R - r}, \quad r \to R. \tag{2.17}$$

2.2.2.4   Boundary conditions

At the fracture inlet, the volumetric flow rate should be equal to the specified value Q_0:

$$\lim_{r \to 0} 2\pi r q(r, t) = \lim_{r \to 0} 2\pi r w(r, t) v(r, t) = Q_o. \tag{2.18}$$

In turn, the crack tip is characterised by zero opening and no-flux condition:

$$w(R, t) = 0, \quad q(R, t) = 0. \tag{2.19}$$

2.2.2.5   Global fluid volume balance

By integrating the continuity equation (2.13) with respect to time and distance and taking into account the boundary conditions (2.18), (2.19), we derive the global fluid balance equation:

$$\underbrace{Q_0 t}_{V_{\text{inj}}} = \underbrace{2\pi \int_0^R r w(r, t) dr}_{V_{\text{crack}}} + \underbrace{2\pi \int_0^t ds \int_0^{R(s)} r g(r, s) dr}_{V_{\text{fluid}-\text{exchange}}}. \tag{2.20}$$

The fluid exchange term has the following form in Carter's leak-off case:

$$V_{\text{fluid}-\text{exchange}} = 4\pi C' \int_0^R r \sqrt{t - t_0(r)} dr \tag{2.21}$$

Equation (2.20) can be interpreted as the injected volume (V_{inj}) is distributed between the crack volume (V_{crack}) and the volume leaked into the permeable formation ($V_{\text{fluid}-\text{exchange}}$).

Chapter 3

Fluid-driven fracture with pressure-dependent leak-off

3.1 Preamble

This chapter revisits the nature of the fluid exchange between the crack channel and the host permeable rock and its coupling to the fluid flow in the fracture and the fracture propagation. As the fluid exchange affects the crack volume and the level of fluid pressurisation in the fracture, it exerts a first-order impact on the crack aperture profile and fracture evolution. The fluid exchange between the pressurised fracture and the rock can be complicated by a priori unknown time-and-space varying fluid pressure in the fracture and that of the resulting process of the pore pressure diffusion in the permeable rock, time-dependent poroelastic effects, and the filter cake building (deposition of fracturing fluid solids at the fracture walls). As a result, many modelling attempts resorted to the use of a phenomenological Carter's model [Carter, 1957], which suggests that the local rate of fluid exchange (leak-off) at the fracture wall can be approximated by the inverse of the square root of the exposure time (the time since the fracture front has arrived at the considered location along the fracture path). The underpinnings of the Carter's relation is the assumption of the invariant (constant in space and time) fluid pressure differential between the fracture wall and the far-field ambient pore pressure in the rock, $p_f - p_o \approx$ const. The latter assumption often justified on the grounds that the fluid pressure in the

39

fracture scales with the far-field confining stress σ_o (in order for the fracture to stay open), $p_f \approx \sigma_o$, while the latter assumed to be distinctly larger than the pore fluid pressure, i.e. $\sigma_o > p_o$, leading to approximately constant pressure differential between the fracture and the rock, $p_f - p_o \approx \sigma_o - p_o$. This reasoning, may it be justifiable on average along the fracture length, does not stand the scrutiny locally when the fluid pressure drop in the flow towards the fracture front is considered. Indeed, near tip solutions for fully-fracturing-fluid-filled hydraulic fracture in impermeable rock [Desroches et al., 1994] and permeable rock with Carter's leak-off [Lenoach, 1995, Garagash et al., 2011] lead to infinite fluid suction at the tip, which not only invalidates the Carter's leak-off assumptions in the vicinity of the fracture tip, but actually calls for the separation (lagging) of the fracturing fluid behind the fracture front [Rubin, 1993, Garagash and Detournay, 2000], and pore fluid leak-in (not fracturing fluid leak-off) into the vacant volume of the (fracturing) fluid lag [Detournay and Garagash, 2003]. A number of recent numerical studies of hydraulic fracture propagation in permeable rock which account for the pore pressure diffusion, e.g., [Carrier and Granet, 2012, Sarris and Papanastasiou, 2011, Golovin and Baykin, 2018], do not show pore fluid leak-in, as a possible consequence of the spatially under-resolved fracture tip region in these simulations. The consideration of the pressure-dependent fluid exchange is also required in the bulk of the hydraulic fracture where the fluid pressure exceeds the value of the confining stress.

Section 3.2 deals with the near-tip region of a fluid-driven fracture propagating in a permeable rock, while allowing for the pressure-dependent fluid leak-off and leak-in and associated pore pressure diffusion in the host rock. In formulating the problem, we build on the original model framework of [Detournay and Garagash, 2003], further generalised by [Kovalyshen, 2010]. The fracture tip is considered as a stationary plane-strain problem of a semi-infinite fracture moving at constant speed. Firstly, we formulate the problem and present the governing equations. After that, we discuss various asymptotic limits of the solution, including the reduction to the Carter's leak-off case [Garagash et al., 2011], which then allows us to frame the general structure of the sought solution and its parametric dependence. Next, we introduce the characteristic scalings of the solution as they pertain to correspond-

ing limiting regimes of the fracture propagation, and the general non-dimensional problem parametric space. The rest of the section is devoted to the analytical and numerical exploration of the solution in the parametric space, including an analysis of the relative importance of the pressure-dependent effects in the fluid exchange process between the fracture and the reservoir.

In Section 3.3, we implement a numerical model for the radial fracture, which accounts for the pressure-dependent fluid exchange. For the accurate description of the processes occurring near the fracture tip, we use the fracture tip model developed in the previous section. The main aim of this part of the thesis is to compare the radial fracture characteristics (opening, pressure, radius and efficiency profiles) obtained via the developed model with the results calculated by the radial fracture model with Carter's leak-off [Madyarova, 2004, Dontsov, 2016a] in order to specify cases, in which the pressure-dependent effects are essential and could not be neglected. Firstly, we outline governing equations for the developed radial hydraulic fracture model. Then, we describe how the near-tip region model is utilised as a propagation criterion for the simulation of fracture growth and enumerate the main components of the numerical algorithm for calculating the dynamics of the crack characteristics with time. Finally, we present the obtained numerical results, comparison with Carter's leak-off case, as well as the analytical analysis that demonstrates for which cases the pressure-dependent leak-off is essential.

3.2 The near-tip region of a hydraulic fracture

3.2.1 Model formulation

Let us discuss the problem formulation for the near-tip region of a hydraulic fracture with the pressure-dependent fluid exchange between the crack channel and ambient permeable formation. Figure 3-1 shows the schematics of the investigated problem. The assumptions and governing equations of the fracture tip model given in Section 2.1 remain the same except those related to the fluid exchange. We focus on them in the current part of the thesis.
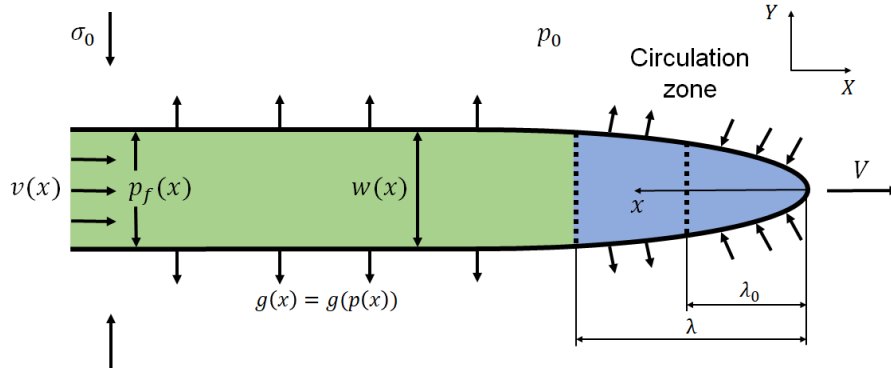
Figure 3-1: Schematic picture of the fracture tip model with the pressure-dependent fluid exchange between the fracture and permeable saturated rock.

The analysed fluid exchange is driven by the pressure difference between the crack channel, $p_f(x)$, and permeable reservoir, p_o. The fluid exchange process is modelled by one-dimensional pressure-dependent leak-off/leak-in (PDL) driven by pore pressure diffusion in the rock [Detournay and Garagash, 2003, Kovalyshen, 2010, Kovalyshen et al., 2013]. This model is a convenient approximation of a full two-dimensional leak-off and associated diffusion problem [Detournay and Garagash, 2003] based on the assumption that the characteristic thickness of the diffusive boundary layer around the crack is small compared to the characteristic lengthscale of the fracture tip problem. We also assume that the pore and fracturing fluids have similar (identical in the model) properties.

Fluid pressure $p_f(x)$ decreases as the fluid flows along the fracture towards the tip. If its value at the tip, $p_f(0)$, drops below p_o, there exists a near-tip zone of some length λ_o, $x \in [0, \lambda_o]$, along which the pore fluid flows into the fracture from the surrounding rock. For distance larger than λ_o, the fluid pressure recovers enough to enable the leak-off of the formation fluid from the fracture back into the rock. Due to the steady crack propagation (problem is stationary in the coordinate system x moving with the crack tip), all of the formation fluid leaked-in along $x \in [0, \lambda_o]$ has to circulate (leak-off) back into the formation, thus defining the pore-fluid circulation zone of some length $\lambda > \lambda_o$ near the fracture tip (Figure 3-1). The crack channel within the interval $[\lambda, +\infty)$ is filled by the hydraulic fracturing fluid which, due to pressure continuity, is also expected to leak-off into the rock.

Local rate of fluid exchange $g(x)$ between the fracture and the rock ($g > 0$ for

leak-off and $g < 0$ for leak-in) is given by the following expression in the pressure-dependent leak-off model:

$$g(x) = Q'\sqrt{V}\left(\frac{p(0) + \sigma_o'}{2\sqrt{x}} + \int_0^x \frac{dp}{dx'}\frac{dx'}{2\sqrt{x - x'}}\right), \qquad (3.1)$$

where $Q' = \frac{4k}{\mu\sqrt{\pi c}}$ is a leak-in coefficient defined in terms of the pore pressure diffusivity coefficient c, reservoir permeability k and fluid viscosity μ, $p(0) = p_f(0) - \sigma_o$ is the net fluid pressure value at the fracture front, and $\sigma_o' = \sigma_o - p_o$ is the ambient value of the effective confining stress. Derivation of (3.1) is written in Appendix A.1.

Integrating (3.1) from the tip $x = 0$ to some distance $x > 0$, we obtain the formula for the cumulative rate of fluid exchange:

$$q_\perp(x) = Q'\sqrt{V}\int_0^x \frac{p(s) + \sigma_o'}{2\sqrt{x - s}}ds = C'\sqrt{Vx} + Q'\sqrt{V}\int_0^x \frac{p(s)}{2\sqrt{x - s}}ds. \qquad (3.2)$$

Here $C' = Q'\sigma_o' = 4k\sigma_o'/(\mu\sqrt{\pi c})$ is the Carter's leak-off coefficient, and it is twice as much as that of in the classic problem definition (Subsection 2.1.2). We define the leak-off coefficient in such a way to be in accordance with C' definition in paper [Garagash et al., 2011] utilised for the comparison of the fracture tip solutions with pressure-dependent fluid exchange and Carter's leak-off.

The first term in the right hand side of (3.2) corresponds to the classical Carter's leak-off expression strictly valid only when $p_f(x) = \sigma_o$ (or $p(x) = 0$), while the second term is the pressure-dependent correction. Since the net fluid pressure $p(x) < 0$ (or $p_f(x) < \sigma_o$) in semi-infinite hydraulic fracture (e.g., Garagash and Detournay [2000]), the corrective pressure-dependent term is always negative, or, in other words, corresponds to a corrective leak-in.

3.2.2 Asymptotes and structure of general solution

3.2.2.1 Vertex solutions

Two different mechanisms govern the propagation regime of a finite hydraulic fracture, (e.g., Garagash et al. [2011]). The first one is the partitioning of the injected

fluid between the fracture and the reservoir as a result of the leak-in and leak-off processes (fracture storage vs fluid exchange with the rock). The second mechanism is the partitioning of the total dissipated energy between the creation of the new fracture surfaces and flow of the viscous fluid along the fracture (toughness vs viscosity).

In the process of fracture growth, the partition of the fracturing fluid and the partition of the dissipated energy change over time, which can lead to the realisation of different limiting regimes dominated by one storage and one dissipation mechanisms at different time. In the context of a semi-infinite hydraulic fracture, the change in the partitioning of the fluid and energy with time can be recast in the change with the distance from the fracture tip.

One can suggest four limiting propagation regimes that are characterised by the dominance of one storage/exchange and one dissipation mechanisms: toughness dominated ($M' = 0$), storage-viscosity dominated ($C' = Q' = 0$, $K' = 0$), leak-off-viscosity dominated ($C' \to \infty$, $K' = 0$), storage-leak-in-viscosity dominated ($K' = 0$, $C' > 0$, $Q' < +\infty$). The corresponding solutions are referred to as 'vertex' solutions in a problem parametric space.

While the leak-in (Q') and the leak-off (C') coefficients define the partitioning of the fluid, viscosity M' and toughness K' parameters are responsible for the partitioning of the dissipated energy.

The first three vertex solutions (k, m, $\widetilde{m}$) are given, e.g., by Garagash et al. [2011], and summarised in table 3.1 for completeness, in terms of the following three characteristic length scales:

$$\ell_k = \left(\frac{K'}{E'}\right)^2, \quad \ell_m = V\frac{M'}{E'}, \quad \ell_{\widetilde{m}} = \left(C'\sqrt{V}\frac{M'}{E'}\right)^{2/3}.$$

The pressure-dependency of the fluid exchange between the fracture and the rock is coupled with the fluid pressure drop in the flow toward the crack tip (when viscosity is non negligible: $M' > 0$). This fact suggests that the leak-in dominates near the fracture front. In other words, we anticipate that in the vicinity of the fracture tip the newly created crack volume (storage) is accommodated entirely by

Limiting solutions	opening $w(x)$	net pressure $p(x)$	velocity $v(x)$
k Toughness ($M' = 0$)	$\ell_k^{1/2} x^{1/2}$	0	$V + \frac{E'C'\sqrt{V}}{K'}$
m Storage-viscosity ($K' = 0, C' = Q' = 0$)	$\beta_0 \ell_m^{1/3} x^{2/3}$	$\delta_0 E' \frac{\ell_m^{1/3}}{x^{1/3}}$	V
$\widetilde{m}$ Leak-viscosity ($K' = 0, C' \to \infty$)	$\widetilde{\beta}_0 \ell_{\widetilde{m}}^{3/8} x^{5/8}$	$\widetilde{\delta}_0 E' \frac{\ell_{\widetilde{m}}^{3/8}}{x^{3/8}}$	$\frac{V}{\widetilde{\beta}_0} \frac{\ell_{\widetilde{m}}^{9/8}}{\ell_m x^{1/8}}$
Coefficients: $\beta_0 = 2^{1/3} 3^{5/6}, \delta_0 = \beta_0 f(2/3), \widetilde{\beta}_0 = 2.534, \widetilde{\delta}_0 = \widetilde{\beta}_0 f(5/8)$, with $f(\lambda) = \lambda \cot(\pi\lambda)/4$			

Table 3.1: Three limiting solutions of a semi-infinite hydraulic fracture for the identified limiting values of problem parameters.

the pore fluid leaking-in from the rock (while the fluid flow towards the fracture tip along the crack channel is negligible there, $v \approx 0$). However, this dominance of the leak-in has to be limited to a finite near tip region, since crack elasticity requires that $p(x)$ vanishes as $x \to \infty$, or $p_f(x) \to \sigma_o > p_o$, thus eventually giving a way to the leak-off process.

Vertices k, m, $\widetilde{m}$ (table 3.1) are the solutions for the entire semi-infinite fracture for the corresponding limiting values of governing parameters. They can be determined from the monomial solution to the crack elasticity equation (2.3):

$$w_\lambda(x) = Bx^\lambda; \quad p_\lambda(x) = E'Bf(\lambda)x^{\lambda-1}, \quad f(\lambda) = \frac{\lambda \cot(\pi\lambda)}{4}, \quad 0 < \lambda < 1,$$

where particular values of the prefactor B and the exponent λ are constrained by the lubrication equation when setting parameters (C', M' and K') to the corresponding limiting values, as detailed by Garagash et al. [2011]. In the $k-$vertex, viscosity is negligible ($M' = 0$), and the solution follows from the propagation condition (2.2). In the $m-$vertex, the fluid exchange ($C' = Q' = 0$) and toughness ($K' = 0$) are negligible, and the solution is recovered by balancing the fluid flux in the crack $w(x)v(x)$ with the storage term $w(x)V$ in the continuity equation. We anticipate that in the general parametric case (i.e. not limited to the stated values of K' and other parameters) the $m-$vertex solution provides the far-field solution asymptote, (e.g., Garagash et al. [2011]). In the $\widetilde{m}-$vertex, the fluid storage ($C' \to \infty$), and toughness ($K' = 0$) are negligible. In this case, the fluid flux in the crack is balanced with the Carter's leak-off term. In general case, the $\widetilde{m}-$vertex can be realised as an intermediate field solution [Garagash et al., 2011].

The new storage-leak-in-viscosity vertex $\widetilde{o}$ emerges as a particular case of the

viscosity-dominated ($K' = 0$) behaviour linked to the dominance of the fluid leak-in (rather than the leak-off) in the near-field ($x \to 0$). It corresponds to the classical zero-toughness behaviour of the crack opening, $w = B_{\widetilde{o}}x^{3/2}$, and the non-singular pressure: $p = -\sigma'_0 - \frac{3}{2}B_{\widetilde{o}}\frac{V^{1/2}}{Q'}x$. The first term in the expression for the net pressure is obtained from balancing the leak-in and leak-off terms in the continuity equation. On the other hand, the second term arises from the matching the leak-in and the fracture storage terms, gains particular importance in/near the zero-leak-off limit ($\sigma'_0 = 0$). This vertex solution contains prefactor $B_{\widetilde{o}}$ (with units $1/\sqrt{m}$) that is unknown and a part of the overall solution. This betrays the fact that the $\widetilde{o}-$asymptote can be realised only as a near or intermediate field of the fracture, as it can not satisfy the elasticity equation over the full semi-infinite crack extent. The second term in the net pressure is found with the assumption that the $\widetilde{o}-$vertex solution is realised in the near-field, and in this case, the left-hand side of the continuity equation ($\sim w^3(x)p'(x)$) for this vertex solution is negligible as compared to the terms in the right-hand side (storage, leak-off and leak-in).

For non-zero fracture toughness $K' > 0$, the near-field ($x \to 0$) behaviour of the fracture opening is given by the $k-$vertex solution (table 3.1), as stems from the propagation condition (2.2). Corresponding asymptotic expression for the net pressure $p(x \to 0) = -\sigma'_0 - \frac{K'V^{1/2}}{E'Q'}$ follows from the fluid continuity equation (2.7) by balancing the fluid exchange (the leak-in pore fluid volume) with the fracture storage. (We note that the fluid flux along the crack wv is negligibly small in the near field fluid balance). The obtained finite net pressure value at the fracture tip is drastically different from the one in the Carter's, pressure-independent leak-off model [Garagash et al., 2011], where the pressure sustains a negative singularity as the fracturing fluid is assumed to reach the tip of the fracture. When reformulated in terms of the fluid pressure, $p_f(x \to 0) = p_o - K'\sqrt{V}/(E'Q')$, this asymptote suggests that the fluid pressure at the crack tip is reduced from its drained value given by the ambient pore pressure p_o by the amount $K'\sqrt{V}/(E'Q')$. The latter, undrained pressure change vanishes for slowly propagating cracks ($V \to 0$) or/and zero rock toughness ($K' \to 0$).

The obtained near-field k ($K' > 0$) and $\widetilde{o}$ ($K' = 0$) asymptotes are summarised

in table 3.2.

	opening $w(x)$	net pressure $p(x)$	velocity $v(x)$
k Toughness ($K' > 0$)	$\ell_k^{1/2} x^{1/2}$	$-\sigma_0' - \frac{K'V^{1/2}}{E'Q'}$	0
õ Storage-leak-in-viscosity ($K' = 0$)	$B_{\widetilde{o}} x^{3/2}$	$-\sigma_0' - \frac{3}{2} B_{\widetilde{o}} \frac{V^{1/2}}{Q'} x$	$-\frac{3}{2} B_{\widetilde{o}}^3 \frac{V^{1/2}}{Q'M'} x^3$
	Coefficients: $B_{\widetilde{o}}$ is a part of the solution.		

Table 3.2: Near-field ($x \to 0$) of semi-infinite hydraulic fracture.

3.2.2.2 Structure of solution and scaling

The general solution of the considered problem can be tracked within the parametric triangular pyramid $m\widetilde{m}\widetilde{o}k$ formed by four aforesaid vertices. The schematic picture of this pyramid is represented in figure 3-2.
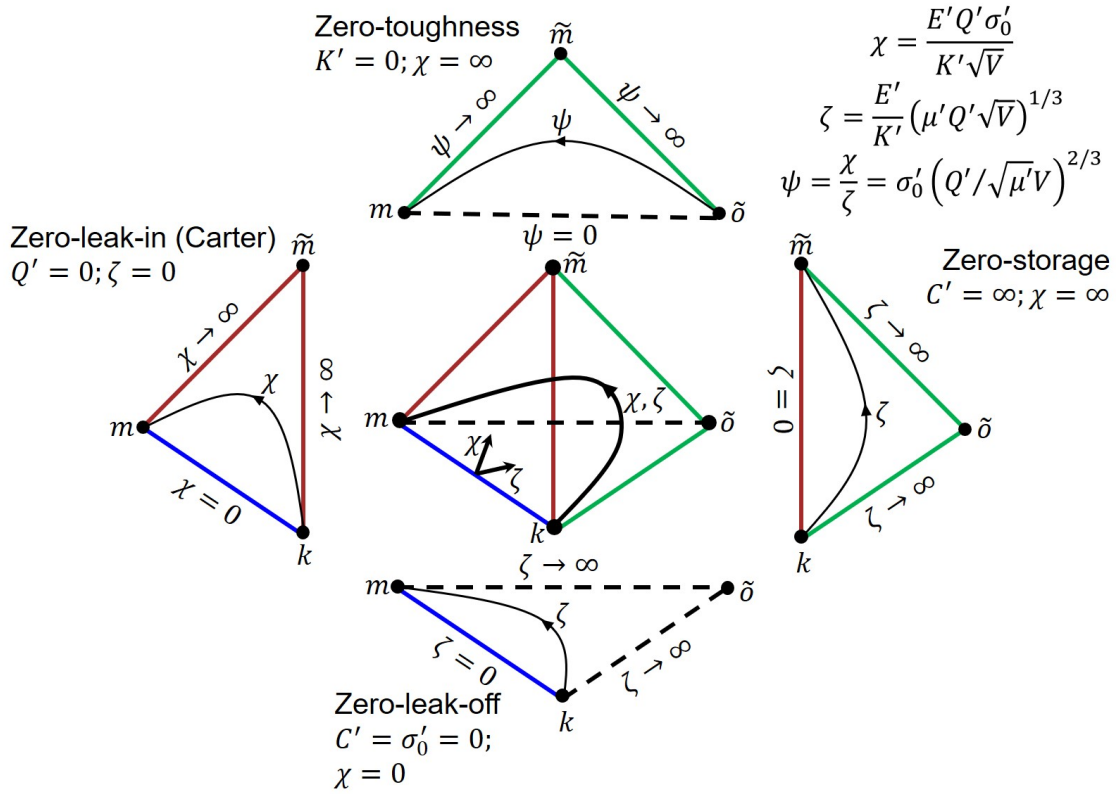
Figure 3-2: Parametric diagram (pyramid $m\widetilde{m}\widetilde{o}k$) and corresponding four limiting faces corresponding to the dominance of one energy dissipation or one fluid storage mechanism. Few solution trajectories parameterised by the leak-off χ and leak-in ζ numbers (or their ratio $\psi = \chi/\zeta$) are also shown.

Four triangular faces of pyramid $m\widetilde{m}\widetilde{o}k$ correspond to either the dominance of one of the three fluid storage/exchange mechanisms *or* one of the dissipation

mechanisms:

- storage-leak-off face $m\widetilde{m}k$: leak-in process is negligible, $Q' = 0$

- storage-leak-in face $m\widetilde{o}k$: leak-off process is negligible, $C' \propto \sigma'_o = 0$

- leak-face $\widetilde{m}\widetilde{o}k$: fluid storage in the fracture is negligible, $C' \to \infty$

- viscosity-face $m\widetilde{m}\widetilde{o}$: toughness is negligible, $K' = 0$

Six edges of the pyramid $m\widetilde{m}\widetilde{o}k$ correspond to the intersection of the corresponding two faces, and thus, reflect the dominance of one of the three fluid storage/exchange mechanisms *and* one of the dissipation mechanisms. For example, $\widetilde{m}\widetilde{o}$ is the leak-viscosity edge ($C' \to \infty$ and $K' = 0$), bounding the leak $\widetilde{m}\widetilde{o}k$ ($C' \to \infty$) and the viscosity $m\widetilde{m}\widetilde{o}$ ($K' = 0$) faces, and, thus, corresponds to the negligible storage and toughness.

Proposed pyramidal parametric space $m\widetilde{m}\widetilde{o}k$ for the fracture tip with the pressure-dependent leak-off is a direct generalisation of the triangular parametric space, face $m\widetilde{m}k$, for Carter's (pressure-independent) leak-off [Garagash et al., 2011], by the addition of the new vertex $\widetilde{o}$. The emergent edges $\widetilde{o}k$, $\widetilde{m}\widetilde{o}$, and $m\widetilde{o}$ are expected to describe the transitions of the corresponding limiting solutions with distance from the crack tip between the corresponding vertices (from the 2$^{\text{nd}}$ to the 1$^{\text{st}}$, i.e. $\widetilde{m}\widetilde{o}-$edge corresponds to the transition from the near-field $\widetilde{o}$ to the far-field $\widetilde{m}$, etc). As discussed in the above, the $\widetilde{o}-$vertex solution can be realised only in the near-field of a semi-infinite fracture, thus, suggesting that the $\widetilde{o}k-$edge may in fact corresponds to the near-field expansion of the $k-$vertex ($w \propto x^{1/2}$) which includes the next order correction given by $\widetilde{o}-$vertex solution ($w \propto x^{3/2}$), and this correction may come to eventually dominate (over the $k-$term) with increasing distance from the tip.

In the case of the other two edges involving the $\widetilde{o}-$vertex as the fracture near-field, i.e. $\widetilde{m}\widetilde{o}$ ($K' = 0$, $C' \to \infty$) and $m\widetilde{o}$ ($K' = 0$, $C' \propto \sigma'_o = 0$), they should in principle provide solutions for the entire semi-infinite HF under the corresponding limiting values of the parameters. Before attempting these (and other edge) solutions, let us attempt to constrain the a priori unknown near-field coefficient $B_{\widetilde{o}}$ in

the $\widetilde{o}$ expression for the opening $w = B_{\widetilde{o}}x^{3/2}$ ($x \to 0$). Using the inverted form of the elasticity equation (2.4) with $K' = 0$, and formally passing to the asymptotic limit $x \to 0$ under the integral, we get

$$B_{\widetilde{o}} = \frac{8}{3\pi E'} \int_0^\infty \frac{p(s)}{s^{3/2}} ds. \qquad (3.3)$$

Since $p(s \to 0) = -\sigma_0' - \frac{3}{2}B_{\widetilde{o}}\frac{V^{1/2}}{Q'}s$ (Table 3.2), the above integral expression for $B_{\widetilde{o}}$ converges (finite) for the $m\widetilde{o}-$edge (when $\sigma_o' = 0$) and diverges for the $\widetilde{m}\widetilde{o}-$edge. This suggests that the underlining formal limit-taking procedure to arrive to (3.3) is not applicable to the latter ($\widetilde{m}\widetilde{o}-$edge), while conversely (3.3) can be used to constrain coefficient $B_{\widetilde{o}}$ in the former case ($m\widetilde{o}-$edge). Specifically, we observe for the $m\widetilde{o}-$edge that if the net pressure is negative in the entire crack coordinate domain ($p(s) < 0$ for all $s > 0$), which is suggested by the negative net pressure values in the both near-field and far-field, then (3.3) results in $B_{\widetilde{o}} < 0$ or, in other words, negative crack opening near the tip. This contradiction rules out the existence of the $m\widetilde{o}-$edge solution (under plausible assumption of the negative net pressure in the crack), which implies that the general solution to the problem does not have well-defined limiting solution when both toughness and leak-off (or, conversely, ambient effective stress) equal zero.

General solution of the fracture tip problem within the parametric pyramid transitions with increasing distance from the tip from the near-field k to the far-field $m-$vertex, and in different limiting cases can collapse onto or be attracted to the series of faces and/or edges, as apparent from their parametric definitions. To identify non-dimensional parameters which fix a given solution trajectory in the parametric space, we follow the methodology of Garagash et al. [2011], and introduce characteristic scales for the transition distance ℓ_*, opening w_*, and pressure p_* closely related to the evolution of the solution along a given edge in the parametric space between the two corresponding vertices, or the 'edge-scalings'.

Edge-scalings mk, $\widetilde{m}k$, and $m\widetilde{m}$ are defined after Garagash et al. [2011] such that the solutions for either $p(x)$ or $w(x)$ for the corresponding two vertices forming the edge in question 'intersect' at $x \sim \ell_*$. For example, in the case of the storage

$mk-$edge, we find the characteristic length by contrasting the k and m asymptotes for the opening, $w_* = \ell_k^{1/2}\ell_*^{1/2} = \ell_m^{1/3}\ell_*^{2/3}$, while p_* follows from the elastic scaling constraint $w_*/\ell_* = p_*/E'$. Edge-scalings which involve vertex $\widetilde{o}$ (i.e. $\widetilde{m}\widetilde{o}$ and $\widetilde{o}k$) are obtained similarly but also recognising that the $\widetilde{o}-$asymptote depends on the solution trajectory (via a priori unknown prefactor). In the $\widetilde{m}\widetilde{o}-$case, the transition lengthscale ℓ_* is found by contrasting the leading order $\widetilde{o}-$asymptote for the net pressure (i.e. $p \approx -\sigma_o'$) with that of the $\widetilde{m}-$vertex, i.e. $p_* = \sigma_o' = E'(\ell_{\widetilde{m}}/\ell_*)^{3/8}$, while w_* follows from the elastic constraint. In the $\widetilde{o}k-$scaling the characteristic pressure is taken equal to $p_* = \sigma_0'$. Using p_*, elastic scaling constraint and balancing $\widetilde{o}$ and k vertex solutions, we find $\ell_* = K'^2/\sigma_o'^2$ and $w_* = K'^2/E'\sigma_o'$. All of the above edge-scalings are recorded in Table 3.3.

Scaling	ℓ_*	w_*	p_*
mk	$\ell_{mk} = \ell_k^3/\ell_m^2$	ℓ_k^2/ℓ_m	$E'\,\ell_m/\ell_k$
$m\widetilde{m}$	$\ell_{m\widetilde{m}} = \ell_{\widetilde{m}}^9/\ell_m^8$	$\ell_{\widetilde{m}}^6/\ell_m^5$	$E'\,(\ell_m/\ell_{\widetilde{m}})^3$
$\widetilde{m}k$	$\ell_{\widetilde{m}k} = \ell_k^4/\ell_{\widetilde{m}}^3$	$\ell_k^{5/2}/\ell_{\widetilde{m}}^{3/2}$	$E'\,(\ell_{\widetilde{m}}/\ell_k)^{3/2}$
$\widetilde{m}\widetilde{o}$	$\ell_{\widetilde{m}\widetilde{o}} = (E'/\sigma_o')^{8/3}\,\ell_{\widetilde{m}}$	$(E'/\sigma_0')^{5/3}\,\ell_{\widetilde{m}}$	σ_0'
$\widetilde{o}k$	$\ell_{\widetilde{o}k} = (K'/\sigma_0')^2$	$K'^2/(E'\sigma_0')$	σ_0'

Table 3.3: Characteristic distance from the tip ℓ_*, pressure p_*, and opening $w_* = (p_*/E')\ell_*$, corresponding to the five scalings of the problem.

Comparing three transition (edge) lengthscales within a given parametric face of the pyramid $m\widetilde{m}\widetilde{o}k$ allows to identify a 'trajectory number' parameterising that face solution. Considering, for example, the zero-leak-in face $m\widetilde{m}k$, one can introduce a single number expressible as a ratio of any two of the this face's three transition lengthscales (ℓ_{mk}, $\ell_{m\widetilde{m}}$, and $\ell_{\widetilde{m}k}$) [Garagash et al., 2011]

$$\chi = \left(\frac{\ell_{m\widetilde{m}}}{\ell_{mk}}\right)^{1/6} = \left(\frac{\ell_{mk}}{\ell_{\widetilde{m}k}}\right)^{1/2} = \left(\frac{\ell_{m\widetilde{m}}}{\ell_{\widetilde{m}k}}\right)^{1/8} = \frac{C'E'}{K'V^{1/2}}. \tag{3.4}$$

This number, which can be interpreted as a dimensionless leak-off or ambient effective stress (since $C' = Q'\sigma_o'$), or non-dimensional reciprocal of toughness, parameterises solution trajectory within the $m\widetilde{m}k-$face. The limiting case $\chi \to 0$

corresponds to the storage-dominated $mk-$edge solution

$$\text{zero leak-in, } \chi = 0: \quad k \underset{\ell_{mk}}{\rightarrow} m, \tag{3.5}$$

which transitions from the k to the m vertex with distance from the tip over length-scale ℓ_{mk} (shown by blue-colour trajectory in figure 3-2). While the other limiting case $\chi \to \infty$ corresponds to the separation of the corresponding transitional scales, $\ell_{\widetilde{m}k} \ll \ell_{m\widetilde{m}}$, (3.4), leading to the nested solution structure corresponding to the succession of the two edge solutions ($\widetilde{m}k$ and $m\widetilde{m}$)

$$\text{zero leak-in, } \chi \to \infty: \quad k \underset{\ell_{\widetilde{m}k}}{\rightarrow} \widetilde{m} \underset{\ell_{m\widetilde{m}}}{\rightarrow} m, \tag{3.6}$$

signifying transition with distance from the tip first from the k to $\widetilde{m}-$vertex over lengthscale $\ell_{\widetilde{m}k}$ and then from the $\widetilde{m}$ to m vertex over lengthscale $\ell_{m\widetilde{m}}$ (shown by brown-colour trajectory in figure 3-2).

Similarly, for the zero-storage face $\widetilde{m}\widetilde{o}k$, $\chi \to \infty$, we define another number in terms of ratios of any two of the corresponding three edge lengthscales ($\ell_{\widetilde{o}k}$, $\ell_{\widetilde{m}\widetilde{o}}$, and $\ell_{\widetilde{m}k}$)

$$\zeta = \left(\frac{\ell_{\widetilde{o}k}}{\ell_{\widetilde{m}k}} \right)^{1/6} = \left(\frac{\ell_{\widetilde{m}\widetilde{o}}}{\ell_{\widetilde{o}k}} \right)^{1/2} = \left(\frac{\ell_{\widetilde{m}\widetilde{o}}}{\ell_{\widetilde{m}k}} \right)^{1/8} = \frac{E'}{K'} \left(M'Q'V^{1/2} \right)^{1/3}, \tag{3.7}$$

which can be interpreted as dimensionless leak-in or a reciprocal of toughness. This number parameterises solution trajectory within the $\widetilde{m}\widetilde{o}k-$face. The limiting case $\zeta \to 0$ corresponds to the leak-off-dominated $\widetilde{m}k-$edge solution, also a part of the limiting trajectory (3.6) in the $m\widetilde{m}k-$face. While $\zeta \to \infty$ corresponds to the separation of the relevant transitional scales, $\ell_{\widetilde{o}k} \ll \ell_{\widetilde{m}\widetilde{o}}$, (3.7), leading to the nested solution structure corresponding to the succession of the two edge solutions ($\widetilde{o}k$ and $\widetilde{m}\widetilde{o}$) with distance from the tip

$$\chi \to \infty, \ \zeta \to \infty: \quad k \underset{\ell_{\widetilde{o}k}}{\rightarrow} \widetilde{o} \underset{\ell_{\widetilde{m}\widetilde{o}}}{\rightarrow} \widetilde{m}. \tag{3.8}$$

For the the zero-toughness face $m\widetilde{m}\widetilde{o}$, $\chi \to \infty$, we can define another number in

terms of ratio of the $\widetilde{m}\widetilde{o}$ and $m\widetilde{m}-$edge lengthscales

$$\psi = \left(\frac{\ell_{m\widetilde{m}}}{\ell_{\widetilde{m}\widetilde{o}}}\right)^{1/8} = \sigma_o' \left(\frac{Q'}{M'^{1/2}V}\right)^{2/3}, \tag{3.9}$$

which can be interpreted as, e.g., dimensionless effective confining stress. Note that ψ is not an independent parameter, but expressible in terms of the previously introduced leak-off χ and leak-in ζ numbers, $\psi = \chi/\zeta$. This number parameterises solution trajectory within the $m\widetilde{m}\widetilde{o}-$face, such that $\psi \to \infty$ corresponds to the separation of the two lengthscales, $\ell_{\widetilde{m}\widetilde{o}} \ll \ell_{m\widetilde{m}}$, (3.9), resulting in the solution comprised of the two edge solutions ($m\widetilde{o}$ and $m\widetilde{m}$)

$$\chi \to \infty, \ \psi = \chi/\zeta \to \infty: \quad \widetilde{o} \underset{\ell_{\widetilde{m}\widetilde{o}}}{\to} \widetilde{m} \underset{\ell_{m\widetilde{m}}}{\to} m. \tag{3.10}$$

The other limit, $\psi = 0$, corresponding to the viscosity-leak-in $m\widetilde{o}-$edge, is not expected to exist per discussion in the above. The behaviour of the solution within the $m\widetilde{m}\widetilde{o}$ and particularly how it approaches the non-existing $m\widetilde{o}-$edge with diminishing value of ψ is to be explored numerically.

We note that in the case when the parametric conditions in (3.8) and (3.10) are combined, i.e. when $\chi \to \infty$, $\zeta \to \infty$, and $\psi = \chi/\zeta \to \infty$, the three scales separate, $\ell_{\widetilde{o}k} \ll \ell_{\widetilde{m}\widetilde{o}} \ll \ell_{m\widetilde{m}}$, and the 'triple-nested' solution structure is realised

$$\chi \to \infty, \ \zeta \to \infty, \ \psi = \chi/\zeta \to \infty: \quad k \underset{\ell_{\widetilde{o}k}}{\to} \widetilde{o} \underset{\ell_{\widetilde{m}\widetilde{o}}}{\to} \widetilde{m} \underset{\ell_{m\widetilde{m}}}{\to} m, \tag{3.11}$$

as shown by the green-colour trajectory in figure 3-2.

For the fourth and final face of the pyramid, the zero-leak-off face $m\widetilde{o}k$, $\chi = 0$, we can use the previously defined non-dimensional leak-in number ζ to track solution trajectories, such that $\zeta = 0$ corresponds to the storage $mk-$edge, and $\zeta \to \infty$ corresponds to the non-existing limit of either $m\widetilde{o}-$edge or the $\widetilde{o}k-$edge. (Note that the $\widetilde{o}k-$edge can only be realised as the near or near-to-intermediate field of a given solution, thus, non-existence of the $m\widetilde{o}$ solution, which would form the intermediate-to-far-field solution in the limit $\zeta \to \infty$, implies the absence of the near-to-intermediate-field, $\widetilde{o}k-$edge, solution within the zero-leak-off face $m\widetilde{o}k$).

3.2.2.3 Asymptotic expansions of the vertices

Some insight into how the solution departs from the vertices in the parametric space in response to small perturbation of problem parameters and distance from the fracture tip can be afforded by constructing corresponding asymptotic expansions.

3.2.2.3.1 Expansion near $k-$vertex

The near-field $k-$vertex expression (table 3.2) for the net pressure is simply given by the value at tip set by the balance between incipient fluid exchange and crack opening, respectively, and thus independent of the fluid flow along the crack channel. The latter becomes more important when moving away from the tip, and can be accounted for by incorporating next order terms in the $k-$vertex asymptotic expansion. The $k-$expansion for the net fluid pressure is given by

$$\zeta > 0: \quad \frac{p}{E'} = \frac{\ell_k^{1/2}}{\ell_1^{1/2}} \left[-\frac{1}{\zeta^3} + \frac{1}{\gamma(\zeta)} \left(\frac{x}{x_o} \right)^{\gamma(\zeta)} \right], \tag{3.12}$$

$$\zeta = 0: \quad \frac{p}{E'} = \frac{\ell_k^{1/2}}{\ell_1^{1/2}} \ln \left(\frac{x}{x_o} \right) \tag{3.13}$$

in the general $\zeta > 0$ case and in the Carter's $\zeta \to 0$ limit [Garagash et al., 2011], respectively. Lengthscale ℓ_1 is defined in terms of a pair of transitional lengthscales

$$\ell_1 = (\ell_{mk}^{-1/2} + \ell_{\widetilde{m}k}^{-1/2})^{-2}.$$

Exponent $\gamma = \gamma(\zeta)$ in (3.12) is provided implicitly by

$$\frac{2}{\sqrt{\pi}} \frac{\Gamma \left(\gamma + \frac{3}{2} \right)}{\Gamma(\gamma)} = \zeta^3,$$

and x_o is a priori unknown part of the solution. One can directly confirm that (3.12) reduces to (3.13) in the Carter's limit $\zeta \to 0$ in view of the vanishing power-law exponent $\gamma(\zeta \to 0) \sim \zeta^3$.

We again point out the marked difference in the net pressure behaviour near the fracture tip between the general (pressure dependent leak-off case $\zeta > 0$) and

the Carter's limit. In the former, the net pressure at the tip is bounded $p(0) = -E'(\ell_k/\ell_0)^{1/2} = -(\sigma'_o + K'V^{1/2}/E'Q)$, while in the latter - logarithmically singular.

Corresponding k-vertex expansion for the crack opening is

$$\zeta > 0 : \quad w = \ell_k^{1/2} x^{1/2} + \frac{\ell_k^{1/2}}{\ell_1^{1/2}} \left[\frac{4 \tan \pi\gamma}{\gamma(1+\gamma)} \frac{x^{\gamma+1}}{x_o^\gamma} + \frac{x^{3/2}}{x_1^{1/2}} \right], \qquad (3.14)$$

$$\zeta = 0 : \quad w = \ell_k^{1/2} x^{1/2} + \frac{\ell_k^{1/2}}{\ell_1^{1/2}} 4\pi x, \qquad (3.15)$$

where x_o and x_1 are a priori unknown parts of the solution. Once again, the Carter's expression (3.15), identical to that of [Garagash et al., 2011] follows from the general expression (3.14) when taking the limit $\zeta \to 0$ in the latter. We observe that the choice of the next order term (after the leading term $\sim x^{1/2}$) in the opening expansion depends on the value of $\gamma(\zeta)$. Specifically, it is given by $x^{\gamma+1}$ term when $\gamma(\zeta) + 1 < 3/2$, corresponding to $\zeta < 0.862$, and by the $x^{3/2}$ term otherwise (when $\zeta > 0.862$). In relation to the problem parametric diagram, the ζ-dependent form of the next order term in (3.14) determines how the solution trajectory emanates from the $k-$vertex along a given ζ trajectory. For example, considering the zero-storage $\widetilde{m}\widetilde{o}k-$face, the zero-leak-in ($\zeta=0$) trajectory exits the k-vertex along the $\widetilde{m}k-$edge described by the linear correction $x^{\gamma(0)+1}$ ($\gamma(0) = 0$) to the opening, and the zero-leak-off ($\zeta = \infty$) trajectory exits the k-vertex along the $\widetilde{o}k-$edge described by the $x^{3/2}$ correction to the opening.

3.2.2.3.2 Expansion near $m-$vertex

The $m-$vertex solution does not depend on the rock toughness and the parameters defining fluid-exchange processes. Moving away from the far-field region, where the $m-$vertex dominates, towards the crack tip, the latter effects start to influence the solution. These higher-order effects can be captured in the m-vertex expansion which can be obtained using the procedure of Garagash et al. [2011] in the following

54

form:

$$w = \ell_m^{1/3} x^{2/3} \left[\beta_0 + \sum_{j=1}^{3} \beta_{-j} \left(\frac{\ell_{m\widetilde{m}}}{x} \right)^{j/6} + \mathring{\beta}_{-3} \left(\frac{\ell_{m\widetilde{o}}}{x} \right)^{1/2} + (\beta_{-4})_*(\chi, \zeta) \left(\frac{\ell_{m*}}{x} \right)^{2/3-h} \right],$$

(3.16)

$$\frac{p}{E'} = \ell_m^{1/3} x^{-1/3} \left[\delta_0 + \sum_{j=1}^{3} \delta_{-j} \left(\frac{\ell_{m\widetilde{m}}}{x} \right)^{j/6} + \mathring{\delta}_{-3} \left(\frac{\ell_{m\widetilde{o}}}{x} \right)^{1/2} + (\delta_{-4})_*(\chi, \zeta) \left(\frac{\ell_{m*}}{x} \right)^{2/3-h} \right],$$

(3.17)

where coefficients β_{-j} are

$$\beta_0 = 2^{1/3} 3^{5/6}, \ \beta_{-1} = \frac{1}{2}, \ \beta_{-2} = -\frac{3^{1/6}}{2^{7/3}}, \ \beta_{-3} = \frac{2^{7/3}}{3^{5/3}}, \ \mathring{\beta}_{-3} = -\frac{2^{7/3}}{3^{5/3}} \frac{9 \Gamma \left(\frac{2}{3} \right) \Gamma \left(\frac{5}{6} \right)}{2\sqrt{\pi}},$$

and $\delta_{-j} = \beta_{-j} f \left(\frac{2}{3} - \frac{j}{6} \right)$ for $j = 0, 1, 2, 3$, $\mathring{\delta}_{-3} = \mathring{\beta}_{-3} f(7/6)$, $(\delta_{-4})_* = (\beta_{-4})_* f(h)$ with $h = 0.138673$.

The terms in equation (3.16) and (3.17) underlined by a single line are scaled by characteristic length $\ell_{m\widetilde{m}}$ and represent leak-off corrections to the m-vertex solution. The term underlined by the double line can be scaled by either of the three pertinent transitional lengthscales (i.e., ℓ_{m*} is given by either ℓ_{mk}, $\ell_{m\widetilde{m}}$, or $\ell_{m\widetilde{o}}$) since the coefficient $\beta_{-4}(\chi, \zeta)$ in front of it can be found only from the complete numerical solution. As a result, this term can be interpreted as correction in either toughness, leak-off, or leak-in. The corresponding expressions for the coefficient $(\beta_{-4})_*$ are linked by the following relations: $(\beta_{-4})_k = \chi^{4-6h} (\beta_{-4})_{\widetilde{m}} = \zeta^{4-6h} (\beta_{-4})_{\widetilde{o}}$.

The structure of the derived $m-$vertex expansion differs from that in the case of the Carter's leak-off [Garagash et al., 2011] by a single term, underlined in the above by a dotted line and corresponding to the pressure-dependent, leak-in correction, scaled by the $\ell_{m\widetilde{o}} = (E'/\sigma_o')^2 (M'Q'V^1/2)^{2/3}$ transitional lengthscale.

3.2.2.3.3 Expansion near $\widetilde{m}-$vertex

The $\widetilde{m}-$vertex solution may arise at intermediate distances $\max (\ell_{\widetilde{m}k}, \ell_{\widetilde{m}o}) \ll x \ll \ell_{\widetilde{m}m}$ from the fracture tip, when the featured transitional lengthscales separate,

55

within one of the corresponding limiting solution trajectories given by $k \to \widetilde{m} \to m$, (3.6), $\widetilde{o} \to \widetilde{m} \to m$, (3.10), or the combination thereof $k \to \widetilde{o} \to \widetilde{m} \to m$, (3.11), and shown by brown and green colour in figure 3-2. The essential condition for the existence of the intermediate $\widetilde{m}$-asymptote is therefore $\chi \gg 1$ and $\psi = \chi/\zeta \gg 1$, where the latter is always satisfied along the zero-leak-in (Carter's) edge, $\zeta = 0$, previously explored by Garagash et al. [2011].

The asymptotic expansion about the $\widetilde{m}-$vertex solution, including small corrections due to toughness, storage, and pressure-dependent leak-off effects is given by

$$
w = \ell_{\widetilde{m}}^{3/8} x^{5/8} \left[\widetilde{\beta}_0 + \sum_{j=1}^{3} \widetilde{\beta}_j \left(\frac{x}{\ell_{m\widetilde{m}}} \right)^{j/8} + \overset{\circ}{\widetilde{\beta}}_{-3} \left(\frac{\ell_{\widetilde{m}\widetilde{o}}}{x} \right)^{\frac{3}{8}} + (\widetilde{\beta}_{-1})_* (\chi, \zeta) \left(\frac{\ell_{\widetilde{m}*}}{x} \right)^{\frac{5}{8} - \widetilde{h}} \right],
$$
(3.18)

$$
\frac{p}{E'} = \ell_{\widetilde{m}}^{3/8} x^{-3/8} \left[\widetilde{\delta}_0 + \sum_{j=1}^{2} \widetilde{\delta}_j \left(\frac{x}{\ell_{m\widetilde{m}}} \right)^{j/8} + \widetilde{\delta}_3 \left(\frac{x}{\ell_{m\widetilde{m}}} \right)^{3/8} \ln \left(\frac{x}{\widetilde{x}_0} \right) + \overset{\circ}{\widetilde{\delta}}_{-3} \left(\frac{\ell_{\widetilde{m}\widetilde{o}}}{x} \right)^{\frac{3}{8}} + (\widetilde{\delta}_{-1})_* (\chi, \zeta) \left(\frac{\ell_{\widetilde{m}*}}{x} \right)^{\frac{5}{8} - \widetilde{h}} \right],
$$
(3.19)

where $\widetilde{h} = 0.0699928$ and known coefficients are given by $\widetilde{\beta}_0 = 2.53356$, $\widetilde{\beta}_1 = 1.30165$, $\widetilde{\beta}_2 = -0.451609$, $\overset{\circ}{\widetilde{\beta}}_{-3} = -0.524805$, and by $\widetilde{\delta}_j = \widetilde{\beta}_j f \left(\frac{5}{8} + \frac{j}{8} \right)$ for $j = 0, 1, 2$; $\overset{\circ}{\widetilde{\delta}}_{-3} = \overset{\circ}{\widetilde{\beta}}_{-3} f(1/4)$; $\widetilde{\delta}_{-1} = \widetilde{\beta}_{-1} f(\widetilde{h})$; and $\widetilde{\delta}_3 = \widetilde{\beta}_3 / 4\pi$. Parameters $\widetilde{\beta}_{-1}$ and $\widetilde{x}_0$ are a priori not known and are a part of the general numerical solution.

The terms underlined by the dotted and double lines correspond to the leak-in and toughness/leak-in corrections to the leading order ($\widetilde{m}-$vertex) term within the $\widetilde{m}\widetilde{o}k-$face solution, appropriately scaled with that face transitional lengthscales. The single line designates corrections due to fracture storage effects in the $m\widetilde{m}-$edge solution, appropriately scaled by that edge transitional lengthscale. In the zero storage case ($\ell_{\widetilde{m}m} = \infty$), the leading term and terms underlined by the double line yield the far-field ($x \gg \ell_{\widetilde{m}k}$) of the $\widetilde{m}k-$edge solution. Further, in the zero toughness case ($\ell_{\widetilde{m}k} = 0$), the leading term and terms underlined by the single line compose

the near-field ($x \ll \ell_{\widetilde{m}m}$) of the $\widetilde{m}m-$edge solution.

3.2.3 Solution

In this section, we will first introduce normalised governing equations based on different 'edge' scalings (table 3.3), followed by exploration of solutions in the problem parametric space (figure 3-2): (i) the parameterless edge-solutions, (ii) one-parametric solution families of solutions for the faces of the parametric pyramid, and (iii) representative examples of two-parametric solution trajectories within the pyramid.

3.2.3.1 Normalised equations

Upon introducing the normalised coordinate $\xi = x/\ell_*$, fracture opening $\Omega = w/w_*$ and net pressure $\Pi = p/p_*$, the corresponding normalised governing equations in different edge-scalings (table 3.3) are given in table 3.4.

Scaling	Lubrication (2.7), (3.2), (2.9)	Elasticity (2.3)	Propagation (2.2) $\xi \to 0$
mk	$\Omega^3 \frac{d\Pi}{d\xi} = \Omega + \chi\,\xi^{1/2} + \zeta^3 \int_0^\xi \frac{\Pi(s)ds}{2\sqrt{\xi-s}}$		$\Omega = \xi^{1/2}$
$m\widetilde{m}$	$\Omega^3 \frac{d\Pi}{d\xi} = \Omega + \xi^{1/2} + \psi^{-3} \int_0^\xi \frac{\Pi(s)ds}{2\sqrt{\xi-s}}$		$\Omega = \chi^{-1}\,\xi^{1/2}$
$\widetilde{m}k$	$\Omega^3 \frac{d\Pi}{d\xi} = \chi^{-1}\Omega + \xi^{1/2} + \zeta^3 \int_0^\xi \frac{\Pi(s)ds}{2\sqrt{\xi-s}}$	$\Pi(\xi) = \frac{1}{4\pi} \int_0^\infty \frac{d\Omega(s)}{\xi-s}$	$\Omega = \xi^{1/2}$
$\widetilde{m}\widetilde{o}$	$\Omega^3 \frac{d\Pi}{d\xi} = \psi^{-1}\Omega + \xi^{1/2} + \int_0^\xi \frac{\Pi(s)ds}{2\sqrt{\xi-s}}$		$\Omega = \zeta^{-1}\,\xi^{1/2}$
$\widetilde{o}k$	$\zeta^{-3}\,\Omega^3 \frac{d\Pi}{d\xi} = \chi^{-1}\Omega + \xi^{1/2} + \int_0^\xi \frac{\Pi(s)ds}{2\sqrt{\xi-s}}$		$\Omega = \xi^{1/2}$

Table 3.4: Normalised governing equations for the scaled opening $\Omega = w/w_*$ and net pressure $\Pi = p/p_*$ as a function of the scaled position $\xi = x/\ell_*$ in different scalings (ℓ_*, w_*, p_*) from table 3.3.

Normalised equations are parameterised by a pair of the non-dimensional numbers; which, depending on the used scaling, are either (χ, ζ) or (ψ, ζ), as defined in (3.4), (3.7) and (3.9).

When presenting the overall solution, we will make the most use of the $mk-$scaling, as it is based on the transition between the near k and the far m field behaviour of the general solution. In the limiting cases, when either one of the dissipation

mechanisms or one of the storage mechanisms is negligible, corresponding to the four different (one-parametric) faces of the parametric pyramid $m\widetilde{m}\widetilde{o}k$, we will use the scaling pertinent to the corresponding near-to-far transition. For example, the zero-leak-in face $m\widetilde{m}k$ ($Q' = 0$) and the zero-leak-off face $m\widetilde{o}k$ ($C' \propto \sigma'_o = 0$), are both conveniently solved in the mk−scaling with $\zeta = 0$ (parameterised by χ) and with $\chi = 0$ (parameterised by ζ), respectively. The zero-storage face $\widetilde{m}\widetilde{o}k$ ($C' = \infty$), is conveniently solved in the $\widetilde{m}k$−scaling with $\chi = \infty$ (parameterised by ζ). Finally, for the zero-toughness face $m\widetilde{m}\widetilde{o}$ ($K' = 0$) and since the $m\widetilde{o}$−edge solution does not exist, we will use the $\widetilde{m}\widetilde{o}$−scaling with $\zeta = \infty$ (parameterised by $\psi = \chi/\zeta$).

To compute the numerical solution, we extend the numerical algorithm of Garagash et al. [2011], their Appendix F, to accommodate for the distinctive features of our model, which include the drastically different, non-singular near field compared to the singular one in the Carter's HF tip analysed in the previous work. The details of the numerical algorithm are given in section 3 of the supplementary material of paper [Kanin et al., 2020d].

3.2.3.2 Edge solutions

The mk, $\widetilde{m}k$, $\widetilde{m}m$−edge solutions have been previously obtained by Garagash et al. [2011], see their figure 3 for the opening and net pressure profiles in the respective edge scalings. The solution for the new $\widetilde{m}\widetilde{o}$−edge in its respective scaling is shown in figure 3-3. For the latter, we estimate $B_{\widetilde{o}} \approx 3.322 \cdot w_{\widetilde{m}\widetilde{o}}/\ell_{\widetilde{m}\widetilde{o}}^{3/2}$ for the dimensional coefficient $B_{\widetilde{o}}$ of the $\widetilde{o}$−vertex ($w = B_{\widetilde{o}}x^{3/2}$) realised in the near-field of this edge. As stipulated earlier, the edge solutions detail the transition with distance from the tip between the corresponding pair of the vertex solutions describing the near and the far field, respectively. For example, figure 3-3 shows such a transition between the near, $\widetilde{o}$−vertex, and the far, $\widetilde{m}$−vertex, fields for the $\widetilde{m}\widetilde{o}$−edge solution.

3.2.3.3 Face solutions

One-parametric families of solutions for the crack opening and net-pressure corresponding to $m\widetilde{m}k$, $m\widetilde{o}k$, $\widetilde{m}\widetilde{o}k$ and $m\widetilde{m}\widetilde{o}$−faces of the parametric pyramid (figure 3-2) are shown in figures 3-4-3-7 in their preferred scalings, (a), and also in the

58
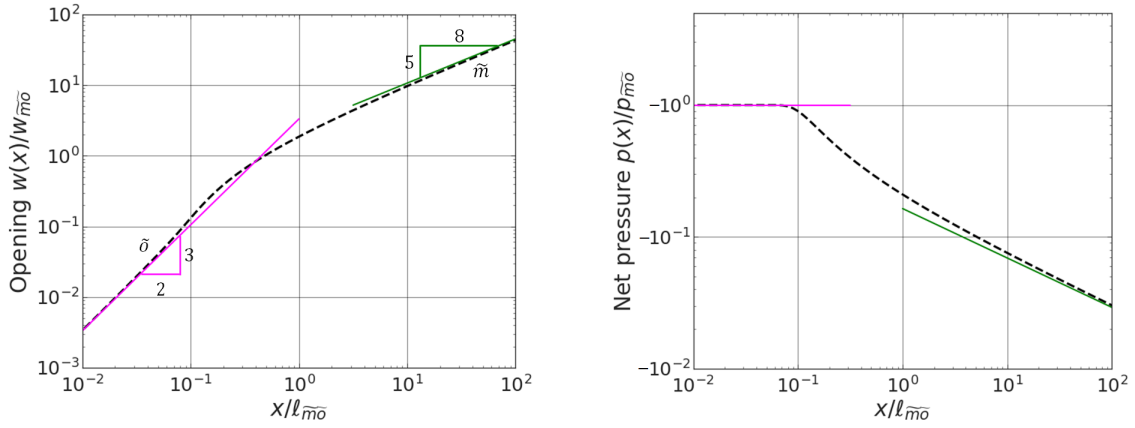
Figure 3-3: Fracture opening (left) and net fluid pressure (right) profiles with distance from the crack tip for the $\widetilde{m}\widetilde{o}-$edge in the pertinent scaling (table 3.3). Vertex solutions corresponding to the near and far-field asymptotes are also shown.

(a)

(b)
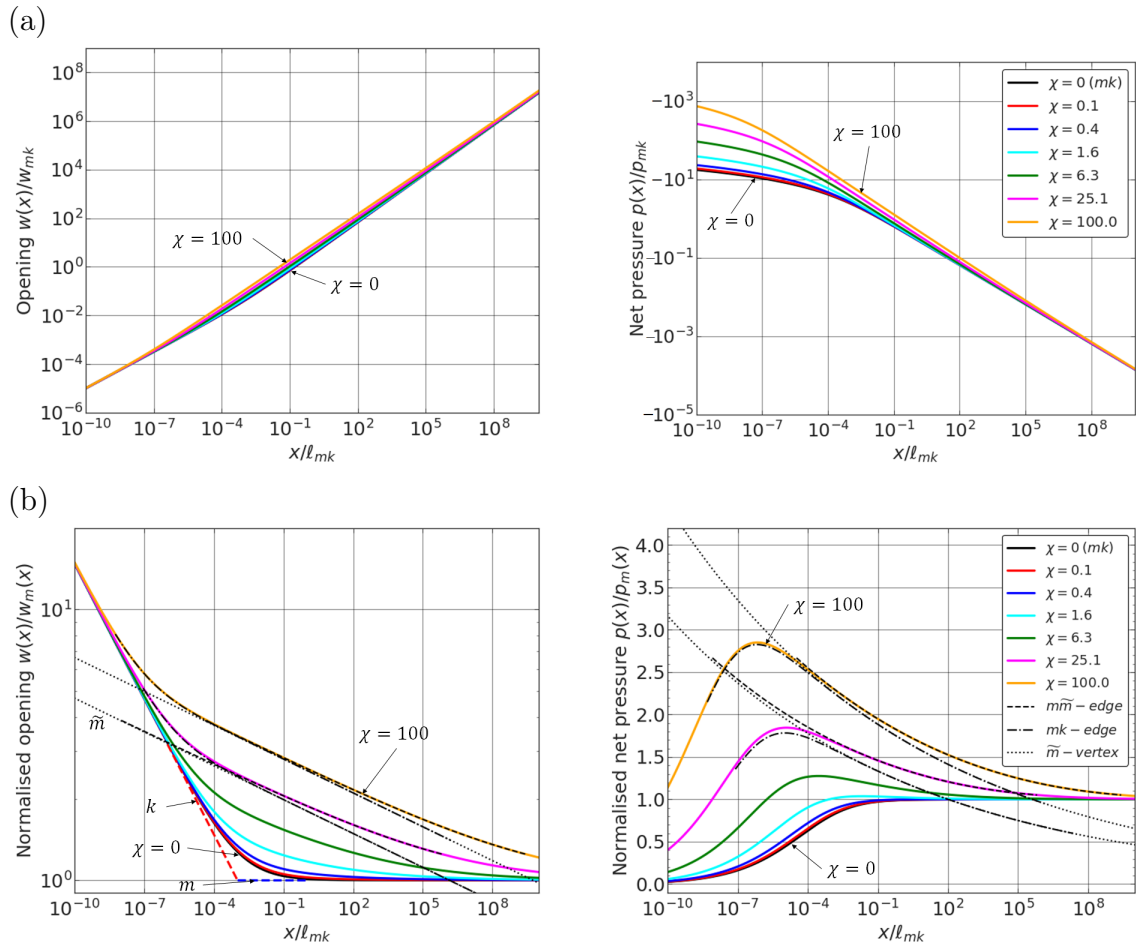
Figure 3-4: Zero-leak-in ($\zeta = 0$) $m\widetilde{m}k-$face solution for the fracture opening (left) and net fluid pressure (right) profiles in the $mk-$scaling for various values of the leak-off number χ. Solutions are shown in (a) the explicit form and (b) normalised by the $m-$vertex solution. The $\widetilde{m}k-$, $m\widetilde{m}-$edges, and k, m and $\widetilde{m}-$vertices are also shown in (b).

59

form normalised by the respective far-field asymptote, (b). In these plots, we also show the vertex solutions, as correspond to the near, far, and (where appropriate) intermediate fields of a given face solution.

The Carter's, zero-leak-in ($\zeta = 0$), $m\widetilde{m}k-$face solution is shown in figure 3-4 for various values of the leak-off number χ from $\chi = 0$ to $\chi = 100$. The former corresponds to the storage $mk-$edge solution trajectory ($k \to m$), while the latter closely approximates the two-edge ($\widetilde{m}k$ and $m\widetilde{m}$) solution trajectory marked by the emergence of the intermediate $\widetilde{m}-$vertex asymptote ($k \to \widetilde{m} \to m$). This face solution has been obtained previously by Garagash et al. [2011] and shown here for completeness.

The zero-leak-off ($\chi = 0$), $m\widetilde{o}k-$face solution is shown in figure 3-5 in the $mk-$scaling for various values of the leak-in number ζ from $\zeta = 0$ to $\zeta = 20$. The former, once again, corresponds to the storage $mk-$edge solution, while the latter signals large leak-in conditions. The solution is seen to evolve with increasing leak-in number such that the region dominated by the near-field $k-$asymptote expands outwards from the fracture tip, while the transition to the far-field $m-$asymptote takes place in increasingly abrupt fashion, as particularly evident for the crack opening (figure 3-5 left). The net pressure near field behaviour is dominated by the nearly constant (tip) value, which domain is seen to expand outward from the tip with increasing leak-in number. For large values of ζ, the net pressure initially decreases with the distance from the tip (signalling the dominance of leak-in and the reversed direction of the fluid flow inside the crack channel there), passes through the minimum, and eventually recover towards the zero value, as solution transitions towards the far-field $m-$asymptote. The net-pressure minimum becomes increasingly abrupt with increasing ζ, marking effective pinching of the fracture there and spatially correlating with the maximum crack opening gradient. The crack is effectively closed over the enlarging with ζ region adjacent to the fracture tip, such that its effective tip corresponds to the 'pinching' at the net-pressure minimum. No emergent intermediate $\widetilde{o}-$vertex (3/2 opening slope) is evident with increasing ζ (which would have led to the two-edge limiting solution trajectory $k \to \widetilde{o} \to m$), underscoring the previous assertion that the $m\widetilde{o}$-edge solution does not exist in the limit $\zeta \gg 1$ limit.
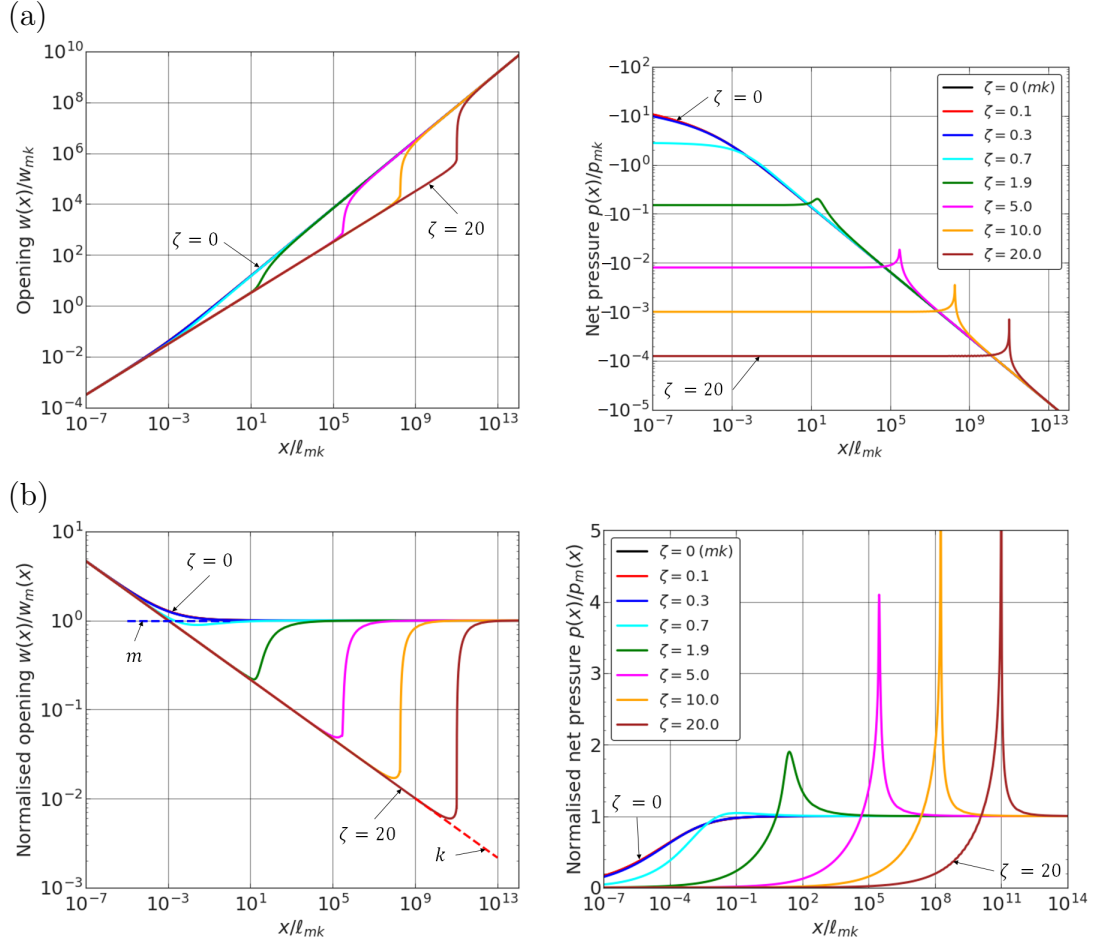
Figure 3-5: Zero-leak-off ($\chi = 0$) $m\widetilde{o}k-$face solution for the fracture opening (left) and net fluid pressure (right) profiles in the $mk-$scaling for various values of the leak-in number ζ: (a) explicit form and (b) normalised by the $m-$vertex solution. The k and $m-$vertices are also shown in (b).

The zero-storage ($\chi = \infty$), $\widetilde{m}\widetilde{o}k-$face solution is shown in figure 3-6 in the $\widetilde{m}k-$scaling for various values of the leak-in number ζ from $\zeta = 0$ to $\zeta = 10$. As previously, the former corresponds to the $mk-$edge solution, while the increasing leak-in leads to somewhat similar evolution of the solution to that within the $m\widetilde{o}k-$face considered in the above (figure 3-5). I.e. increasing leak-in leads to the expansion of the near k field outward from the crack tip, seen as the nearly constant net pressure (tip) value in figure 3-6a (left), with one important distinction from the $m\widetilde{o}k-$face in that the net-pressure is now monotonically increasing everywhere along the crack, without developing a pinching point (the local minimum). As a result, the intermediate $\widetilde{o}$ behaviour is seen to emerge at large leak-in ($\zeta = 10$), indicating the convergence of the solution trajectory towards the two-edge ($\widetilde{o}k$ and

61

$\widetilde{m}\widetilde{o}$) trajectory, $k \to \widetilde{o} \to \widetilde{m}$.

The zero-toughness ($\chi = \infty$), $m\widetilde{m}\widetilde{o}-$face solution is shown in figure 3-7 for various values of the effective-stress number $\psi = \chi/\zeta$ from $\psi = 0.5$ to $\psi = 100$. The small ψ value solution is approaching the non-existing $m\widetilde{o}-$edge limit, which is, as discussed previously in the context of approaching $m\widetilde{o}-$edge from within the $\widetilde{m}\widetilde{o}k-$face, characterised by the net pressure minimum and the crack pinching point. Large ψ solution approaches the limit of the two-edge ($\widetilde{m}\widetilde{o}$ and $m\widetilde{m}$) solution trajectory $\widetilde{o} \to \widetilde{m} \to m$ which is realised over very wide range of distances from the tip.

(a)

(b)
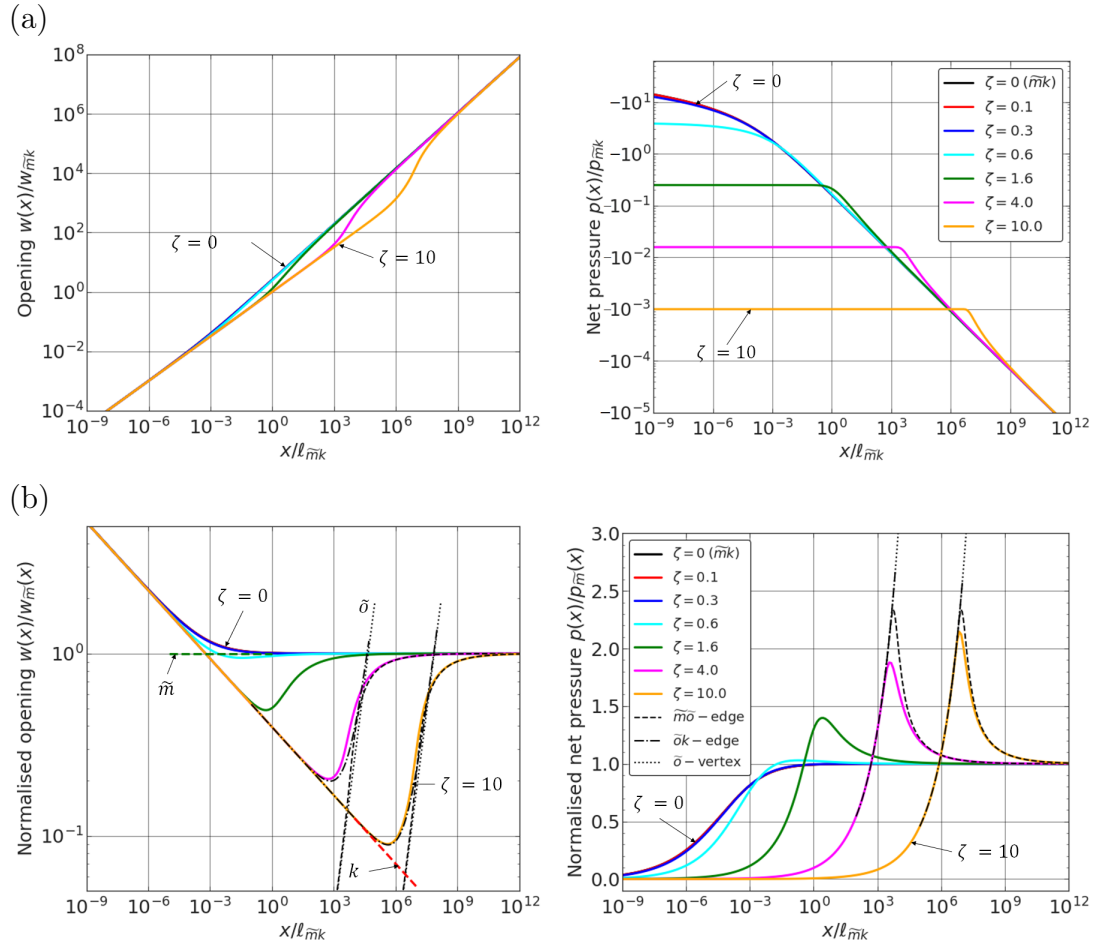
Figure 3-6: Zero-storage ($\chi = \infty$) $\widetilde{m}\widetilde{o}k-$face solution for the fracture opening (left) and net fluid pressure (right) profiles in the $\widetilde{m}k-$scaling for various values of the leak-in number ζ: (a) explicit form and (b) normalised by the $\widetilde{m}-$vertex solution. The $\widetilde{m}\widetilde{o}-$, $\widetilde{o}k-$edges, and k, $\widetilde{m}$ and $\widetilde{o}-$vertices are also shown in (b).

(a)

(b)
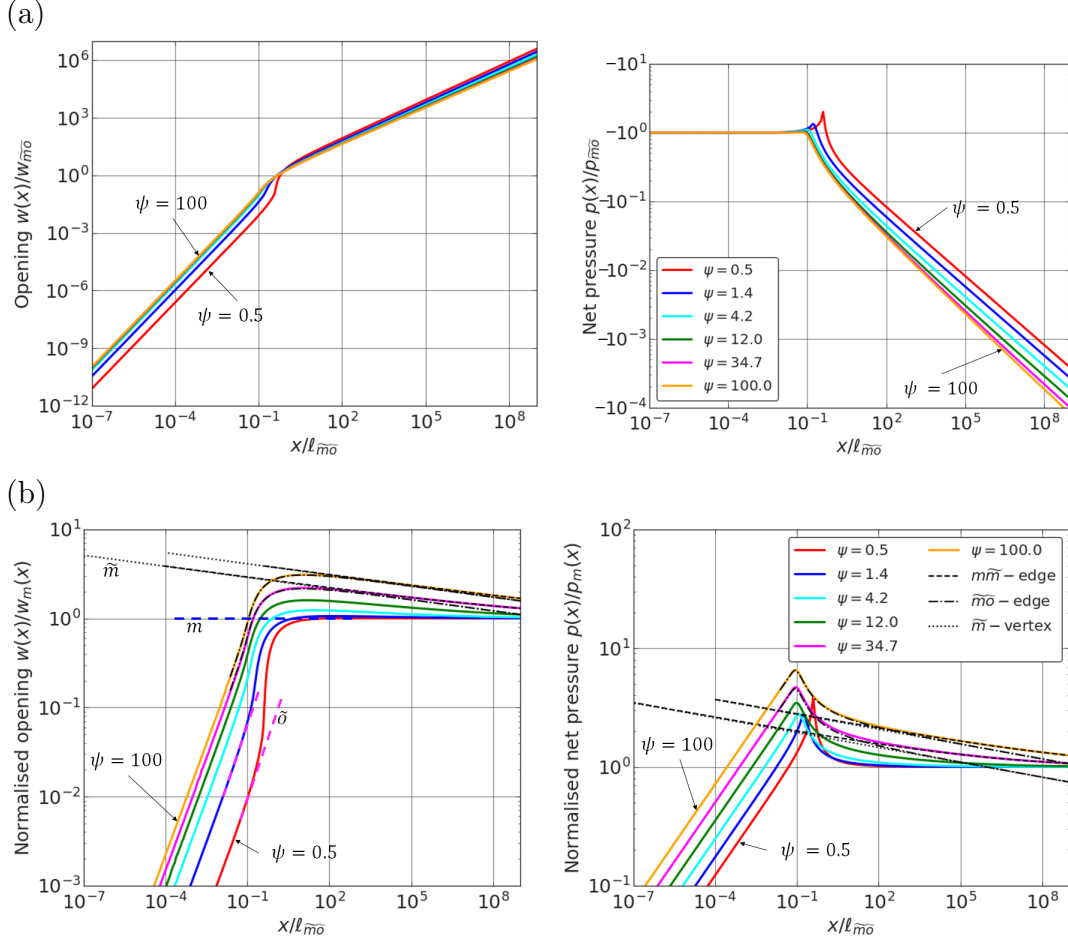
Figure 3-7: Zero-toughness ($\chi = \infty$) $m\widetilde{m}\widetilde{o}-$face solution for the fracture opening (left) and net fluid pressure (right) profiles in the $m\widetilde{o}-$scaling for various values of the leak-off-to-leak-in ratio $\psi = \chi/\zeta$: (a) explicit form and (b) normalised by the $m-$vertex solution. The $\widetilde{m}\widetilde{o}-$, $m\widetilde{m}-$ edges, and $\widetilde{o}$, m and $\widetilde{m}-$vertices are also shown in (b).

3.2.3.4   Examples of the general solution inside the parametric pyramid

For the presentation of particular solution trajectories within the parametric pyramid (i.e. when $0 < \chi, \zeta < \infty$), we choose several values of the leak-off parameter: $\chi = 0.1$, 1 and 10, and values of the leak-in parameter ζ are selected so that to maintain constant $O(1)$ non-dimensional leak-off-to-leak-in ratio $\chi/\zeta^3 = 1$, i.e. $\zeta = \chi^{1/3} = 0.46$, 1, 2.15, respectively. Fracture opening and net fluid pressure profiles for the aforesaid cases are shown in the $mk-$scaling in figure 3-8 and normalised by the m-vertex solution in figure 3-9. The corresponding Carter's leak-off solutions ($\zeta = 0$) are also shown by dashed black lines for comparison. Additionally, in figure 3-9, we show the near-field (k), the far-field (m) and the intermediate-

field ($\widetilde{m}$) vertex-solutions and their expansions (Section 3.2.2.3) by coloured dashed lines in order to underscore the corresponding asymptotic domains and degree of approximation for the solution afforded by the asymptotic expansions.

One of the distinguishing features of the obtained profiles as compared to the Carter's leak-off case is the finite value of the net fluid pressure at the fracture tip. In the $mk-$scaling, it is defined by the equation: $p(0)/p_{mk} = -(\chi + 1)/\zeta^3$ (table 3.2). From figures 3-8a, 3-9a one can find out that the departure of the solution from the Carter's one is small for $\chi = 0.1$ case, but it becomes more considerable for $\chi = 1$ (figures 3-8b, 3-9b) and $\chi = 10$ (figures 3-8c, 3-9c).

The applicability zone of the $m-$expansion shrinks when the value of the leak-off parameter χ increases. At the same time, the coordinate range, where $k-$expansion approximates the numerical solution, expands, and its length is much larger than in the Carter's leak-off case. Neither $\widetilde{m}$ nor $\widetilde{o}-$vertex solutions are realised as intermediate asymptotes in the solutions for the parametric choices in figures 3-8-3-9, i.e. $\chi \leq 10$ and $\zeta \leq 2.15$, since the conditions for these intermediate behaviours call for $\chi, \psi = \chi/\zeta \gg 1$ and $\chi, \zeta \gg 1$, respectively (see (3.10) and (3.8)). However, the intermediate $\widetilde{m}-$expansion (3.18), (3.19) does appear to closely approximate the numerical solution in the intermediate field in the case of $\chi = 10$ (figure 3-9c) signalling the emergent intermediate asymptotic behaviour. Indeed, this trend persists in figure 3-10, where we show the normalised solutions for higher values of the leak-off and leak-in numbers, $\chi = 100$, $\zeta = 4.64$ and $\chi = 1000$, $\zeta = 10$. We observe that the solution is closely approximated by (i) the $\widetilde{m}\widetilde{o}k-$face solution ($\chi = \infty$, see figure 3-6) and (ii) the $m\widetilde{m}-$edge solution matched over intermediate distances from the tip. In other words, corresponding solution trajectories are approaching the limit of $k \to (\widetilde{o}) \to (\widetilde{m}) \to m$ (see green-coloured trajectory in figure 3-2) where parenthesised intermediate vertices are emergent within the considered solutions.

In order to further highlight the dependence of the general numerical solution on the leak-in number ζ, we plot two series of solutions in figures 3-11 and 3-12 for fixed values of the leak-off number, $\chi = 1$ and $\chi = 100$, respectively, and variable leak-in number ζ. We confirm the significant departure of the solution from the zero leak-in Carter's case with increasing ζ, which can be in part attributed to (i) the near-field

(a) $\chi = 0.1$, $\zeta = 0.46$

(b) $\chi = 1$, $\zeta = 1$
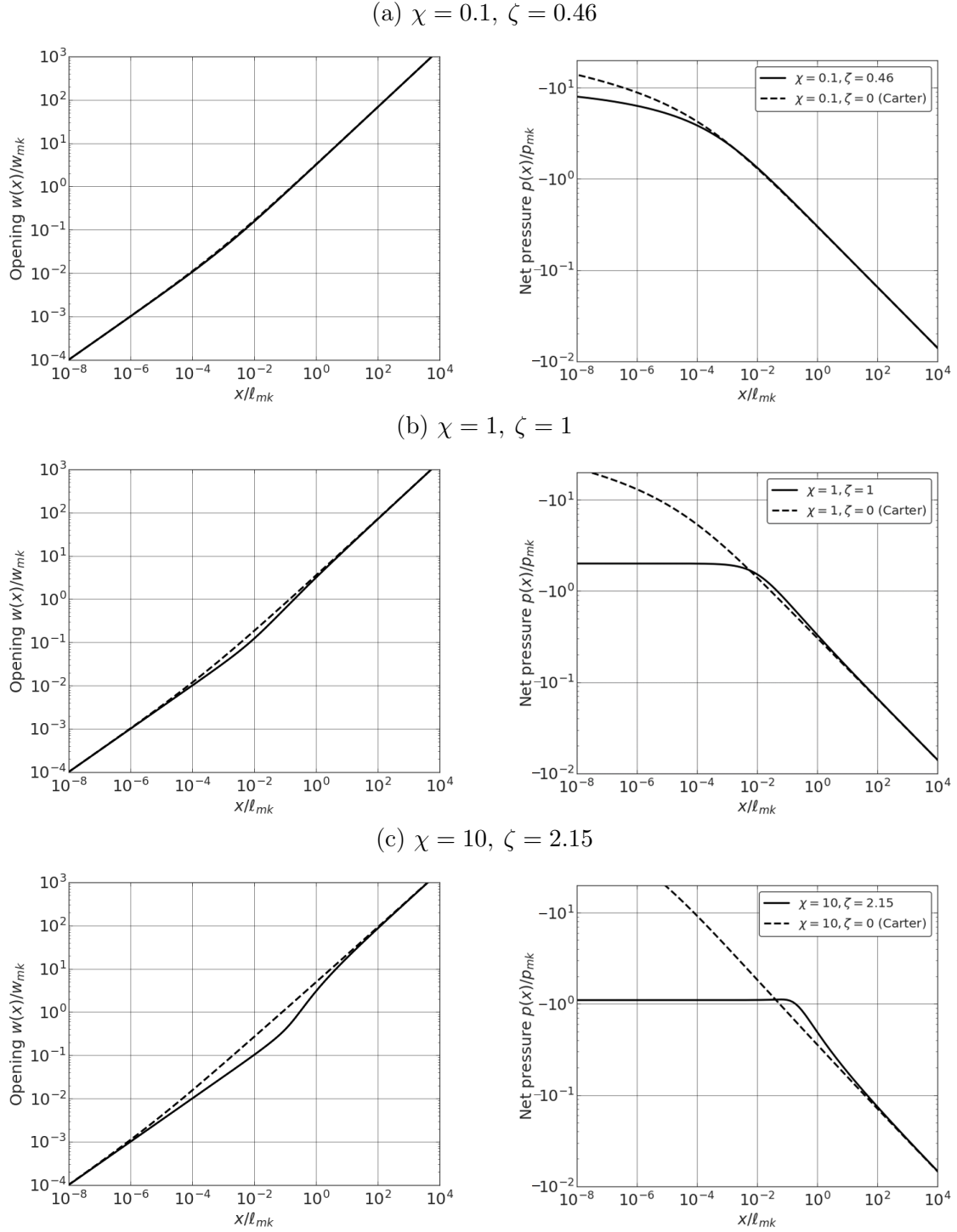
(c) $\chi = 10$, $\zeta = 2.15$

Figure 3-8: Solution for the fracture opening (left) and net fluid pressure (right) shown in the $mk-$scaling for fixed ratio $\chi/\zeta^3 = 1$ and different values of χ: (a) $\chi = 0.1$, $\zeta = 0.46$, (b) $\chi = 1$, $\zeta = 1$, (c) $\chi = 10$, $\zeta = 2.15$. The corresponding Carter's solutions ($\zeta = 0$) are shown by dashed lines for comparison.

behaviour ($\sim \sqrt{x}$ for the opening and constant value for the net pressure) reaching further away from the fracture tip; and (ii) significant reduction in the net-pressure

(a) $\chi = 0.1$, $\zeta = 0.46$
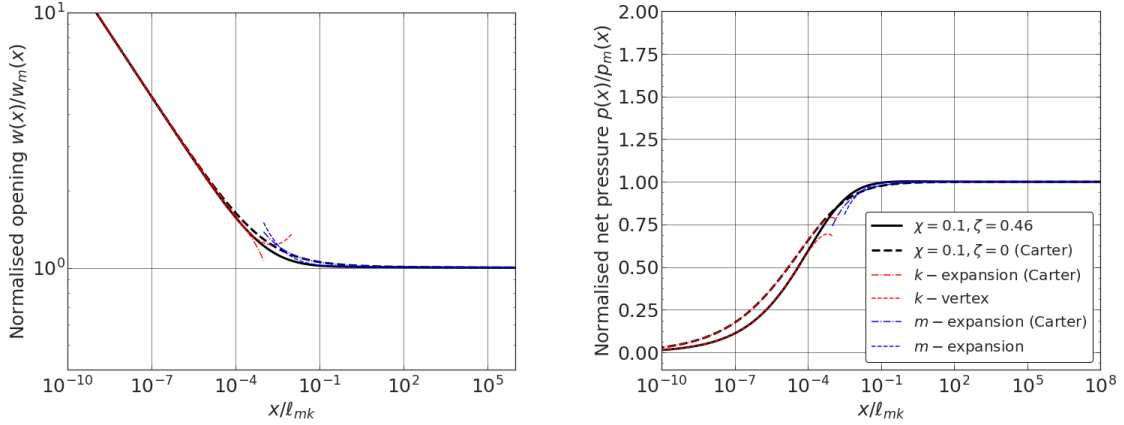
(b) $\chi = 1$, $\zeta = 1$
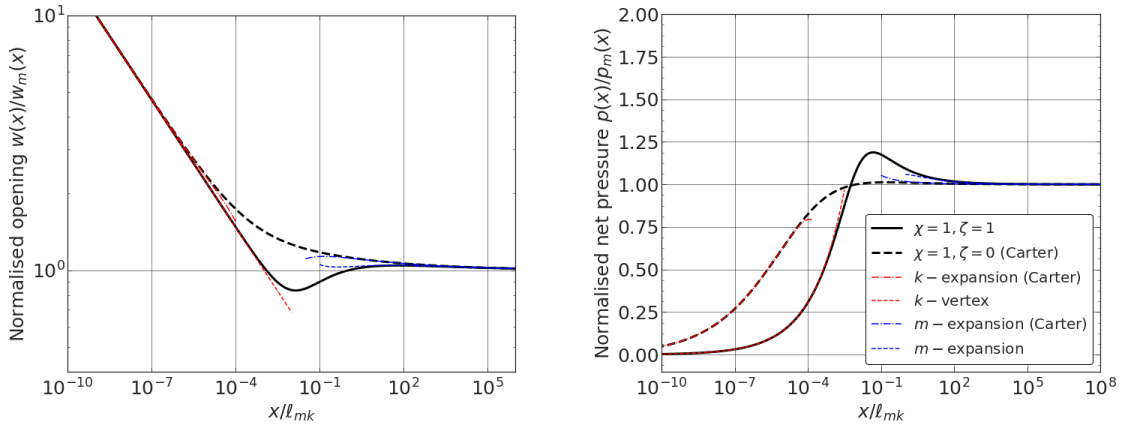
(c) $\chi = 10$, $\zeta = 2.15$
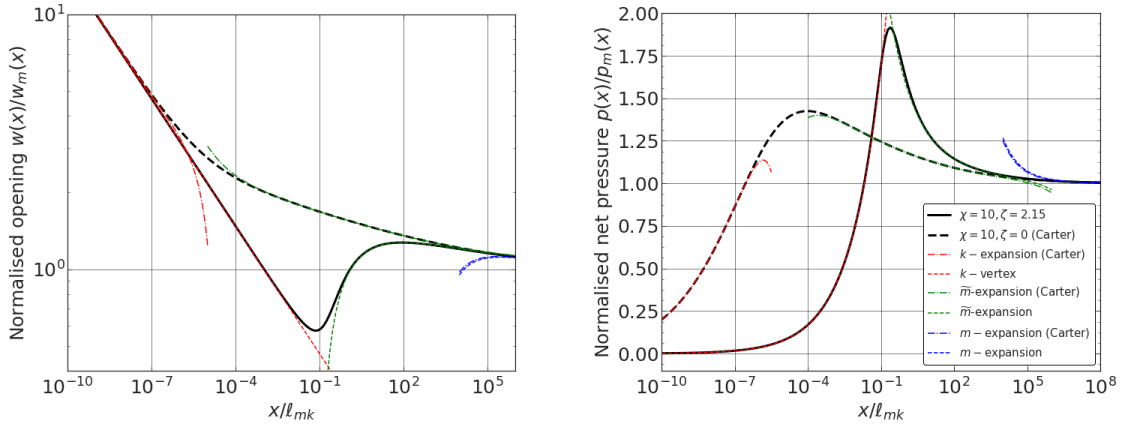
Figure 3-9: Solution for the fracture opening (left) and net fluid pressure (right) from figure 3-8 normalised by the far-field m-vertex solution. Near-, intermediate- ($\chi = 10$) and far-field asymptotic expansions are shown by dashed coloured lines.

and crack opening in the intermediate-field with increasing ζ.
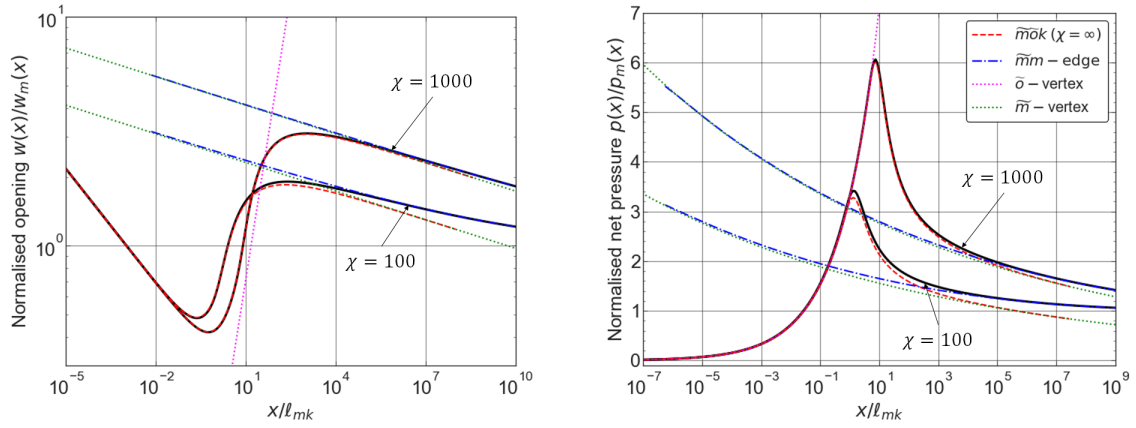
Figure 3-10: Fracture opening and net fluid pressure profiles normalised by the $m-$vertex solution for cases: $\chi = 100$, $\zeta = 4.64$ and $\chi = 1000$, $\zeta = 10$.
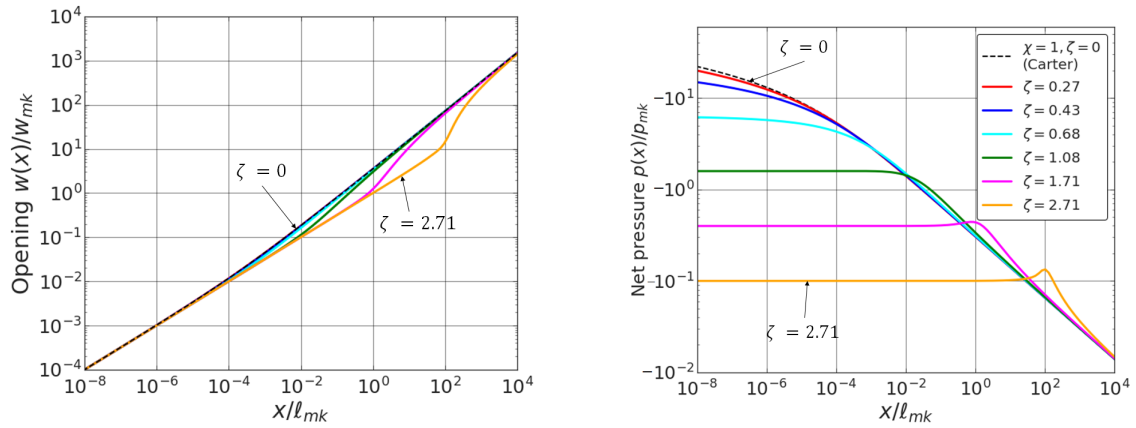
Figure 3-11: Fracture opening and net fluid pressure profiles with distance from the crack tip in $mk-$scalings (table 3.3) for $\chi = 1$ and the set of ζ values: $\zeta = 0, 0.27, 0.43, 0.68, 1.08, 1.71, 2.71$. By dashed line the Carter's leak-off solution is plotted.

3.2.4 Discussion

3.2.4.1 Representative values of problem parameters

In order to frame the discussion of the obtained solutions to the hydraulic fracture tip problem, we consider estimates for typical values/ranges of dimensional problem parameters, as pertain to the application of hydraulic fracturing in petroleum reservoir stimulation field, and the corresponding ranges of the non-dimensional HF tip parameters χ and ζ (or their ratio χ/ζ^3). We base parametric estimates on two types of hydrocarbon reservoir rock: low-permeability formation and sandstone, which typify the lower and higher limits of reservoir rock volumetric and filtration
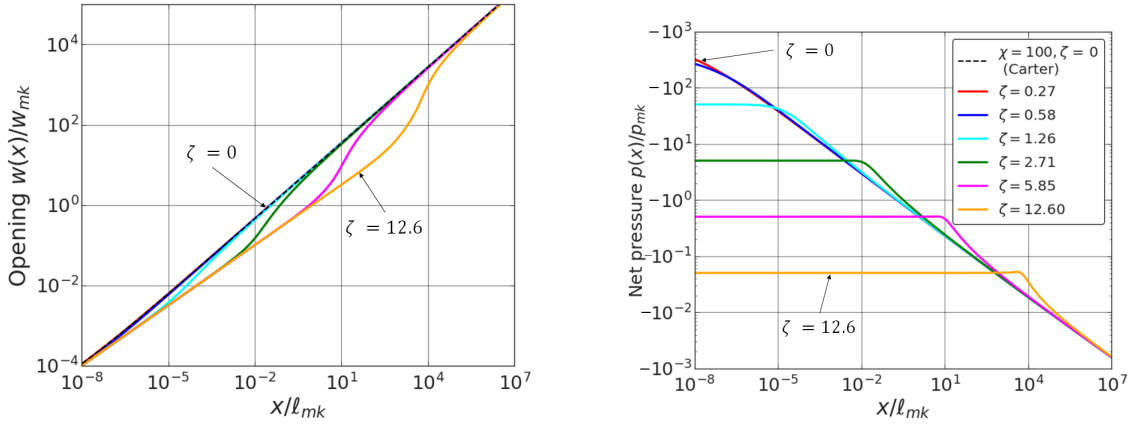
Figure 3-12: Fracture opening and net fluid pressure profiles with distance from the crack tip in $mk-$scalings (table 3.3) for $\chi = 100$ and the set of ζ values: $\zeta = 0, 0.27, 0.58, 1.26, 2.71, 5.85, 12.6$. By dashed line the Carter's leak-off solution is plotted.

properties, respectively while having similar geomechanical properties. Specifically, we take the following value ranges:

- for the geomechanical properties and stress - plane-strain elastic modulus $E' = 30$ GPa, pore volume total compressibility $c_t = 1/$GPa (water in pore space); rock fracture toughness K_{Ic} between 0.3 and 1 MPa·$\sqrt{\text{m}}$ [Chandler et al., 2016], and confining stress $\sigma_o = 30$ MPa;

- for the formation reservoir properties and pore pressure - permeability in the range $k = 0.1 \div 100$ mD [Li et al., 2016], porosity $\phi = 5 \div 25\%$ [Magara, 1980, Manger, 1963], and pore-pressure-to-stress-ratio $p_o/\sigma_o = 0.95 \div 0.4$ [Walsh, 1981] - where the bounds correspond to a low-permeability formation and sandstone type reservoir (the latter is assumed to be at the hydrostatic pore pressure, while the former is overpressured)

- fluid characteristics: $\mu = 1$ cP (water), 5 cP (slick water);

- fracture propagation velocity: V between 0.1 and 1 m/s.

Figure 3-13 shows the parametric domain in the space of the HF tip non-dimensional parameters χ and χ/ζ^3 when the dimensional parameters are *independently* varied within the ranges described in the above (e.g., allowing for overpressured reservoirs with sandstone properties and normally pressured reservoirs with

low-permeability formation properties, etc.). At each boundary of shown polygon one or two dimensional parameters are varied while others remain fixed at their lower or upper bound (as applicable). The sense of change of $(\chi, \chi/\zeta^3)$ with an increase of a given dimensional parameter are shown by arrows.
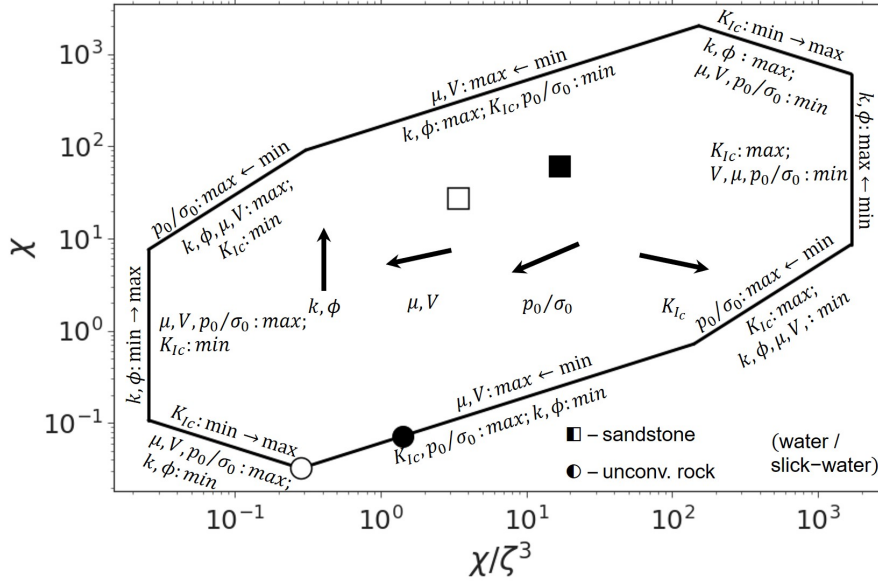
Figure 3-13: Parametric domain in terms of the non-dimensional leak-off number χ and leak-off-to-leak-in ration χ/ζ^3 representative of the field range estimates of the problem parameters. Symbols show particular field cases (sandstone vs. low-permeability formation and slick-water vs. water fracturing fluid) from table 3.5.

In addition, we consider four specific limiting parametric choices corresponding to the overpressured / normally-pressured reservoir types (with parametric values given by the lower/upper bounds of the assumed ranges), water / slick-water fluid types, while taking $K_{Ic} = 1$ MPa·$\sqrt{\text{m}}$ and $V = 1$ m/s. The corresponding four parametric points $(\chi, \zeta, \chi/\zeta^3)$ are recorded in table 3.5 and shown by symbols on the map of figure 3-13.

3.2.4.2   Asymptotic fields and fluid-exchange domains

Now we consider the applicability boundaries of various asymptotic fields (vertex solutions) within the general HF tip solution. An asymptotic bound is defined here as a distance from the fracture tip where the crack opening solution deviates from the considered asymptote (e.g., k, m, etc. vertex) by 5%. Specifically, we

		Sandstone	Low-permeability formation	
HF tip parameter	Water	Slick water	Water	Slick water
χ	61	27.3	0.07	0.03
ζ	1.8	4	0.03	0.06
χ/ζ^3	17	3.4	1.4	0.3
λ/ℓ_{mk}	$6 \cdot 10^{-5}$	0.01	0.02	2.2
x_C/ℓ_{mk}	0.5	32	174	$2 \cdot 10^4$

Table 3.5: Values of non-dimensional leak-off χ, leak-in ζ parameters, and of ratio χ/ζ^3 for sandstone/low-permeability reservoir, and water/slick-water fluid, as specified in the text. The corresponding solutions for the size of the near tip pore fluid circulation zone λ and the boundary x_C of the Carter's leak-off domain $(x > x_C)$ are also shown normalised by the mk transitional lengthscale ($\ell_{mk} \approx 9$ m for water and 0.4 m for slick-water).

refer to x_0 as the upper boundary of the $k-$vertex asymptotic region $0 < x < x_0$, and x_∞ as the lower boundary of the $m-$vertex asymptotic region $x_\infty < x < \infty$. Similarly, we define the 5% asymptotic thresholds corresponding to the intermediate $\widetilde{m}$, $\widetilde{x}_\infty < x < \widetilde{x}_0$, and $\widetilde{o}$, $\widetilde{x}_\infty^o < x < \widetilde{x}_0^o$, asymptotes, whenever either of them is realised in the solution.

Furthermore, to characterise the effect of the fluid-exchange on the hydraulic fracture tip solution, we introduce the boundary x_S of the 'crack-storage-domain' $x_S < x < \infty$ where the rate of the cumulative fluid exchange between the fracture and the rock $q_\perp$ constitutes 5% of the crack storage wV, $q_\perp(x_S) = 0.05 \cdot w(x_S)V$.

In the complimentary domain $0 < x < x_S$, the fluid exchange is non-negligible, and the relative significance of Carter's leak-off and leak-in correction terms in the expression for $q_\perp$ can be gauged by their ratio as a function of the distance from the tip,

$$\text{PDI}(x) = -\frac{1}{\sigma_o'\sqrt{x}} \int_0^x \frac{p(s)}{2\sqrt{x-s}}ds,$$

which we refer to as the pressure-dependent leak-off index (PDI). We can use this function to evaluate the extent λ of the near tip pore fluid circulation zone in the fracture, $0 < x < \lambda$, (figure 3-1), for which

$$\text{PDI}(\lambda) = 1,$$

and the boundary x_C of the far-field fracture domain dominated by Carter's leak-off, $x_C < x < \infty$, defined as distance from the tip where the cumulative leak-in

correction is at 5% of the cumulative Carter's leak-off, i.e.

$$\text{PDI}(x_C) = 0.05.$$

Figure 3-14 shows maps of the asymptotic fields (left) and various fluid-exchange domains (right) along the fracture (x/ℓ_{mk}) as a function of the leak-off number χ for four fixed values of the leak-off-to-leak-in ratio $\chi/\zeta^3 = 0.1, 1, 10$, and 1000 (a-d). For each of the above four cases, the corresponding range of χ representative of the field conditions (see parametric domain in figure 3-13) is indicated by a thick-line interval on the χ-axis.

When considering the asymptotic vertex domains within the general solution (figure 3-14 (left)), we observe that the near-field k domain expands with increasing leak-in (corresponding to the decreasing leak-off-to-leak-in ratio χ/ζ^3 from the case with $\chi/\zeta^3 = 1000$, (d), to $\chi/\zeta^3 = 0.1$, (a)) over most of the shown leak-off χ range (vertical axis in figure 3-14). In turn, the far-field m domain dependence on χ/ζ^3 is non-monotonic, as it is seen to expand from the case with $\chi/\zeta^3 = 10$, (c), to $\chi/\zeta^3 = 1$, (b), and then shrink to the case with $\chi/\zeta^3 = 0.1$, (a). The former expansion of the m and k domains with diminishing χ/ζ^3 is likely linked to diminishing leak-off effects and the disappearance of the intermediate Carter's leak-off $\widetilde{m}$ behaviour, while the further $m-$domain contraction may be caused by proliferation of the pressure-dependent leak-in effects at the smallest value of the ratio considered here $\chi/\zeta^3 = 0.1$, figure 3-14(a). (This can be further substantiated by expanding size λ of the pore-fluid circulation zone with diminishing χ/ζ^3, as seen in figure 3-14 (right)). The intermediate field $\widetilde{m}-$domain appears only in the case $\chi/\zeta^3 = 1000$, (d), when the pressure dependent leak-in effects are small, and, additionally, the leak-off is large ($\chi > 50$). The intermediate viscosity-leak-in $\widetilde{o}$ domain does not appear in all considered cases since the conditions of its existence ($\chi, \zeta \gg 1$) are not met.

Let us now consider the effects of the fluid exchange between the fracture and the rock onto the solution summarised in the PDI maps in figure 3-14 (right). We observe that the crack-storage-dominated domain in the semi-infinite fracture ($x > x_S$)

71

shrinks, or migrates further away from the tip, with both (i) increasing leak-off χ at fixed leak-off-to-leak-in ratio χ/ζ^3 and (ii) increasing pressure-dependent leak-in effects corresponding to diminishing value of the ratio χ/ζ^3, from $\chi/\zeta^3 = 1000$, (d), to $\chi/\zeta^3 = 0.1$, (a). The increasing influence of the leak-in with diminishing value of χ/ζ^3 is also reflected by overall increase of the pressure-dependent-index PDI (hotter colours in figure 3-14 (right)), corresponding growth of the near tip circulation zone λ, and shrinkage, or migration away from the tip, of the Carter's leak-off domain $(x > x_C)$.

The importance of the pressure-dependent fluid exchange effects to the propagation of a finite hydraulic fracture (for which we have provided the near tip solution here) can be gauged by comparing the Carter's leak-off boundary x_C in the near tip solution with the representative lengthscale ℓ of the finite fracture, e.g., the radius of a penny-shape hydraulic fracture or the half-length of a plane-strain KGD fracture, etc. If $x_C \ll \ell$, then the pressure-dependent fluid exchange effects are not important on the scale of the finite parent fracture, as they are confined to the very small near tip region effectively shielded by Carter's leak-off domain from the rest of the fracture. In this case, Carter's leak-off model is an appropriate approximation. Otherwise, i.e. when x_C comparable or larger than ℓ, the pressure-dependent fluid exchange effects are prominent in the finite fracture propagation, and Carter's model should be abandoned. Since, the Carter's bound $x_C = \ell_{mk}\, \xi_C(\chi, \zeta)$ is a dynamic lengthscale (i.e. it depends on the fracture tip propagation velocity $V = d\ell/dt$ via the tip lengthscale ℓ_{mk} and via the non-dimensional tip parameters χ and ζ, see corresponding definitions in table 3.2 and equations (3.4) and (3.7)), the regime of the fluid exchange (pressure-dependent vs. Carter's), as it corresponds to the ratio x_C/ℓ may change during the propagation.

To underscore the above discussion, consider a particular example of the HF propagation with $\chi = \zeta = 1$, which, according to the parametric estimates in figure 3-13 and table 3.5, corresponds to a slick-water HF in a reservoir with intermediate values of hydraulic properties (roughly geometric mean of the 'low-permeability formation' and 'sandstone' cases in table 3.5). Figure 3-14b indicates that $\lambda \approx \ell_{mk}$ and $x_C \approx 3 \times 10^3\, \ell_{mk}$, while lengthscale ℓ_{mk} is in the range from 0.4 to 40 me-

ters for the range of the propagation velocity V from 1 to 0.1 m/s, respectively, ($K_{Ic} = 1$ MPa$\times$m$^{1/2}$ and $E' = 30$ GPa). Thus, in this case, the tip circulation cavity is of metric size, while the effects of the pressure-dependent fluid exchange are always prominent unless impractically long, kilometric in length and larger ($\ell > x_C$), fractures are considered. If we are now to consider the limiting cases of the 'low-permeability' and 'sandstone' reservoirs from table 3.5, we observe that similar conclusions about the general inadequacy of the Carter's approximation (which calls for unrealistically long fracture) to slick-water fracture apply. However, in the case of a 'low-permeability reservoir', the fracture tends to propagate in the storage-dominated regime ($\chi < 0.1$), which allows one to reasonably neglect the fluid exchange altogether.

3.2.4.3 Some limitations of the model

3.2.4.3.1 1D pore pressure diffusion

Our model of the pressure-dependent leak-off is hinged on the assumption of the 1D pore pressure diffusion in the permeable rock surrounding the fracture. As pointed out by Detournay and Garagash [2003], the 1D assumption is approximately valid when the pore pressure perturbation introduced by fracturing is contained to a boundary layer abating the fracture that is thin compared to the characteristic lengthscale of fluid pressure change along the part of the fracture where the fluid exchange process is important. Taking for the latter the size λ of the near-tip pore fluid circulation zone, and for the former the corresponding thickness of the pore pressure boundary layer $\sqrt{ct}$ built up over the time $t = \lambda/V$ it takes for the fracture tip to propagate distance λ, the 1D condition reads

$$\lambda \gg \ell_d, \quad \ell_d = c/V.$$

Detournay and Garagash [2003] refer to this condition as the 'large velocity limit' of the circulation cavity problem in reference to the inverse dependence of the 'diffusion lengthscale' ℓ_d on the fracture propagation velocity.

When evaluating the above 1D condition, it is convenient to express diffusion
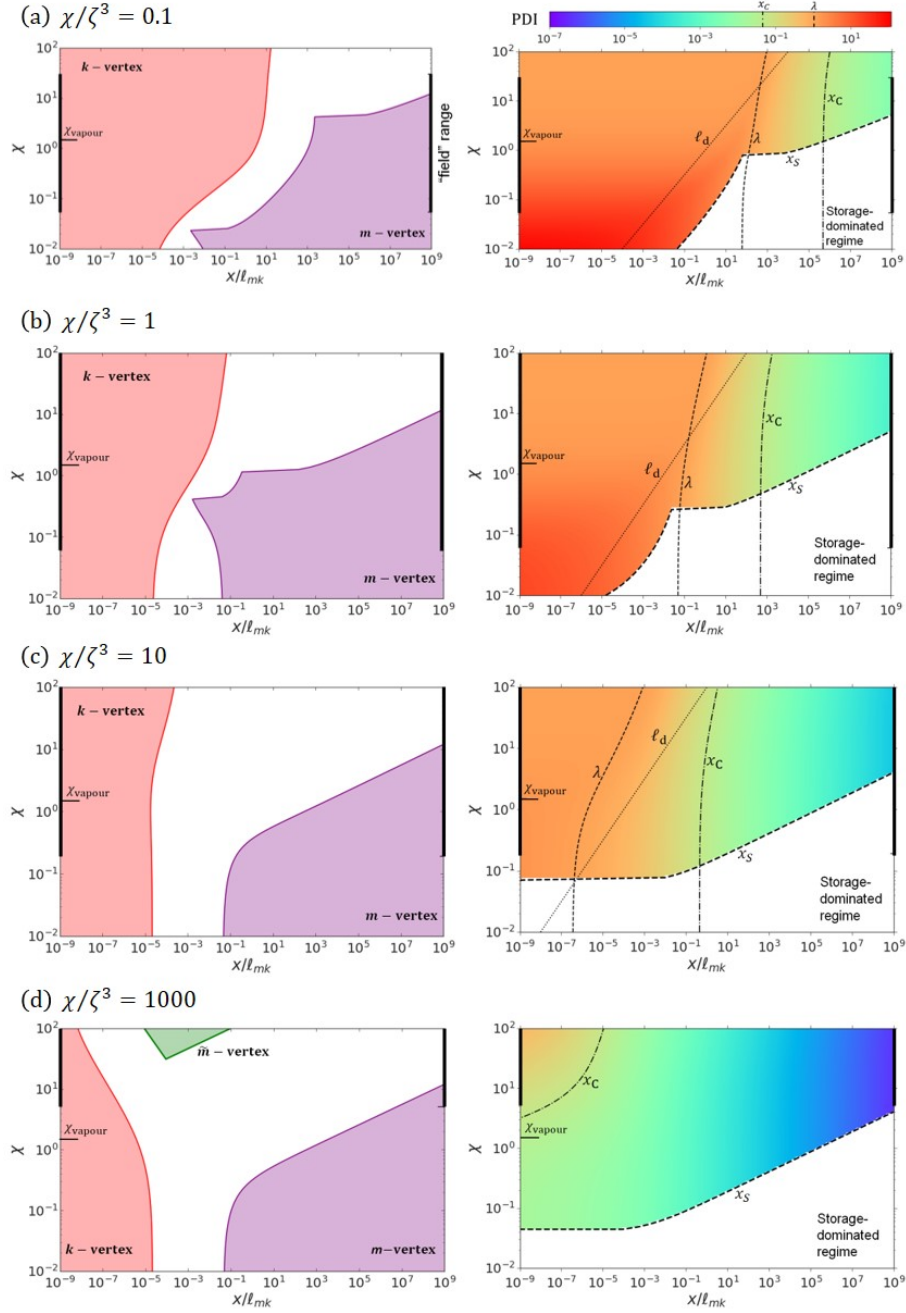
Figure 3-14: Regime maps showing spatial domains of the fracture dominated by the vertex solutions (left) and the Pressure-Dependent Leak-off Index (PDI) maps with several characteristic boundaries of the fluid exchange process $(\lambda, \ell_d, x_C, x_S)$ (right) as a function of the leak-off number χ for the fixed values of leak-off-to-leak-in-ratio $\chi/\zeta^3 = 0.1$ (a), 1 (b), 10 (c), and 1000 (d). (The χ-ranges representative of the field fracture are highlighted on the axis).

lengthscale ℓ_d in the $mk-$scaling, $\ell_d/\ell_{mk} = cE'^4 M'^2 V/K'^6 = (\pi/16)(SE')^{-2}\zeta^6$. In the latter, the non-dimensional product $E'S$ of the rock elastic modulus E' and rock

pore space storativity $S = \phi c_t$ is weakly dependent on the rock type and can be estimated based on the previously discussed typical values of these parameters as $E'S \sim 3$, resulting in $\ell_d/\ell_{mk} \sim 0.01\zeta^6$. This estimate is shown in the maps in figures 3-14(right) where it can be directly compared to the circulation zone length λ/ℓ_{mk}. We observe that 1D fluid-exchange condition is satisfied for all considered values of χ in the case $\chi/\zeta^3 = 0.1$, figure 3-14(a), for $\chi \lesssim 0.1$ in the case $\chi/\zeta^3 = 1$, figure 3-14(b), and finally, for $\chi \lesssim 5$ in the case $\chi/\zeta^3 = 10$, figure 3-14(c). In other words, the 1D approximation of the pore pressure diffusion is more readily justified when the pressure-dependent leak-in effects are more prominent (i.e. smaller values of the leak-off-to-leak-in ratio χ/ζ^3 and correspondingly larger circulation zone size λ).

3.2.4.3.2 Sameness of the formation and fracturing fluids

The assumption that the formation and fracturing fluids have identical properties is a restrictive one, in that it limits practical applications of this analysis (as a result, we focused here on the slick-water fracturing parametric examples, as the latter viscosity ~ 5 cP may be similar to that of the light oil). The future work will consider relaxing this assumption in order to extend the analysis to conventional fracturing fluids (polymeric gel) with the viscosity orders of magnitude larger than that of the formation fluid, and possibly to the 'cake building' due to leak-off (i.e. deposition of fracturing fluid solids and polymers into a thin, semi-solid, low-permeability 'cake' at the fracture wall). Kovalyshen et al. [2013] provide a workable theoretical framework to include these effects by distinguishing between the pore and fracturing fluid viscosities in the fluid flow in the fracture and tracking the 'cake' build-up, while reasonably assuming that the leaked-off filtrate (i.e. the base of the fracturing fluid when stripped from the solids and polymers) displacing the pore fluid in the permeable rock abating the fracture has properties identical to that of the formation pore fluid.

3.2.4.3.3 Potential vaporisation of the pore fluid at the fracture tip

The near tip region of the fracture dominated by the pore fluid leak-in corresponds to the absolute fluid pressure below the ambient field value p_o. Specifically at the

tip, we have (table 3.2)

$$p_f(0) = p_o - \Delta p_{\text{und}}, \quad \Delta p_{\text{und}} = \frac{K'V^{1/2}}{E'Q'} = \frac{\sigma'_o}{\chi},$$

where Δp_{und} corresponds to the undrained value of the pressure drop. The fluid will vaporise and form so-call 'fluid lag' adjacent to the fracture tip if pressure drops below the saturated vapour value. Taking the latter to be small compared to the reservoir ambient pore pressure value, the incipient fluid lag condition requires $p_o < \Delta p_{\text{und}}$, which in view of (3.2.4.3.3) can be rewritten in terms of the leak-off number

$$\text{fluid lagging:} \quad \chi < \chi_{\text{vapour}} = \frac{\sigma'_o}{p_o} = \frac{\sigma_o}{p_o} - 1.$$

The above threshold value of χ can be estimated as $\chi_{\text{vapour}} \approx 1.5$ for the normally-pressurised and ≈ 0.05 for the overpressured reservoirs. The normally-pressurised reservoir value of χ_{vapour} is indicated on the parametric maps of figure 3-14. The vaporisation at the fracture tip, when predicted, does not necessarily invalidate the considered solutions, as long as the vapour-filled region (fluid lag) remains small compared to the predicted circulation zone size λ.

3.3 A radial hydraulic fracture

3.3.1 Model formulation

The present section outlines the problem formulation for a radial hydraulic fracture with the pressure-dependent fluid exchange between the crack channel and ambient permeable reservoir. The schematics of the radial fracture model is shown in Figure 3-15a. Most of the model assumptions and governing equations provided by Section 2.2 remain the same, and we will not repeat them for brevity. However, the fluid exchange mechanism is modified, and we will focus on it in the current part of the thesis.

The distinctive feature of the proposed model is a dependence of the fluid exchange between the fracture and ambient permeable rock on the fluid pressure in-
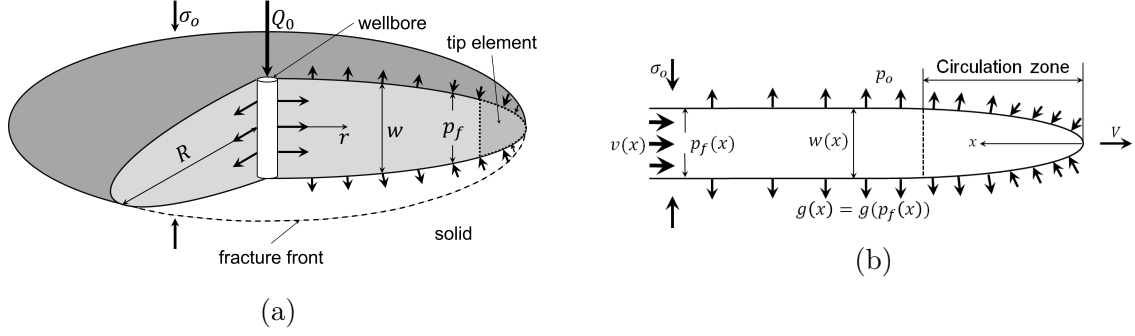
Figure 3-15: A radial fracture model (a) with the pressure-dependent fluid exchange and its near-tip region (b) described by a semi-infinite fracture model.

side the fracture. For the simplification of the fluid exchange description, firstly, we suppose that the pore and fracturing fluids are Newtonian liquids with the same properties, i.e., viscosity μ and total compressibility c_t are identical; secondly, we apply a one-dimensional approach. The fluid exchange rate $g(r,t)$ is coupled with the fracture propagation history and the history of fluid pressure. In addition, it depends on pore fluids properties, porosity ϕ_r, reservoir permeability k, and the far-field pore fluid pressure p_o. By including the pressure dependence of the fluid exchange, we potentially allow pore fluid to inflow into the fracture in the near-tip region under the condition that the fluid pressure $p_f(r,t)$ becomes less than the pore pressure p_o in that zone. The pore fluid volume flowed into the fracture eventually leaks out from the fracture. This leads to the establishment of the circulation zone, in which the total leak-in and leak-off are balanced. Since the pore fluid is allowed to flow into dynamically depressurised fracture tip region, the fluid and fracture fronts coincide.

Further, we move on to the discussion of the alterations in the system of governing equations given in Section 2.2.2. In the current model, the problem solution consisting of radius dynamics $R(t)$, opening $w(r,t)$ and net pressure $p(r,t)$ profiles depends on time t, distance from the source r, injection rate Q_0, and the expanded set of material parameters:

$$E' = \frac{E}{1-\nu^2}, \quad K' = 4\sqrt{\frac{2}{\pi}}K_{Ic}, \quad M' = 12\mu, \quad Q' = \frac{2k}{\mu\sqrt{\pi c}}, \quad C' = Q'\sigma'_o, \quad (3.20)$$

where Q' is the pressure-dependent leak-off (PDL) coefficient (c is the diffusivity

coefficient defined as $c = k/(\phi_r c_t \mu))$, and C' is Carter's leak-off coefficient ($\sigma'_o = \sigma_o - p_o$ is the effective confining stress).

We define the local fluid exchange rate $g(r,t)$ corresponding to the pressure-dependent leak-off as:

$$g(r,t) = \frac{C'}{\sqrt{t - t_0(r)}} + Q' \int_{-\infty}^{t} \frac{\partial}{\partial s} \left[H(s - t_0(r)) p(r,s) \right] \frac{ds}{\sqrt{t - s}}. \tag{3.21}$$

Here $H(x)$ is Heaviside step function, $t_0(r)$ is the inverse radius function: $t_0(r) = R^{-1}(t)$. As can be seen from the equation (3.21), the fluid exchange process is controlled by two coefficients C' and Q'. The Carter's leak-off coefficient C' is commonly utilised in many hydraulic fracturing models. The PDL coefficient Q' was introduced in Section 3.2, and it scales the level of the fluid exchange pressure dependence, i.e. the departure from Carter's law given by the first term in equation (3.21). Derivation of (3.21) is provided by Appendix A.1.

Using the continuity equation (2.13), Poiseuille's law (2.15), and the expression (3.21) for the fluid exchange rate, we obtain the Reynolds equation:

$$\frac{\partial w}{\partial t} = \frac{1}{M'} \frac{1}{r} \frac{\partial}{\partial r} \left(r w^3 \frac{\partial p}{\partial r} \right) - \frac{C'}{\sqrt{t - t_0(r)}} - Q' \int_{-\infty}^{t} \frac{\partial}{\partial s} \left[H(s - t_0(r)) p(r,s) \right] \frac{ds}{\sqrt{t - s}}. \tag{3.22}$$

Finally, we should write out the formula for $V_{\text{fluid-exchange}}$ term taken part in the global fluid balance equation (2.20):

$$V_{\text{fluid-exchange}} = \underbrace{4\pi C' \int_0^R r \sqrt{t - t_0(r)} dr}_{V_C} + \underbrace{2\pi Q' \int_0^R r dr \int_{t_0(r)}^t \frac{p(r,s) ds}{\sqrt{t-s}}}_{V_{\text{PDL}}}. \tag{3.23}$$

One can notice that the volume $V_{\text{fluid-exchange}}$ is comprised of Carter's cumulative leaked volume V_C and PDL volume correction V_{PDL}.

3.3.2 Summary of the fracture tip model with pressure-dependent fluid exchange

It is known that the square-root asymptotic behaviour (2.17) for the fracture opening is valid only in a small region adjacent to the fracture front [Garagash and Detournay, 2000, Garagash et al., 2011]. In fracture simulators, the numerical grid is typically not sufficiently fine to capture the square-root asymptote along the tip element. To deal with the problem and to increase the accuracy of the numerical calculations, fracture tip models are utilised, since they allow us to describe fracture characteristics near its front accurately [Peirce and Detournay, 2008, Dontsov and Peirce, 2017c, Zia and Lecampion, 2020].

Schematics of the fracture tip model with the pressure-dependent fluid exchange is presented in figure 3-15b. The detailed description of this model is provided in Section 3.2, while here, we resemble the main findings relevant to the current study for the completeness. Fracture tip model is represented by a semi-infinite fracture propagating with a constant velocity V. Since the propagation velocity is constant, it is possible to convert the whole problem to a stationary form in which all characteristics of the semi-infinite fracture, namely, opening w_a, net fluid pressure p_a and fluid exchange rate g_a, depend only on the distance x from the crack front and do not depend on time explicitly (see Figure 3-15b). In addition to the distance x, the near-tip region solution is influenced by the propagation velocity V and the set of the dimensional parameters defined in (3.20) which we denote here as $\mathcal{Q}$.

A distinguishing feature of the near-tip region model with the pressure-dependent fluid exchange is the presence of the circulation zone (see Figure 3-15b). It is a region near the crack front along which the cumulative fluid exchange rate is equal to zero: the pore fluid flows into this zone near the tip and afterwards leaks-off. Since the fracture tip model is steady-state, the circulation zone length is fixed.

The system of governing equations for a semi-infinite hydraulic fracture with the pressure-dependent fluid exchange consists of the following relations:

- *Elasticity:* $p_a(x) = \frac{E'}{4\pi} \int_0^\infty \frac{dw_a(s)}{ds} \frac{ds}{x-s}$;

- *Lubrication:* $w_a v_a = w_a V + q_\perp,\quad q_\perp = \int_0^x g_a(s)ds = 2C'\sqrt{Vx} + Q'\sqrt{V}\int_0^x \frac{p_a(s)}{\sqrt{x-s}}ds.$
  The fluid exchange rate $g_a(x)$ and its cumulative value $q_\perp(x)$ are derived in Appendix A.1. Note that the definitions of the PDL coefficient Q' and Carter's coefficient C' are different from those in Section 3.2 by a factor of two;

- *Poiseuille's law:* $v_a = \frac{w_a^2}{M'}\frac{dp_a}{dx};$

- *Crack propagation:* $w_a = \frac{K'}{E'}\sqrt{x},\quad x \to 0.$

To reduce the number of parameters, the solution is written in terms of normalised variables. In particular, we utilise the so-called $mk-$scaling, so that:

$$\xi = \frac{x}{\ell_{mk}},\quad \Omega_a = \frac{w_a}{w_{mk}},\quad \Pi_a = \frac{p_a}{p_{mk}}. \tag{3.24}$$

The characteristic length, fracture width and fluid pressure scales are set according to the following equations [Garagash et al., 2011]:

$$\ell_{mk} = \frac{\ell_k^3}{\ell_m^2} = \frac{K'^6}{E'^4 V^2 M'^2},\quad w_{mk} = \frac{\ell_k^2}{\ell_m} = \frac{K'^4}{E'^3 V M'},\quad p_{mk} = E'\frac{\ell_m}{\ell_k} = \frac{E'^2 V M'}{K'^2}, \tag{3.25}$$

where we utilise the complimentary length scales $\ell_k = (K'/E')^2$ and $\ell_m = VM'/E'$.

In the normalised variables, solution for the problem of the semi-infinite fracture depends on the dimensionless coordinate ξ and two dimensionless numbers:

$$\chi = \frac{2C'E'}{K'\sqrt{V}},\quad \zeta = \frac{E'}{K'}\left(M'Q'\sqrt{V}\right)^{1/3}, \tag{3.26}$$

where the first parameter χ is related to dimensionless leak-off and the second parameter ζ reflects the normalised strength of PDL effects.

The near-tip solution described above is used as a propagation condition of the parent (finite) hydraulic fracture in this study in lieu of (2.17). The near-tip behaviour for the finite fracture can then be formulated as:

$$w(r,t,Q_0,\mathcal{Q}) = w_a(R-r,V,\mathcal{Q}) = w_{mk}\cdot\Omega_a\left(\frac{R-r}{\ell_{mk}},\chi,\zeta\right),\quad R-r \ll R, \tag{3.27}$$

where the dimensionless function Ω_a is known from the solution of the semi-infinite

fracture problem described above.

We also utilise the fracture-tip model for calculating the cumulative fluid exchange rate for the fracture tip element. For this purpose, we express leak-off flux $q_\perp(x)$ in terms of the dimensionless function that comes from the solution of the semi-infinite fracture problem as:

$$q_\perp(R - r, V, \mathcal{Q}) = w_{mk} V \cdot \Upsilon \left(\frac{R - r}{\ell_{mk}}, \chi, \zeta \right),$$

$$\Upsilon(\xi, \chi, \zeta) = \chi \sqrt{\xi} + \zeta^3 \int_0^\xi \frac{\Pi_a(s, \chi, \zeta) ds}{\sqrt{\xi - s}}, \quad R - r \ll R. \tag{3.28}$$

In the above equation, the dimensionless function Υ is provided by the tip solution, w_{mk} is the scale for the fracture width defined in (3.25), while the tip velocity $V = dR/dt$ is obtained from the solution of the coupled problem for the whole fracture.

3.3.3   Numerical implementation

In the current section, we outline the main features of the numerical algorithm for calculating the general solution for the radial fracture model. The implemented algorithm is similar to the scheme used in Dontsov [2016a].

The algorithm can be divided into several stages:

- discretisation of the system of governing equations specified in sections 2.2 and 3.3.1;

- description of the tip element using the tip asymptotic solution outlined in Section 3.3.2;

- combination of the discretised equations into a single system of equations;

- numerical solution of the system of equations.

To proceed with the numerical solution, we first utilise the normalised spatial coordinate $\rho = r/R(t)$. Since ρ depends on time, it is necessary to rewrite the time

and spatial derivatives in terms of ρ and t:

$$\left.\frac{\partial}{\partial t}\right|_r = \left.\frac{\partial}{\partial t}\right|_\rho - \frac{\rho V(t)}{R(t)}\left.\frac{\partial}{\partial \rho}\right|_t, \qquad \left.\frac{\partial}{\partial r}\right|_t = \frac{1}{R(t)}\left.\frac{\partial}{\partial \rho}\right|_t, \qquad (3.29)$$

where we used the following expressions for the time and spatial derivatives of normalised distance: $\frac{\partial \rho}{\partial t} = -\frac{\rho V(t)}{R(t)}$, $\frac{\partial \rho}{\partial r} = \frac{1}{R}$.

Further, we rewrite the elasticity (2.11) and Reynolds (3.22) equations by accounting for the derivatives transformation (3.29):

- *Elasticity:*

$$p(\rho, t) = -\frac{E'}{2\pi R(t)} \int_0^1 G(\rho, s) \frac{\partial w(s,t)}{\partial s} ds, \qquad (3.30)$$

  where the integral kernel $G(\rho, s)$ is given by equation (2.12);

- *Reynolds:*

$$\frac{\partial w}{\partial t} - \frac{V(t)}{R(t)}\rho\frac{\partial w}{\partial \rho} = \frac{1}{M'R(t)^2}\frac{1}{\rho}\frac{\partial}{\partial \rho}\left(\rho w^3 \frac{\partial p}{\partial \rho}\right) - \frac{C'}{\sqrt{t - t_0(\rho R)}} -$$

$$- Q'\int_{-\infty}^t \frac{\partial}{\partial s}[H(s - t_0(\rho R(t)))p(\rho, s)]\frac{ds}{\sqrt{t-s}}+$$

$$+ Q'\int_{-\infty}^t \frac{\rho V(s)}{R(s)}\frac{\partial[H(s - t_0(\rho R(t)))p(\rho, s)]}{\partial \rho} \cdot \frac{ds}{\sqrt{t-s}}. \qquad (3.31)$$

The discretisation involves setting up the mesh for time and spatial coordinate. The time is discretised on a logarithmic scale using K steps as: $t_i = t_{\min} + 10^{i\Delta T}$, $i = 1, \ldots, K$, where $\Delta T = \log_{10}(t_{\max}/t_{\min})/K$, while $t_{\min}$ corresponds to the initial condition time, and $t_{\max}$ is the maximum simulation time. The spatial coordinate ρ is divided linearly into N segments with length $\Delta\rho = 1/N$. The spatial mesh nodes are located in the middle of the segments: $\rho_j = (j - 0.5)\Delta\rho$, $j = 1, \ldots, N$. We use $N = 50$ in the present work.

With regard to the problem variables, the radial fracture radius $R(t)$ and the propagation velocity $V(t)$ are taken as piecewise constant functions of time, i.e. $R(t) = R_i$, $V(t_i) = V_i$ for $t \in [t_{i-1}, t_i]$, $i = 1, \ldots, K$. Similarly, the crack opening $w(\rho, t)$ and net fluid pressure $p(\rho, t)$ are discretised as piecewise constant functions of time and normalised coordinate: $w(\rho, t) = w_j^i$, $p(\rho, t) = p_j^i$ for $t \in [t_{i-1}, t_i]$, $i =$

$1, \ldots, K$ and $\rho \in [\rho_{j-1/2}, \rho_{j+1/2}]$, $j = 1, \ldots, N$, where $\rho_{j-1/2} = \rho_j - \Delta\rho/2$, $\rho_{j+1/2} = \rho_j + \Delta\rho/2$ are boundaries of the segment with sequence number j. We also introduce $\mathbf{w}^i$ as the column with fracture width values in each spatial segment for the time interval i and $\mathbf{p}^i$ as the column containing the net fluid pressure values.

Let us start with the discretised form of the elasticity equation (3.30):

$$\mathbf{p}^i = \frac{\mathbf{C}E'}{R_i}\mathbf{w}^i, \quad C_{mn} = \frac{1}{2\pi}\left[G(\rho_m, \rho_{n+1/2}) - G(\rho_m, \rho_{n-1/2})\right]; m, n = 1, \ldots, N, i = 1, \ldots, K,$$

(3.32)

where $\mathbf{C}$ is the dimensionless elasticity matrix for the problem.

Further, we move on to the discretisation of the Reynolds equation (3.31). Firstly, we perform the integration over the time interval $i : [t_{i-1}, t_i]$, and afterwards, we average the Reynolds equation over the circle $\mathcal{A}_\rho$ with boundary $\mathcal{C}_\rho$: $r \in [\rho_{j-1/2}, \rho_{j+1/2}]$, $\theta \in [0, 2\pi]$. The averaging is carried out in the following way:

$$\frac{2\pi \int_{\rho_{j-1/2}}^{\rho_{j+1/2}} \rho f(\rho)d\rho}{\pi(\rho_{j+1/2}^2 - \rho_{j-1/2}^2)} \approx \frac{\int_{\rho_{j-1/2}}^{\rho_{j+1/2}} \rho f(\rho)d\rho}{\rho_j \Delta\rho}.$$

(3.33)

By applying the averaging procedure, the discretised system of equations becomes

$$\mathbf{w}^i - \mathbf{w}^{i-1} = \mathbf{B}\mathbf{w}^i + \left(\mathbf{A}(\mathbf{w}^i) + \hat{\mathbf{S}}^i\right)\mathbf{p}^i + \mathbf{S}^i, \quad i = 1, \ldots, K.$$

(3.34)

see Appendix A.2 for details. Here the term on the left hand side represents the time derivative of the width, the matrix $\mathbf{B}$ captures the term proportional to the tip velocity originating from using the moving mesh, the matrix $\mathbf{A}$ describes the flux term, the vector $\mathbf{S}^i$ contains all the source and leak-off terms that are independent of the solution at the time instant t_i (i.e. the fluid injection, Carter's leak-off, history of the pressure-dependent fluid exchange except for the current time step), and vector $\hat{\mathbf{S}}^i\mathbf{p}^i$ signifies the pressure-dependent part of leak-off that includes the pressure value at the current time step. The presented numerical scheme (3.34) differs from that for Carter's leak-off case [Dontsov, 2016a] by the presence of the term $\hat{\mathbf{S}}^i\mathbf{p}^i$ and the components of $\mathbf{S}^i$ that are related to PDL. Expressions for the matrices $\mathbf{A}, \mathbf{B}, \mathbf{S}^i, \hat{\mathbf{S}}^i$ are given by Appendix A.2.

Equation (3.34) has a special form for the tip element since the propagation

condition is imposed there. In particular, the penultimate element (i.e. $j = N - 1$) is used to compute the fracture tip propagation velocity V. With the reference to figure 3-16 and results in section 3.3.2, the propagation velocity for the considered time interval i is given implicitly as

$$w_{N-1}^i = w_a \left(\frac{3}{2} \Delta \rho R_i, V_i, \mathcal{Q} \right), \tag{3.35}$$

where w_a is the tip asymptotic solution for the fracture width (see previous section), the distance from the fracture front is taken to the middle of the $N-1$th element, and the set $\mathcal{Q}$ specifies material parameters. Equation (3.35) allows us to compute propagation velocity for a given value of width w_{N-1}^i. Once the velocity is computed, the radius is updated as:

$$R_i = R_{i-1} + V_i \Delta t, \quad \Delta t = t_i - t_{i-1}, \tag{3.36}$$

where Δt is the ith time step.

In addition, since the tip asymptotic solution is imposed via the $N-1$th element, the fracture width in the tip, i.e. Nth element, should follow the same tip asymptote as well. As a result, width of the tip element can be computed by integration of the width solution as

$$w_N^i = \frac{1}{R_i \Delta \rho} \int_0^{\Delta \rho R_i} w_a(s, V_i, \mathcal{Q}) ds. \tag{3.37}$$

Note that to compensate for the fact that w_N^i is not an independent parameter anymore, pressure at the tip, i.e. p_N^i is treated as an unknown.

It is also necessary to estimate the cumulative fluid exchange volume along the tip element which we denote as $V_{\text{fluid-exchange}}^N$. This quantity is calculated with the help of the tip asymptotic solution via equation (3.28):

$$V_{\text{fluid-exchange}}^N = \Delta t \cdot 2\pi \int_{R_i(1-\Delta \rho)}^{R_i} s g_a(R_i - s) ds \approx \Delta t \cdot 2\pi \rho_N R_i q_\perp(\Delta \rho R_i) =$$

$$= \Delta t \cdot 2\pi \rho_N R_i \left[\frac{K'^4}{E'^3 M'} \cdot \Upsilon \left(\frac{\Delta \rho R_i}{\ell_{mk}}, \chi_i, \zeta_i \right) + 2Q' \sqrt{V_i} \sqrt{\Delta \rho R_i} \delta p^i \right].$$

It is known that the validity of the pressure asymptote is smaller than that for the

84

width. Therefore we introduce a correction to the pressure δp^i:

$$\delta p^i = p^i_{N-1} - p_a\left(\frac{3}{2}\Delta\rho R_i, V_i, \mathcal{Q}\right) = p^i_{N-1} - \frac{E'^2 V_i M'}{K'^2} \cdot \Pi_a\left(\frac{3}{2}\frac{\Delta\rho R_i}{\ell_{mk}}, \chi_i, \zeta_i\right),$$

which results in an additional component in the cumulative fluid exchange rate. Note that the volume $V^N_{\text{fluid-exchange}}$ is related to the column element $[\mathbf{S}^i]_N$ via the following relation: $[\mathbf{S}^i]_N = -V^N_{\text{fluid-exchange}}/(2\pi\rho_N\Delta\rho R_i^2)$. Appendix A.2 summarises the details.

$$w(r) \approx w_a(R - r)$$
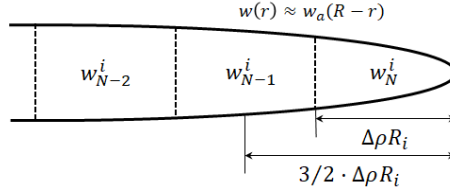
Figure 3-16: Schematics of the discretised near-tip region of a hydraulic fracture.

To summarise, the numerical solution for a radial hydraulic fracture is governed by the nonlinear system of N equations. Since the width of the tip segment is governed by the specific model within the frame of the numerical algorithm, it is convenient to split the variables into the channel (internal) elements and the tip element [Peirce and Detournay, 2008], so that

$$\mathbf{w}^i = [\mathbf{w}^i_c, w^i_N], \qquad \mathbf{p}^i = [\mathbf{p}^i_c, p^i_N],$$

where the arrays $\mathbf{w}^i_c$ and $\mathbf{p}^i_c$ denote the width and pressure for all the internal nodes (i.e. $j = 1, \ldots, N - 1$), while w^i_N and p^i_N are their counterparts at the tip (i.e. $j = N$). Further, the system of governing equations is linearised, and it is solved for $\mathbf{w}^i_c$ and p^i_N by an application of a standard solver for the system of linear equations and the fixed point iteration method.

3.3.4 Results and discussion

This section focuses on the implications of using the pressure-dependent leak-off in a hydraulic fracture model. In particular, a general numerical solution for the problem of a radial fracture is computed for different sets of parameters and behaviour of

the solution in the dimensionless parametric space is investigated. In addition, the radial crack characteristics are compared to the corresponding solution that utilises Carter's leak-off model, thus, allowing one to understand better the level of influence of the pressure-dependent leak-off.

The main characteristics of the radial fracture that are used for the comparison in this study are the width value at the wellbore $w(0,t)$, net fluid pressure in the middle of the fracture $p(R(t)/2,t)$, its radius $R(t)$, and efficiency $\eta(t)$ defined as a ratio between the fracture volume and the volume injected into the fracture:

$$\eta(t) = \frac{V_{\text{crack}}}{V_{\text{inj}}} = \frac{2\pi}{Q_0 t} \cdot \int_0^R r w(r,t) dr. \tag{3.38}$$

Fracture efficiency is an important quantity and allows us to quickly determine whether the leak-off is important or not.

3.3.4.1 Examples for field parameters

We consider two sets of the problem parameters which differ by the fluid viscosity: $\mu_1 = 1$ cP and $\mu_2 = 10$ cP. All other parameters are kept the same, namely:

$$E' = 30 \text{ GPa}, \qquad K' = 3.19 \text{ MPa} \cdot \sqrt{\text{m}}, \qquad Q_0 = 0.01 \text{ m}^3/\text{s}, \qquad t_{\text{end}} = 6000 \ s,$$
$$\sigma_o = 8 \text{ MPa}, \qquad p_o = 4.8 \text{ MPa}, \qquad k = 10 \text{ mD}, \qquad \phi_r = 20\%, \qquad c_t = 10^{-3} \text{MPa}^{-1}. \tag{3.39}$$

Further, we calculate Carter's leak-off and PDL coefficients based on the parameters above as:

$$1) \ Q_1' = 5.1 \cdot 10^{-2} \text{ mm}/(\sqrt{\text{s}} \cdot \text{MPa}), \qquad C_1' = 1.63 \cdot 10^{-1} \text{ mm}/\sqrt{\text{s}},$$
$$2) \ Q_2' = 1.6 \cdot 10^{-2} \text{ mm}/(\sqrt{\text{s}} \cdot \text{MPa}), \qquad C_2' = 5.2 \cdot 10^{-2} \text{ mm}/\sqrt{\text{s}}. \tag{3.40}$$

Figure 3-17 shows results of the numerical simulation in terms of the fracture aperture at the wellbore, pressure in the middle of the crack, radius and efficiency profiles versus time. In addition to the results of the radial fracture model with PDL (solid lines), we also depict the corresponding profiles computed by the model

with Carter's leak-off (dashed lines), i.e. for $Q' = 0$. We utilise blue colour lines for the lower viscosity μ_1 and green ones for the case with a more viscous fluid μ_2. Results demonstrate that both the fracture radius and width are overestimated for the Carter's leak-off cases. This is because the efficiency (and hence the fracture volume) is different. The pressure profiles are much closer to each other. The relative difference at the end of pumping in the first case ($\mu_1 = 1$ cP) is 2% for the fracture width at the wellbore, 4.2% for the radius, 1.9% for the pressure in the middle, and 10.8% for the efficiency, and in the second case ($\mu_2 = 10$ cP) is 2.4% for $w(0, t_{\text{end}})$, 4.3% for $R(t_{\text{end}})$, 1.5% for $p(R(t_{\text{end}})/2, t_{\text{end}})$, and 11.8% for $\eta(t_{\text{end}})$. This observation demonstrates that there might be an observable difference between the solution with the PDL and Carter's leak-off. Next sections provide a more systematic analysis of the difference between the two models.
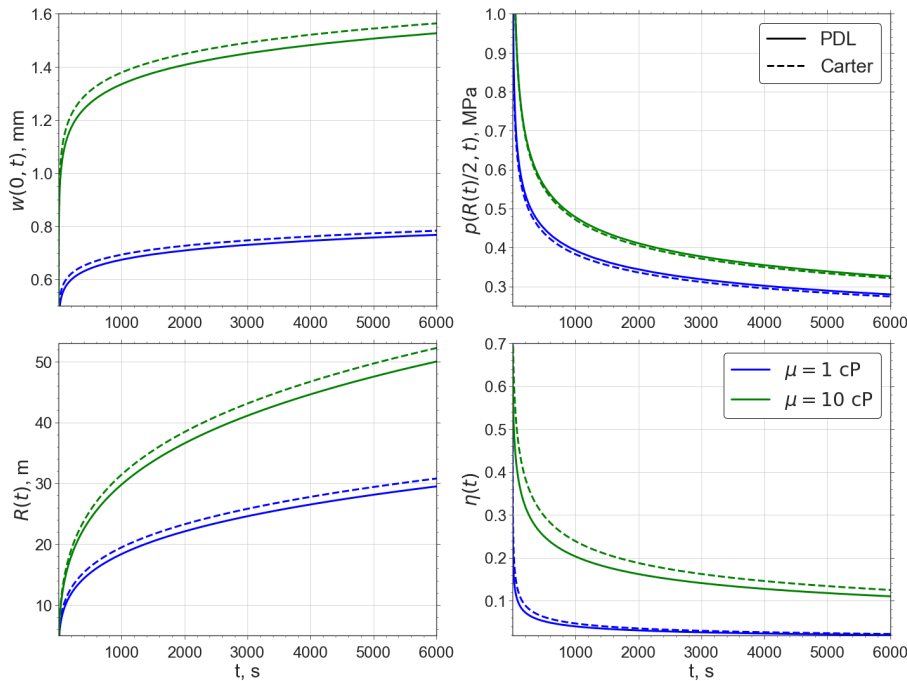
Figure 3-17: Numerical solution for the problem of a radial hydraulic fracture in terms of the fracture width at the wellbore $w(0, t)$, pressure in the middle of the fracture $p(R(t)/2, t)$, radius $R(t)$, and efficiency $\eta(t)$ versus time t computed for the problem parameters (3.39) and (3.40). Blue lines correspond to the case with $\mu = 1$ cP, while the green lines represent the higher viscosity case $\mu = 10$ cP. The pressure-dependent fluid exchange cases are depicted by solid lines, while dashed lines plot the results for Carter's leak-off.

3.3.4.2 Representative parameters in the parametric space

To reduce number of the problem parameters, it is convenient to reformulate the radial fracture model in a dimensionless form. By following the mk-scaling for the radial fracture with Carter's leak-off [Detournay, 2004, 2016], we can normalise the problem parameters as follows:

$$\rho = \frac{r}{R}, \quad \tau = \frac{t}{t_{mk}}, \quad \gamma(\tau) = \frac{R}{L}, \quad \Omega(\rho, \tau) = \frac{w}{\epsilon L}, \quad \Pi(\rho, \tau) = \frac{p}{\epsilon E'}, \qquad (3.41)$$

where the timescale t_{mk}, the lengthscale L, and the scale for strain ϵ are defined by

$$t_{mk} = \left(\frac{M'^5 E'^{13} Q_0^3}{K'^{18}} \right)^{1/2}, \quad L = \left(\frac{Q_0^3 E' t_{mk}^4}{M'} \right)^{1/9}, \quad \epsilon = \left(\frac{M'}{E' t_{mk}} \right)^{1/3}. \qquad (3.42)$$

The solution depends on the dimensionless time τ, coordinate ρ, and two dimensionless numbers representing Carter's leak-off ϕ and PDL ψ defined as

$$\phi = \frac{C'^4 E'^{11} M'^3 Q_0}{K'^{14}}, \qquad \psi = \frac{Q'^4 E'^5 M'}{K'^2 Q_0}. \qquad (3.43)$$

The PDL number ψ characterises the strength of pressure dependence of the fluid exchange process. The system of governing equations written in the normalised form is presented by Kanin et al. [2020c] in Appendix C.

In order to place the results of this investigation in the framework of the previous studies, it is useful to outline parametric space for the problem of a radial hydraulic fracture with Carter's leak-off. As presented in a review paper Detournay [2016], there are four limiting cases: storage-viscosity M, leak-off-viscosity $\tilde{M}$, storage-toughness K, and leak-off-toughness $\tilde{K}$. These four cases correspond to dominance of either fluid viscosity or fracture toughness as the primary dissipation mechanism, and either fracture (small leak-off) or permeable rock (large leak-off) as the primary storage for the injected fluid. Figure 3-18(a) presents the parametric space for the problem in terms of the dimensionless time τ and leak-off ϕ [Dontsov, 2016a]. The dashed coloured lines indicate zones of applicability of the limiting solutions, which are defined as the zones in which the relative difference between the general

solution and the limiting solutions is below 1%, see [Dontsov, 2016a] for more details. Note that the vertex solutions for the radial fracture with Carter's leak-off were obtained earlier in Savitski and Detournay [2002], Madyarova [2004], Bunger et al. [2005]. Figure 3-18(b) depicts conceptual representation of the problem parametric space (the same as in Figure 3-18(a)) with a rectangular shape and several solution trajectories in time parameterised by the dimensionless leak-off coefficient ϕ. Each trajectory starts from the viscosity-storage regime (vertex M) and ends at the leak-off toughness regime (vertex $\widetilde{K}$). In other words, M and $\widetilde{K}$ regimes always represent the early and large time solutions. In turn, the remaining two vertices (K and $\widetilde{K}$) can be realised at intermediate times, which is determined by the value of ϕ. Three cases of ϕ are considered and are shown on both the conceptual rectangular diagram and in the parametric space. For small values of ϕ, the solution originates in the M vertex, passes near the K vertex, and ends in the $\tilde{K}$ vertex. For intermediate values of ϕ, the solution transitions from M to $\tilde{K}$ directly. And for large values of ϕ, solution starts from M, transitions near $\tilde{M}$, and ends at $\tilde{K}$ vertex.
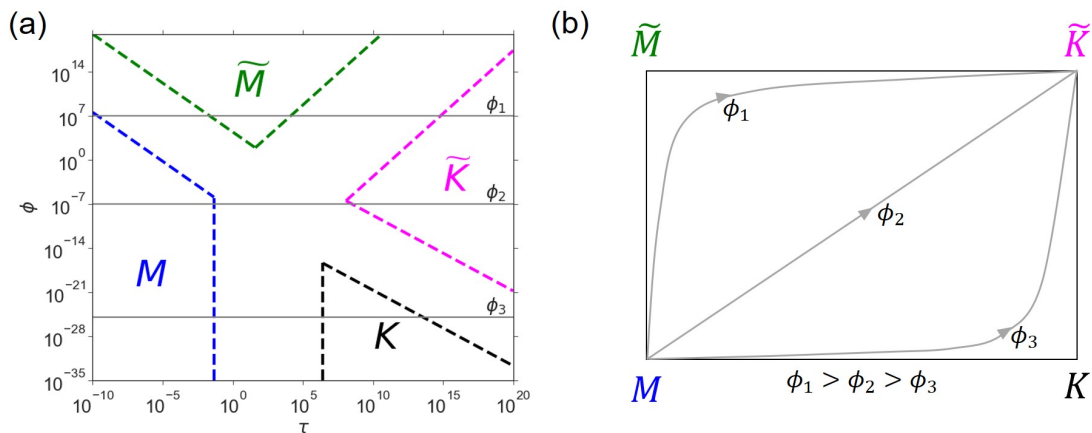
Figure 3-18: Parametric space for the problem of a radial fracture with Carter's leak-off in the (τ, ϕ) coordinates (a) and conceptual representation (b). Panel (a) shows the applicability domains of M (dashed blue), K (dashed black), $\widetilde{M}$ (dashed green) and $\widetilde{K}$ (dashed magenta) vertex solutions. Solution trajectories for different dimensionless leak-off ϕ are indicated for the reference.

Having established the parametric space for the problem of Carter's leak-off, i.e. when the PDL number $\psi = 0$, we proceed with the estimate of typical values for ψ representative of field applications. In order to do this, some problem parameters that do not vary significantly are kept fixed, while the other are varied. In particular,

let us consider the following parameters:

- geomechanics:

  - plane-strain elastic modulus: $E' = 30$ GPa;

  - fracture toughness: $K_{Ic} = 0.3 \div 1$ MPa $\cdot \sqrt{m}$;

  - far-field confining stress: $\sigma_o = 10 \div 30$ MPa;

- reservoir:

  - permeability: $k = 0.1 \div 100$ mD;

  - porosity: $\phi_r = 5 \div 25\%$;

  - ratio of the pore pressure and confinement stress: $p_o/\sigma_o = 0.95 \div 0.4$;

- fluid:

  - viscosity $\mu = 1 \div 5$ cP;

  - total compressibility $c_t = 10^{-3}$ MPa^{-1};

- injection:

  - $Q_0 = 0.01 \div 0.1$ m$^3/s$;

The above problem parameters are varied independently within their respective ranges. We calculate parameters ϕ and ψ by using equation (3.43) and the definitions of C' and Q' provided by equation (3.20). As a result, we obtain the parametric domain depicted in figure 3-19(a), in which the blue coloured area represents all possible combinations of problem parameters within the considered ranges. From this figure, one can notice that the values of governing parameters are located within the intervals: $\phi \in [7.1 \cdot 10^{-8},\ 3.1 \cdot 10^{15}]$ and $\psi \in [2.4 \cdot 10^{-9},\ 33.5]$. Black circular and square markers in figure 3-19(a) identify two particular parametric cases that were discussed in Section 3.3.4.1. Both of them are located in the upper half of the (ϕ, ψ) parametric space.

To better understand the influence of various problem parameters on the location inside the non-dimensional parametric space (ϕ, ψ) in figure 3-19(a), we also analyse

a set of subdomains with bounds corresponding to the limiting (minimum and maximum) values of a given dimensional parameter. The polygon coloured by orange in figure 3-19(a) corresponds to the maximum value of the permeability ($k = 100$ mD), while the green coloured polygon contains points related to the minimum value ($k = 0.1$ mD). Hence, the limiting values of the dimensionless PDL number ψ are governed by the predefined permeability range. Further, the polygon for a particular permeability value consists of two hexagons corresponding to the limiting values of the rock toughness. For example, there are two hexagons corresponding to $K_{Ic} = 0.3 \mathrm{MPa} \cdot \sqrt{\mathrm{m}}$ (dashed red line) and $K_{Ic} = 1 \mathrm{MPa} \cdot \sqrt{\mathrm{m}}$ (dashed blue line) inside the orange polygon (maximum permeability case). Similarly, we draw such hexagons inside the green polygon by dash-dotted lines (minimum permeability case). The final part of the parametric domain analysis is concerned with the hexagon structure presented by figure 3-19(b). It shows locations of data points corresponding to the minimum and maximum values of other parameters (μ, ϕ_r, p_o/σ_o, Q_0, σ_o) by red and blue colours, correspondingly. Such a representation allows us to find the range of possible values of the dimensionless parameters ϕ and ψ for practical values of physical parameters.

In addition to ϕ and ψ, the solution also depends on the dimensionless time τ, defined in (3.41). By taking the characteristic injection period equal to one hour, we can estimate the interval for the dimensionless time corresponding to the various combinations of other dimensional parameters discussed above as $\tau \in [10^{-6}, 10^2]$. Note that the range of considered values for fluid viscosity is relatively narrow, since we assumed that the viscosities of the reservoir fluid and the fracturing fluid have the same properties. Wider range of fracturing fluid viscosities would lead to a wider range for the dimensionless time τ.

3.3.4.3 Numerical solution inside the parametric space

The scope of this section is to identify values of the governing parameters for which the pressure-dependent effects are crucial, i.e. we define zones where the use of Carter's leak-off model leads to the inaccurate results. On the other hand, the analysis allows us to identify regions in which the traditional approach yields results
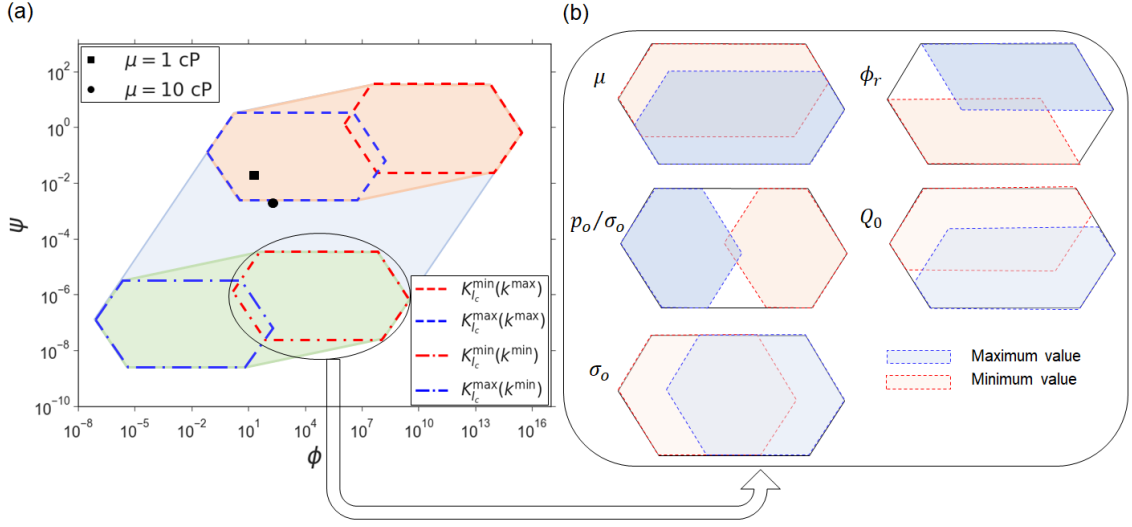
Figure 3-19: Parametric domain in terms of the leak-off parameter ϕ and PDL parameter ψ which corresponds to typical field parameters (blue polygon on panel (a)). Orange and green polygons on the left-hand side show locations of data points corresponding to the maximum and minimum permeability values. We also highlight regions (hexagons) related to the maximum and minimum values of the fracture toughness by the blue and red colours correspondingly (dashed line in case of the maximum permeability and dash-dotted line in case of the minimum permeability). The right-hand panel (b) shows the structure of the hexagon cell by considering variation of each individual parameters. By black square and circle markers, we mark cases discussed in section 3.3.4.1 corresponding to $\mu = 1$ cP and $\mu = 10$ cP respectively.

with acceptable accuracy, and the refinement of the fluid-exchange mechanism is unnecessary.

Based on the diagram shown in figure 3-19, we choose the following intervals for the dimensionless parameters for the analyses:

- normalised time: $\tau \in [10^{-5}, 10^4]$,

- leak-off number: $\phi \in [10^{-10}, 10^2]$,

- PDL number: $\psi \in \psi_{\{\}} = \{10^{-5}, 10^{-3}, 10^{-1}, 10^1\}$.

The selected ranges for ϕ and ψ correspond to the top left corner of the field parameters shown in figure 3-19. This is the zone, for which the PDL parameter is relatively large, but the leak-off parameter is relatively small so that there is the highest chance to observe the effect of the pressure-dependent leak-off.

Once the target interval of the problem parameters is established, we carry out numerical modelling of the radial fracture growth in the case of different combi-

nations of governing parameters ϕ and ψ for the pressure-dependent fluid exchange mechanism and for Carter's leak-off law. We consider each value of the PDL number in the list $\psi_{\{\}}$ separately and vary ϕ on a logarithmic scale between the minimum and maximum values. After that, the relative difference between the two solutions is computed as

$$\delta_A^{\phi,\psi}(\tau) = |A - A_c|/|A_c|, \quad A = \{\Omega(0,\tau),\ \Pi(1/2,\tau),\ \gamma(\tau),\ \eta(\tau)\}, \qquad (3.44)$$

where the subscript 'c' denotes solution for Carter's case, and the quantities without the subscript correspond to the solution with the pressure-dependent leak-off. Specifically, we evaluate the relative difference between the two solutions for the fracture width at the wellbore $\Omega(0,\tau)$, net pressure in the middle of the fracture $\Pi(1/2,\tau)$, fracture radius $\gamma(\tau)$, and efficiency $\eta(\tau)$ defined in (3.38). The values of $\delta_A^{\phi,\psi}(\tau)$ can be used to quantitatively demonstrate applicability of the Carter's leak-off model by plotting the maps in the coordinates (τ, ϕ) for the considered value of ψ.

As a starting point, the smallest value of the PDL number from the set $\psi = 10^{-5}$ is considered. Figure 3-20 shows numerical solution for the normalised fracture width, pressure, radius, and efficiency versus dimensionless time for different values of the leak-off number ϕ for the pressure-dependent and Carter's leak-off cases. Solid lines correspond to the solution with the pressure-dependent leak-off, while dashed lines represent the corresponding cases for Carter's leak-off. Results demonstrate that the difference between two models is relatively small, but present. Recall, that this is the case for the smallest value of the PDL coefficient ψ. To better quantify the difference, figure 3-21 shows the relative difference between the models computed using (3.44) for an extended range of the parameters τ and ϕ. Results in figure 3-21 demonstrate that the difference between the two solutions is distributed approximately uniformly, except for the case of small efficiencies, for which error decreases and the solution approaches Carter's model. In addition, there are intersections between the two solutions in terms of pressure and radius values, which are clearly visible on the plots and correspond to the concentrated zones of small error. Based

93
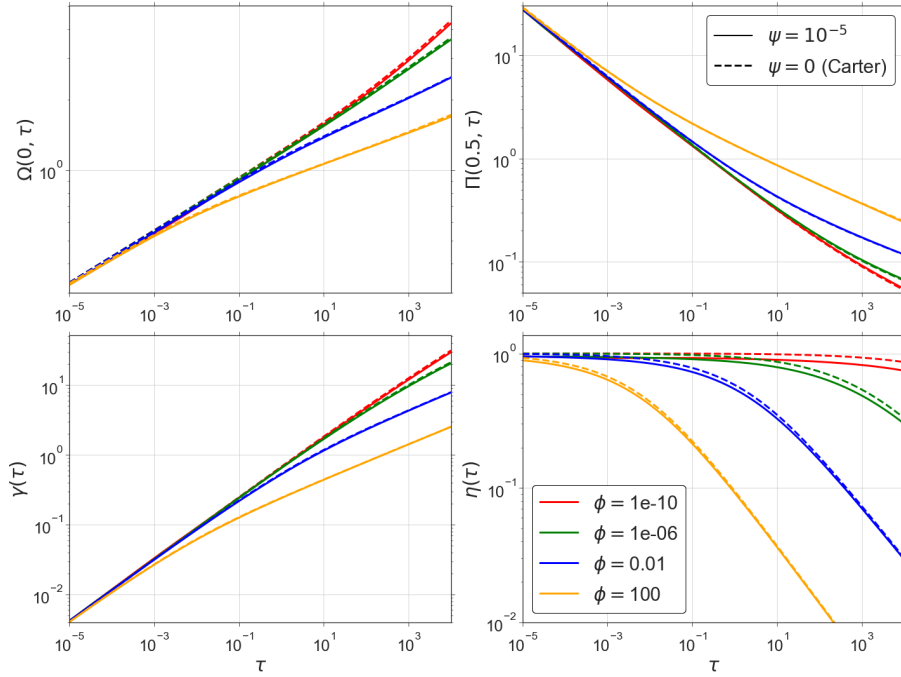
Figure 3-20: Solution profiles for the normalised fracture opening at the wellbore (top left), net pressure (top right), radius (bottom left), and efficiency (bottom right) versus dimensionless time τ for different values of the leak-off parameter ϕ in the case of $\psi = 10^{-5}$. Solid lines show the solution for the pressure-dependent leak-off and dashed lines show the corresponding solution with Carter's leak-off.

on the calculated $\delta_A^{\phi,\psi}(\tau)$ values depicted in figure 3-21, it is possible to quantify the averaged (across the considered time and leak-off number intervals) deviations of various fracture characteristics. The aperture near the wellbore and radius differ by approximately 2.5% and 2.9% respectively, while the variation of the net fluid pressure in the middle of the fracture is equal to 2.8%. Since both fracture width at the wellbore and radius affect on the fracture efficiency, its mean deviation is higher and is equal to 8.7%. Moreover, we can also determine the maximum values for the relative difference: 6.9% for $\Omega(0, \tau)$, 13.6% for $\gamma(\tau)$, 8.4% for $\Pi(0.5, \tau)$ and 30.3% for $\eta(\tau)$.

Then, we consider the dimensionless PDL number $\psi = 10^{-1}$. The solution profiles computed for this ψ value are presented in figure 3-22 while figure 3-23 depicts maps that show the deviation from the Carter's leak-off case. The effect of the pressure-dependent leak-off is much more pronounced in this case. Fracture efficiency is noticeably lower for the case of the pressure-dependent fluid exchange and, as a result, the width and radius are smaller as well. At this point, we would like
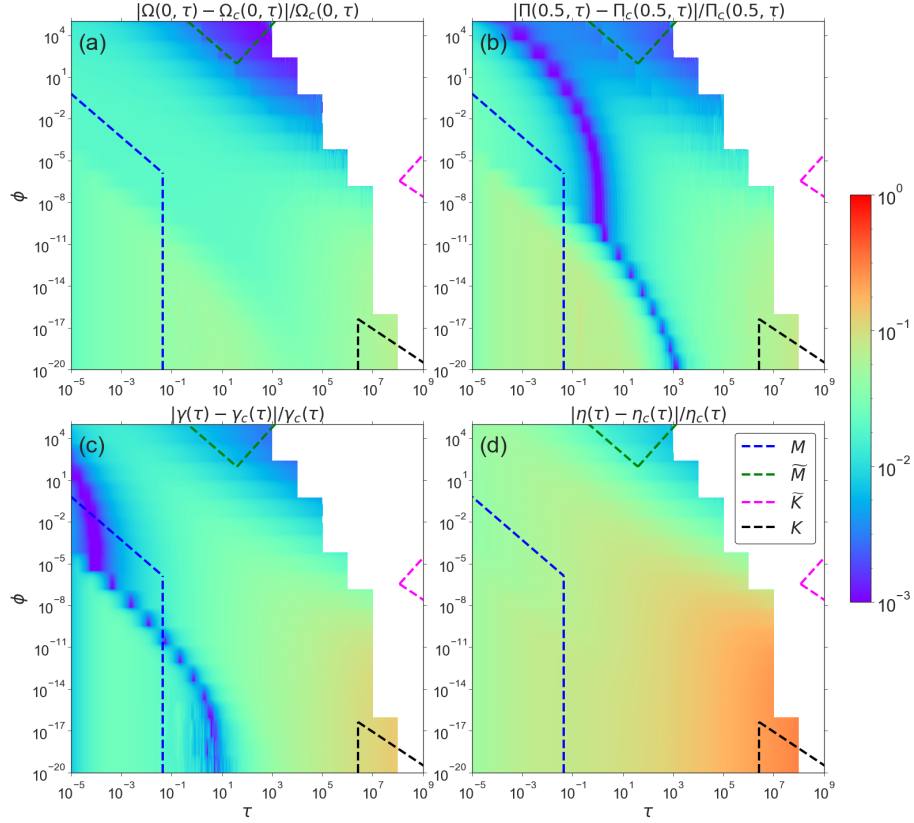
Figure 3-21: Relative difference between the solution with the pressure-dependent leak-off and the one that uses Carter's leak-off model inside (τ, ϕ) parametric space for $\psi = 10^{-5}$. The applicability domains of the limiting solutions for the radial fracture model with Carter's leak-off are shown by dashed coloured lines [Dontsov, 2016a].

to note that the pressure-dependent mechanism of the fluid exchange process leads to the higher values of the leak-off rate as compared to Carter's leak-off case, which results in the lower fracture efficiency and smaller fracture size. This is because the net fluid pressure $p(r,t)$ inside the fracture is mostly positive $(p_f(r,t) > \sigma_o)$, in which case the pressure-dependent leak-off correction in the Reynolds equation (3.22) has the same sign as Carter's leak-off term and adds to the total leak-off. The described behaviour of the net fluid pressure is qualitatively different from that for the near-tip region model [Kanin et al., 2020d], where it is negative throughout the fracture. Consequently, the pressure-dependent term in the cumulative fluid exchange reduces the total leaked-off volume near the tip. It is interesting to observe that the efficiency, width, and radius computed for the solution with the pressure-dependent leak-off reach an asymptotic behaviour for small dimensionless times for all values of ϕ considered. This asymptotic behaviour is different from that for

95
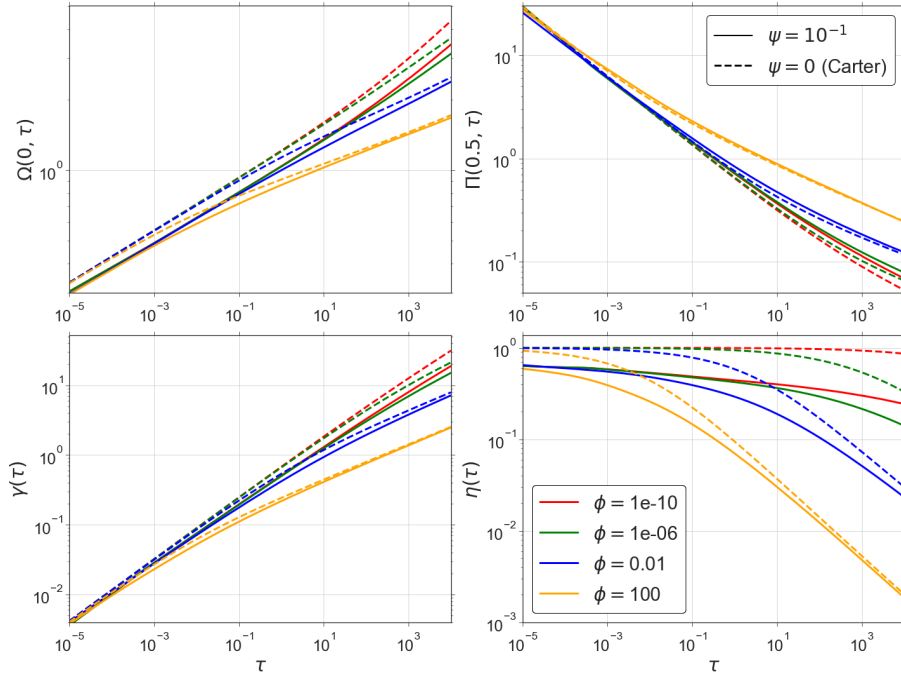
Figure 3-22: Solution profiles for the normalised fracture opening at the wellbore (top left), net pressure (top right), radius (bottom left), and efficiency (bottom right) versus dimensionless time τ for different values of the leak-off parameter ϕ in the case of $\psi = 10^{-1}$. Solid lines show the solution for the pressure-dependent leak-off and dashed lines show the corresponding solution with Carter's leak-off.

Carter's leak-off case. At the same time, the difference between the models reduces for larger times, for which the fracture efficiency gets reduced due to leak-off. Results in figure 3-23 reveal that the solution profiles behaviour is approximately the same as in the previous case, but the magnitude of the difference is increased substantially. The mean values of the relative differences of the fracture opening at the wellbore and pressure are equal to 13.6%. At the same time, the deviations for the radius and efficiency are 22.9% and 49.4%, respectively. The maximum values for these quantities are 38% for the width at the wellbore; 62.9% for the net pressure at the middle of the crack, 61.9% for the radius and 91% for the efficiency. As before, the difference reduces towards the leak-off viscosity regime, for which the efficiencies are small. This result is consistent with the observations in figure 3-22.

To summarise the average and maximum discrepancies between the two models, Table 3.6 shows values of the average and maximum variations for the fracture width, pressure, radius, and efficiency for different values of ψ. All four values of the PDL coefficient are considered for completeness. Clearly, the difference increases

96
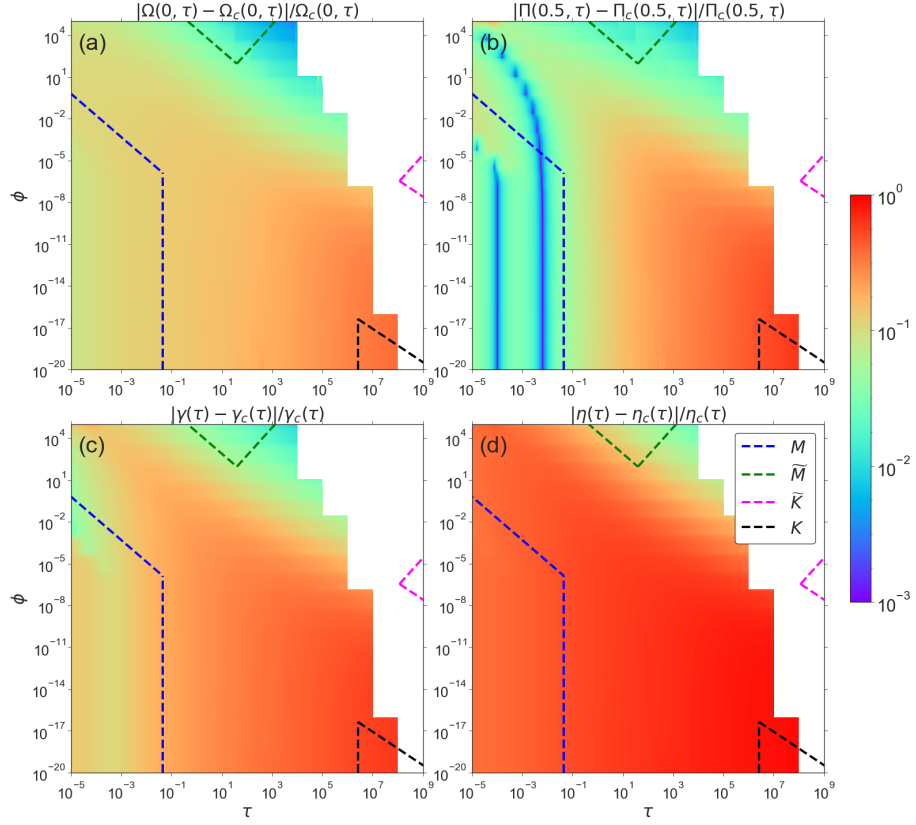
Figure 3-23: Relative difference between the solution with the pressure-dependent leak-off and the one that uses Carter's leak-off model inside (τ, ϕ) parametric space for $\psi = 10^{-1}$. The applicability domains of the limiting solutions for the radial fracture model with Carter's leak-off are shown by dashed coloured lines [Dontsov, 2016a].

substantially for larger values of ψ and becomes nearly negligible for the small values of the dimensionless PDL number ψ.

	Deviation (%)							
	Average				Maximum			
ψ	$\Omega(0,\tau)$	$\Pi(0.5,\tau)$	$\gamma(\tau)$	$\eta(\tau)$	$\Omega(0,\tau)$	$\Pi(0.5,\tau)$	$\gamma(\tau)$	$\eta(\tau)$
10^{-5}	2.5	2.8	2.9	8.7	6.9	8.4	13.6	30.3
10^{-3}	5.9	4.6	8.4	23.3	18.5	23.6	34.0	64.6
10^{-1}	13.6	13.6	22.9	49.4	38.0	62.9	61.9	91.0
10^{1}	26.8	42.5	47.0	78.1	56.6	134.0	81.5	98.5

Table 3.6: Average and maximum relative differences between solutions of the pressure-dependent and Carter's radial fracture models.

3.3.4.4 Radial fracture model with a simplified tip asymptote

We have demonstrated that the PDL affects the propagation of the radial hydraulic fracture. This effect manifests itself by i) diminishing the leak-off intensity in the tip region of the HF compared to the model with Carter's leak-off, where the fluid pressure is below the confining stress σ_o, and ii) increasing the leak-off compared to Carter's baseline away from the fracture tip where the fluid pressure exceeds σ_o. The latter effect of the enhanced leak-off dominates over the former leak-off reduction in the tip region and leads to overall larger leak-off compared to Carter's case. To evaluate the relative importance of the near and away from the tip PDL, we carry out an alternative radial HF solution which accounts for the pressure-dependency of the leak-off away from the fracture tip, in all spatial elements other than the tip element, while use Carter's leak-off near-tip solution [Garagash et al., 2011] for the latter. Particularly, in this alternative numerical solution for radial HF we implement the approximate Carter's tip solution [Dontsov and Peirce, 2015b], which offers advantages of the simpler implementation and faster computation times as compared to the full Carter's tip solution [Garagash et al., 2011].

The developed numerical solution for the radial hydraulic fracture utilises the pressure-dependent leak-off within the fracture and also employs the corresponding solution for the tip as a propagation condition. The latter tip solution comes from solving the problem of a semi-infinite hydraulic fracture [Kanin et al., 2020d]. At the same time, there is a possibility to use the tip solution corresponding to Carter's leak-off together with the pressure-dependent leak-off inside the fracture. The advantage of such an approach is that there is an approximate tip solution for Carter's model [Dontsov and Peirce, 2015b], and therefore the computation of the propagation condition using such a solution is simpler and quicker. This approach is especially relevant for planar or multi-planar fracture cases [Dontsov and Peirce, 2017c, Zia and Lecampion, 2020], for which the tip asymptote is used throughout the fracture front. Therefore, the purpose of this section is to evaluate the error caused by using the simplified tip asymptote on the radial solution.

To compare effectiveness of the proposed approximation, as was done previously,

we introduce the relative difference as $\delta_A^{\phi,\psi}(\tau) = |A - A_s|/|A|$, where the subscript 's' denotes the solution that is calculated by the simplified approach with the tip asymptote with Carter's leak-off. The comparison is performed in terms of the fracture aperture $\Omega(0,\tau)$ and radius $\gamma(\tau)$. As in the previous section, we present deviation maps for two cases $\psi = 10^{-5}$ and 10^{-1}, and the mean and maximum variations for all values of the PDL number are provided in the tabular form.

Figure 3-24 shows a comparison between the full and simplified solutions inside the parametric spaces. Colour filling indicates the relative difference between the exact and simplified solutions. The top row (figures (a) and (b)), corresponds to the case with the PDL number $\psi = 10^{-5}$, and the bottom row (figures (c) and (d)) is for $\psi = 10^{-1}$. The left figures ((a) and (c)) compare fracture width at the wellbore and the right figures ((b) and (d)) compare radius. As can be seen from the figure, the maximum difference between the solutions occurs for smaller and larger values of the dimensionless time τ in the case of small ϕ and only at the initial stage of the fracture growth for large values of the Carter's coefficient. Summary of the maximum and average relative difference between the full and simplified solutions is presented in table 3.7. All four values of ψ are considered for completeness. One can see that the deviations increase for larger values of ψ. These values need to be taken in relation to the corresponding numbers presented in table 3.6, which indicate the overall influence of the pressure-dependent leak-off. Using the presented values in table 3.7, one can find out that for the PDL number $\psi < 10^{-3}$ the effect can be captured without the correct tip asymptote. However, the contribution of the tip solution for larger values of the PDL coefficient is non-negligible and can contribute up to 40% of the overall difference between the full solution with the pressure-dependent leak-off and that with Carter's model. Given the above results, we can summarise the following: 1) by increasing the value of ψ, we observe the growing importance of the PDL tip asymptote (figure 3-24 and table 3.7), so it is expected that for the large enough values of ψ Carter's tip model no longer results in good approximation for the radial HF; 2) the error depends on time, namely, the large error values are seen at both small and large times, so the "goodness" of the tip with Carter's leak-off as an approximation embedded into the radial crack with

the PDL will depend in practice on the problem parameters (which scale time) and time of relevance in the application.
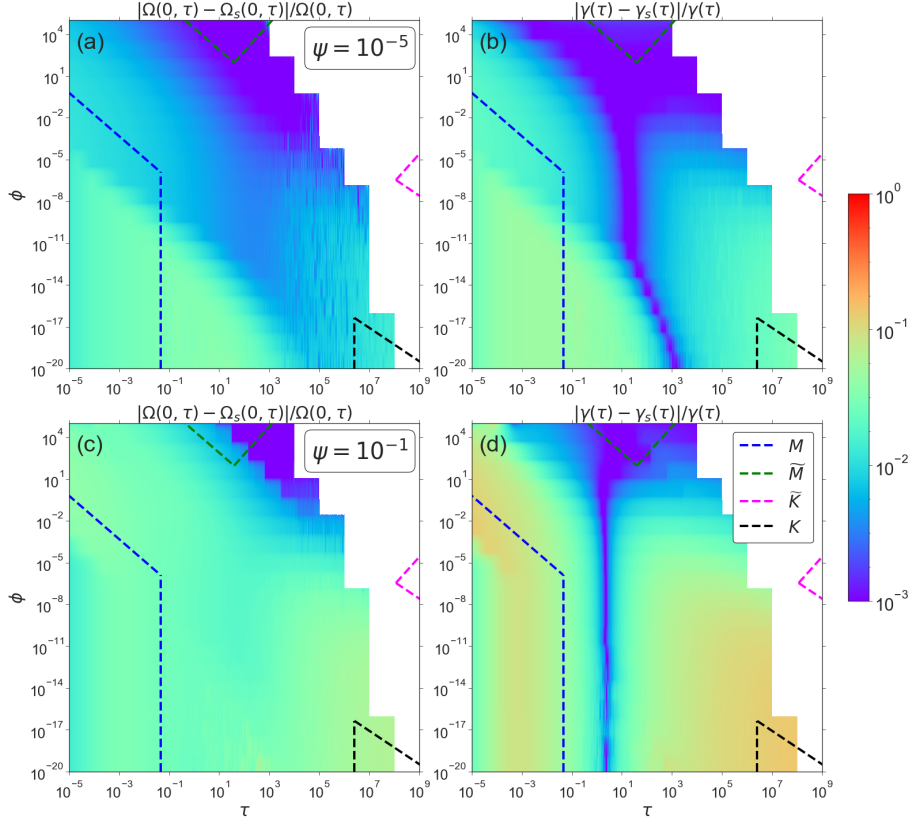
Figure 3-24:   Relative difference between the radial fracture solution with the pressure-dependent leak-off and the simplified solution that uses Carter's tip asymptote together with the pressure-dependent leak-off inside the fracture. Figures (a) and (b) present results in the case of $\psi = 10^{-5}$, while (c) and (d) are related to $\psi = 10^{-1}$. Figures (a) and (c) compare fracture width at the wellbore, while (b) and (d) compare the fracture radius. The applicability domains of the limiting solutions for the radial fracture model with Carter's leak-off are shown by dashed coloured lines [Dontsov, 2016a].

3.3.4.5   Estimation of the effect of the pressure-dependent leak-off based on the solution with Carter's leak-off

The purpose of this section is to determine the domain in the parametric space (τ, ϕ) in which the PDL solution is substantially different from Carter's solution for a certain value of the PDL number ψ . We begin with the analyses of the whole parametric space (τ, ϕ) by using the complete Carter's solution proposed by Dontsov [2016a]. After that, we perform estimations for the limiting propagation regimes M, $\widetilde{M}$, K and $\widetilde{K}$ utilising their exact solutions.

| | Deviation (%) | | | |
| | Average | | Maximum | |
ψ	$\Omega(0,\tau)$	$\gamma(\tau)$	$\Omega(0,\tau)$	$\gamma(\tau)$
10^{-5}	1.1	1.6	3.9	5.0
10^{-3}	1.7	2.5	4.8	7.9
10^{-1}	2.5	4.9	7.8	14.1
10^{1}	3.2	8.9	16.3	38.4

Table 3.7: Average and maximum relative differences between the full and simplified solutions.

Let us define $\psi_\alpha = \psi_\alpha(\tau, \phi)$ as the value of the PDL number ψ for which the pressure-dependent leak-off volume correction V_{PDL} at given time τ and Carter's leak-off number ϕ comprises a small fraction of the injected volume V_{inj}: $\alpha = V_{\mathrm{PDL}}/V_{\mathrm{inj}}$. The values of ψ_α for a choice of a small α allow us to illustrate regions inside the parametric space (τ, ϕ), which are more susceptible to the PDL effects.

By using an approximate solution for the radial fracture with Carter's leak-off [Dontsov, 2016a], we numerically evaluate $V_{\mathrm{PDL}}(\tau, \phi, \psi)$ and the corresponding $\psi_\alpha(\tau, \phi)$ for $\alpha = 5\%$, see figure 3-25a. The maximum value of ψ_α is set at 100, thus (τ, ϕ) subdomain with $\psi_\alpha > 100$ in figure 3-25a appears 'blank'. In figure 3-25a, we also show a set of isolines $\psi_\alpha(\tau, \phi) = \psi$ for fixed $\psi = 10^{-9}, 10^{-7}, 10^{-5}, 10^{-3}, 10^{-1}, 10$. For a particular value of ψ, for example $\psi = 10^{-5}$ in figure 3-25a, the corresponding isoline shown by black line defines domain $\psi_\alpha(\tau, \phi) \geq \psi$ extending from the isoline in the direction of the gradient of ψ_α (as shown by the arrows). This domain is interpreted as a parametric region where Carter's leak-off solution provides results with an acceptable accuracy for the chosen value of the PDL number ψ. In contrast, outside of this zone, i.e. where $\psi_\alpha(\tau, \phi) < \psi$ it is essential to take into account for the pressure-dependent leak-off since it has a significant impact on the solution.

Further, we derive asymptotic expressions for ψ_α when the complete Carter's solution reduces to one of four limiting regimes of fracture propagation: storage-toughness K, leak-off-toughness $\tilde{K}$, storage-viscosity M, and leak-off-viscosity $\tilde{M}$. In figure 3-25a, the applicability domains of the limiting regimes of Carter's solution are outlined by dashed lines. The corresponding limiting solutions for the pressure

profile Π and crack radius γ in the mk-scaling are [Savitski and Detournay, 2002, Madyarova, 2004, Bunger et al., 2005]:

$$\Pi_k = \frac{\pi}{2^{7/2}\sqrt{\gamma_k}}, \qquad \gamma_k = \left(\frac{9}{2\pi^2}\right)^{1/5}\tau^{2/5},$$

$$\Pi_{\widetilde{k}} = \frac{\pi}{2^{7/2}\sqrt{\gamma_{\widetilde{k}}}}, \qquad \gamma_{\widetilde{k}} = \frac{\sqrt{2}}{\pi}\tau^{1/4}\phi^{-1/8},$$

$$\Pi_m = \left[A_1\left(A_2 - \frac{2}{3}\left(1 - \rho^{-1/3}\right)\right) - A_3\left(\ln\left(\frac{\rho}{2}\right) + 1\right)\right]\tau^{-1/3}, \qquad \gamma_m = 0.6955\tau^{4/9},$$

$$\Pi_{\widetilde{m}} = \left[B_1(4 - \left(1 - \rho^2\right)^{-3/8}) - B_2(3(2\rho^2 - 1) - 1) + B_3\left(\ln\left(\frac{2}{\rho}\right) - 1\right)\right]\tau^{-3/16}\phi^{3/32},$$

$$\gamma_{\widetilde{m}} = \frac{\sqrt{2}}{\pi}\tau^{1/4}\phi^{-1/8},$$

where $A_1 = 0.3581$, $A_2 = 2.479$, $A_3 = 0.09269$, $B_1 = 0.2596$, $B_2 = 0.0169$, $B_3 = 0.1403$.

To proceed, we substitute each limiting case from the above equations into the formula for the PDL volume. By presenting the dimensionless pressure Π and radius γ in the form $\Pi = Af(\rho)\tau^{\alpha}\phi^{\beta}$, $\gamma = B\tau^{\delta}\phi^{\epsilon}$ suitable for each vertex solution and putting them into equation (3.23), we obtain the following expression for V_{PDL}:

$$V_{\mathrm{PDL}} = 2\pi\psi^{1/4}\cdot AB^2\tau^{\alpha+1/2+2\delta}\phi^{\beta+2\epsilon}\int_0^1 \rho f(\rho)\left[\sqrt{\pi}\frac{\Gamma(\alpha+1)}{\Gamma\left(\alpha+\frac{3}{2}\right)} - B\left(\rho^{1/\delta}; \alpha+1, \frac{1}{2}\right)\right]d\rho, \tag{3.45}$$

where we utilise the Euler gamma function $\Gamma(x)$ and the incomplete beta function $B(x; a, b)$. We should note that the spatial integral is calculated analytically for the toughness dominated regimes, while numerical integration is performed for the viscosity dominated regimes.

By letting $V_{\mathrm{PDL}} = \alpha V_{\mathrm{inj}}$, we arrive to:

$$K - \text{vertex}: \quad \alpha\tau = 1.04\psi^{1/4}\tau^{11/10} \quad \Longrightarrow \quad \psi_\alpha = 0.845\alpha^4\tau^{-2/5},$$

$$\widetilde{K} - \text{vertex}: \quad \alpha\tau = 0.43\psi^{1/4}\tau^{7/8}\phi^{-3/16} \quad \Longrightarrow \quad \psi_\alpha = 27.8276\alpha^4\tau^{1/2}\phi^{3/4},$$

$$M - \text{vertex}: \quad \alpha\tau = 1.32\psi^{1/4}\tau^{19/18} \quad \Longrightarrow \quad \psi_\alpha = 0.33\alpha^4\tau^{-2/9},$$

$$\widetilde{M} - \text{vertex}: \quad \alpha\tau = 0.82\psi^{1/4}\tau^{13/16}\phi^{-5/32} \quad \Longrightarrow \quad \psi_\alpha = 2.25\alpha^4\tau^{3/4}\phi^{5/8}. \tag{3.46}$$

In order to ensure the validity of the numerically calculated ψ_α values when a solution trajectory is passing (with time) through the vertex solution domains, we plot figure 3-25b. In this chart, we present ψ_α evolution with dimensionless time τ for three solution trajectories with $\phi = 10^{-24}, 10^{-6}$, and 10^6, respectively. The corresponding curves obtained from the vertex solutions (3.46) are depicted by dashed lines. One can observe that the compete solution coincides with the asymptotic behaviour within the corresponding asymptotic time domain.

Using the map in figure 3-25a, we can notice that the problem solution inside the storage-toughness (K) domain differs from Carter's solution at already very small values of the PDL parameter ψ, on the order of 10^{-9}. Moreover, ψ_α is a decreasing function on τ in this region. The viscosity-storage (M) regime becomes affected by the PDL for ψ on the order of 10^{-5}. Similarly to the toughness-storage regime, ψ_α decreases with τ. In contrast, the limiting solutions corresponding to high leak-off, namely $\widetilde{M}$ and $\widetilde{K}$, become affected by the pressure dependency only for much larger values of ψ. In addition, there is a strong gradient towards the direction of smaller efficiencies. It is also interesting to observe that the M, $\widetilde{M}$, and $\widetilde{K}$ vertices are gradually displaced with the increase of ψ, but are still present in the limiting cases. At the same time, the K vertex solution disappears after exceeding a relatively small ψ value. This is because ψ_α decreases with τ and is independent of ϕ for the K vertex. As a result, the maximum value of ψ at which K vertex can be still partially realised corresponds to ψ_α at the vertical boundary of applicability (red dashed line). Consequently, once ψ exceeds this value, the K vertex disappears. In addition, we notice that ψ_α decreases with dimensionless time for small τ, then reaches a minimum, and eventually increases with τ. Depending on the value of ϕ this minimum shifts from very large values of τ (see $\phi = 10^{-24}$ case, for which the minimum has not been reached), to intermediate values ($\phi = 10^{-6}$), and eventually to small values of τ ($\phi = 10^6$).

The analysis presented in this section is consistent with the previously obtained numerical results shown in figure 3-23, for which $\psi = 10^{-1}$ is used. In this case, the relative difference between the PDL and Carter's solutions is greater than 5% for almost all (τ, ϕ), i.e. they differ considerably (apart from the domain with large
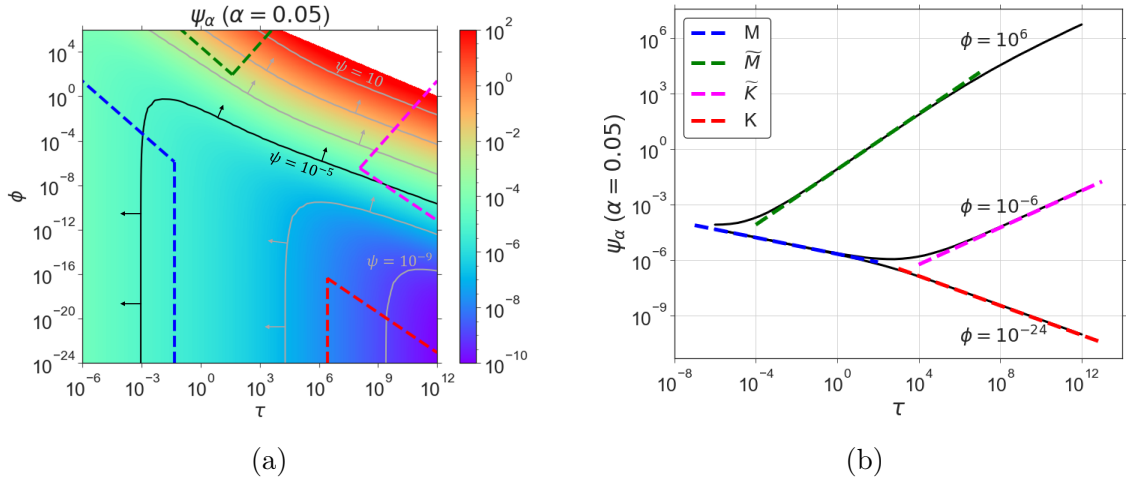
Figure 3-25: (a) Values of the parameter ψ as a function of normalised time τ and leak-off number ϕ for which the PDL provides a contribution of $\alpha = 0.05$ to the volume balance: $\psi_\alpha(\tau, \phi)$ computed based on the approximate solution for the radial fracture with Carter's leak-off [Dontsov, 2016a]. The boundaries of the asymptotic regions where the limiting solutions for the radial fracture model with Carter's leak-off are applicable are shown by dashed coloured lines in (a) for reference. Particular set of isolines $\psi_\alpha = \{10^{-9}, 10^{-7}, 10^{-5}, 10^{-3}, 10^{-1}, 10^1\}$ are shown by solid grey/black lines. Domain $\psi_\alpha(\tau, \phi) \geq \psi$ bounded by a particular isoline and extending in the direction of the gradient of ψ_α (as indicated by arrows) corresponds to the region of approximate validity of the Carter's leak-off for the given value of ψ. (b) Variation of ψ_α with time τ for the cases of $\phi = \{10^{-24}, 10^{-6}, 10^6\}$ computed using Carter's solution [Dontsov, 2016a] (black solid lines) and the corresponding curves computed from the vertex solutions [Savitski and Detournay, 2002, Madyarova, 2004, Bunger et al., 2005] (coloured dashed lines).

ϕ). Indeed, with the reference to figure 3-25a, it is clear that most of the points inside the parametric space correspond to the ψ_α values that are below 10^{-1}. The contribution of PDL reduces for larger values of leak-off, which is again consistent with earlier observations.

Figure 3-25a can be used to judge whether to include the PDL effects into the analysis or not. In order to do so, one needs to compute the dimensionless parameters τ, ϕ, and ψ by using equations (3.41)–(3.43) for the given problem parameters. The values of τ and ϕ provide a location inside the parametric space (τ, ϕ). Then, ψ_α can be determined from figure 3-25a for this particular combination of τ and ϕ. If the value of ψ for the given problem parameters is above ψ_α, then the effect of PDL is above 5%, and it is recommended to include it in computations. On the other hand, if ψ is smaller than ψ_α, then PDL effects can be neglected and Carter's leak-off model can be used.

Chapter 4

Turbulent flow effects in a slickwater fracture propagation

4.1 Preamble

When the water-based fracturing fluid with relatively low viscosity (1 - 10 cP) is used in reservoir stimulation, the injection rate can be set relatively high. It is required for the compensation of undesirable effects linked with fluid viscosity on the proppant settling and in order to create a crack aperture sufficiently large for proppant placement [Barati and Liang, 2014]. High injection rate of low-viscous fluid leads to the onset of the turbulent flow regime in the part of the fracture adjacent to the wellbore. The remaining part of the fracture, i.e., the region from the transition boundary to the fracture front, is occupied by laminar flow. Since Reynolds number for the plane channel flow depends on the aperture, the laminar flow regime always exists near the fracture front where the aperture value tends to zero.

Turbulent flow effects were first discussed in the context of hydraulic fracture propagation by Perkins et al. [1961] for the PKN fracture geometry. Further, Nilson [1981] analysed a model for a plane strain gas-driven fracture, and this work discusses the flow regime transformation inside the crack channel from turbulent to laminar in the direction of the fracture front. The limiting propagation regimes associated with turbulent flow inside magma dykes were studied by Emerman et al. [1986], Lister and Kerr [1991]. Tsai and Rice [2010] considered a plane strain crack

with fully turbulent flow in application to natural water-driven fracture in glaciers. Different aspects of the turbulent flow regime impact on the fracture growth with PKN geometry have been investigated in the following works [Kano et al., 2015, Zia and Lecampion, 2017, Zolfaghari et al., 2017]. The analyses of either fully turbulent or turbulent-laminar flow influence on the crack propagation have also been carried out for fractures with different geometries including a plane strain [Tsai and Rice, 2012, Zolfaghari et al., 2018], radial [Zolfaghari and Bunger, 2018, 2019, Lecampion and Zia, 2019], planar 3D [Dontsov and Peirce, 2017b] fracture, and a semi-infinite fracture [Dontsov, 2016c, Lecampion and Zia, 2019].

The fluid injection into the reservoir at a relatively high volumetric flow rate requires significant energy consumption for fluid pumping [Yang et al., 2019], especially during the simultaneous growth of multiple cracks, i.e., multistage hydraulic fracturing treatment. The limitation of the operational costs can be achieved by adding specific polymers to pure water resulting in a mixture called slickwater. The used additives slightly increase the fluid viscosity and considerably decrease the friction, up to 70% compared to that of the pure water [Nieuwstadt et al., 2016]. The experiments of Virk [1971, 1975] demonstrate how the flow friction factor declines depending on the used polymer additive type and its concentration. It was also determined in this work that the friction reduction has a so-called maximum drag reduction (MDR) or Virk's asymptote, which can be achieved at a relatively small concentration of the polymers.

Section 4.2 examines the near-tip region of a hydraulic fracture propagating in a permeable reservoir. We take into account the possible transfer of the flow regime from laminar to turbulent at some distance from the fracture front where Reynolds number of the fluid flow inside the crack becomes higher than the critical value. The hydraulic fracturing fluid in our model is slickwater, and we assume that the MDR asymptote governs its friction factor during the turbulent flow regime. For the problem formulation, we will rely on the original model framework of Lecampion and Zia [2019], where the authors investigate a similar problem in the case of an impermeable reservoir. In this work, we analyse how the presence of the leak-off process governed by Carter's law affects the transition to the turbulent flow regime.

Firstly, we provide the problem formulation and main equations. Secondly, we outline the limiting propagation regimes. Thirdly, we present particular solution profiles for the fracture opening and fluid pressure and carry out a comparison with an impermeable reservoir case [Lecampion and Zia, 2019]. Finally, we analyse the parametric space of the problem by constructing the regime maps showing the applicability domains of the limiting solutions and examine the behaviour of the transition boundary between the flow regimes.

Section 4.3 considers a radial hydraulic fracture propagating in a permeable reservoir and driven by turbulent-laminar slickwater flow. The main aim of the exploration is to analyse the combined effects of the laminar-turbulent flow of the fracturing fluid with drag reduction agents and the fluid leak-off into the ambient rock on the propagation of a finite hydraulic fracture. Firstly, we outline the problem formulation relying on Lecampion and Zia [2019], system of equations and introduces the numerical scheme. Next, the solution examples corresponding to typical field cases are considered. Further, we investigate the limiting propagation regimes, namely, revisit the existing limiting solutions and derive new ones. Finally, we describe the results of the problem parameter space investigation.

4.2 Semi-infinite fracture model

4.2.1 Model formulation

We begin with the problem formulation for the near-tip region of a hydraulic fracture driven by turbulent-laminar flow. Figure 4-1 shows the schematics of the investigated problem. The assumptions and governing equations of the fracture tip model given in Section 2.1 remain the same except those linked with the fluid flow inside the fracture channel. We will discuss the latter in detail in the current section.

In the current problem, fracturing fluid is slickwater which can be characterised as Newtonian liquid with viscosity μ and density ρ in the laminar flow regime, while the rheological response from the onset of the transition to turbulent flow will be described further.
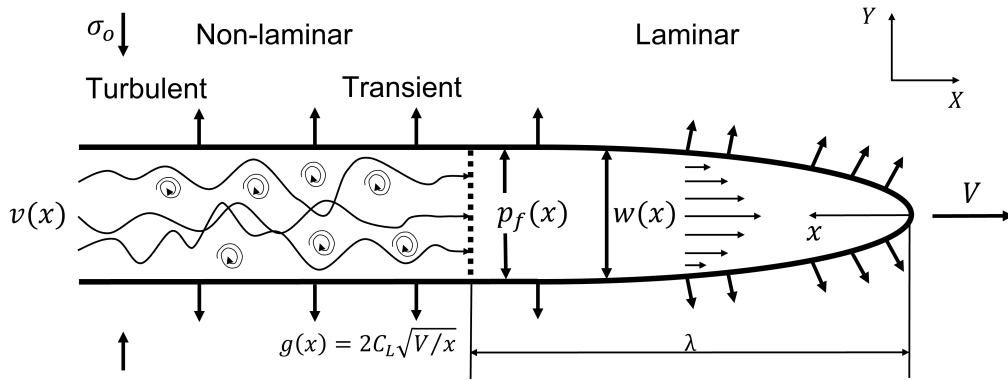
Figure 4-1: Schematics of the fracture-tip model with turbulent flow and leak-off.

Let us define Reynolds number for the channel flow as $Re = \rho v w / \mu$, where v is the fluid velocity. Reynolds number grows from 0 to infinity if we move away from the tip. We suppose that Re is less than the critical value Re_c along the fracture region $x \in (0, \lambda)$ (Figure 4-1) resulting in the laminar flow regime there. The onset of the flow regime transition to turbulence is located at point $x = \lambda$, and the flow regime along the domain $x \in (\lambda, +\infty)$ is non-laminar (from transient to fully-turbulent). In the model, the flow regime transition is captured via the friction factor f usage.

Next, we consider the width-averaged momentum conservation equation:

$$v^2 = \frac{w}{\rho f} \frac{dp}{dx}, \qquad (4.1)$$

where f is the Fanning friction factor. In the case of the laminar flow regime, equation (4.1) has the form of Poiseuille's law given by (2.9). By comparing equations (4.1) and (2.9), one can obtain the friction factor expression for the laminar flow regime: $f^{\text{lam}} = 12/Re$. In turn, the Fanning friction factor for pipe laminar flow equals $f_d^{\text{lam}} = 16/Re_d$, where $Re_d = \rho v d/\mu$ is Reynolds number for pipe flow suggesting $Re_d = 4/3 \cdot Re$. This formula is essential for translating the friction factor curves established for pipe flow, e.g., see [Brill and Mukherjee, 1999]), to the case of channel flow (in the fracture), i.e. $f = f(Re_d) = f(4/3 \cdot Re)$ [Lecampion and Zia, 2019]. Further, we introduce the normalised friction factor $\tilde{f} = f/f^{\text{lam}}$ [Dontsov,

2016c] and rewrite equation (4.1) in the form:

$$v = \frac{w^2}{M'\tilde{f}}\frac{dp}{dx},$$ (4.2)

We have already described the flow behaviour during the laminar flow regime. Now, we move on to the discussion of turbulent flow. Since fracturing fluid is slickwater, we consider the friction factor f governed by the MDR asymptote: a phenomenological relation proposed by Virk [1971, 1975], when $Re > Re_c$ (non-laminar flow):

$$\frac{1}{\sqrt{f}} = 19\log_{10}\left(Re_d\sqrt{f}\right) - 32.4,$$ (4.3)

To facilitate the solution of the fracture tip problem, we will utilise a power-law approximation of (4.3) proposed by Lecampion and Zia [2019]:

$$f = f_0 Re_d^{-n} = f_0' Re^{-n},$$ (4.4)

where $f_0 = 1.78$, $n = 0.7$ and $f_0' = f_0(4/3)^{-n} = 1.46$.

Figure 4-2 presents the function $f(Re)$ during laminar and turbulent regimes in traditional (a) and Prandtl-Karman (b) coordinates. Apart from the MDR asymptote (green line), we also show Blasius asymptote for turbulent pipe flow (smooth walls case) of pure water adjusted to the channel geometry in order to demonstrate quantitatively how the slickwater drag reduction agents decrease friction. The MDR approximation (4.4) closely approximates Virk's asymptote (4.3) within the range $Re \in (10^3, \ 1.5 \cdot 10^4)$ with a relative deviation less than 5%.

Further, we define the friction factor function for the whole range of Reynolds numbers, i.e. from the laminar regime to the turbulent one, similar to Lecampion and Zia [2019]:

$$f = \begin{cases} 12/Re, & Re \le Re_c, \\ f_0' Re^{-n}, & Re > Re_c, \end{cases}$$ (4.5)

where Re_c is the critical Reynolds number for slickwater case. The critical value is defined as an intersection of the laminar and turbulent (equation (4.4)) branches in order to ensure the function $f(Re)$ continuity: $Re_c = (12/f_0')^{1/(1-n)} = 1132.6$. The
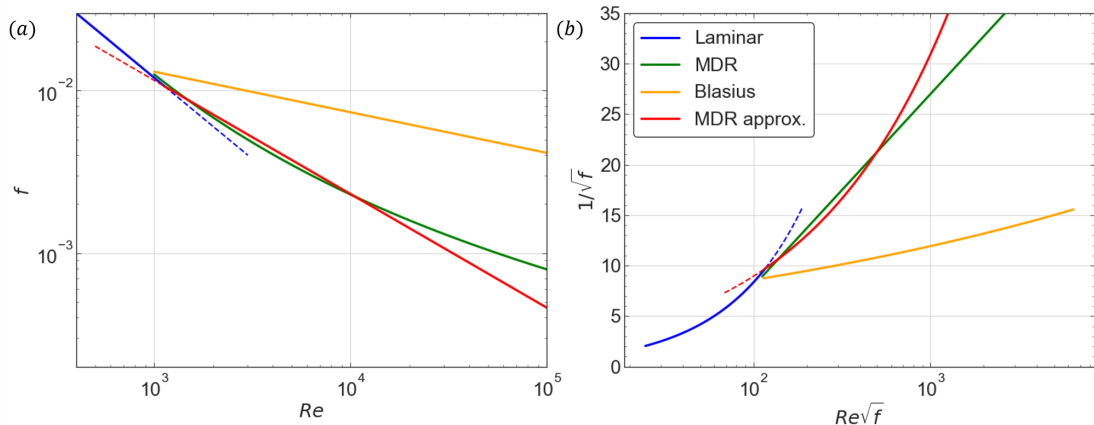
Figure 4-2: Friction factor depending on Reynolds number in ordinary (a) and Prandtl-Karman (b) coordinates. The laminar branch is shown by blue colour, MDR asymptote (4.3) and its approximation (4.4) are depicted by solid green and red lines, correspondingly. Blasius asymptote (pure water, smooth walls) is plotted by solid orange line. Dashed lines present functions continuation beyond the intersection point between laminar and MDR simplified curves.

defined $f(Re)$ by equation (4.5) is shown in figure 4-2 by the combination of blue (laminar part) and red (turbulent part) solid lines.

Similarly to equation (4.5), we write out the expression for the scaled friction factor $\tilde{f}$:

$$\tilde{f} = \begin{cases} 1, & Re \leq Re_c, \\ f_0'' \cdot Re^{1-n}, & Re > Re_c, \end{cases} \tag{4.6}$$

where $f_0'' = f_0'/12 = 0.122$.

Finally, one can compare the critical Reynolds number value for slickwater with the pure water case. It is known that the discussed value for the pipe flow is approximately $Re_d^c \approx 2100$ meaning that for channel flow it is equal to $Re^c = 3/4 \cdot Re_d^c \approx 1575$. As a result, the laminar-to-turbulent transition for the slickwater occurs at smaller Reynolds number.

4.2.2 Limiting propagation regimes of a semi-infinite fracture with leak-off and laminar/turbulent flow

It is known that two different mechanisms govern the propagation regime of a finite hydraulic fracture (see review of Detournay [2016] and references there in). The

first one is concerned with the distribution of the total dissipated energy between the creation of new fracture surfaces (toughness) and viscous fluid flow inside the fracture channel (viscosity). The second mechanism is related to the distribution of the total injected fluid between the fracture (storage) and the reservoir (leak-off). During fracture propagation, the partitioning of the dissipated energy and injected fluid changes over time, resulting in the realisation of various limiting propagation regimes dominated by toughness/viscosity and storage/leak-off mechanisms. E.g., in the case of penny-shaped/KGD cracks these regimes (also called as vertex solutions) are described by Savitski and Detournay [2002], Bunger et al. [2005], Garagash [2006d], Adachi and Detournay [2008], and their applicability domains are determined by Madyarova [2004], Hu and Garagash [2010] and Dontsov [2016a, 2017]. The similar concept can be applied when we study a semi-infinite fracture propagating with constant velocity, e.g., Garagash et al. [2011], in which case the partitions of the dissipated energy and that of the injected fluid evolve with the distance for the moving fracture tip.

The leak-off parameter C' controls the partitioning of the injected fluid, M' and K' have an influence on the dissipated energy distribution, and Reynolds number indicates the occurring flow regime. Five limiting propagation regimes can be distinguished in the model: three of them are related to laminar flow and the remaining two for turbulent flow:

k:　　toughness ($M' = 0$);

m:　　laminar-storage-viscosity ($C' = 0$, $K' = 0$, $Re < Re_c$);

$\tilde{m}$:　　laminar-leak-off-viscosity ($C' \to \infty$, $K' = 0$, $Re < Re_c$);

t:　　turbulent-storage-viscosity ($C' = 0$, $K' = 0$, $Re > Re_c$);

$\tilde{t}$:　　turbulent-leak-off-viscosity ($C' \to \infty$, $K' = 0$, $Re > Re_c$).

We begin with the laminar flow regime case: k, m and $\tilde{m}$ vertices. The detailed description of this fracture tip model is provided by Garagash et al. [2011], and here we summarise the main points for the completeness. These limiting propagation regimes are the solutions for the entire semi-infinite fracture, and they can be found in the form of a monomial solution of the elasticity equation (2.3) [Kanninen and

Limiting solutions	opening $w(x)$	net pressure $p(x)$	velocity $v(x)$
k Toughness ($M' = 0$)	$\ell_k^{1/2} x^{1/2}$	0	$V + E'C'\sqrt{V}/K'$
m Storage-viscosity ($K' = C' = 0$)	$\beta_0 \ell_m^{1/3} x^{2/3}$	$\delta_0 E'(\ell_m/x)^{1/3}$	V
m̃ Leak-off-viscosity ($K' = 0, C' \to \infty$)	$\tilde{\beta}_0 \ell_{\tilde{m}}^{3/8} x^{5/8}$	$\tilde{\delta}_0 E'(\ell_{\tilde{m}}/x)^{3/8}$	$V/\tilde{\beta}_0 \cdot (\ell_{\tilde{m}}^9/(\ell_m^8 x))^{1/8}$

Coefficients: $\beta_0 = 2^{1/3}3^{5/6}, \delta_0 = \beta_0 f(2/3), \tilde{\beta}_0 = 2.534, \tilde{\delta}_0 = \tilde{\beta}_0 f(5/8)$.

Table 4.1: Laminar vertex solutions of a semi-infinite hydraulic fracture with Carter's leak-off.

Popelar, 1985]:

$$w_\lambda(x) = Bx^\lambda, \quad p_\lambda(x) = E'Bf(\lambda)x^{\lambda-1}; \quad f(\lambda) = \lambda \cot(\pi\lambda)/4, \quad \lambda \in (0,1), \quad (4.7)$$

where coefficients B and λ are determined from the lubrication equation (2.7) with the corresponding values of governing parameters (C', M', K') mentioned above. In toughness dominated regime (k), the fluid viscosity can be neglected ($M' = 0$) leading to zero pressure and the fracture opening profile in accordance with the propagation condition (2.2). In the storage-viscosity case (m), the leaked-off volume and toughness are null ($C' = K' = 0$), and the solution can be derived by balancing the fluid flow velocity v (2.9) with the propagation velocity V. In the leak-off-viscosity dominated case ($\tilde{m}$), the leaked-off volume is much larger than the stored in the fracture ($C' \to \infty$), and the toughness is negligible ($K' = 0$). That is why, the $\tilde{m}$-vertex solution is found by comparing the fluid flux velocity v (2.9) with Carter's leak-off term. All three vertex solutions are written out in table 4.1 through the following length scales:

$$\ell_k = (K'/E')^2, \quad \ell_m = VM'/E', \quad \ell_{\tilde{m}} = \left(C'\sqrt{V}M'/E'\right)^{2/3}. \quad (4.8)$$

As it is shown in [Garagash et al., 2011], in the general case when K', C' and M' have finite non-zero values, the k-vertex solution is applicable in the near-field of the general solution, while $\tilde{m}$ and m emerge in the intermediate (for large leak-off) and far-field correspondingly. However, when we introduce into the model the flow regime transition from laminar to turbulent, the region occupied by the laminar flow regime is bounded and located near the fracture front (since $Re \to 0$ when $x \to$

0). Hence, the applicability domain of the laminar-storage-viscosity (m) solution is expected to shift to the intermediate field.

Further, we move on to the turbulent-storage-viscosity (t) and turbulent-leak-off-viscosity ($\tilde{t}$) regimes. These vertex solutions have been derived by Dontsov [2016c] for pure water case, and t-asymptote is presented by Lecampion and Zia [2019] for slickwater (MDR asymptote). In the further discussion, we write out the t-vertex solution and derive formulas for the $\tilde{t}$-vertex for Virk's asymptote.

Using the expression for the scaled friction factor $\tilde{f}$ for turbulent flow (4.6) and substitute it into lubrication equation (4.2) combined with (2.7), we obtain the following formula that is similar to power-law fluid case [Desroches et al., 1994]:

$$\left(V + 2C'\frac{\sqrt{Vx}}{w}\right)^m = \frac{w^{n+1}}{c}\frac{dp}{dx}, \tag{4.9}$$

where $m = 2 - n$ and $c = f_0'\mu^n\rho^{1-n}$.

Based on the reasoning similar to that of Garagash et al. [2011] for the laminar flow case, the turbulent-storage-viscosity (t) regime is expected to provide the asymptotic behaviour of the general solution in the far-field. In order to derive the analytical solution for this vertex, we should substitute the monomial solution (4.7) into equation (4.9) and balance V^m with the right-hand-side. As a result, we obtain the vertex solution previously identified by Lecampion and Zia [2019]:

$$w_t = \beta_t\ell_t^{n/(n+2)}x^{2/(n+2)}, \qquad p_t = \delta_t E'\left(\ell_t/x\right)^{n/(n+2)}; \qquad \ell_t = \left(cV^m/E'\right)^{1/n}, \tag{4.10}$$

where ℓ_t is the characteristic length scale associated with t-asymptote, and prefactors are given by:

$$\beta_t = \left(\frac{2(n+2)^2}{n}\tan\left(\frac{-2\pi}{n+2}\right)\right)^{1/(n+2)}, \qquad \delta_t = \beta_n f\left(\frac{2}{n+2}\right). \tag{4.11}$$

Using equations (4.10) and (4.11), one can notice that the t-asymptote takes a form of the m-vertex solution (table 4.1) when $n = m = 1$ and $c = M'$ (powers and coefficients correspond to the laminar flow regime).

Now, we consider the turbulent-leak-off-viscosity $\left(\tilde{t}\right)$ asymptote which is expected

to be realised in the intermediate-field of the general solution when both turbulent and leak-off effects are large (these are to be formally quantified by corresponding non-dimensional numbers χ and $\mathcal{R}$ introduced in the next Section). To derive this limiting solution, we balance the Carter's term on the left-hand-side of equation (4.9) with its right hand side, and look for the solution in the monomial form (4.7) with the following result:

$$w_{\tilde{t}} = \tilde{\beta}_{\tilde{t}} \ell_{\tilde{t}}^{(m+2n)/(2(m+n+2))} x^{(m+4)/(2(m+n+2))}, \qquad p_{\tilde{t}} = \tilde{\delta}_{\tilde{t}} E' \left(\ell_{\tilde{t}}/x \right)^{(m+2n)/(2(m+n+2))};$$
(4.12)

where $\ell_{\tilde{t}} = \left(2^m c C'^m V^{m/2}/E' \right)^{2/(m+2n)}$ is the newly introduced length scale $(w_{\tilde{t}}(\tilde{t}) \sim \ell_{\tilde{t}})$ and coefficients:

$$\tilde{\beta}_{\tilde{t}} = \left(\frac{2^4 (m+n+2)^2}{(m+4)(m+2n)} \tan \left(-\frac{\pi(m+4)}{2(m+n+2)} \right) \right)^{1/(m+n+2)}, \quad \tilde{\delta}_{\tilde{t}} = \tilde{\beta}_n f \left(\frac{m+4}{2(m+n+2)} \right).$$
(4.13)

If we substitute values of c, n, m responsible for laminar flow into equations (4.12), (4.13), we obtain $\tilde{m}$-vertex solution (table 4.1).

4.2.3 Solution

4.2.3.1 Normalisation of governing equations

In this section, we discuss the normalised variables and the dimensionless form of governing equations. The normalisation is required for reducing the number of problem parameters, and we will calculate the general numerical solution in the dimensionless form. We choose the mk-scaling proposed by Garagash et al. [2011] for which the characteristic length, width and pressure scales have the following form:

$$\ell_{mk} = \frac{\ell_k^3}{\ell_m^2} = \frac{K'^6}{E'^4 V^2 M'^2}, \qquad w_{mk} = \frac{\ell_k^2}{\ell_m} = \frac{K'^4}{E'^3 V M'}, \qquad p_{mk} = \frac{E' \ell_m}{\ell_k} = \frac{E'^2 V M'}{K'^2};$$
(4.14)

This scaling characterises the transition between the toughness (k) and storage-viscosity (m) propagation regimes in laminar flow case. Further, we introduce the

normalised distance to the tip, opening and fluid net pressure, respectively,

$$\xi = x/\ell_{mk}, \quad \Omega = w/w_{mk}, \quad \Pi = p/p_{mk}. \tag{4.15}$$

Using the set of parameters (4.15), we rewrite the system of governing equations in the normalised form:

- Propagation:

$$\Omega = \sqrt{\xi}, \quad \xi \to 0. \tag{4.16}$$

- Elasticity:

$$\Pi(\xi) = \frac{1}{4\pi} \int_0^\infty \frac{d\Omega}{ds} \frac{ds}{\xi - s}. \tag{4.17}$$

- Lubrication:

$$\frac{\Omega^2}{\tilde{f}} \frac{d\Pi}{d\xi} = 1 + \frac{\chi\sqrt{\xi}}{\Omega}, \tag{4.18}$$

where we introduce the dimensionless Carter's leak-off coefficient (factor of two larger than that in [Garagash et al., 2011]):

$$\chi = \frac{2C'E'}{\sqrt{V}K'}, \tag{4.19}$$

and the normalised friction factor $\tilde{f}$:

$$\tilde{f} = \begin{cases} 1, & \xi \le \Lambda, \\ f_0'' \cdot \mathcal{R}^{1-n}(\Omega + \chi\sqrt{\xi})^{1-n}, & \xi > \Lambda, \end{cases} \tag{4.20}$$

In equation (4.20), we utilise the characteristic Reynolds number introduced by Lecampion and Zia [2019]:

$$\mathcal{R} = 12\rho K'^4/(E'^3 M'^2) \tag{4.21}$$

and the notation $\Lambda(\chi, \mathcal{R}) = \lambda/\ell_{mk}$ for the transition point between the laminar and

the turbulent flow regimes which is a solution of the following equation:

$$\Omega(\Lambda) + \chi\sqrt{\Lambda} = Re_c/\mathcal{R}. \qquad (4.22)$$

As it can be seen from the system of equations (4.16) – (4.20), the problem solution, i.e. the crack opening and net fluid pressure profiles, depends on two parameters χ and $\mathcal{R}$, and the normalised distance from the tip ξ: $\Omega(\xi, \chi, \mathcal{R})$ and $\Pi(\xi, \chi, \mathcal{R})$. The present model has two limiting cases: 1) when $\chi \to 0$ it reduces to the tip model of Lecampion and Zia [2019], and 2) when $\mathcal{R} \to 0$, it has the form of Garagash et al. [2011] model.

The general solution to the problem (4.16) – (4.20) is computed numerically by using the algorithm described in [Garagash et al., 2011]. This approach utilises the exact form of the near- and far-field asymptotic behaviour of the solution, and, in this case, they are toughness (k) and turbulent-storage-viscosity (t) regimes. Using the mk-scaling (equation (4.15) with (4.14)), we write out their exact forms (since the 'zero'-order term of the pressure profile at k-vertex is zero, we utilise the next order term from the asymptotic expansion [Garagash et al., 2011]):

Near-field (k): $\Omega_k = \xi^{1/2}$, $\Pi_k = (1 + \chi)\ln(\xi/\xi_0)$;

Far-field (t): $\Omega_t = \beta_t \xi^{2/(n+2)} \mathcal{R}^{(1-n)/(n+2)} f_0^{''\ 1/(2+n)}, \Pi_t = \delta_t \xi^{-n/(n+2)} \mathcal{R}^{(1-n)/(n+2)} f_0^{''\ 1/(2+n)};$

$$(4.23)$$

where the coefficient ξ_0 is a part of the numerical solution.

Before presenting the solution results, we provide typical values for the governing parameters χ and $\mathcal{R}$ corresponding to field applications. We utilise the technique described by Kanin et al. [2020d] in which several dimensional parameters are varied independently according to their representative value ranges while other are fixed. The field domains of the parameters are taken from [Kanin et al., 2020d] with the addition of the value for the HF fluid density $\rho = 10^3$ kg/m^3. Further, we compute the field domains of the dimensionless parameters $\mathcal{R}$ and χ in the parametric space $(\chi, \mathcal{R})$, and it has approximately a rectangular shape with the following boundaries: $\mathcal{R} \in (0.1, 320.2)$ and $\chi \in (0.007, 2032.4)$. It is also possible to highlight that the rock

toughness K_{Ic} has the largest impact (among other parameters) on the boundary values of the characteristic Reynolds number $\mathcal{R}$, while the reservoir permeability k defines the leak-off number χ variations.

4.2.3.2 Examples of the general solution

In this part of the thesis, we present the numerically calculated fracture opening Ω and net fluid Π pressure profiles for various values of the governing parameters χ and $\mathcal{R}$. We begin with the discussion of the case in which the Carter's leak-off number equals to $\chi = 500$ and the characteristic Reynolds number is $\mathcal{R} = 100$.

Figure 4-3 shows the obtained results. Fracture opening and net fluid pressure profiles in the mk-scaling are presented in (a) and (b), while these characteristics normalised by the far-field asymptote (t-vertex) are depicted in (c) and (d). Apart from the solution with leak-off (solid black line), we also plot the corresponding profiles with zero leak-off (dashed black line). For comparison purposes, we show the laminar solution with leak-off by a dotted black line. In addition, in figures 4-3(c) and (d), we also present the asymptotic regimes by coloured dashed lines.

Let us look at the opening profiles. Using the numerical calculations accounting for the laminar-to-turbulent transition, we can notice that both profiles (with and without leak-off) have the same asymptotic behaviour in the near- (red dashed line) and far-field (brown dashed line) governing by k and t-vertex solutions, respectively. From figure 4-3(c), one can find out that the applicability domains of the toughness and turbulent-storage-viscosity regimes are much larger for $\chi = 0$ than for the case with $\chi = 500$ implying shrinkage of storage dominated domains with increasing leak-off number χ. Two considered solutions differ significantly in the intermediate-field, namely, the fracture aperture is larger for all distances ξ in the shown coordinate range for the non-zero leak-off case. When $\chi = 0$, we observe the laminar-storage-viscosity (m) asymptote in the intermediate-field (blue dashed line) which is in the agreement with results of Lecampion and Zia [2019]. In turn, in the intermediate-field of the solution with $\chi = 500$, we obtain two different limiting regimes: laminar-leak-off-viscosity ($\tilde{m}$) closer to the tip and then turbulent-leak-off-viscosity ($\tilde{t}$) depicted by green and magenta dashed lines, respectively. Using
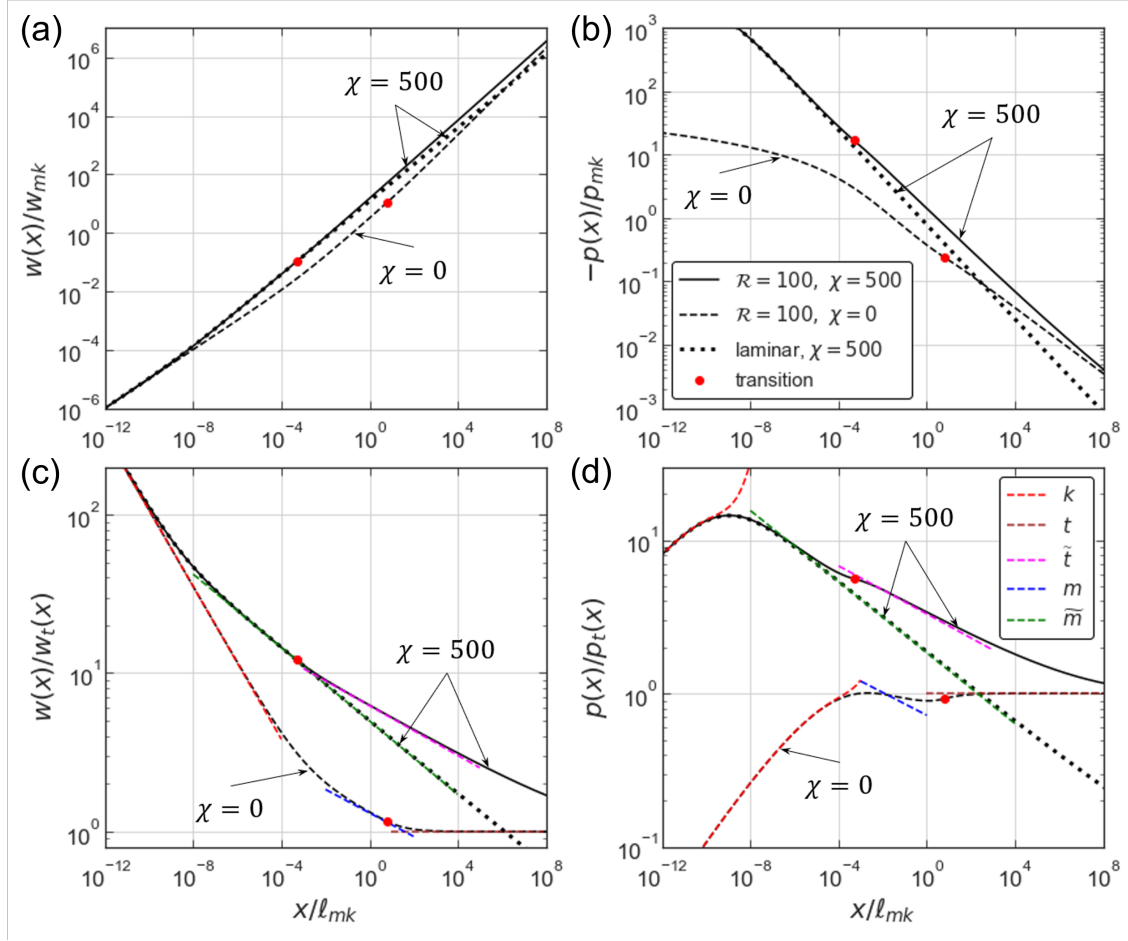
Figure 4-3: Solution for the fracture opening (a) and net fluid pressure (b) is shown in the mk-scaling for $\chi = 500$ and $\mathcal{R} = 100$. These characteristics normalised by t-vertex solution are presented in (c) and (d). The corresponding solution without leak-off ($\chi = 0$) is depicted by a dashed black line. The laminar solution with leak-off ($\chi = 500$) is presented by a dotted black line. In (c) and (d), different vertex solutions are depicted by coloured dashed lines. In (d), the k asymptotic expansion (red dashed line) is plotted twice: for both solutions (with and without leak-off) individually. By red circle dots, we mark the locations of laminar-to-turbulent transition points for laminar-turbulent solutions with and without leak-off.

figure 4-3, one can also determine that the laminar-to-turbulent transition point for the solution with leak-off is located much closer to the moving fracture tip compared to the solution with zero leak-off ($\Lambda(500, 100) \approx 5 \cdot 10^{-4}$ and $\Lambda(0, 100) \approx 6.7$). Comparing the opening profiles of the purely laminar ($n = 1$, $f_0'' = 1$) and laminar-turbulent ($\mathcal{R} = 100$) fracture solutions with leak-off ($\chi = 500$), one can observe that they coincide in the laminar flow region ($\xi < \Lambda(500, 100)$), while the opening in the laminar-turbulent fracture exceeds that in the purely laminar solution past the transition point $\xi > \Lambda(500, 100)$. In the intermediate-field of the laminar solution

118

with leak-off, the laminar-leak-off-viscosity regime ($\tilde{m}$) is realised (figure 4-3(c)).

Further, we move on to the net pressure profiles (figures 4-3(b) and (d)). One can observe that the pressure solutions with $\mathcal{R} = 100$ for Carter's leak-off and impermeable reservoir cases are different in the near and intermediate-fields, and they have the same t-asymptote in the far-field. Since the net pressure is zero for k-vertex, we utilise the next-order term of the asymptotic expansion [Garagash et al., 2011] which depends on χ (in this step, we assume that the k-vertex is located inside the region with laminar flow). As a result, there are two different red dashed lines in figure 4-3 (d) corresponding to respective value of the leak-off parameter. From this figure, it can also be noticed that the appearance of the intermediate asymptotes (m, $\tilde{m}$ and $\tilde{t}$), and their applicability domains are smaller as compared to those for the crack aperture. Similar to the opening profiles, we notice that the pressure profiles for the laminar and turbulent cases with leak-off are the same along the zone with laminar flow but its length is much smaller than Λ: $\xi < 10^{-6}$.

Dependence of the problem solution on the governing parameters χ and $\mathcal{R}$ is further explored in figure 4-4. In figure 4-4(a), we exemplify how the crack opening
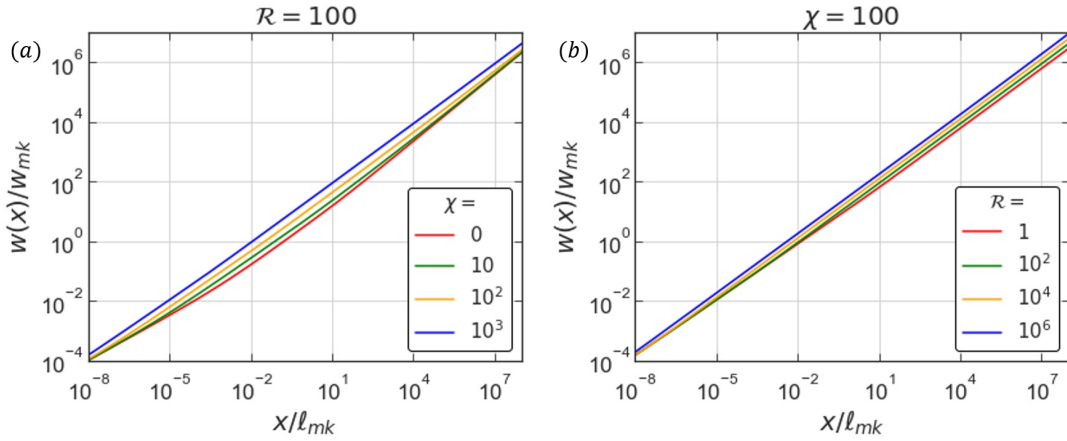
Figure 4-4: Solutions for the fracture opening in the mk-scaling corresponding to (a): $\mathcal{R} = 100$ and $\chi = 0$, 10, 10^2, 10^3 and (b): $\chi = 100$ and $\mathcal{R} = 1$, 10^2, 10^4, 10^6.

profile varies with the leak-off number χ while the characteristic Reynolds number value is fixed. One can find out that all profiles start from the near-field asymptote, and, in the far-field, they approach the t-vertex solution. In the intermediate-field, the crack aperture is seen to increase with the Carter's number χ. Figure 4-4(b)

examines the dependence of the fracture aperture on Reynolds number at a fixed leak-off value. The profiles have the same near-field and different far-field asymptotic behaviour since $\Omega_t \sim \mathcal{R}^{(1-n)/(n+2)}$ in the latter, i.e. higher values of the characteristic Reynolds number $\mathcal{R}$ lead to larger aperture in the far-field. Overall, and across scales, figures 4-4(a) and (b) illustrate the increase of the fracture opening with increase of either leak-off (χ) or turbulence ($\mathcal{R}$) intensities.

4.2.4   Discussion

4.2.4.1   Examination of the transition length

In this section, we determine how the laminar-to-turbulent transition length depends on the governing parameters which is expressed in the $mk-$scaling as $\Lambda(\chi, \mathcal{R})$. This characteristic distance is a solution of the non-linear equation (4.22), and we calculate it from the numerical solution for crack opening profile.

When we introduce the leak-off process into the tip model, we effectively increase the fluid flow velocity $v(x)$ by the value of Carter's term, and Reynolds number becomes higher than the critical value Re_c much closer to the moving tip. This concept is confirmed by the numerical results presented in the previous section in which $\Lambda(500, 100) = 5 \cdot 10^{-4}$ and $\Lambda(0, 100) = 6.7$ indicating that the crack region with the laminar flow regime in the case of $\chi > 0$ has smaller size as compared to an impermeable reservoir case, or, in other words, the turbulent flow regime occupies a wider fracture domain.

Further, we move on to the investigation the whole parametric space $(\chi, \mathcal{R})$. In figure 4-5(a), we present the colour map with the values of $\Lambda(\chi, \mathcal{R})$ function. In turn, figure 4-5(b) shows the dependence the transition length on the leak-off number when the characteristic Reynolds number is constant, and figure 4-5(c) depicts the opposite situation (χ is constant, and $\mathcal{R}$ varies). In other worlds, figures 4-5(b) and (c) are slices of figure 4-5(a) along χ (OX) and $\mathcal{R}$ (OY) axes, correspondingly. Using figures 4-5(a) and (b), one can notice that for each $\mathcal{R}$, the transition length remains constant until certain value of χ, i.e. the leak-off does not impact the flow regime transition until some threshold value of χ. If we continue to increase the leak-off number χ, the
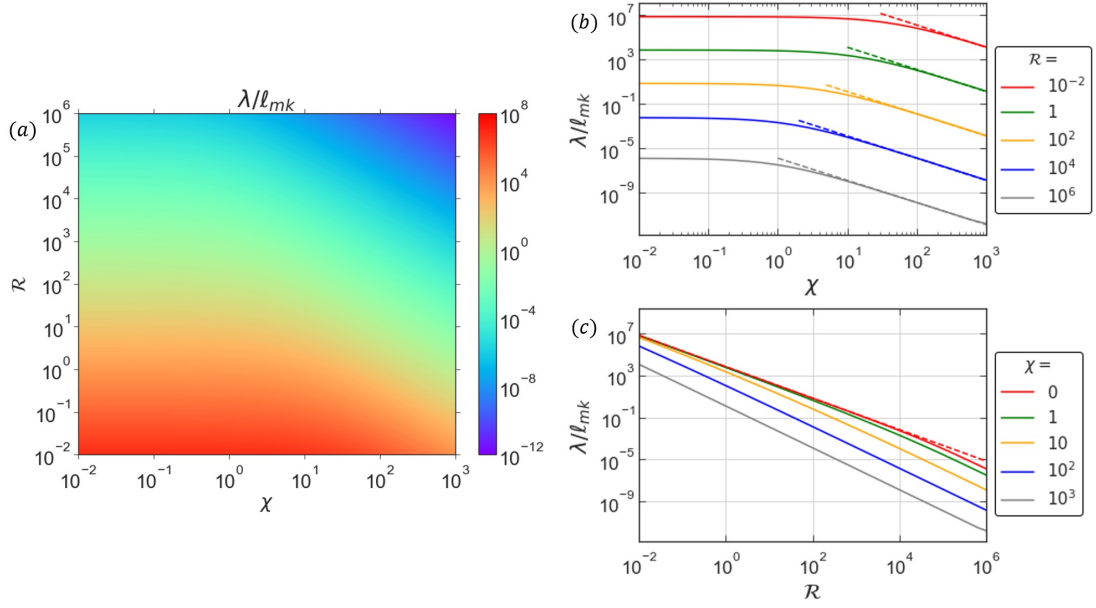
Figure 4-5: Transition length (i.e. distance from the moving tip where the laminar flow regime transforms to the turbulent one) depending on the leak-off χ and characteristic Reynolds $\mathcal{R}$ numbers (equation (4.22)). The colour map with $\Lambda(\chi, \mathcal{R})$ values is presented in (a). Several cross-section of (a) figure are shown in: (b), where the characteristic Reynolds number is fixed, and (c), in which the leak-off coefficient is constant. Using coloured dashed lines, we present analytical asymptotes for $\Lambda(\chi \gg 1, \mathcal{R} = \text{const})$ in (b) and for $\Lambda(0, \mathcal{R})$ in (c).

transition length eventually decreases, meaning that the fracture domain with the laminar flow regime shrinks. Looking at the profiles depicted in figure 4-5(c), we find out that the transition length is a decaying function on the characteristic Reynolds at fixed leak-off. We also determine that the transition length is closely approximated by $\Lambda \sim Re_c^2(\mathcal{R}\chi)^{-2}$ for $\chi \gg 1$ stemming from neglecting the storage term, i.e. $\Omega(\Lambda)$, compared to the leak-off in (4.22) (coloured dashed lines in figure 4-5(b)). It is also possible to notice that $\Lambda(0, \mathcal{R})$ (constant values in figure 4-5(b) for small χ or red curve in figure 4-5(c)) can be approximated by $\Lambda \sim Re_c^{3/2}(\beta_0\mathcal{R})^{-3/2} = 6826\mathcal{R}^{-3/2}$ for $\mathcal{R} < 10^4$ (dashed red line in figure 4-5(c)). This result is obtained by neglecting the leak-off term in equation (4.22) and substituting m-vertex solution for the opening. Lecampion and Zia [2019] utilise this power law, i.e. $\sim \mathcal{R}^{-3/2}$, to fit the transition length $\Lambda(0, \mathcal{R})$ in the whole range of the characteristic Reynolds numbers in their zero-leak-off solution and obtain $\Lambda \sim 5000\mathcal{R}^{-3/2}$.

4.2.4.2 Applicability domains of the vertex solutions

In the present section, we consider spatial domains where the general numerical solution can be approximated by the limiting (vertex) solutions. Similar to Garagash et al. [2011], we define an asymptotic bound as the distance from the moving tip at which the crack opening profile deviates from the considered vertex solution (Table 4.1 and equations (4.10), (4.12)) by 1%. Let us denote the upper bound of the k-vertex asymptotic domain by x_k, i.e. this regime is located inside the interval $x \in (0, x_k)$, and by x_t, we define the lower bound of the t-vertex asymptotic region: $x \in (x_t, +\infty)$. In the same way, one can define the domains of the vertices that realise in the intermediate field: $x \in (x_m^0, x_m^\infty)$ for the m-vertex, $x \in (x_{\tilde{m}}^0, x_{\tilde{m}}^\infty)$ for the $\tilde{m}$-vertex, $x \in (x_{\tilde{t}}^0, x_{\tilde{t}}^\infty)$ for the $\tilde{t}$-vertex. Similar to Kanin et al. [2020d], we define the storage domain boundary $x_S = \xi_S \ell_{mk}$: $\Omega(\xi_S) = \chi\sqrt{\xi_S}/0.05$ such that the cumulative leaked-off volume is a small fraction (5%) of the fracture storage when $x > x_S$. Since the approximation of the MDR asymptote (equation (4.4)) has limited applicability domain ($Re < 1.5 \cdot 10^4$), we also introduce the boundary $x_B = \xi_B \ell_{mk}$ connected with this limit: $\Omega(\xi_B) + \chi\sqrt{x_B} = 1.5 \cdot 10^4/\mathcal{R}$ which defines the validity region $x < x_B$ of our approximation of the slickwater turbulent behaviour.

Figure 4-6 shows the regime maps in the parametric space $(\chi, \mathcal{R})$ for $\chi = 0,\ 0.1,\ 1, 10,\ 50,\ 100,\ 500$ and 1000. By coloured lines, we present the domain boundaries of the vertex solutions, the laminar-to-turbulent transition length is shown by black dashed line; x_S and x_B lengths are depicted by dashed-dotted and dotted lines, respectively.

Figure 4-6(a) presents the zero leak-off case, and the results are in agreement with the regime map constructed by Lecampion and Zia [2019]. Let us consider the near-field (k) and far-field (t) asymptotes first. Based on figures 4-6(a)–(h), one can observe that $\xi_k = x_k/\ell_{mk}$ (red lines) is a function of the leak-off number only (in the considered range of $\mathcal{R}$), i.e. the characteristic Reynolds number does not affect this limiting solution, and $\xi_k(\chi)$ coincides with that of Garagash et al. [2011] for the laminar flow regime. Such observation can be explained by the fact that k-vertex is always realised in the crack region with laminar flow within the parametric
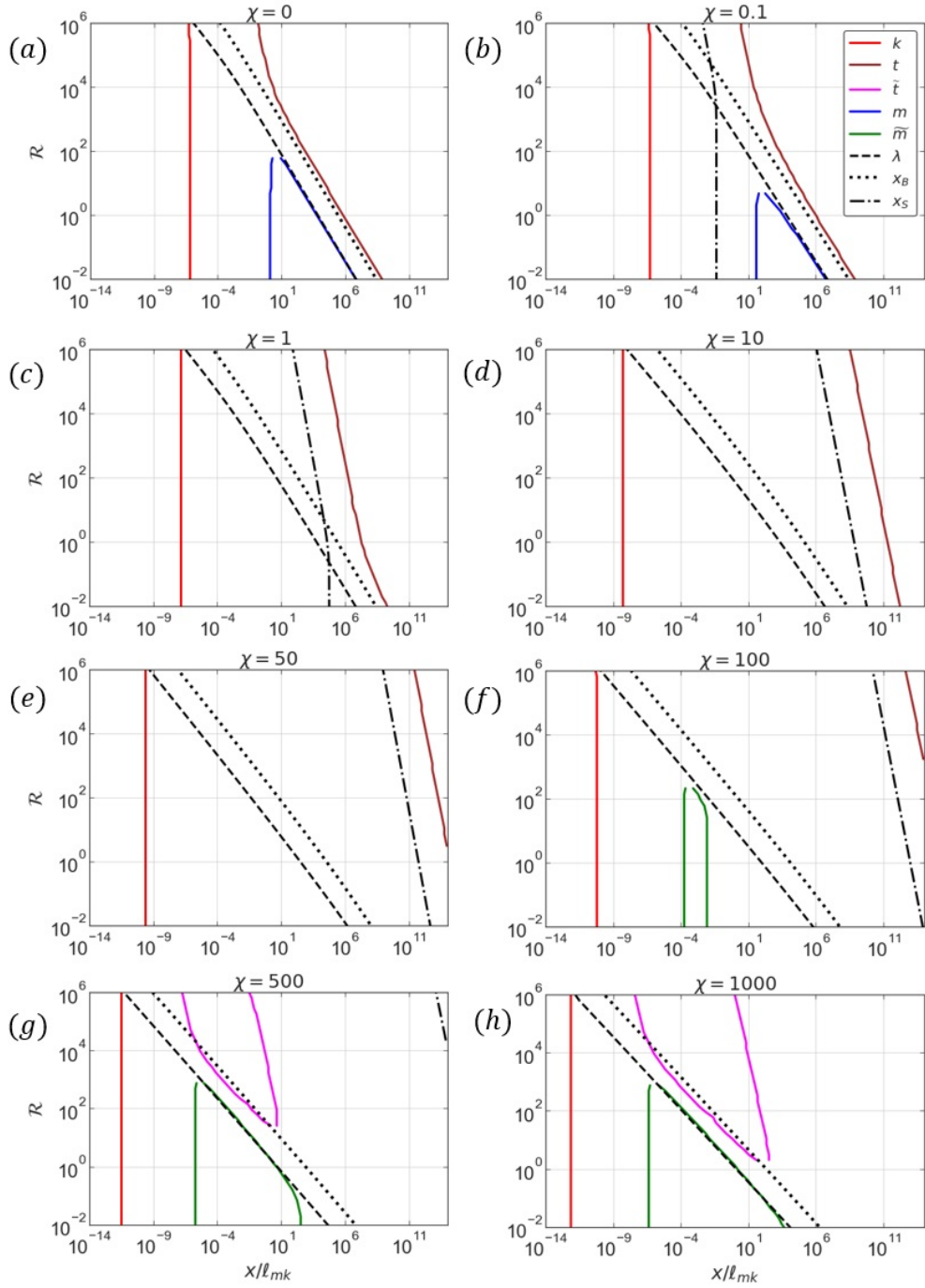
Figure 4-6: Regime maps presenting the boundaries of the spatial domains corresponding to the various limiting propagation regimes (vertex solutions) (Table 4.1 and equations (4.10), (4.12)) in coordinates $(x/\ell_{mk}, \mathcal{R})$ for various values of χ. We show the laminar-to-turbulent transition length λ by a dashed line, the storage domain boundary x_S by a dashed-dotted line and the applicability limit of the approximation of the MDR asymptote x_B by a dotted line.

region shown in the figure 4-6; however, for large enough $\mathcal{R} > 10^6$ (not shown), the upper boundary of the k-vertex skirts the turbulent zone and is expected to

depend on the value of the characteristic Reynolds number there. The near-field asymptotic domain shrinks with increase in the leak-off intensity, i.e. x_k moves towards the fracture tip. In turn, the lower bound of the t-vertex domain (brown lines) moves away from the tip when χ grows (in figures 4-6(g) and (h), it is out of the computational domain). The boundary $\xi_t = x_t/\ell_{mk}$ is a non-linear function of both governing parameters. In figures 4-6(a) and (b), we find out the presence of the laminar-storage-viscosity (m) regime (blue line), it can be noticed for $\chi < 0.5$ for the chosen range of the characteristic Reynolds number. Starting from $\chi = 80$, we observe the $\tilde{m}$-vertex in the intermediate-field (figures 4-6(f)–(g), green line), and for the leak-off number values $\chi > 120$, the turbulent-leak-off-viscosity ($\tilde{t}$) regime also approximates the general numerical solution (magenta line). When we increase χ value, the asymptotic domains of $\tilde{m}$ and $\tilde{t}$ expands.

Let us move on to the discussion of the characteristic boundaries presented in figure 4-6. The transition boundary between the laminar and turbulent flow regimes (λ) is shown by dashed black line. Based on the results, we find out that the crack zone occupied by laminar flow decreases when the leak-off number χ grows, i.e. the transition boundary moves closer to the fracture front. As a result, in the permeable reservoir case, the turbulent flow regime has a more significant impact on the crack tip characteristics since it is realised on the larger part of a semi-infinite fracture as compared to the zero-leak-off case [Lecampion and Zia, 2019]. By dotted-dashed line, we present the boundary of the crack-storage-domain (x_S) which is on the right-hand side of this line ($x > x_S$). The leak-off process can be neglected in this region, and from figure 4-6, we observe that the crack-storage-domain shrinks (x_S migrates away from the tip) with χ growth. The final boundary (x_B) is marked by dotted line, and it depicts the upper limit of the applicability region of the MDR asymptote approximation (4.4). One can remark that the proposed near-tip solution is correct along the spatial region $x \in (0, x_B)$, and for larger distances from the tip (i.e. $x > x_B$), it provides a semi-infinite fracture characteristics corresponding to the fluid flow inside the crack channel with an underestimated friction (figure 4-2). From figure 4-6, we notice that x_B boundary is parallel (in double logarithmic scale) to the transition length, and the size of the crack domain with the 'correct' solution

diminishes with increasing leak-off.

Further, we determine the orientation of various boundaries of the asymptotic domains in figure 4-6 using analytical considerations, i.e. we approximate the boundaries using power law function $\mathcal{R} \sim \xi^{\alpha}$ and calculate the exponents α (the proportionality coefficients can be estimated from the numerical solution). It is known that the boundaries orientation is governed by the characteristic length scales of the transitions between various limiting propagation regimes.

In figures 4-6(a) and (b), the boundary x_m^0 is located inside the region with laminar flow meaning, and it does not depend on $\mathcal{R}$ (vertical line). The same explanation can be applied for the $\tilde{m}$-vertex boundaries (figures 4-6(f) – (h)): $x_{\tilde{m}}^0$ and $x_{\tilde{m}}^{\infty}$ (segments below the transition boundary). Let us consider the boundaries x_m^{∞} and x_t (segments: $\mathcal{R} < 100$ for $\chi = 0$ and 0.1; $\mathcal{R} < 1$ for $\chi = 1$), and they have the certain inclination angle which we determine according to the following derivations. The lengthscale ℓ_{tm} which characterises the tm-transition can be found from the comparison of the opening profiles: $w_m(\ell_{tm}) \sim w_t(\ell_{tm})$, and it is proportional to $\ell_{tm} \sim \mathcal{R}^{-3/2}\ell_{mk}$. Such transitions between vertices are also called as edge-solutions [Garagash et al., 2011]. Each considered boundary corresponds to constant value of x/ℓ_{tm}, and these constants can be found from the numerical solution. Using the determined expression for the length scale ℓ_{tm}, we obtain that the boundaries x_m^{∞} and x_t ($\mathcal{R} < 100$ for $\chi = 0$ and 0.1; $\mathcal{R} < 1$ for $\chi = 1$) are described by: $\mathcal{R} \sim \xi^{-2/3}$. Further, we consider the tk-transition, and the characteristic length scale in this case is $\ell_{tk} \sim \mathcal{R}^{(2n-2)/(2-n)}\ell_{mk}$. Using this formula and the calculations, we determine that the boundary x_t ($\mathcal{R} > 10^4$ for $\chi = 0$ and 0.1; $\mathcal{R} > 100$ for $\chi = 1$; $\chi = 10, 50, 100$) corresponds to certain constant x/ℓ_{tk}, and it is governed by the equation $\mathcal{R} \sim \xi^{-(2-n)/(2-2n)}$. Furthermore, it is possible to assume that x_k boundary is also have this form when it is located inside the region with the turbulent flow regime, e.g. for $\mathcal{R} > 10^6$ and $\chi = 0, \ldots, 1000$. Further, we move on to the transition $\tilde{t}k$, and the characteristic length scale is proportional to $\ell_{\tilde{t}k} \sim \mathcal{R}^{(2n-2)/(2-n)}\chi^{-2}\ell_{mk}$. As a result, the boundary $x_{\tilde{t}}^0$ for $\mathcal{R} > 10^4$ (figure 4-6(g) and (h)) has the form: $\mathcal{R} \sim \xi^{-(2-n)/(2-2n)}$ (χ is fixed on each map and is not accounted for in the formula). Moreover, if we consider the $t\tilde{t}$-edge, we obtain $\ell_{t\tilde{t}} \sim \mathcal{R}^{(2n-2)/(2-n)}\chi^{-2(n+2)/(2-n)}\ell_{mk}$

meaning that $x_{\tilde{t}}^{\infty}$ is parallel the boundary $x_{\tilde{t}}^{0}$ ($\mathcal{R} > 10^4$). Next, we can derive the inclination angle related to the boundaries $x_{\tilde{t}}^{0}$ ($\mathcal{R} < 10^4$) and $x_{\tilde{m}}^{\infty}$ (the segment which coincides with the transition length). For its determination, we look at the $\tilde{t}\tilde{m}$-transition whose length scale is $\ell_{\tilde{t}\tilde{m}} \sim \mathcal{R}^{-2}\chi^{-2}\ell_{mk}$. By taking into account that each considered boundary corresponds to constant value of $x/\ell_{\tilde{t}\tilde{m}}$, we obtain: $\mathcal{R} \sim \xi^{-1/2}$.

4.3   A penny-shaped fracture model

4.3.1   Model formulation

Let us discuss the model formulation for a radial hydraulic fracture driven by turbulent-laminar flow. The sketch of the model is presented in Figure 4-7. In contrast to the classic model for a penny-shaped crack (Section 2.2) in which it was assumed that the flow of Newtonian fluid inside the fracture channel is laminar, the current model accounts for the possible flow regime transformation from laminar to turbulent moving away from the fracture front. We will discuss the latter in the current part of the thesis. The model assumptions and governing equations which we will not mention here remain the same as in Section 2.2.
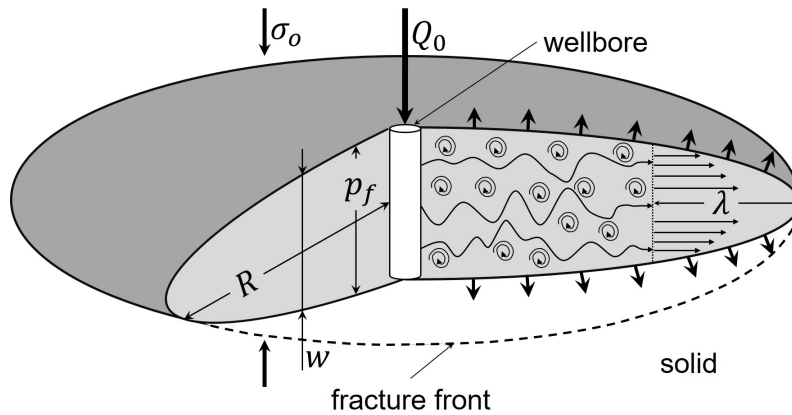
Figure 4-7:   A radial hydraulic fracture model with the laminar-turbulent channel flow and leak-off.

We consider a radial hydraulic fracture driven by slickwater flow. Slickwater has viscosity μ, density ρ, and behaves like a Newtonian fluid in the laminar flow regime. When turbulent flow occurs, slickwater rheological response is modelled by

the maximum drag reduction (MDR) asymptote. Reynolds number for the plane channel flow, $Re = \rho v w / \mu$, is increasing with distance from the crack front where $Re = 0$. The laminar-to-turbulent flow regime transformation happens at distance λ from the tip (this value is a part of the solution), where Reynolds number equals to the critical value, $Re = Re_c$. Consequently, the laminar flow domain of extent λ is adjacent to the front, i.e., observed within the interval $r \in (R - \lambda, R)$ along which $Re < Re_c$, while the non-laminar flow, i.e., transient and fully turbulent, happens inside the domain $r \in (0, R - \lambda)$ characterised by $Re > Re_c$. We implement the flow regime transformation into the model via the usage of the fluid friction factor $f(Re)$.

Using the width-averaged momentum conservation equation in which the inertial terms are neglected [Lecampion and Zia, 2019], we determine the expression for velocity of the fluid flow $v(r, t)$:

$$v\,|v| = -\frac{w}{\rho f}\frac{\partial p}{\partial r}, \tag{4.24}$$

where f is the Fanning friction factor.

As mentioned in Section 4.2.1, the friction factor for laminar flow $(Re < Re_c)$ in plane channel equals $f^{\text{lam}} = 12/Re$. Using the definition of the normalised friction factor $\tilde{f} = f/f^{\text{lam}}$, we rewrite equation (4.24) in the form:

$$v = -\frac{w^2}{M'\tilde{f}}\frac{\partial p}{\partial r}. \tag{4.25}$$

The combination of the continuity (2.13) and momentum conservation (4.25) together with the Carter's law (2.14) yields Reynolds equation:

$$\frac{\partial w}{\partial t} = \frac{1}{M'}\frac{1}{r}\frac{\partial}{\partial r}\left(\frac{rw^3}{\tilde{f}}\frac{\partial p}{\partial r}\right) - \frac{C'}{\sqrt{t - t_0(r)}}. \tag{4.26}$$

In the turbulent flow regime $(Re > Re_c)$, the slickwater frictional behaviour is governed by the MDR asymptote. We have already discussed the MDR asymptote in Section 4.2.1, and its exact and approximate forms were given by equations (4.3) and (4.4), respectively.

Using the analysis of Section 4.2.1, here, we summarise the behaviour of the friction f and normalised friction $\tilde{f} = f/f^{\mathrm{lam}}$ in the entire range of Reynolds number values:

$$f = \begin{cases} 12/Re, & Re \leq Re_c, \\ f_0' Re^{-n}, & Re > Re_c, \end{cases} \qquad \tilde{f} = \begin{cases} 1, & Re \leq Re_c, \\ f_0'' \cdot Re^{1-n}, & Re > Re_c, \end{cases} \tag{4.27}$$

with prefactor $f_0'' = f_0'/12$. Re_c value for the slickwater case can be estimated from the intersection of the laminar and turbulent branches, to ensure the continuity of $f(Re)$: $Re_c = (12/f_0')^{1/(1-n)}$.

Finally, we provide the numerical values of the parameters in rheological relations (4.4), (4.27) for the slickwater (power-law approximation of MDR) and pure water (Blasius correlation) cases based on [Lecampion and Zia, 2019] and [Blasius, 1913], correspondingly:

slickwater: $f_0 = 1.78, \quad n = 0.7, \quad f_0' = 1.46, \quad f_0'' = 0.122, \quad Re_c = 1132.6;$

water: $f_0 = 0.079, \quad n = 0.25, \quad f_0' = 0.074, \quad f_0'' = 0.006, \quad Re_c = 1650.$ (4.28)

The critical Reynolds number for the channel flow of Newtonian fluid (pure water) is evaluated from the corresponding parameter for the pipe flow and equals $Re_c = 1650$.

4.3.2   Solution approach

The current section describes the numerical algorithm utilized in the solution of the radial hydraulic fracture propagation problem. The method is based on the Gauss-Chebyshev quadrature and Barycentric Lagrange interpolation techniques. Viesca and Garagash [2018] review these techniques and apply them to the solution of various fracture propagation problems with coupled physics. Liu et al. [2019] adapt the methodology to radial fracture propagation. It is important to mention that the numerical scheme does not require an explicit implementation of the near tip region asymptote (if different from the classical LEFM one) compared to other approaches which use the 'tip logic', e.g., [Peirce and Detournay, 2008, Peirce, 2015, Dontsov,

2016a, Dontsov and Peirce, 2017c, Zia and Lecampion, 2020]. In the present work, we follow the method developed by Liu et al. [2019] and extend it to account for different HF fluid rheology and for fluid leak-off.

Firstly, we introduce the dimensionless distance from the source as $\xi = r/R(t)$, $\xi \in [0,1]$, and rewrite the system of governing equations through ξ variable using the transformation of the time and coordinate derivatives: $\partial/\partial t|_r = \partial/\partial t|_\xi - [\xi V(t)/R(t)] \cdot \partial/\partial \xi|_t$, $\partial/\partial r|_t = R(t)^{-1}\partial/\partial \xi|_t$, $V = dR/dt = \dot{R}$. The application of Gauss-Chebyshev quadrature requires considering the problem on the spatial coordinate segment $\xi \in [-1,1]$. In this regard, the spatiotemporal fracture characteristics and governing equations are extended symmetrically to negative ξ. Such modified form of the elasticity equation (2.11) is given by:

$$p(\xi,t) = -\frac{E'}{4\pi R(t)} \int_{-1}^{1} G(\xi,s) \frac{\partial w(s,t)}{\partial s} ds, \quad \xi \in [-1,1], \qquad (4.29)$$

where the corresponding form of the integral kernel is provided by Liu et al. [2019]:

$$G(\xi,s) = \begin{cases} \text{sign}(\xi s) \left[\frac{1}{\xi}\text{K}\left(\frac{s^2}{\xi^2}\right) + \frac{1}{s-\xi}\text{E}\left(\frac{s^2}{\xi^2}\right) \right], & |\xi| > |s|, \\ \frac{1}{s-\xi}\text{E}\left(\frac{\xi^2}{s^2}\right), & |\xi| < |s|. \end{cases} \qquad (4.30)$$

Spatial derivative of the opening profile is written as:

$$\frac{\partial w}{\partial \xi} = \mathcal{W}(\xi)F(\xi,t), \quad \mathcal{W}(\xi) = \frac{1}{\sqrt{1-\xi^2}}, \quad \xi \in [-1,1],$$

where the singular weight function $\mathcal{W}(\xi)$ is chosen in accordance with the fracture opening behavior near the tip, i.e., $\partial w/\partial \xi \sim 1/\sqrt{1-|\xi|}$, $\xi \to \pm 1$, and $F(\xi,t)$ is an unknown regular function. Since $w(\xi,t)$ and $\mathcal{W}(\xi)$ are even functions, function $F(\xi,t)$ should be odd.

Next, the coordinate domain $\xi \in [-1,1]$ is discretized using two sets of nodes connected with the selected weight function (the details are provided by Viesca and Garagash [2018]): primary $\mathbf{s} = \{s_j\}_{j=1}^N = \{\cos[\pi(j-1/2)/N]\}_{j=1}^N$ and complementary $\mathbf{z} = \{z_i\}_{i=1}^M = \{\cos(\pi i/N)\}_{i=1}^M$, $M = N-1$, sets. Hereafter we utilize bold symbols for vectors. Primary and complementary nodes are the roots of the Cheby-

shev's polynomials of the first and the second kind. We further make use of the values of $F(\xi, t)$ at the primary nodes: $\mathbf{F} = \{F(s_j, t)\}_{j=1}^N$, while the crack aperture $w(\xi, t)$, net pressure $p(\xi, t)$ and fluid flow velocity $v(\xi, t)$ are evaluated at the complementary nodes: $\mathbf{w} = \{w(z_i, t)\}_{i=1}^M$, $\mathbf{p} = \{p(z_i, t)\}_{i=1}^M$, $\mathbf{v} = \{v(z_i, t)\}_{i=1}^M$.

Let us turn to the discretization of the governing equations. We focus on the Reynolds and global fluid balance equations since the remaining equations (elasticity, propagation criterion, and boundary conditions) are identical to those in [Liu et al., 2019] and given by their equations (3), (10), (8). Integrating Reynolds equation (4.26) in space from a given position along the crack ξ to the tip $\xi = 1$, applying discretization and substituting discretized elasticity (equation (41) of Liu et al. [2019]), we arrive to

$$-\frac{\mathbf{z}^2}{2}\frac{\partial \mathbf{w}}{\partial t} + \frac{1}{2}\frac{\partial}{\partial t}\left[\mathbb{S} \times (\mathbf{s}^2\mathbf{F})\right] + \frac{V}{R}(\mathbb{S} \times (\mathbf{s}^2\mathbf{F})) - \frac{\mathbf{z}\mathbf{w}\mathbf{v}}{R} + C'\mathbb{R} \times \frac{\mathbf{z}}{\sqrt{t - t_0(\mathbf{z}R)}} = 0, \quad \mathbf{w} = \mathbb{S} \times \mathbf{F},$$

$$\mathbf{v} = -\frac{\mathbf{w}^2}{M'\tilde{f}R}\mathbf{p}_\xi, \quad \mathbf{p}_\xi = \frac{E'}{4R}\mathbb{D} \times (\mathbb{G}_2 \times \mathbf{F}), \quad \tilde{f} = \begin{cases} 1, & \mathbf{Re} \leq Re_c, \\ f_0''\mathbf{Re}^{1-n}, & \mathbf{Re} > Re_c, \end{cases}, \quad \mathbf{Re} = \frac{12\rho\mathbf{w}\mathbf{v}}{M'}.$$

Here, we utilize the sign '$\times$' for the matrix multiplication. Components of the matrices $\mathbb{S}, \mathbb{D}, \mathbb{G}_2$ are provided by Liu et al. [2019] in their equations (34), (39), (43), while matrix $\mathbb{R}$ is given by:

$$\mathbb{R} = \{R_{ii'}\} = \left\{\sum_{k=0}^{M-1}\left[\Psi_k(1) - \Psi_k(z_i)\right]B_{ki'}\right\}, \quad \Psi_k(z) = \cos\left[(k+1)\theta\right]/(k+1), \quad \theta = \arccos z,$$

$B_{ki'} = 2/N \cdot \sin(\pi i'/N)\sin(\pi i'(k+1)/N)$.

The rate form of the global fluid balance equation (2.20) can be discretized as follows:

$$\frac{Q_0}{\pi}\left(\frac{1}{R^2} - \frac{2tV}{R^3}\right) = -\mathbb{S}_H \times (\mathbf{s}^2\dot{\mathbf{F}}) + 2C'\mathbb{R}_H \times \frac{\mathbf{z}}{\sqrt{t - t_0(\mathbf{z}R)}} - \frac{2C'V}{R^3}\int_0^t \frac{R^2(s)ds}{\sqrt{t - s}},$$

where the matrix $\mathbb{S}_H$ is defined by Liu et al. [2019] in their equation (38), while $\mathbb{R}_H$

is given by:

$$\mathbb{R}_H = \left\{ \sum_{k=0}^{m-1} \left[\Psi_k(1) - \Psi_k(0) \right] B_{ki'} \right\}.$$

In the right-hand-side of the global fluid balance equation we have the integral with respect to time, and it can be evaluated via application of the Simpson's rule.

The discretized Reynolds equations (with the elasticity equation and boundary conditions already taken into account in it) together with the global fluid balance and propagation condition can be combined into a system of ordinary differential equations (ODEs):

$$\mathbb{A}(\mathbf{X}, t) \frac{d\mathbf{X}}{dt} = \mathbf{B}(\mathbf{X}, t), \quad \mathbf{X} = \{R, \mathbf{F}\},$$

where $\mathbf{X}$ is the solution vector. Once the above system of ordinary differential equations is integrated, the crack radius evolution is known, $R = R(t)$, while the solution for opening, net pressure profiles, and efficiency is evaluated from $F(\xi, t)$ using the following representation:

$$\mathbf{w} = \mathbb{S} \times \mathbf{F}, \quad \mathbf{p} = \frac{E'}{4R} \mathbb{G}_2 \times \mathbf{F}, \quad \eta(t) = -\frac{\pi R^2}{Q_0 t} \left\{ \mathbb{S}_A \times (\mathbf{s}^2 \mathbf{F}) \right\},$$

where matrix $\mathbb{S}_A$ is defined in [Liu et al., 2019] by their equation (37).

Due to the form of the elasticity equation [Liu et al., 2019], the number of primary nodes N should be odd. Since function $F(\xi, t)$ is odd, the target vector $\mathbf{F}$ has the form: $\mathbf{F} = \{F_1, \ldots F_{(N-1)/2}, 0, -F_{(N-1)/2}, \ldots, -F_1\}$. The total number of the independent unknown parameters is $(N-1)/2 + 1$ which constrains the system of governing ODEs to be composed of the Reynolds equations at the complementary nodes $z_1, \ldots, z_{(N-1)/2-1}$, the global fluid balance equation and the propagation condition. We choose $N = 101$, and the initial condition is represented by the storage-viscosity-turbulent limiting propagation regime originally developed by Lecampion and Zia [2019], and further discussed in Section 4.3.4. The time computational domain is discretized on a logarithmic scale, and we apply ODE solver for each time step. The numerical algorithm is implemented in Python programming language, the system of ODEs is solved via `solve_ivp` function of SciPy library Virtanen et al.

The verification results of the numerical approach described in the current section are shown in Appendix A.3 on the example of a radial fracture driven by laminar flow of Newtonian fluid in a permeable rock. We demonstrate the comparison of the algorithm outcomes with several reference solutions (numerical and semi-analytical).

4.3.3 Solution examples for typical field applications

In this section, we demonstrate the results of the simulations for radial hydraulic fracture growth in which the model parameters are close to typical field cases. We would like to achieve the following objectives. First of all, we investigate how the laminar-to-turbulent flow regime transformation inside the fracture channel changes the problem solution compared to the fully laminar flow case for both impermeable and permeable reservoirs. Moreover, we perform calculations not only for slickwater but also for pure water driven cracks to examine the influence of the frictional behavior on the fracture parameters.

The injection volumetric flow rate is assumed to be a fairly high $Q_0 = 0.1$ m^3/s (e.g, see representative ranges in the reviews [Barati and Liang, 2014, Barbati et al., 2016]). For simplicity, we consider a situation when the polymer molecules do not change the solvent (pure water) viscosity which equals $\mu = 1$ cP, i.e., they modify the frictional behavior during turbulent flow only (the MDR asymptote instead of the Blasius approximation). The following rock and fluid properties are chosen:

$$E' = 20 \text{ GPa}, \quad K_{Ic} = 1 \text{ MPa} \cdot \sqrt{\text{m}}, \quad \sigma_o = 10 \text{ MPa}, \quad p_o = 6 \text{ MPa},$$
$$\mu = 1 \text{ cP}, \quad c_t = 10^{-3} \text{ MPa}^{-1}, \quad \rho = 10^3 \text{ kg/m}^3,$$
$$k = 10 \text{ mD (permeable rock)}, \quad \phi = 20\%. \tag{4.31}$$

Using the set of parameters (4.31), one can estimate the Carter's leak-off number corresponding to the permeable rock case, $C' = 2.04 \cdot 10^{-4}$ m/$\sqrt{\text{s}}$, while $C' = 0$ for impermeable rock.

Figures 4-8(a), (b) and (c) present the turbulent-laminar solutions for the evolution of the fracture radius $R(t)$, opening at the wellbore $w(0, t)$ and net pressure

$p(0.1, t)$ at the distance $r = 0.1$ m normalized by the corresponding laminar solutions (Figure 4-9). As a result, the laminar solutions in these charts are simply unity along the entire time domain. The choice of the location for the pressure monitoring is conditioned by the pressure singularity at $r = 0$ in the point fluid source model and by the value of a typical borehole radius. We also note that, with exception of very early propagation time (not shown), $R(t) \gg 0.1$ m, and the point source modeling is deemed appropriate.
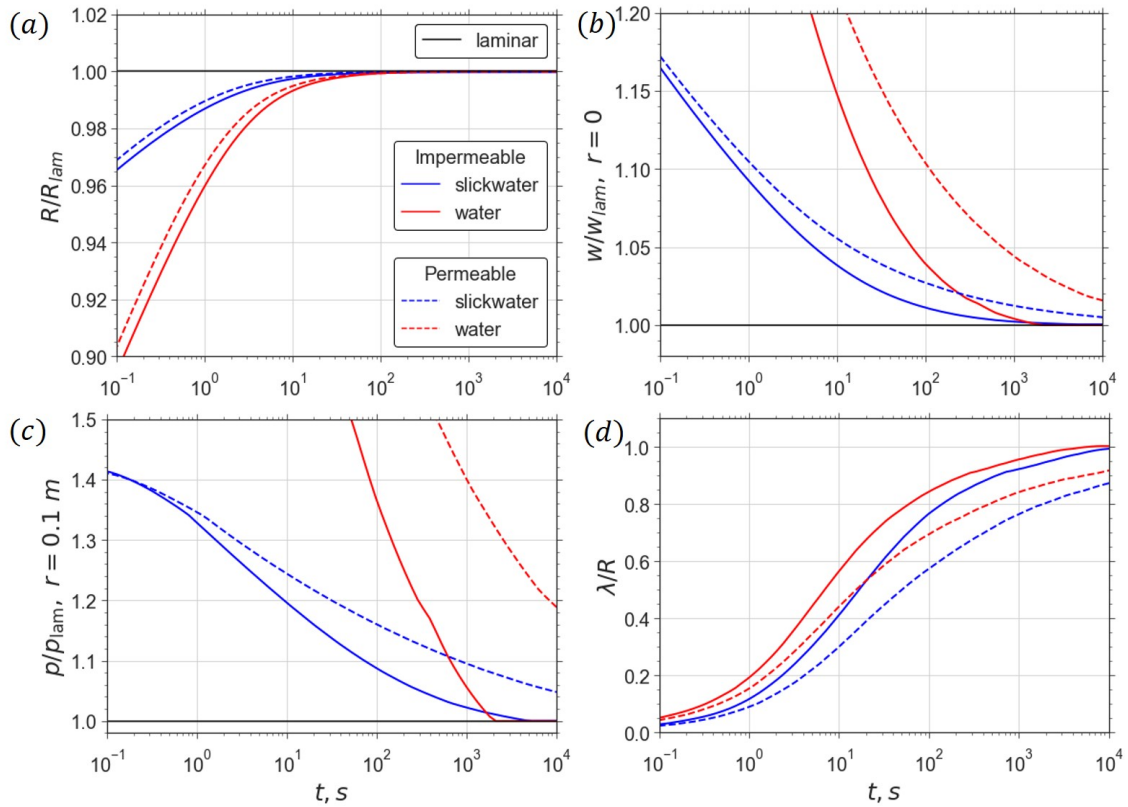
Figure 4-8: Evolution of fracture radius $R(t)$, (a), opening at the wellbore $w(0, t)$, (b), and net pressure $p(0.1, t)$ at the distance $r = 0.1$ m, (c), in the turbulent-laminar solutions, normalized by the corresponding solutions of the fully-laminar model (Figure 4-9). Evolution of length $\lambda(t)$ of the laminar flow domain, (d), normalized by fracture radius $R(t)$ (the laminar flow domain extends distance λ from the crack tip, see Figure 4-7). The slickwater (water) solutions are presented by blue (red) color, while solid (dashed) lines indicate impermeable (permeable) rock case.

Using these figures, one can notice that the laminar-to-turbulent flow regime transformation inside the crack channel affects the fracture parameters during an initial period of the propagation, leading to a shorter radius, larger opening at the wellbore, and pressure values compared to the fully-laminar model. Turbulent effects
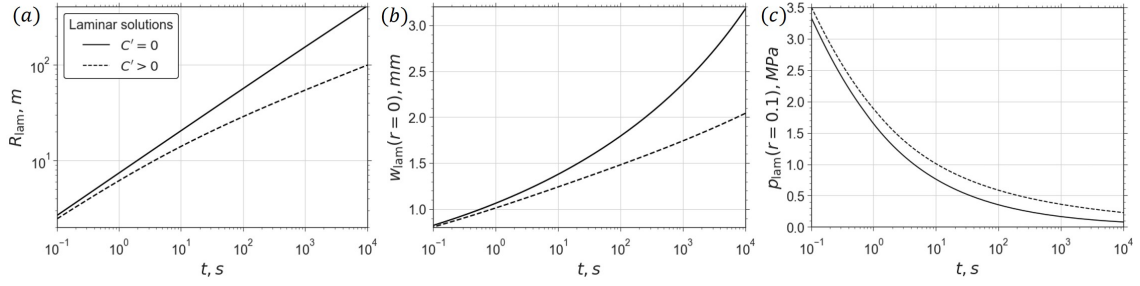
Figure 4-9: Evolution of the fracture radius $R(t)$, (a), maximum opening $w(0,t)$, (b), and net pressure $p(0.1,t)$ at the distance $r = 0.1\ m$ in the laminar solutions. The solid (dashed) lines indicate the impermeable (permeable) rock case.

Table 4.2: The table contains the time moments (in seconds) starting from which the relative differences between the fracture characteristics $R(t)$, $w(0,t)$, $p(0.1,t)$ estimated by the turbulent-laminar and fully-laminar solutions are less than 5%.

		t_*, s			
HF fluid		slickwater		water	
rock type		impermeable	permeable	impermeable	permeable
$\mathcal{A}$	$R(t)$	0.03	0.02	0.7	0.5
	$w(0,t)$	5.5	14.2	70.5	745.3
	$p(0.1,t)$	308	8933	1079	67383

eventually become negligible, and the turbulent-laminar and fully-laminar solutions become nearly identical. It is important to highlight that the threshold time is different for radius, opening, and pressure for a particular choice of the governing parameters of the model.

Let us define a time moment t_* when a time-dependent fracture characteristic $\mathcal{A}(t)$ (radius, opening, pressure) corresponding to the turbulent-laminar solution can be closely approximated by $\mathcal{A}_{\text{lam}}(t)$ from the fully-laminar solution as follows: $|\mathcal{A}(t_*) - \mathcal{A}_{\text{lam}}(t_*)|/|\mathcal{A}_{\text{lam}}(t_*)| = 5\%$. We summarize the values t_* for the crack parameters depicted in Figure 4-8 for all considered cases, namely, slickwater (blue lines) and pure water (red lines) fracturing in the impermeable (solid lines) and permeable (dashed lines) reservoirs, in Table 4.2.

It is clear from Table 4.2 that the noticeable difference in the fracture radius values $R(t)$ and $R_{\text{lam}}(t)$ appears on the timescale less than one second, suggesting that in practice, the deviation of the fracture size in the turbulent-laminar solution from that assuming fully-laminar flow can be neglected. The flow regime transformation impacts opening at the wellbore during approximately 5 and 15 seconds for slick-

water fracturing in an impermeable and permeable rock, correspondingly. These quantities for pure water fracturing are around 1 and 12 minutes, respectively. The interpretation of the results for $w(0, t)$ leads to the following conclusions: (i) the leak-off process prolongs the duration of the turbulent flow regime influence on the crack aperture near the wellbore, and (ii) the turbulence effects are more pronounced for the pure water case since they continue during much longer period of time. However, even when the crack geometries (radius and aperture) are approximately the same in the turbulent-laminar and fully-laminar models, the pressure values near the wellbore ($r = 0.1$ m) can still differ significantly. This observation means that larger amount of energy is required to create a hydraulic fracture driven by turbulent-laminar flow compared to the value predicted by the fully-laminar model. From Figure 4-8 and Table 4.2, we identify for the slickwater case that $p \approx p_{\text{lam}}$ (less than 5%) after 5 minutes from the fracture initiation in an impermeable formation, while in a permeable rock, this period reaches 2.5 hours. In turn, when the HF fluid is pure water, the alignment of the pressure values occurs after 0.5 and 18 hours (beyond typical HF treatment duration in the field), correspondingly.

Figure 4-8(d) shows the extent $\lambda(t)$ of the region $r \in (R - \lambda, R)$ with laminar flow as a fraction of the crack radius $R(t)$. It is an increasing function on time evolving from $\lambda/R \approx 0$ at early time and approaching $\lambda/R \approx 1$ at large time. In other words, the turbulent flow regime is realized along the entire fracture at the beginning of the propagation, while the laminar regime is spatially dominant at large time. For example, we observe in the permeable rock case that near the end of a typical fluid injection ($t \sim 10^4$ s) only a small part of the crack $\sim 0.1R$ near the wellbore is occupied by turbulent flow, whereas the remainder of the crack $\sim 0.9R$ supports laminar flow. Turbulent flow spatial extent is yet smaller for the case of impermeable rock. By comparing slickwater and water injection cases in Figure 4-8(d), we notice that the spatial domain with turbulent flow is larger for slickwater HF, i.e., λ/R at all times is smaller, yet the water HF corresponds to larger deviations of $R(t)$, $w(0, t)$, $p(0.1, t)$ from the laminar solution.

Figure 4-10 demonstrates how the fracture efficiency η changes over time in the permeable reservoir case. Here, we present turbulent-laminar solutions for slickwater

(dashed blue line) and pure water (dashed red line) fracturing and compare them with $\eta(t)$ obtained in the fully laminar model (solid grey line). One can notice that both turbulent-laminar solutions become indistinguishable from fully laminar solution after 100 seconds of fluid injection. The main differences are observed during the first few seconds of radial crack propagation: here, the fracture efficiency in the turbulent-laminar model is greater than that of in the fully laminar model. Moreover, crack efficiency corresponding to slickwater solution is smaller than the similar characteristic is the pure water case.
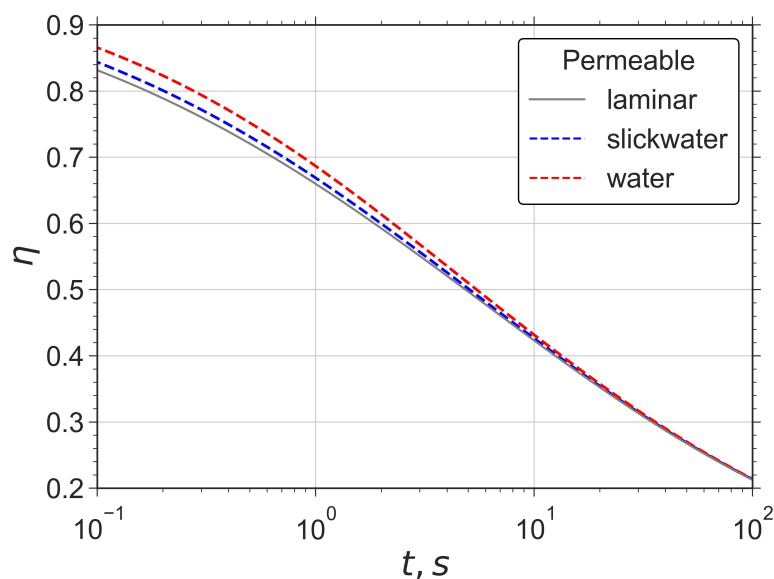
Figure 4-10: Evolution of the fracture efficiency $\eta(t)$ in the permeable formation case. The solid grey line shows the outcome of the fully-laminar model, while dashed blue and red lines present the slickwater and water solutions, respectively.

We now discuss how the spatial distributions of the fracture aperture and net pressure along the fracture evolve with time. These distributions are shown in Figure 4-11 for three time moments $t = \{1, 10, 100\}$ s. As it has been already mentioned, a radial crack driven by turbulent-laminar flow has a shorter radius compared to the fully-laminar model, at early time, the opening and pressure profiles for $t = 1$ s in Figure 4-11 confirm this fact. In the subsequent time moments, i.e., $t = 10$ and 100 s, the difference between $R(t)$ and $R_{\mathrm{lam}}(t)$ values is imperceptible. The turbulent-laminar solutions become very close to their laminar 'analogs' starting from a certain distance from the fluid source. In turn, in the remainder of the crack,

136

i.e., along the zone adjacent to the wellbore, a considerable difference, decreasing over time, is observed where the turbulent-laminar crack has a wider opening and larger net pressure. In general, the HF in a permeable rock (Figures 4-11(b) and (d)) has a smaller volume due to the leak-off compared to the crack propagation in the impermeable reservoir, which is manifested in a shorter radius and aperture in the leak-off cases. On the other hand, the net pressure profile has greater values in the cases with leak-off.

Using Figures 4-11(c) and (d), one can observe the presence of the pressure singularities at the wellbore and the fracture front. For example, the pressure behavior near the wellbore ($r \ll R$) is governed by $p \sim |\log r|$ for the fully-laminar crack, while $p \sim r^{-3/10}$ and $p \sim r^{-3/4}$ are applicable for slickwater and pure water fracturing, respectively, in the turbulent-laminar model. The near-tip region of a hydraulic fracture ($R - r \ll R$) has multiscale nature (see, e.g., [Garagash et al., 2011]) such that the dominant tip singularity depends on both fracture length and propagation speed. It can take form of either toughness asymptote $p \sim -|\log r|$ or storage-viscosity asymptote [Garagash et al., 2011]. The latter is given by $p \sim -(R-r)^{-1/3}$ [Desroches et al., 1994] in the laminar flow regime and by $p \sim -(R-r)^{-7/27}$ for slickwater or $p \sim -(R-r)^{-1/9}$ for pure water in the turbulent flow regime [Lecampion and Zia, 2019, Kanin et al., 2020b].

4.3.4 Limiting propagation regimes

Two different mechanisms control the propagation regime of a finite hydraulic fracture. The first one regulates the total dissipated energy distribution between the creation of new fracture surfaces at the tip and viscous fluid flow inside the fracture channel. The second mechanism is related to the partitioning of the injected fluid volume between the fracture and host permeable rock (due to leak-off). During the crack growth, the allocation of the dissipated energy and injected volume can change over time resulting in the realization of the limiting propagation regimes characterized by one dissipation (out of two) and one fluid balance (out of two) mechanisms. The partitioning of the dissipated energy is influenced by the viscosity M' and toughness K' parameters, while the leak-off parameter C' affects the
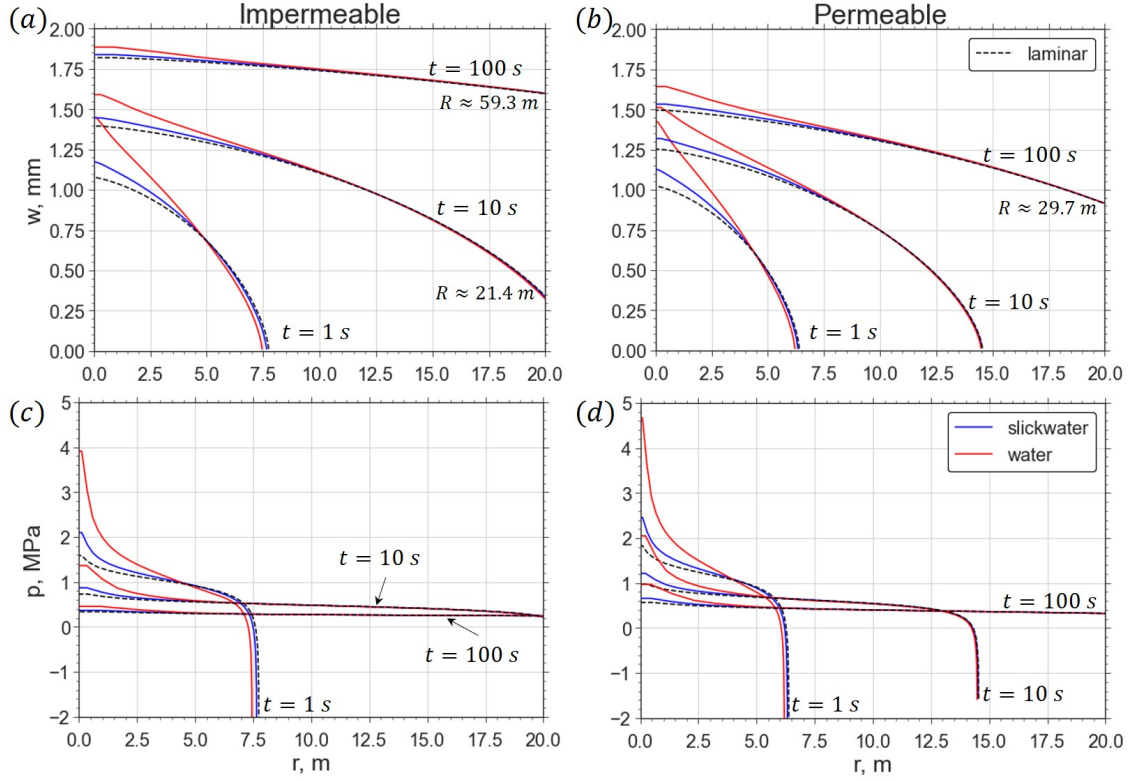
Figure 4-11: The spatial variations of the fracture opening (top raw) and net fluid pressure (bottom raw) at the time moments $t = \{1,\ 10,\ 100\}$ s. The figures (a) and (c) are related to the impermeable rock case, while (b) and (d) show the discussed crack characteristics during the growth at the permeable formation. The solution profiles for the slickwater (water) fracturing are depicted by solid blue (red) lines. The fully-laminar solutions are presented by black dashed lines.

distribution of the injected volume.

In the present radial fracture model, we distinguish six limiting propagation regimes (also known as the vertex solutions or vertices). Four of them can be observed in the penny-shaped HF model with laminar flow realized along the whole fracture channel (see a review paper of Detournay [2016] and references therein):

- **M** – storage-viscosity-laminar – $C' = K' = 0$, $Re \leq Re_c$;

- $\tilde{\boldsymbol{M}}$ – leak-off-viscosity-laminar – $C' \to +\infty$, $K' = 0$, $Re \leq Re_c$;

- **K** – storage-toughness – $C' = M' = 0$;

- $\tilde{\boldsymbol{K}}$ – leak-off-toughness – $C' \to +\infty$, $M' = 0$.

The toughness dominated regimes K and $\tilde{K}$ do not depend on the flow regime type.

Therefore, the remaining two limiting regimes emerge in the viscosity-dominated case, when the entire fracture is occupied by turbulent flow:

- **T** – storage-viscosity-turbulent – $C' = K' = 0$, $Re > Re_c$;

- $\tilde{\boldsymbol{T}}$ – leak-off-viscosity-turbulent – $C' \to +\infty$, $K' = 0, Re > Re_c$.

Although the laminar flow always exists near the hydraulic fracture front, the above two regimes correspond to the limit when the laminar domain becomes negligibly small.

Savitski and Detournay [2002] derived solutions for M and K vertices, while $\tilde{K}$ and $\tilde{M}$ solutions are given by Bunger et al. [2005], and by [Madyarova, 2004, Peirce and Detournay, 2008], respectively. Moreover, Dontsov [2016a] present approximate solutions for all laminar limiting regimes. The semi-analytical and approximate solutions for the storage-viscosity-turbulent regime, T-vertex, are found by Lecampion and Zia [2019].

Further, we summarize scalings in different limiting regimes of the solution following [Detournay, 2016] for the laminar regimes and [Lecampion and Zia, 2019] for the turbulent ones. Firstly, we introduce the dimensionless radius γ, opening Ω, net pressure Π and fluid velocity $\mathcal{V}$ as follows:

$$
R(t) = L(t)\gamma(\mathcal{P}), \quad w(r,t) = \epsilon(t)L(t)\Omega(\xi, \mathcal{P}),
$$
$$
p(r,t) = E'\epsilon(t)\Pi(\xi, \mathcal{P}), \quad v(r,t) = L(t)\mathcal{V}(\xi, \mathcal{P})/t, \tag{4.32}
$$

where $\xi = r/R(t)$ is the normalized distance from the source, $\mathcal{P} = \{\mathcal{P}_1, \mathcal{P}_2, \mathcal{P}_3\}$ are dimensionless evolution parameters depending on time, material parameters (2.10), fluid density ρ and injection rate Q_0. $L(t)$ is a lengthscale of the same order as the crack radius, and $\epsilon(t)$ is a small dimensionless parameter.

Next, we substitute formulas (4.32) into the governing equations and obtain their normalized form:

- *Elasticity:*
$$
\Pi = -\frac{1}{2\pi\gamma} \int_0^1 G(\xi, s) \frac{\partial \Omega}{\partial s} ds; \tag{4.33}
$$

- *Reynolds:*

$$\mathcal{G}_v \left(\left[\frac{\dot{\epsilon}t}{\epsilon} + \frac{\dot{L}t}{L} \right] \Omega + \dot{\Omega}t - \xi \left(\frac{\dot{L}t}{L} + \frac{\dot{\gamma}t}{\gamma} \right) \frac{\partial \Omega}{\partial \xi} \right) + \frac{\mathcal{G}_c}{\sqrt{1 - \tau_0 (\xi L \gamma)}} = -\frac{1}{\gamma \xi} \frac{\partial \left(\xi \Omega \tilde{\mathcal{V}} \right)}{\partial \xi};$$

$$\tilde{\mathcal{V}} = G_v \mathcal{V} = \begin{cases} -(\mathcal{G}_m^{\mathrm{lam}})^{-1} \Omega^2 \gamma^{-1} \nabla \Pi, & \mathcal{R}|\mathcal{V}|\Omega \leq Re_c, \\ -(\mathcal{G}_m^{\mathrm{turb}})^{-1} \mathrm{sign}\,(\nabla \Pi) \left[\Omega^{n+1} \gamma^{-1} |\nabla \Pi| \right]^{1/(2-n)}, & \mathcal{R}|\mathcal{V}|\Omega > Re_c; \end{cases}$$

(4.34)

- *Propagation condition:*

$$\Omega = \mathcal{G}_k \sqrt{\gamma} \sqrt{1 - \xi}, \quad \xi \to 1; \tag{4.35}$$

- *Boundary conditions:*

$$\lim_{\xi \to 0} \xi \Omega \mathcal{V} = \frac{\mathcal{G}_v^{-1}}{2\pi \gamma}, \quad \Omega(1, t) = 0, \quad \Omega(1, t)\mathcal{V}(1, t) = 0; \tag{4.36}$$

- *Global fluid balance:*

$$\frac{1}{\pi \gamma^2} = 2\mathcal{G}_v \int_0^1 \Omega \xi d\xi + 4\mathcal{G}_c \int_0^1 \sqrt{1 - \tau_0 (\xi \gamma L)} \xi d\xi; \tag{4.37}$$

where $\tau_0(t) = t_0(r)/t$ is the dimensionless inverse radius function, $\nabla \Pi = \partial \Pi / \partial \xi$ is the pressure gradient, and $\mathcal{R} = 12 \rho \epsilon L^2 / (M't)$ is the characteristic Reynolds number. We also introduce five dimensionless groups:

$$\mathcal{G}_v = \frac{\epsilon L^3}{Q_0 t}, \quad \mathcal{G}_c = \frac{C'L^2}{Q_0 \sqrt{t}}, \quad \mathcal{G}_k = \frac{K'}{E'\epsilon \sqrt{L}}, \quad \mathcal{G}_m^{\mathrm{lam}} = \frac{M'Q_0}{E'L^3 \epsilon^4},$$

$$\mathcal{G}_m^{\mathrm{turb}} = \left(\frac{f_0''(12\rho)^{1-n} M'^n Q_0^{2-n}}{E'L^{4-n}\epsilon^4} \right)^{1/(2-n)} = \left(f_0'' \mathcal{G}_m^{\mathrm{lam}} (\mathcal{R}/\mathcal{G}_v)^{1-n} \right)^{1/(2-n)}. \tag{4.38}$$

Numbers $\mathcal{G}_v$ and $\mathcal{G}_c$ quantify the fluid volume stored inside the fracture and leaked into the rock, respectively, in reference to the total injected volume. Numbers $\mathcal{G}_k$, $\mathcal{G}_m^{\mathrm{lam}}$, and $\mathcal{G}_m^{\mathrm{turb}}$ with the meaning of the non-dimensional rock toughness, fluid viscosity, and equivalent viscosity of turbulent flow, correspondingly, relate to the

partition of the dissipated energy between solid and fluid.

To derive scalings linked to the limiting regimes (i.e., lengthscale $L(t)$ and factor $\epsilon(t)$ in equation (4.32)), we assign one out of two storage numbers $(\mathcal{G}_v, \mathcal{G}_c)$ and one out of three dissipation numbers $(\mathcal{G}_m^{\mathrm{lam}}, \mathcal{G}_m^{\mathrm{turb}}, \mathcal{G}_k)$ equal to one. The remaining three groups constitute the evolution parameters $\mathcal{P}$. When all three of these parameters tend to zero in a given scaling, one can observe the emergence of the corresponding vertex solution.

We consider the storage-viscosity-turbulent scaling $\mathcal{G}_v = \mathcal{G}_m^{\mathrm{turb}} = 1$. The following formulas for the lengthscale and small parameter follow:

$$L_t = \left(\frac{E't^4 Q_0^{n+2}}{(12\rho)^{1-n} f_0'' M'^n} \right)^{1/(8+n)}, \qquad \epsilon_t = \frac{Q_0 t}{L_t^3}. \tag{4.39}$$

while three non-dimensional evolution parameters $\mathcal{P}$ (i.e., toughness $\mathcal{G}_k$, leak-off $\mathcal{G}_c$, and laminar-viscosity $\mathcal{G}_m^{\mathrm{lam}}$) are:

$$
\begin{aligned}
\mathcal{K}_t &= K' \left(\frac{t^{4-2n}}{(12\rho)^{5-5n}(f_0'')^5 E'^{11+2n} M'^{5n} Q_0^{6-3n}} \right)^{1/(16+2n)}, \\
\mathcal{C}_t &= C' \left(\frac{E'^4 t^{8-n}}{(12\rho)^{4-4n}(f_0'')^4 M'^{4n} Q_0^{8-2n}} \right)^{1/(16+2n)}, \\
\mathcal{M}_t &= \left(\frac{E'^{1-n} M'^{8-8n} t^{4-4n}}{(12\rho)^{9-9n}(f_0'')^9 Q_0^{6-6n}} \right)^{1/(8+n)}.
\end{aligned}
\tag{4.40}
$$

The solution in the storage-viscosity-turbulent regime (T-vertex) is then obtained from the normalized equations (4.33)–(4.37) in the above scaling when the evolution parameters (4.40) are set to zero. The solution is computed numerically using the method defined in Section 4.3.2, and is given below for the time evolution of the fracture radius, opening at the wellbore, and pressure at the half-radius:

$$R_t(t) = 0.759 L_t, \qquad w_t(0,t) = 1.11 \left(\frac{(f_0'')^2 (12\rho)^{2-2n} M'^{2n} Q_0^{4-n} t^n}{E'^2} \right)^{1/(8+n)},$$

$$p_t(R_t(t)/2, t) = 0.5 \left(\frac{(f_0'')^3 E'^{n+5} M'^{3n} (12\rho)^{3-3n} Q_0^{2-2n}}{t^{4-n}} \right)^{\frac{1}{n+8}}. \tag{4.41}$$

In expressions (4.41) for radius $R_t(t)$, maximum opening $w_t(0,t)$, and pressure at the half radius $p_t(R_t(t)/2, t)$, coefficients are determined from the fitting of the full

numerical solution by analytical dependencies (4.32) supplemented by formulas for the lengthscale L_t and small parameter ϵ_t (4.39).

The storage-viscosity-laminar scaling $\mathcal{G}_v = \mathcal{G}_m^{\text{lam}} = 1$ and corresponding scales L_m and ϵ_m can be alternatively obtained by setting $n = f_0'' = 1$ in expressions (4.39) for L_t, ϵ_t. Fracture characteristics in the M-vertex solution ($\mathcal{G}_k = \mathcal{G}_c = \mathcal{G}_m^{\text{turb}} = 0$) have the following form [Savitski and Detournay, 2002]:

$$
R_m(t) = 0.699 \left(\frac{E' Q_0^3 t^4}{M'} \right)^{1/9}, \qquad w_m(0,t) = 1.188 \left(\frac{M'^2 Q_0^3 t}{E'^2} \right)^{1/9},
$$

$$
p_m(R_m(t)/2, t) = 0.62 \left(\frac{E'^2 M'}{t} \right)^{1/3}, \tag{4.42}
$$

where, as before, the numerical prefactors are evaluated from the full numerical solution of the problem.

Next, we look at the leak-off-viscosity-turbulent scaling $\mathcal{G}_c = \mathcal{G}_m^{\text{turb}} = 1$ and derive the formulas for the lengthscale and small parameter provided below:

$$
L_{\tilde{t}} = t^{1/4} \sqrt{\frac{Q_0}{C'}}, \qquad \epsilon_{\tilde{t}} = \frac{(12\rho)^{(1-n)/4}(f_0'')^{1/4} C'^{(4-n)/8} M'^{n/4}}{E'^{1/4} Q_0^{n/8} t^{(4-n)/16}}. \tag{4.43}
$$

Fracture characteristics in the $\tilde{T}$-vertex solution for the leak-off-viscosity-turbulent regime ($\mathcal{G}_v = \mathcal{G}_k = \mathcal{G}_m^{\text{lam}} = 0$) can be obtained in the following form:

$$
R_{\tilde{t}}(t) = \frac{\sqrt{2}}{\pi} L_{\tilde{t}}, \qquad w_{\tilde{t}}(0,t) = \frac{(12\rho)^{\frac{1-n}{4}}(f_0'')^{1/4} M'^{n/4} Q_0^{(4-n)/8} t^{n/16}}{E'^{1/4} C'^{n/8}},
$$

$$
p_{\tilde{t}}(R_{\tilde{t}}(t)/2, t) = 0.75 \left(\frac{E'^{12}(f_0'')^4 C'^{8-2n} M'^{4n}(12\rho)^{4-4n}}{Q_0^{2n} t^{4-n}} \right)^{1/16}, \tag{4.44}
$$

where the numerical prefactors (for opening and pressure) are computed from the full numerical solution of the governing equations (4.33)–(4.37) in the $\tilde{T}$-scaling when the evolution parameters equal zero; the coefficient for the fracture radius is found analytically (exact).

The substitution $n = f_0'' = 1$ in equations (4.43) for $L_{\tilde{t}}$, $\epsilon_{\tilde{t}}$ leads to the leak-off-viscosity-laminar scaling $\mathcal{G}_c = \mathcal{G}_m^{\text{lam}} = 1$ and corresponding scales $L_{\tilde{m}}$ and $\epsilon_{\tilde{m}}$. The

fracture properties in the $\tilde{M}$-vertex solution ($\mathcal{G}_k = \mathcal{G}_v = \mathcal{G}_m^{\text{turb}} = 0$) are given below:

$$R_{\tilde{m}}(t) = R_{\tilde{t}}(t), \quad w_{\tilde{m}}(0,t) = 1.05 \left(\frac{M'^4 Q_0^6 t}{C'^2 E'^4} \right)^{1/16},$$

$$p_{\tilde{m}}(R_{\tilde{m}}(t)/2, t) = 0.84 \left(\frac{E'^{12} C'^6 M'^4}{Q_0^2 t^3} \right)^{1/16}, \tag{4.45}$$

where the numerical coefficients for the opening and pressure are calculated from the full numerical solution of the problem.

The toughness dominated vertex solutions (K and $\tilde{K}$) do not depend on the realized flow regime inside the fracture channel since the corresponding energy dissipation in the fluid flow is assumed negligibly small. For the completeness, we write out expressions for the radius, opening at the wellbore and pressure (uniform along the whole crack) in these regimes [Savitski and Detournay, 2002, Bunger et al., 2005]:

$$R_k = \left(\frac{3}{\sqrt{2\pi}} \right)^{2/5} \left(\frac{E' Q_0 t}{K'} \right)^{2/5}, \quad w_k(0,t) = \left(\frac{3}{8\pi} \right)^{1/5} \left(\frac{K'^4 Q_0 t}{E'^4} \right)^{1/5},$$

$$p_k(t) = \left(\frac{\pi^6}{2^{17} 3} \cdot \frac{K'^6}{t E' Q_0} \right)^{1/5}; \tag{4.46}$$

$$R_{\tilde{k}}(t) = R_{\tilde{t}}(t), \quad w_{\tilde{k}}(0,t) = \frac{1}{2^{1/4}\sqrt{\pi}} \left(\frac{K'^8 Q_0^2 t}{C'^2 E'^8} \right)^{1/8}, \quad p_{\tilde{k}}(t) = \frac{\pi^{3/2}}{2^{15/4}} \frac{C'^{1/4} K'}{Q_0^{1/4} t^{1/8}}. \tag{4.47}$$

4.3.5 Normalization of the governing equations

Normalized solution (4.32) in one of the vertex-scalings of Section 4.3.4 depends on three non-dimensional evolution parameters which quantify the departure from the corresponding vertex solution. Either of these three parameters can be regarded as non-dimensional 'time' in the problem. Alternative, so-called 'mixed' scalings have also been used [Madyarova, 2004, Bunger et al., 2005, Adachi and Detournay, 2008, Dontsov, 2016a] to compute solution evolution in time between the limiting regimes (vertices).

One of such scalings, the mk-scaling [Detournay, 2016], is defined in terms of the

timescale t_{mk} quantifying the solution transition period between M and K regimes. Specifically, t_{mk} is the time moment when the $K-$vertex and $M-$vertex lengthscales are the same, i.e., $L_k(t) = L_m(t)$ at $t = t_{mk}$. The corresponding length $L_{mk} = L_m(t_{mk}) = L_k(t_{mk})$ and non-dimensional small parameter $\epsilon_{mk} = \epsilon_m(t_{mk}) = \epsilon_k(t_{mk})$ are used to define the mk-scaling:

$$\xi = \frac{r}{R}, \quad \tau = \frac{t}{t_{mk}}, \quad \gamma = \frac{R}{L_{mk}}, \quad \Omega = \frac{w}{\epsilon_{mk}L_{mk}}, \quad \Pi = \frac{p}{E'\epsilon_{mk}}, \quad \mathcal{V} = \frac{v}{L_{mk}/t_{mk}}, \quad (4.48)$$

where the characteristic scales evaluated as:

$$t_{mk} = \sqrt{\frac{E'^{13}M'^5Q_0^3}{K'^{18}}}, \qquad L_{mk} = \left(\frac{E'Q_0^3 t_{mk}^4}{M'}\right)^{1/9}, \qquad \epsilon_{mk} = \left(\frac{M'}{E't_{mk}}\right)^{1/3}. \qquad (4.49)$$

We note that either vertex scalings (Section 4.3.4) or the alternative 'mixed' mk-scaling can be utilized to obtain general solution and its evolution in time. In the following, we apply the mk-scaling, since it allows for more direct interpretation of the normalized solution (since the scales L_{mk} and ϵ_{mk} are constants compared to the time-dependent vertex scales $L(t)$ and $\epsilon(t)$).

The substitution of (4.48), (4.49) into the system of the governing equations yields their normalized form:

- *Elasticity:*
$$\Pi = -\frac{1}{2\pi\gamma}\int_0^1 G\left(\xi, s\right)\frac{\partial\Omega}{\partial s}ds;$$

- *Reynolds:*

$$\frac{\partial\Omega}{\partial\tau} - \frac{\xi\dot{\gamma}}{\gamma}\frac{\partial\Omega}{\partial\xi} + \frac{1}{\xi\gamma}\frac{\partial}{\partial\xi}\left(\xi\Omega\mathcal{V}\right) + \frac{\phi^{1/4}}{\sqrt{\tau - \tau_0\left(\xi L_{mk}\gamma\right)}} = 0,$$

$$\mathcal{V} = -\frac{\Omega^2}{\tilde{f}\gamma}\frac{\partial\Pi}{\partial\xi},$$

$$\tilde{f} = \begin{cases} 1, & \mathcal{R}\Omega|\mathcal{V}| \leq Re_c, \\ f_0''\left(\mathcal{R}\Omega|\mathcal{V}|\right)^{1-n}, & \mathcal{R}\Omega|\mathcal{V}| > Re_c; \end{cases}$$

- *Propagation condition:*

$$\Omega = \sqrt{\gamma}\sqrt{1-\xi}, \quad \xi \to 1;$$

- *Boundary conditions:*

$$\lim_{\xi \to 0} \xi\Omega\mathcal{V} = \frac{1}{2\pi\gamma}, \quad \Omega(1,t) = 0, \quad \Omega(1,t)\mathcal{V}(1,t) = 0;$$

- *Global fluid balance:*

$$\frac{\tau}{\pi\gamma^2} = 2\int_0^1 \xi\Omega d\xi + 4\phi^{1/4}\int_0^1 \xi\sqrt{\tau - \tau_0(\xi\gamma L_{mk})}d\xi.$$

The normalized solution of the above set of equations depends on non-dimensional spatial coordinate ξ, time τ, and two dimensionless numbers, leak-off ϕ and characteristics Reynolds number $\mathcal{R}$:

$$\phi = \frac{C'^4 E'^{11} M'^3 Q_0}{K'^{14}}, \quad \mathcal{R} = \frac{12 K'^4 \rho}{E'^3 M'^2}. \tag{4.50}$$

Let us evaluate the ranges for the governing parameters ϕ and $\mathcal{R}$ corresponding to typical field applications. We choose the following intervals for the dimensional model parameters:

- geomechanics:

  - plane-strain elastic modulus: $E' = 10 \div 50$ GPa;

  - rock toughness: $K_{Ic} = 0.5 \div 2.5$ MPa $\cdot \sqrt{\text{m}}$;

  - far-field confining stress: $\sigma_o = 10 \div 30$ MPa;

- reservoir:

  - permeability: $k = 0.1 \div 100$ mD;

  - porosity: $\phi = 5 \div 25\%$;

  - ratio of the pore pressure and confining stress: $p_o/\sigma_o = 0.4 \div 0.95$;

- fluid:

    ∘ viscosity: $\mu = 1 \div 5$ cP;

    ∘ total compressibility: $c_t = 10^{-3}$ MPa^{-1};

    ∘ density: $\rho = 10^3$ kg/m^3;

- volumetric injection rate:

    ∘ $Q_0 = 0.01 \div 0.1$ m^3/s

We vary each parameter independently and evaluate the ranges: $\phi \in [1.1 \cdot 10^{-18}, 6.7 \cdot 10^{14}]$, $\mathcal{R} \in [0.2, 3.4 \cdot 10^5]$. The plane-strain modulus and fracture toughness have the most considerable impact on the dispersion of ϕ and $\mathcal{R}$. Typical duration of the fluid injection $t_{\text{end}} = 1$ hour, which results in the following range for the non-dimensional injection time: $\tau_{\text{end}} \in [2.5 \cdot 10^{-6}, 3 \cdot 10^8]$.

4.3.6   Problem parameter space analyses

Let us investigate the parametric space of the model for a radial crack driven by turbulent-laminar flow of slickwater in both impermeable and permeable reservoirs. We perform the analyses using the problem formulation in the dimensionless form (Section 4.3.5) where the parameter space is three dimensional with the axes: time τ, leak-off number ϕ, and characteristics Reynolds number $\mathcal{R}$.

Firstly, we determine the applicability domains of the limiting propagation regimes (Section 4.3.4) and present them as the regime maps. Such analysis is useful to frame the general solution inside the parameter space resulting in better understanding of the propagation conditions as a function of time. Similar to Dontsov [2016a], we utilize the following criterion for the determination of the validity zone of the considered limiting solution i:

$$\sqrt{\left(1 - \frac{\Omega_i(0, \tau)}{\Omega(0, \tau)}\right)^2 + \left(1 - \frac{\gamma_i(\tau)}{\gamma(\tau)}\right)^2} < 0.01, \tag{4.51}$$

where the subscript i can be M, $\tilde{M}$, K, $\tilde{K}$, T, $\tilde{T}$. In other words, the measure of the relative difference between the general numerical solution and given limiting

case i is taken to be less than 1%, (4.51), for the limiting solution to be considered a valid approximation, and the fracture to be said to propagate in the corresponding limiting regime.

Further, we demonstrate the solution series for different time-dependent crack characteristics such as $\gamma(\tau)$, $\Omega(0,\tau)$, $\Pi(0.5,\tau)$, $\eta(\tau)$ by fixing one (out of two) control parameters (e.g., $\mathcal{R}$) while the remaining (e.g., ϕ) is varied.
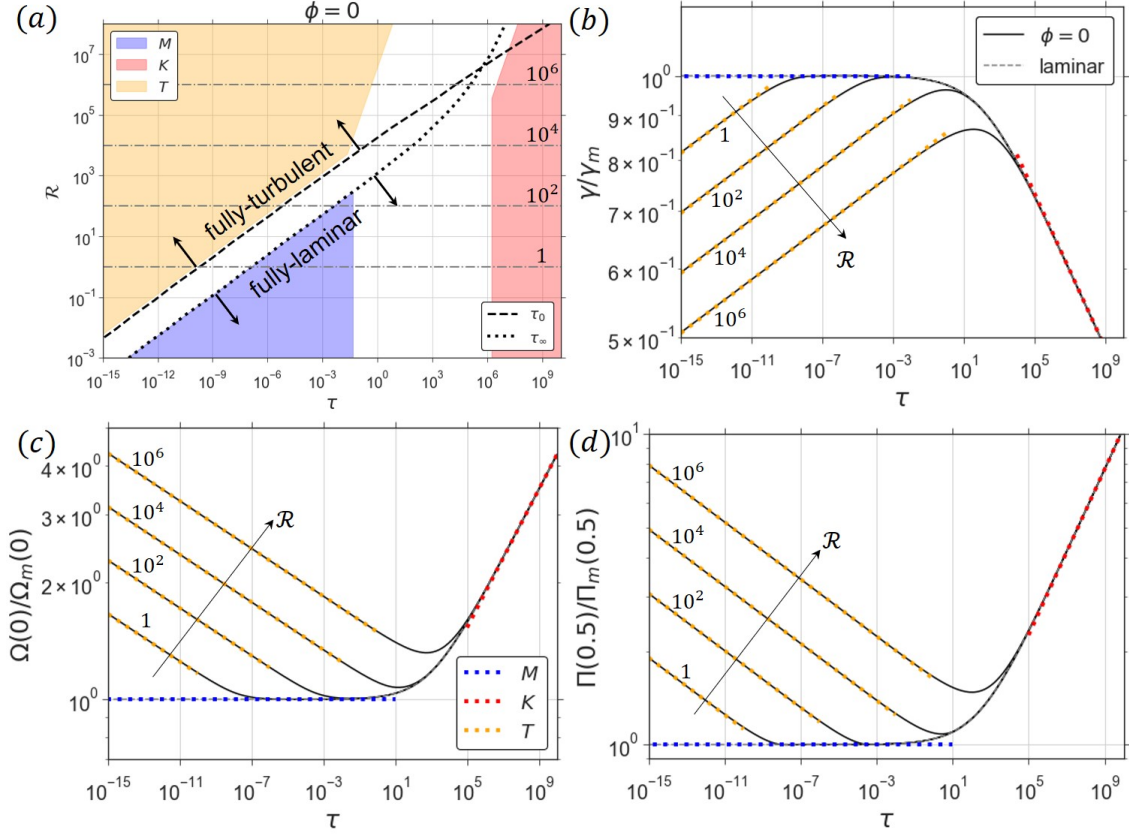
Figure 4-12: The problem solution for a radial fracture in an impermeable rock ($\phi = 0$) driven by turbulent-laminar flow of slickwater. Panel (a) illustrates the regime map in the coordinates (τ, $\mathcal{R}$), where the colored zones denote the validity domains of the limiting propagation regimes. Two supplemental time bounds are shown: (i) time $\tau_0(\mathcal{R})$ (dashed black line) at which the transition between laminar and turbulent flow within the crack channel is located at small distance $\lambda_0 = R/25$ from the tip (such that laminar flow spatial domain is small $\lambda < \lambda_0$ for $\tau < \tau_0(\mathcal{R})$), and (ii) time $\tau_\infty(\mathcal{R})$ (dotted black line) past which the fracture radius and opening are approximately given by the fully-laminar solution. The time-dependent fracture characteristics (radius $\gamma(\tau)$, opening at the wellbore $\Omega(0,\tau)$, and pressure at the half-radius $\Pi(1/2,\tau)$) normalized by the storage-viscosity-laminar limiting solution (M-vertex) are shown in panels (b) – (d) for the set of values of $\mathcal{R} = \{1,\ 10^2,\ 10^4,\ 10^6\}$. The fully-laminar solution is depicted by dashed grey line, and the colored dotted lines present the vertex solutions. In panel (a), the grey dash-dotted lines underline the $\mathcal{R}$-trajectories demonstrated in (b)–(d).

4.3.6.1   Zero leak-off case (impermeable rock)

Lecampion and Zia [2019] has already considered a radial crack propagation in an impermeable formation; however, the authors did not include the regime map for the corresponding reduced parameteric space $(\tau, \phi = 0, \mathcal{R})$, and we would like to fill this gap. Figure 4-12(a) presents the applicability domains of the vertex solutions observed in the current model, i.e., storage-viscosity-turbulent (T), storage-viscosity-laminar (M), and toughness (K) regimes. The problem solution evolves from the T- to K- vertex, and the M-vertex emerges during an intermediate propagation time if $\mathcal{R} < 10^2$. For larger values of the characteristic Reynolds number, the validity zone of the T-vertex expands, while the M-region shrinks. The laminar-to-turbulent flow transformation affects the boundary of the toughness-dominated regime (K) in the range $\mathcal{R} > 10^6$, leading to its shift to larger time.

Further, we would like to clarify how exactly we determine the applicability boundaries shown in Figure 4-12(a). We estimate the borders numerically via criterion (4.51) at sample points at small and large $\mathcal{R}$ and then fit the evaluated points by the appropriate analytical functions derived from the transition timescales between the limiting regimes. As an example, let us consider the validity zone of the T-vertex solution shown by orange color in Figure 4-12(a). It is bounded by two power-law functions of time which are straight lines in the log-log scale. The first boundary located in the region $\mathcal{R} < 10^4$ relates to the TM-transition, i.e., between T and M vertices. We expect that it corresponds to $t \sim t_{mt}$, where the time-scale t_{mt} is the solution of $L_t(t) = L_m(t)$. This boundary expressed in the normalized time is $\tau \sim t_{mt}/t_{mk} = \mathcal{R}^{9/4}$, where the proportionality coefficient is found from the fitting procedure at small $\mathcal{R}$. The functional dependence for the second curve is obtained from the TK transition analysis and has the following form: $\tau \sim t_{tk}/t_{mk} = \mathcal{R}^{(5n-5)/(2n-4)}$, where the numerical prefactor is found from a similar fitting procedure at large $\mathcal{R}$. Both curves are extended until the intersection point, bounding the domain depicted in Figure 4-12(a). The full usage of criterion (4.51) in the entire parametric space of the solution yields a very similar region but with a smoother boundary (without sharp corner point evident in the domain

approximation shown in Figure 4-12(a)).

We also display two time bounds in Figure 4-12(a). The first one $\tau_0(\mathcal{R}, \phi = 0)$ (dashed black line) indicates the time moment when the spatial extent of the laminar flow domain is a small fraction $\lambda = \lambda_0 = R/25$ of the fracture radius. As a result, the crack can be approximately considered as fully-turbulent for $\tau < \tau_0(\mathcal{R}, \phi = 0)$ (and $\lambda < \lambda_0$). One can observe that $\tau_0(\mathcal{R}, \phi = 0)$ is an increasing function of the characteristic Reynolds number $\mathcal{R}$, i.e., the time interval, within which the length of the laminar flow region is small, and turbulent effects dominate, grows with an increase of $\mathcal{R}$. For $\mathcal{R} < 10^3$, the dashed line is very close to the border of the T-vertex validity domain. The second bound $\tau_\infty(\mathcal{R}, \phi = 0)$ (dotted black line) corresponds to the time moment following which the crack geometry (radius and aperture) in the turbulent-laminar case is approximately the same as the fully-laminar model provides. In other words, one can interpret the fracture as fully-laminar for $\tau > \tau_\infty(\mathcal{R}, \phi = 0)$. This bound is computed via equation (4.51) where i should be understood as a fully-laminar solution. The function $\tau_\infty(\mathcal{R}, \phi = 0)$ is an increasing one (similarly to $\tau_0(\mathcal{R}, \phi = 0)$), and for $\mathcal{R} < 10^2$, the dotted line coincides with the boundary of the M-vertex domain.

Next, we discuss the time bound $\tau_0(\mathcal{R}, \phi = 0)$ in the context of the tip element concept. Many numerical models for hydraulic fracture growth are based on the 'tip logic' [Peirce and Detournay, 2008, Peirce, 2015, Dontsov, 2016a, 2017, Zia and Lecampion, 2020]. It means that specialized near-tip region model is applied within such algorithms to determine the fracture front position at each time step (propagation criterion) and to describe crack characteristics (aperture, pressure) near the tip. The fracture tip model should include all physical phenomena that can be realized during the fracture evolution and resolve their influence on the propagation. It is assumed that the near-tip region model is valid along small distance from the fracture front, and in the case of 1D models (plane strain or penny-shaped) the typical tip element length equals λ_0. When we analyze the turbulent-to-laminar flow transformation within the crack channel, two different options for the near-tip region model exist. Firstly, when $\lambda > \lambda_0$ or for $\tau > \tau_0(\mathcal{R}, \phi = 0)$ laminar flow occurs along the entire tip element, one can apply the model of Garagash et al.

[2011] or its approximate and computationally efficient version [Dontsov and Peirce, 2015b]. On the other hand, when $\lambda < \lambda_0$ or for $\tau < \tau_0(\mathcal{R}, \phi = 0)$, it is recommended to utilize the laminar-turbulent tip model developed by Lecampion and Zia [2019].

Figures 4-12(b) – (d) demonstrate the time-dependent fracture characteristics such as radius $\gamma(\tau)$, opening at the wellbore $\Omega(0, \tau)$, and pressure at the half-radius $\Pi(1/2, \tau)$ normalized by the storage-viscosity-laminar limiting solution (M-vertex). The turbulent-laminar solutions for $\mathcal{R} = \{1, 10^2, 10^4, 10^6\}$ are contrasted to the fully-laminar solution profiles shown by grey lines. The flow regime transformation inside the fracture channel leads to a shorter radius, wider aperture, and greater pressure values at the beginning of the propagation compared to the fully-laminar case. The time span when the turbulent-laminar and the fully-laminar solutions differ significantly grows with an increase of the characteristic Reynolds number.

4.3.6.2 Non-zero leak-off case (permeable rock)

Figure 4-13 shows the regime map for the fully-laminar model ($\mathcal{R} = 0$) with non-zero leak-off ϕ in the coordinates (τ, ϕ), while Figure 4-14 demonstrates its modifications for the turbulent-laminar model for different values of the characteristic Reynolds number: $\mathcal{R} = \{1, \ 10^2, \ 10^4, \ 10^6\}$. In the latter case, the problem solution evolves from the storage-viscosity-turbulent (T) solution at early time to the leak-off-toughness ($\tilde{K}$) limiting solution at large time. Moreover, the solution can approach M, K, $\tilde{M}$, or $\tilde{T}$ vertices at intermediate times depending on the values of the governing parameters ϕ, $\mathcal{R}$ (e.g., see trajectories $\phi = $ const in Figure 4-14(b) shown by dash-dotted grey lines). By looking at panels (a) and (b) in Figure 4-14, one can notice that the validity regions of the turbulent limiting propagation regimes, T and $\tilde{T}$, expand with an increase of $\mathcal{R}$ and gradually reduce the applicability zones of the laminar regimes, M and $\tilde{M}$, until their complete disappearance (see panels (c) and (d) in Figure 4-14). Similar behavior is observed for the toughness-dominated regimes, K and $\tilde{K}$, from the regime map in Figure 4-14(d); however, they do exist for all $\mathcal{R}$ and large enough τ.

In Section 4.3.6.1, we have already discussed the physical meaning of the temporal bounds τ_0 and τ_∞, and here, we analyze their behavior with the alteration of the
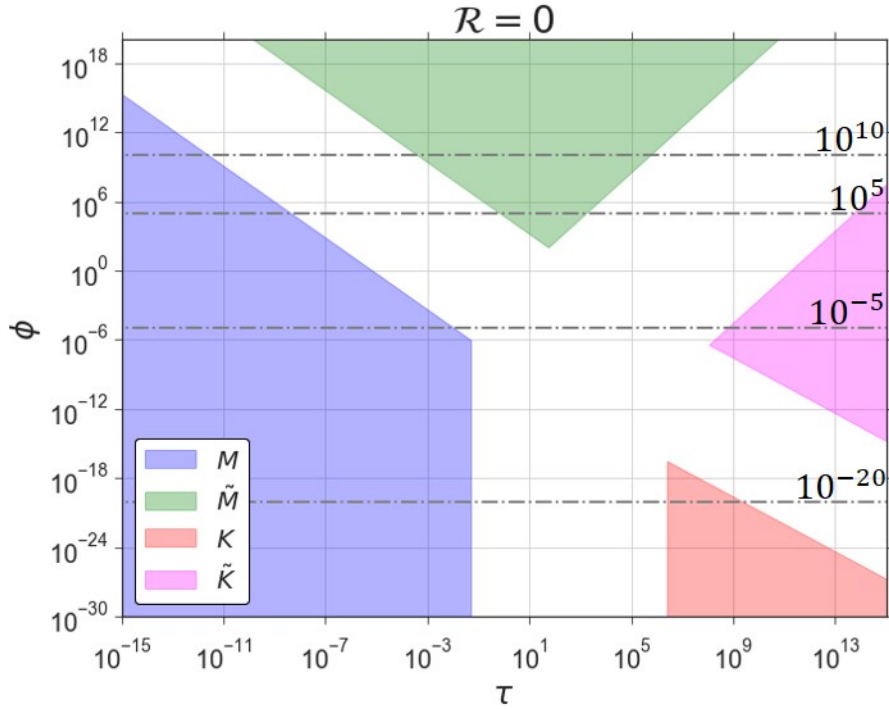
Figure 4-13: The parameter space of the model for a radial hydraulic fracture driven by laminar flow ($\mathcal{R} = 0$) in a permeable rock ($\phi > 0$). The coordinate system (τ, ϕ) is applied to build the regime map in which the applicability domains of the limiting propagation regimes are filled by different colors. The grey dash-dotted lines highlight the considered solution trajectories discussed in the current section.

governing parameters $\mathcal{R}$ and ϕ (see Figure 4-14). For $\mathcal{R} = $ const, both timescales are independent of ϕ when it is small. However, for large values of the leak-off number ϕ, we determine that $\tau_0, \tau_\infty \sim \phi^2$. When the characteristic Reynolds number grows, the bounds shift towards larger time since the turbulent flow regime prevails inside the fracture channel during longer time period for greater values of $\mathcal{R}$. We should also mention that it is recommended to apply the turbulent-laminar fracture tip model [Kanin et al., 2020b] as a propagation criterion in more complex numerical models for HF growth (such as Planar3D) to simulate the crack evolution when the laminar flow domain is small, corresponding to the parametric zone bounded by the dashed black line in Figure 4-14, i.e., when $\tau < \tau_0(\mathcal{R}, \phi)$.

Figure 4-15 demonstrates the crack characteristics in the turbulent-laminar ($\mathcal{R} = 10^2$) and fully-laminar (dashed grey lines) cases for different values of the leak-off number $\phi = \{10^{-20}, \ 10^{-5}, \ 10^5, \ 10^{10}\}$. Since the characteristic Reynolds number is constant, we focus on the impact of the leak-off on the propagation of a radial
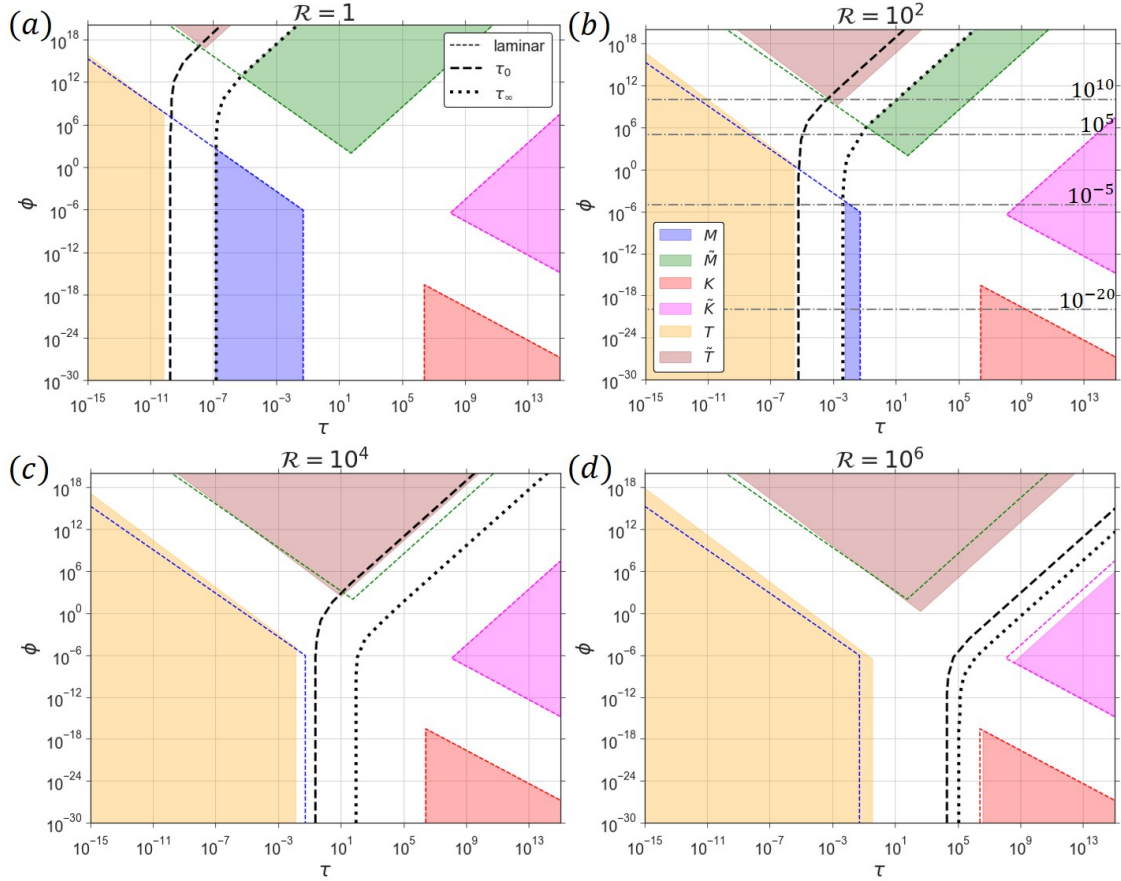
Figure 4-14: The parameter space of the model for a radial hydraulic fracture driven by turbulent-laminar flow of slickwater in a permeable rock ($\phi > 0$). The regime maps are shown in the coordinates (τ, ϕ) for different values of the characteristic Reynolds number $\mathcal{R} = \{1, 10^2, 10^4, 10^6\}$. The colored zones denote the applicability regions of the vertex solutions. For comparison purposes, we add to the plot the regime boundaries corresponding to the fully-laminar model by using the dashed colored lines. The dashed black lines illustrate the time $\tau_0(\mathcal{R}, \phi)$ at which the flow regime transformation inside the crack channel occurs at small distance $\lambda_0 = R/25$ from the tip, i.e., the length of the laminar flow spatial domain is small $\lambda < \lambda_0$ for $\tau < \tau_0(\mathcal{R}, \phi)$. The dotted black lines show the time $\tau_\infty(\mathcal{R}, \phi)$ starting from which the fracture radius and aperture is approximated by the fully-laminar solution. In panel (b), the grey dash-dotted lines emphasize the considered solution trajectories discussed in the current section.

crack driven by turbulent-laminar flow. The storage-viscosity-laminar (M) limiting solution is utilized to normalize the time-dependent properties such as the radius $\gamma(\tau)$, opening at the wellbore $\Omega(0, \tau)$ and pressure at the half-radius $\Pi(1/2, \tau)$ in panels (a) – (c) in Figure 4-15. It is evident from Figure 4-15(a) that larger values of leak-off number ϕ lead to shorter time duration over which the fracture radius differs significantly from the fully-laminar case (i.e., when turbulent effects on the fracture run-out are significant). The situation is opposite for the opening at the

wellbore and pressure at the half-radius (see Figures 4-15(b) and (c)) for which increase of the leak-off extends the influence of the turbulent flow effects. Finally, the fracture efficiency is roughly independent of the laminar-to-turbulent flow regime transformation in all considered cases, as exposed in Figure 4-15(d).
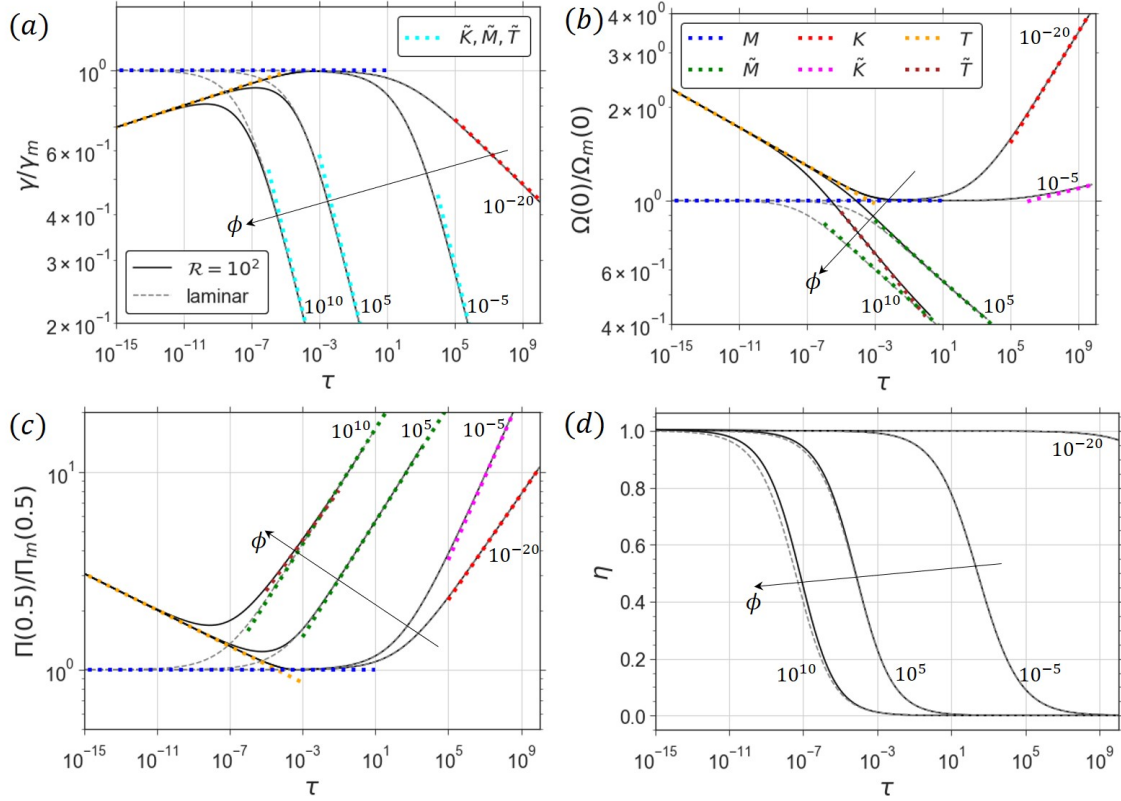
Figure 4-15: The time-dependent characteristics of a radial hydraulic fracture driven by turbulent-laminar flow of slickwater in a permeable rock ($\phi > 0$): (a) radius $\gamma(\tau)$, (b) opening at the wellbore $\Omega(0, \tau)$, (c) pressure at the half-radius $\Pi(1/2, \tau)$, and (d) efficiency $\eta(\tau)$. The properties in panels (a) – (c) are normalized by storage-viscosity-laminar (M) limiting solution. The solution profiles corresponding to $\mathcal{R} = 10^2$ and $\phi = \{10^{-20}, 10^{-5}, 10^5, 10^{10}\}$ are shown. The analogous profiles from the fully-laminar solutions are depicted by the grey dashed lines. We plot the vertex solutions by the colored dotted lines; in panel (a), the leak-off dominated regimes ($\tilde{K}$, $\tilde{M}$, $\tilde{T}$) have the same color since the fracture radii in these regimes are governed by the same relation (e.g., see equation (4.44)).

Chapter 5

Hydraulic fracture driven by a Herschel–Bulkley fluid

5.1 Preamble

A number of parameters can be adjusted to optimise the fracturing treatment, such as volumetric injection rate and hydraulic fracturing fluid properties. Besides breaking the rock, the hydraulic fracturing fluid also carries proppant inside the crack channel, which prevents complete crack closure after shut-in. The fracturing fluid rheology and pumping schedule are typically engineered to achieve the following goals [Economides et al., 1989, Barbati et al., 2016]: creation of the sufficient crack aperture for proppant placement, minimisation of proppant particle settling [Osiptsov, 2017], reducing the risk of the bridging [Garagash et al., 2019], reduction of fluid leak-off rate into the permeable reservoir.

The fracturing fluid is a complex mixture that contains specific additives, e.g., polymeric substances, which allows one to achieve the desired rheological properties [Osiptsov, 2017]. Typical fracturing fluid exhibits non-Newtonian shear-thinning behaviour within a specific range of the shear rate values, i.e. the fluid viscosity declines with the shear rate growth, while for small and large shear rates, the fluid viscosity reaches constant values [Moukhtari and Lecampion, 2018]. At the same time, fracturing foams [Gu and Mohanty, 2015, Faroughi et al., 2018, Fu and Liu, 2019], emulsions, suspensions with proppant and fibers [Stickel and Powell, 2005,

Osiptsov, 2017] tend to exhibit a shear-thinning rheology with yield stress.

Various rheological models are established for describing the fracturing fluid properties. In the case of pure water or slickwater, Newtonian fluid model is often applied for which the shear stress is linearly proportional to the shear rate. When fracturing fluid has shear-thinning behaviour, we can utilise power-law model [Bird et al., 1987]. However, it overestimates and underestimates the fluid viscosity at low and high shear rates correspondingly. This discrepancy can be fixed with the help of more complex rheological models such as Cross [Cross, 1965], Carreau [Carreau, 1972], truncated power-law [Lavrov, 2015], or Ellis model [Brodkey and Brodkey, 1967]. The rheological models mentioned above do not take into account yield stress, whose impact on the flow behaviour can be significant for some fracturing fluids. Herschel–Bulkley rheological model [Herschel and Bulkley, 1926] is a generalisation of the power-law model, and it includes the effect of the yield stress. The limiting cases of Herschel–Bulkley model are Newtonian, power-law and Bingham plastic [Bingham, 1922] models.

In Chapter 1, we outlined the near-tip region and radial crack models in which a fracture is driven by non-Newtonian fluids. Here, we would like to mention additional works linked with KGD and PKN fracture geometries. Garagash and Sarvaramini [2012] investigated the conditions for the onset of the plain-strain fracture propagation with plastic fluid; Wrobel [2020], Wrobel et al. [2020] considered the models of PKN and KGD hydraulic fractures filled by the fluid with the truncated power-law rheology, Pereira and Lecampion [2021] analyzed the behaviour of a KGD crack driven by a shear-thinning fluid with a Carreau rheology.

The vast majority of previous studies do not consider the impact of fluid yield stress on propagation of a finite hydraulic fracture, so we would like to fill the gap and discuss this topic through the example of a radial fracture. To take into account the effect of yield-stress, we assume that the Herschel-Bulkley model governs the fracturing fluid rheological behaviour. The main aims of the current exploration are the following: (i) to implement a solver for calculating an accurate numerical solution for the radial fracture, (ii) to construct an approximate computationally efficient solution for rapid estimations, (iii) to derive limiting propagation regimes

occurring in the model, (iv) to explore the problem parametric space and (v) to analyse variations of the fracture characteristics depending on the yield stress and leak-off intensity for different values of the flow index.

This chapter is organised as follows. Firstly, we outline the problem formulation and the governing equations. Secondly, we describe the methodology for calculating the numerical solution, and, after that, we provide insights into getting the simplified approximate solution. Further, we revisit the known limiting propagation regimes for a radial crack in a permeable rock and introduce the new members associated with the dominance of yield stress. Finally, we present the analysis of the results, including estimation of the ranges for the dimensionless parameters corresponding to typical field applications, extensive exploration of the parameter space, and discuss examples for several typical field cases.

5.2 Model formulation

In the current section, we will formulate the problem of a penny-shaped hydraulic fracture driven by the fluid characterised by the non-zero yield stress and non-linear behaviour of the shear stress. Figure 5-1 shows the sketch of the considered model. Compared to the classic problem statement for a radial hydraulic fracture (Section 2.2), assumptions and relations linked with the fracturing fluid flow inside the fracture channel are modified. We will discuss them in detail here, while we will not repeat the remaining items for brevity.
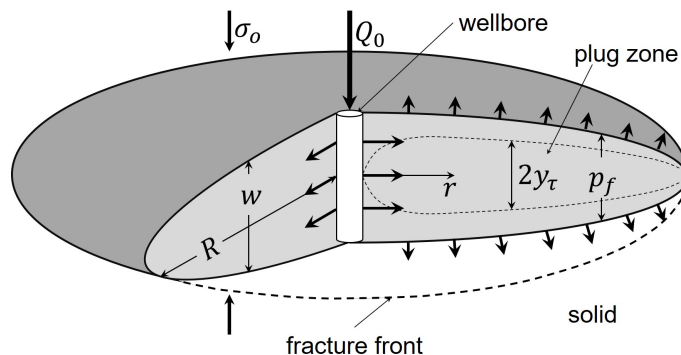
Figure 5-1: A radial fracture model driven by a Herschel–Bulkley fluid.

We assume that the fracturing fluid rheology is governed by Herschel-Bulkley

156

model, and it is described by the following constitutive relation:

$$\tau_m = \tau_0 + M\dot{\gamma}^n, \tag{5.1}$$

where τ_m is the shear stress, τ_0 is the yield stress, $\dot{\gamma}$ is the shear rate, M is the consistency index, and n is the flow index. When the yield stress is non-zero ($\tau_0 > 0$), and the shear stress is less than the yield stress ($\tau_m < \tau_0$), the unyielded (or plug) zone is formed where the fluid behaves like a solid. Since the shear stress is linear across the aperture and equals zero at the centerline, a plug zone is formed in the middle of the crack channel, and its width $2y_\tau(r,t)$ is an unknown function of position and time (Figure 5-1). The Herschel-Bulkley rheological model has three limiting cases: (i) Newtonian fluid when $\tau_0 = 0$ and $n = 1$ (M corresponds to the dynamic viscosity), (ii) power-law fluid when the yield stress is zero $\tau_0 = 0$, and, finally, (iii) it reduces to Bingham model when $\tau_0 \neq 0$ and $n = 1$.

We simulate the fluid exchange process between the crack channel and ambient permeable rock by Carter's leak-off law. Since the hydraulic fracturing fluid has Herschel-Bulkley rheology, the leak-off process can be more complex than that described by Carter's model. However, Carter's law can be acceptable assuming that the filter cake forms along the surface of the fracture and restrains all heavy polymer molecules contained in the fracturing fluid. As a result, the fracturing fluid filtrate with properties close to that of water (viscosity μ and total compressibility c_t) is leaked into the formation. When there is no filter-cake, and the leaked fluid properties are identical to the pore fluid characteristics, the Carter's coefficient is calculated from [Collins, 1976]: $C_L = k(\sigma_o - p_o)/(\mu\sqrt{\pi c})$, where p_o is the far-field pore pressure, and $c = k/(\phi_r c_t \mu)$ is the diffusivity coefficient. This expression provides an upper bound value for the case realised in the current model.

The problem solution, namely, radius $R(t)$, opening $w(r,t)$ and net fluid pressure $p(r,t)$ profiles, depends on time t, distance from the point source r, injection rate Q_0, yield stress τ_0, and the set of material parameters:

$$E' = \frac{E}{1-\nu^2}, \quad K' = 4\sqrt{\frac{2}{\pi}}K_{Ic}, \quad M' = \frac{2^{n+1}(2n+1)^n}{n^n}M, \quad C' = 2C_L, \tag{5.2}$$

157

where the viscosity parameter M' accounts for the non-linearity of the shear stress (5.1).

Let us consider the momentum conservation equation. By looking at the problem of a Herschel-Bulkley fluid flow under a constant pressure gradient inside a constant width channel, one can derive the velocity profile from the combination of the momentum conservation equation and the constitutive relation (5.1). Averaging the latter across the channel [Bessmertnykh and Dontsov, 2019], the following equation for the fluid flow velocity is obtained:

$$v = -\frac{w^{1+1/n}}{M'^{1/n}}\frac{\partial p}{\partial r}\left|\frac{\partial p}{\partial r}\right|^{1/n-1}\left(1-\frac{2y_\tau}{w}\right)^{1+1/n}\left(1+\frac{n}{n+1}\frac{2y_\tau}{w}\right), \qquad y_\tau = \tau_0\left|\frac{\partial p}{\partial r}\right|^{-1},$$
$$(5.3)$$

where y_τ is the half-size of the plug zone. One can notice that at the fluid source and at the tip $y_\tau(0,t) = y_\tau(R(t),t) = 0$ since the pressure gradient is singular there. Therefore, the spatial profile $y_\tau(r,t)$ always has an intermediate maximum value as shown schematically in Figure 5-1.

Equation (5.3) reduces to Poiseuille's law for Newtonian fluid case when $\tau_0 = 0$ and $n = 1$:

$$v = -\frac{w^2}{M'}\frac{\partial p}{\partial r}.$$

and to the power-law fluid case when $\tau_0 = 0$ [Economides et al., 1989]:

$$v = -\frac{w^{1+\frac{1}{n}}}{M'^{1/n}}\frac{\partial p}{\partial r}\left|\frac{\partial p}{\partial r}\right|^{\frac{1}{n}-1}.$$

The Reynolds equation is obtained by substitution of the fluid velocity (5.3) into the continuity equation (2.13) combined with Carter's leak-off law (2.14).

5.3 Solution methodology

This section outlines methods used to compute numerical solution of the posed problem. We utilise two different approaches. The first one is a direct numerical approach that allows us to evaluate the crack parameters accurately, and it is based on Gauss-Chebyshev quadrature and Barycentric Lagrange interpolation techniques.

It was first proposed for solving hydraulic fracture propagation problems by Viesca and Garagash [2018]. Liu et al. [2019] expanded this methodology for modelling the propagation of finite fractures (radial and KGD), and here, we use their approach and adjust it to capture Herschel–Bulkley rheology and leak-off. Interestingly, due to fine resolution near the tip, the calculation procedure does not require explicit implementation of the full tip asymptotic solution, which differentiates the method from the commonly used approach in which the near tip model is used as a propagation criterion, e.g., [Peirce and Detournay, 2008, Peirce, 2015, Dontsov, 2016a, Dontsov and Peirce, 2017c, Zia and Lecampion, 2020]. The second approach helps us to construct a simplified approximate solution based on the full-crack continuation of the near-tip region asymptote and the global fluid balance equation (see [Dontsov, 2016a] for radial crack and [Dontsov, 2017] for KGD crack). The simplified approach is computationally efficient and allows us to rapidly calculate the problem solution for any values of the input parameters. In addition, using the approximate method, we can simulate the fracture propagation corresponding to large leak-off and/or large yield stress values. In contrast, the fully numerical method has difficulties to converge for such cases. Overall, the rapid approximate solution is more beneficial to perform estimations for the whole problem parametric space, which is one of the primary goals of this study.

Before moving to the description of algorithms, we introduce the normalised distance to the source: $\rho = r/R(t)$. It depends on time, which results in the following transformation of the derivatives:

$$\left.\frac{\partial}{\partial t}\right|_r = \left.\frac{\partial}{\partial t}\right|_\rho - \frac{\rho V(t)}{R(t)} \left.\frac{\partial}{\partial \rho}\right|_t, \qquad \left.\frac{\partial}{\partial r}\right|_t = \frac{1}{R(t)} \left.\frac{\partial}{\partial \rho}\right|_t, \qquad (5.4)$$

where $V = dR/dt = \dot{R}$ is the crack tip velocity. Further, we re-write the elasticity (2.11), Reynolds (2.13), (2.14), (5.3), and the global fluid balance (2.20) equations, as well as the propagation condition (2.17) in terms of ρ:

- *Elasticity:*

$$p(\rho, t) = -\frac{E'}{2\pi R(t)} \int_0^1 G(\rho, s) \frac{\partial w(s,t)}{\partial s} ds. \qquad (5.5)$$

For implementation of the numerical solution, we utilise the elasticity equation with an extended interval:

$$p(\rho, t) = -\frac{E'}{4\pi R(t)} \int_{-1}^{1} G_e(\rho, s) \frac{\partial w(s,t)}{\partial s} ds, \quad \rho \in [-1,1], \qquad (5.6)$$

where the opening profile $w(\rho, t)$ continues symmetrically to negative ρ, and the integral kernel has the following form Liu et al. [2019]:

$$G_e(\rho, s) = \begin{cases} \text{sign}(\rho s) \left[\frac{1}{\rho} \text{K}\left(\frac{s^2}{\rho^2}\right) + \frac{1}{s-\rho} \text{E}\left(\frac{s^2}{\rho^2}\right) \right], & |\rho| > |s|, \\ \frac{1}{s-\rho} \text{E}\left(\frac{\rho^2}{s^2}\right), & |\rho| < |s|. \end{cases} \qquad (5.7)$$

It can be shown that this formulation of the elasticity equation is identical to (2.11).

- *Reynolds:*

$$\frac{\partial w}{\partial t} - \frac{V}{R}\rho\frac{\partial w}{\partial \rho} + \frac{1}{R\rho}\frac{\partial(\rho wv)}{\partial \rho} + \frac{C'}{\sqrt{t - t_0(\rho R)}} = 0, \qquad (5.8)$$

where the fluid velocity:

$$v = -\frac{w^{1+1/n}}{M'^{1/n}R^{1/n}}\frac{\partial p}{\partial \rho}\left|\frac{\partial p}{\partial \rho}\right|^{1/n-1}\left(1 - \frac{2y_\tau}{w}\right)^{1+1/n}\left(1 + \frac{n}{n+1}\frac{2y_\tau}{w}\right), \quad y_\tau = \tau_0 R\left|\frac{\partial p}{\partial \rho}\right|^{-1}. \qquad (5.9)$$

- *Global fluid balance:*

$$\frac{Q_0 t}{\pi R^2} = 2\int_0^1 \rho w d\rho + 4C'\int_0^1 \rho\sqrt{t - t_0(\rho R)}d\rho. \qquad (5.10)$$

- *Propagation condition:*

$$w = \frac{K'\sqrt{R}}{E'}\sqrt{1 - \rho}, \quad \rho \to 1. \qquad (5.11)$$

5.3.1 Numerical solution

By following the approach of Liu et al. [2019], we present gradient of the fracture opening profile in the form:

$$\frac{\partial w}{\partial \rho} = \mathcal{W}(\rho) F(\rho, t), \quad \mathcal{W}(\rho) = \frac{1}{\sqrt{1 - \rho^2}}, \quad \rho \in [-1, 1],$$

where $F(\rho, t)$ is the required unknown function, and the weight function $\mathcal{W}(\rho)$ includes the tip behaviour of $\partial w/\partial \rho$, i.e. $\partial w/\partial \rho \sim 1/\sqrt{1 - |\rho|}$, $\rho \to \pm 1$. The function $F(\rho, t)$ is odd, which ensures that the fracture opening profile $w(\rho, t)$ is symmetric. Further, we perform discretisation of the computational domain $\rho \in [-1, 1]$ by introducing two systems of nodes corresponding to the chosen weight function [Viesca and Garagash, 2018]: primary $\mathbf{s} = \{s_j\}_{j=1}^{N_p} = \{\cos[\pi(j - 1/2)/N_p]\}_{j=1}^{N_p}$ and complementary $\mathbf{z} = \{z_i\}_{i=1}^{N_c} = \{\cos(\pi i/N_p)\}_{i=1}^{N_c}$, $N_c = N_p - 1$. The bold symbols designate vectors, and N_p and N_c are the number of primary and complementary nodes, respectively. The primary and complementary nodes are the roots of Chebyshev polynomials of the first $\phi_{N_p}(\rho) = \cos(N_p\theta)$ and the second $\psi_{N_c}(\rho) = \sin[(N_c + 1)\theta]/\sin(\theta)$ kind, where $\theta = \arccos\rho$. Values of the function $F(\rho, t)$ are defined at the primary nodes: $\mathbf{F} = \{F(s_j, t)\}_{j=1}^{N_p}$, while the crack aperture $w(\rho, t)$ and the net pressure $p(\rho, t)$ are defined at the complementary nodes: $\mathbf{w} = \{w(z_i, t)\}_{i=1}^{N_c}$, $\mathbf{p} = \{p(z_i, t)\}_{i=1}^{N_c}$.

Now, we move on to the discretisation of the governing equations. For brevity, the matrix notation is utilised. Using the derivations of Liu et al. [2019], we write out the discretised form of the elasticity equation (5.6):

$$\mathbf{p} = \frac{E'}{4R}\mathbb{G} \times \mathbf{F}, \quad \mathbb{G} = \mathbb{H} + \frac{1}{2\mathbf{z}}\mathbb{T} \times \mathbb{H} + \Delta\mathbb{G}, \tag{5.12}$$

where "$\times$" denotes matrix multiplication; $\mathbb{G}$ is the elasticity quadrature matrix, and its representation composed of the following matrices:

- $\mathbb{H} = \left\{\frac{1}{N_p}\frac{1}{z_i - s_j}\right\}$;

- $\mathbb{T} = \{T_{ii'}\} = \left\{\sum_{k=0}^{N_c-1}[\Psi_k(z_i) - \Psi_k(0)]B_{ki'}\right\}$, $\Psi_k(z) = \cos[(k + 1)\theta]/(k + 1)$, $\theta = \arccos z$,

161

$$B_{ki'} = 2/N_p \cdot \sin\left(\pi i'/N_p\right) \sin\left(\pi i'(k+1)/N_p\right)$$

(in this section, symbol k is a summation index, not formation permeability);

- $\Delta\mathbb{G} = \left\{ \frac{1}{N_p} \Delta G(z_i, s_j) \right\}$, $\Delta G(z, s) = G_e(z, s) - \frac{1}{z-s} - \frac{\ln|z-s|}{2z}$.

Let us now focus on the discretisation of Reynolds equation (5.8), (5.9). Similarly to Liu et al. [2019], we integrate equation (5.8) with respect to ρ from each node z_i to the tip, i.e. $\rho = 1$. As a result, we obtain the following discretised form:

$$-\frac{\mathbf{z}^2}{2}\frac{\partial\mathbf{w}}{\partial t} + \frac{1}{2}\frac{\partial}{\partial t}\left[\mathbb{S} \times (\mathbf{s}^2\mathbf{F})\right] + \frac{V}{R}(\mathbb{S} \times (\mathbf{s}^2\mathbf{F})) - \frac{\mathbf{z}\mathbf{w}\mathbf{v}}{R} + C'\mathbb{R} \times \frac{\mathbf{z}}{\sqrt{t - t_0(\mathbf{z}R)}} = 0,$$

$$\mathbf{w} = \mathbb{S} \times \mathbf{F},$$

$$\mathbf{v} = -\frac{\mathbf{w}^{1+1/n}}{M'^{1/n}R^{1/n}}\mathbf{p}_\rho \left|\mathbf{p}_\rho\right|^{1/n-1}\left(1 - \frac{2\mathbf{y}_\tau}{\mathbf{w}}\right)^{1+1/n}\left(1 + \frac{n}{n+1}\frac{2\mathbf{y}_\tau}{\mathbf{w}}\right),$$

$$\mathbf{y}_\tau = \frac{\tau_0 R}{|\mathbf{p}_\rho|}, \qquad \mathbf{p}_\rho = \frac{E'}{4R}\mathbb{D} \times (\mathbb{G} \times \mathbf{F}), \tag{5.13}$$

where vector $|\mathbf{p}_\rho|$ contains the absolute values of the pressure gradient at the complementary nodes, and the following matrices are introduced [Liu et al., 2019]:

- $\mathbb{S} = \{S_{ij}\} = \left\{ \sum_{k=0}^{N_c} \left[\Phi_k(z_i) - \Phi_k(1)\right] B_{kj} \right\}$, where $\Phi_k(z) = -\sin(k\theta)/k$, $\theta = \arccos z$ and

  $B_{kj} = 1/N_p$ for $k = 0$ and $2/N_p \cdot \cos\left[\pi k(j - 1/2)/N_p\right]$ for $k > 0$;

- $\mathbb{R} = \{R_{ii'}\} = \left\{ \sum_{k=0}^{N_c-1} \left[\Psi_k(1) - \Psi_k(z_i)\right] B_{ki'} \right\}$;

- $\mathbb{D} = \{D_{ii'}\} = \left\{ \frac{\omega_{i'}/\omega_i}{z_i - z_{i'}} \text{ for } i \neq i'; \quad -\sum_{i'=1, i' \neq i}^m D_{ii'} \text{ for } i = i' \right\}$, where $\omega_i = (-1)^i \sin^2(\pi i/N_p)$.

To account for the boundary condition at the source, we should embed the global fluid balance into the discretised system. For that purpose, equation (5.10) is differentiated with respect to time:

$$\frac{Q_0}{\pi}\left(\frac{1}{R^2} - \frac{2tV}{R^3}\right) = -\mathbb{S}_H \times (\mathbf{s}^2\dot{\mathbf{F}}) + 2C'\mathbb{R}_H \times \frac{\mathbf{z}}{\sqrt{t - t_0(\mathbf{z}R)}} - \frac{2C'V}{R^3}\int_0^t \frac{R^2(s)ds}{\sqrt{t - s}}, \tag{5.14}$$

where the matrices $\mathbb{S}_H$ and $\mathbb{R}_H$ are:

- $\mathbb{S}_H = \left\{ \sum_{k=0}^{N_c} \left[\Phi_k(1) - \Phi_k(0)\right] B_{kj} \right\}$;

- $\mathbb{R}_H = \left\{ \sum_{k=0}^{N_c-1} \left[\Psi_k(1) - \Psi_k(0) \right] B_{ki'} \right\}.$

In equation (5.14), the last term on the right-hand-side, i.e., the integral with respect to time, is computed using Simpson's rule.

Finally, we write out the propagation condition in the matrix form (see details in [Liu et al., 2019]) and differentiate it with respect to time:

$$\mathbf{Q} \times \dot{\mathbf{F}} = -\frac{K'V}{2\sqrt{2RE'}}, \tag{5.15}$$

where $\mathbf{Q} = \{Q_j\}_{j=1}^{N_p} = \left\{ (-1)^{j+1} \frac{\cot{(\theta_j/2)}}{N_p} \right\}_{j=1}^{N_p}$, where $\theta_j = \arccos s_j = \pi(j - 1/2)/N_p$.

Here, we should make a comment regarding the application of the propagation condition (5.15). The LEFM asymptote (5.11) is always valid near the fracture tip. In certain situations, e.g., vanishingly small toughness, its spatial applicability domain can be tiny. Even when the vanishing LEFM region can not be accurately resolved by the method, Chebyshev's nodes high density near the tip accurately captures the dominant asymptotic behaviour.

Further, we combine equations (5.13), (5.14), (5.15) into a system of ordinary differential equations (ODEs) which can be written as:

$$\mathbb{A}(\mathbf{X}, t) \frac{d\mathbf{X}}{dt} = \mathbf{B}(\mathbf{X}, t), \quad \mathbf{X} = \{R, \mathbf{F}\}, \tag{5.16}$$

where the vector $\mathbf{X}$ consists of the unknown parameters, and we use the fact that $V = \dot{R}$.

The value of N_p should be odd since the opposite choice leads to the presence of the infinite components in the elasticity matrix $\mathbb{G}$ (5.12) (see $\mathbf{z}$ in the denominator). The function $F(\rho, t)$ is odd, and the the vector $\mathbf{F}$ has in the following form [Liu et al., 2019]: $\mathbf{F} = \{F_1, \dots F_{(N_p-1)/2}, 0, -F_{(N_p-1)/2}, \dots, -F_1\}$. The total number of the independent unknown parameters is $(N_p - 1)/2 + 1$, i.e., radius and independent components of the vector $\mathbf{F}$, meaning that the system of ODEs should be composed of the first $(N_p - 1)/2 - 1$ discretised Reynolds equations (5.13), i.e., corresponding to the complementary nodes $z_1, \dots, z_{(N_p-1)/2-1}$, the global fluid balance equation (5.14), and the propagation condition (5.15). We choose $N_p = 101$, and the storage-

viscosity dominated regime (M-vertex) for the power-law fluid is taken as an initial condition for all considered values of the flow index (the fracture properties in this regime are provided by Section 5.4.1). Despite the fact that for $n < 0.5$ the early time solution corresponds to the storage-toughness regime (K-vertex, see details in Section 5.4.1), the algorithm works fine with the selected initial condition, even though requiring a certain time-span to adjust the solution to the actual trajectory. The specified time interval is discretised uniformly on a logarithmic mesh, and the solver is applied within each time segment. Python programming language is used for implementation of the numerical algorithm, and the system of resulting ODEs is solved via "`solve_ivp`" function of SciPy library [Virtanen et al., 2020].

5.3.2   Rapid approximate solution

This section outlines a rapid approximate solution for the problem. This approach is based on the idea that the near-tip region behaviour predominantly determines the finite fracture characteristics. As a result, the crack opening profile is presented in the following form [Dontsov, 2016a]:

$$w(\rho, t) = \left(\frac{1 + \rho}{2}\right)^{\lambda} (1 - \rho)^{\bar{\delta}} w_a(R), \qquad (5.17)$$

where $w_a(s)$ is the opening asymptote near the fracture tip stemming from the solution for the semi-infinite geometry, and it is a function of the distance from the front s, material parameters (5.2), yield stress τ_0 and time t (through $R(t)$ and $\dot{R}(t)$). In equation (5.17), we also utilise parameters λ and $\bar{\delta}$: the first one originates from comparisons with the accurate solution for limiting cases (that will be defined later), and the second one is a slowly varying parameter from the tip asymptotic solution, i.e. $w_a(s) \propto s^{\bar{\delta}}$. Since the fracture radius is a power-law function of time in the known limiting propagation regimes (e.g. review paper [Detournay, 2016]), we assume that $R(t) \propto t^{\alpha}$, where α is a slowly varying function of time. Consequently, the inverse radius function is expressed in the form: $t_0(\rho R) = t\rho^{1/\alpha}$. By substituting the opening profile (5.17) and $t_0(\rho R)$ into the global fluid balance equation (5.10),

we obtain:

$$\frac{Q_0 t}{2\pi R^2} = w_a(R) \int_0^1 \rho \left(\frac{1+\rho}{2}\right)^\lambda (1-\rho)^{\bar{\delta}} d\rho + 2C'\sqrt{t} \int_0^1 \rho\sqrt{1-\rho^{1/\alpha}} d\rho. \quad (5.18)$$

The integrals in the above equation can be estimated using special functions, and the result becomes:

$$\frac{Q_0 t}{2\pi R^2} = w_a(R)\mathcal{B}(\lambda, \bar{\delta}) + 2C'\sqrt{t}\alpha B\left(2\alpha, \frac{3}{2}\right),$$

$$\mathcal{B}(\lambda, \bar{\delta}) = 2^{1+\bar{\delta}}\left[B_0\left(\frac{1}{2}; \lambda+2, \bar{\delta}+1\right) - B_0\left(1/2; \lambda+1, \bar{\delta}+2\right)\right], \quad (5.19)$$

where $B_0(x; a, b) = B(a, b) - B(x; a, b)$, $B(a, b)$ is the beta function, and $B(x; a, b)$ is the incomplete beta function.

As can be seen from the above result, one of the building blocks in the approximate solution is the tip asymptote $w_a(R)$. We utilise an approximate near-tip region solution developed in Bessmertnykh and Dontsov [2019], which is computed using a combination of the yield stress dominated tip solution (w_τ) and the one corresponding to the power-law fluid (w_{pl}):

$$w_a(R) = \left(w_{\text{pl}}^\zeta(R) + w_\tau^\zeta(R)\right)^{1/\zeta}, \quad w_\tau(R) = \sqrt{\frac{8\pi\tau_0}{E'}}R, \quad \zeta = -0.3107n + 1.9924,$$

$$\sqrt{\frac{R}{\ell}} = \mathcal{H}\left(\frac{w_{\text{pl}}E'}{K'\sqrt{R}}, \frac{2C'E'}{\sqrt{V}K'}\right), \quad \ell = \left(\frac{K'^{n+2}}{M'V^n E'^{n+1}}\right)^{2/(2-n)}, \quad V = \dot{R} = \frac{\alpha R}{t},$$

$$(5.20)$$

where the function $\mathcal{H}(\widetilde{w}, \chi)$ is defined as follows [Dontsov and Kresse, 2018]:

$$\mathcal{H}(\widetilde{w}, \chi) = \left(\delta_1(\widetilde{w}, \chi)\widetilde{w}^{(2+n)/(1+\theta)} \left\{ \delta_m^{1+\theta}\beta_m^{2+n} + \delta_{\widetilde{m}}^{1+\theta}\beta_{\widetilde{m}}^{2+2n} \left[\left(1 + \frac{\chi}{\widetilde{w}}\right)^n - 1 \right] \right\}^{-1/(1+\theta)} \right)^{(1+\theta)/(2-n)};$$

$$\delta_1(\widetilde{w}, \chi) = \frac{\delta_m \delta_{\widetilde{m}} V_m V_{\widetilde{m}} \left[\beta_m^{(2+n)/n} V_{\widetilde{m}}^{(1+\theta)/n} + \frac{\chi}{\widetilde{w}}\beta_{\widetilde{m}}^{(2+2n)/n} V_m^{(1+\theta)/n} \right]}{\delta_{\widetilde{m}} V_{\widetilde{m}} \beta_m^{(2+n)/n} V_{\widetilde{m}}^{(1+\theta)/n} + \delta_m V_m \frac{\chi}{\widetilde{w}}\beta_{\widetilde{m}}^{(2+2n)/n} V_m^{(1+\theta)/n}};$$

$$V_m = 1 - \widetilde{w}^{-(2+n)/(1+\theta)}, \qquad V_{\widetilde{m}} = 1 - \widetilde{w}^{-(2+2n)/(1+\theta)};$$

$$\beta_m = \left[\frac{2(2+n)^2}{n} \tan\left(\frac{\pi n}{2+n}\right) \right]^{1/(2+n)}, \qquad \beta_{\widetilde{m}} = \left[\frac{64(1+n)^2}{3n(4+n)} \tan\left(\frac{3\pi n}{4+4n}\right) \right]^{1/(2+2n)};$$

$$\delta_m = \frac{2-n}{2+n}, \qquad \delta_{\widetilde{m}} = \frac{2-n}{2+2n};$$

$$\theta = 0.0452n^2 - 0.1780n + 0.1753. \tag{5.21}$$

The parameter $\bar{\delta}$ in the global fluid balance equation (5.19) can be computed from the following relation:

$$\bar{\delta} = \frac{\delta + 1}{2}, \qquad \delta = \frac{w_{\mathrm{pl}}^\zeta \delta_1 + w_\tau^\zeta}{w_{\mathrm{pl}}^\zeta + w_\tau^\zeta},$$

where the function δ_1 is defined in the equation (5.21), and it enters approximation for the power-law solution: $w_{\mathrm{pl}}(s) \propto s^{(\delta_1+1)/2}$, where s is the distance from the tip.

Further, we solve the non-linear algebraic system of equations composed of the global fluid balance (5.19) and the tip asymptote (5.20). Let us discuss the overall approach in more details. Initially, the desired time interval is discretised uniformly on a logarithmic scale, and the target parameters $\mathcal{X} = \{\alpha, R, w_a\}$ are computed iteratively step-by-step for each time instant. Let us consider the example of time step t_i. From the previous result at t_{i-1}, we know the values of $\mathcal{X}_{i-1} = \{\alpha_{i-1}, R_{i-1}, (w_a)_{i-1}\}$, and they are used as an initial guess for the current computation. We calculate the solution for two time instants: t_i and t_i^*, where the latter is a fraction of the current time moment, e.g., it can be $t_i^* = 0.9 \cdot t_i$. Further, the value of α_i initially taken as α_{i-1} is updated by using the equation: $\alpha_i = d\log(R)/d\log(t) = [\log(R_i) - \log(R_i^*)] / [\log(t_i) - \log(t_i^*)]$. After that, the system is solved again with the new initial guess presented by the parameters from this iteration. The process continues until the convergence in the value of α_i is reached. It is also necessary to mention that for the first time step $(i = 1)$, we

take the initial guess $\alpha_0 = (2n + 2)/(3n + 6)$, R_0 and $(w_a)_0$ corresponding to the storage-viscosity dominated limiting propagation regime (Section 5.4.1).

Once the solution $\mathcal{X}$ is computed, the fracture opening profile $w(\rho, t)$ is evaluated using equation (5.17), while the pressure $p(\rho, t)$ profile is calculated based on the transformed elasticity (5.5) equation [Dontsov, 2016a]:

$$p = \frac{E' w_a(R)}{R} \mathcal{F}(\rho, \lambda, \bar{\delta}), \quad \mathcal{F}(\rho, \lambda, \bar{\delta}) = \frac{1}{2^{\lambda+1} \pi} \int_0^1 \frac{\partial G(\rho, s)}{\partial s} (1+s)^\lambda (1-s)^{\bar{\delta}} ds, \quad (5.22)$$

where the function $\mathcal{F}$ is evaluated numerically. Finally, we also compute the fracture efficiency as:

$$\eta = \frac{2\pi R^2 w_a(R) \mathcal{B}}{Q_0 t}, \quad (5.23)$$

where the function $\mathcal{B}$ is introduced in equation (5.19).

The exact functional form of the function λ is given in Appendix A.4. We have built it following the two steps: (i) we estimated the values of λ for the specific cases called limiting propagation regimes by fitting the result to the fully-numerical solution (see all details in Section 5.4.1) (these computations are performed once); (ii) we created an interpolation function that allows us to compute λ for any values of the input parameters, i.e., for both limiting cases and in between them.

5.4 Conceptual representation of the solution

5.4.1 Limiting propagation regimes

Two different physical mechanisms govern the propagation regime of a finite hydraulic fracture (see review paper by Detournay [2016] and references therein). The first one is related to the distribution of the total dissipated energy between the creation of new fracture surface and viscous fluid flow including the movement of the solid plug inside the fracture channel. The latter energy component, namely movement of the solid plug, is included since the fracturing fluid has non-zero yield stress. In this case, the whole fracture can be filled with the un-yielded solid material. The second mechanism is the partitioning of the injected fluid volume between

the fracture and the host permeable rock (due to leak-off). When the fracture grows, the partitioning of the dissipated energy and the injected volume change over time, leading to the emergence of the various limiting propagation regimes with one dissipation (out of two) and one storage (out of two) mechanisms at different time moments. The leak-off parameter C' influences distribution of the injected fluid volume, while the viscosity M', toughness K', and the yield stress τ_0 have an effect on the partitioning of the dissipated energy.

Six limiting regimes (also known as the vertex solutions or vertices) can be distinguished in the current radial fracture model. Four of them correspond to the propagation of a penny-shaped crack filled by a fluid with the power-law rheology ($\tau_0 = 0$):

- **M** – storage-viscosity – $K' = C' = \tau_0 = 0$;

- **M̃** – leak-off-viscosity – $K' = \tau_0 = 0$, $C' \to +\infty$;

- **K** – storage-toughness – $M' = C' = \tau_0 = 0$;

- **K̃** – leak-off-toughness – $M' = \tau_0 = 0$, $C' \to +\infty$.

The remaining two regimes correspond to the dominance of the yield stress:

- **T** – storage-yield-stress – $K' = C' = M' = 0$, $\tau_0 > 0$;

- **T̃** – leak-off-yield-stress – $K' = M' = 0$, $\tau_0 > 0$, $C' \to +\infty$.

Let us now consider scalings associated with the limiting propagation regimes. First of all, we present the main crack characteristics as:

$$w(r,t) = \epsilon(t)L(t)\Omega(\rho, \mathcal{P}), \quad p(r,t) = \epsilon(t)E'\Pi(\rho, \mathcal{P}), \quad R(t) = L(t)\gamma(\mathcal{P}), \quad (5.24)$$

where we utilise the notations for the dimensionless coordinate $\rho = r/R(t)$, radius γ, opening Ω, and pressure Π; $\mathcal{P} = \{\mathcal{P}_1, \mathcal{P}_2, \mathcal{P}_3\}$ are dimensionless evolution parameters depending on t, material parameters (5.2), Q_0 and τ_0; $L(t)$ is a length scale and $\epsilon(t)$ is a small dimensionless parameter with the meaning of a characteristic strain in the rock. The explicit expressions for $L(t)$, $\epsilon(t)$, and $\mathcal{P}$ are derived below for each

of the considered scalings. We apply the representation of fracture radius in the form (5.24) because for each scaling, $\gamma(\mathcal{P}) \sim O(1)$ in the limiting regime governed the given scaling, i.e., $R(t)$ is of same order as the lengthscale $L(t)$ for the selected scaling; however, it is important to note that $\gamma(\mathcal{P})$ can take both large and small values outside the limiting regime.

Further, we substitute the expressions from equation (5.24) into the system of governing equations written in terms of the normalised distance from the source ρ, i.e. the elasticity (5.5), Reynolds (5.8), (5.9), global fluid balance (5.10) equations and the propagation condition (5.11):

- *Elasticity:*

$$\Pi = -\frac{1}{2\pi\gamma} \int_0^1 G(\rho, s) \frac{\partial \Omega}{\partial s} ds;$$

- *Reynolds:*

$$\mathcal{G}_v \left(\left[\frac{\dot{\epsilon} t}{\epsilon} + \frac{\dot{L} t}{L} \right] \Omega + \dot{\Omega} t - \rho \left(\frac{\dot{L} t}{L} + \frac{\dot{\gamma} t}{\gamma} \right) \frac{\partial \Omega}{\partial \rho} \right) + \frac{\mathcal{G}_c}{\sqrt{1 - \theta_0}} =$$

$$= \frac{1}{\mathcal{G}_m} \frac{1}{\gamma\rho} \frac{\partial}{\partial \rho} \left[\frac{\rho}{\gamma^{1/n}} \Omega^{2+1/n} \frac{\partial \Pi}{\partial \rho} \left| \frac{\partial \Pi}{\partial \rho} \right|^{1/n-1} \left(1 - \mathcal{G}_t \frac{2\gamma}{\Omega} \left| \frac{\partial \Pi}{\partial \rho} \right|^{-1} \right)^{1+1/n} \times \right.$$

$$\left. \times \left(1 + \mathcal{G}_t \frac{2\gamma}{\Omega} \left| \frac{\partial \Pi}{\partial \rho} \right|^{-1} \frac{n}{n+1} \right) \right];$$

- *Global fluid balance:*

$$\frac{1}{\pi\gamma^2} = 2\mathcal{G}_v \int_0^1 \Omega\rho d\rho + 4\mathcal{G}_c \int_0^1 \sqrt{1 - \theta_0} \rho d\rho;$$

- *Propagation condition:*

$$\Omega = \mathcal{G}_k \sqrt{\gamma} \sqrt{1 - \rho}, \quad \rho \to 1.$$

Here, we utilise the function $\theta_0(\rho, t) = t_0(r)/t$ and introduce five dimensionless

numbers:

$$\mathcal{G}_v = \frac{\epsilon L^3}{Q_0 t}, \quad \mathcal{G}_c = \frac{C' L^2}{Q_0 \sqrt{t}}, \quad \mathcal{G}_m = \frac{Q_0 M'^{1/n}}{L^3 E'^{1/n} \epsilon^{2+2/n}}, \quad \mathcal{G}_t = \frac{\tau_0}{\epsilon^2 E'}, \quad \mathcal{G}_k = \frac{K'}{E' \epsilon \sqrt{L}}.$$
(5.25)

$\mathcal{G}_v$ and $\mathcal{G}_c$ parameters quantify the fluid volume stored in the fracture and the volume leaked into the ambient permeable rock, respectively. In turn, the numbers $(\mathcal{G}_m, \mathcal{G}_t)$ and $\mathcal{G}_k$ are related to the energy dissipation in the fluid flow inside the crack channel in overcoming fluid viscosity and solid plug yield strength and in the brittle rock failure, correspondingly.

To derive various scalings, i.e., $L(t)$ and $\epsilon(t)$ in (5.24), we set one out of two fluid storage parameters $(\mathcal{G}_v, \mathcal{G}_c)$ be equal to one. Similarly, among the three parameters responsible for energy dissipation $(\mathcal{G}_m, \mathcal{G}_t, \mathcal{G}_k)$, one should be made equal to one. The remaining three dimensionless groups are the evolution parameters $\mathcal{P}$ mentioned earlier. When the evolution parameters are approximately zero in a given scaling, the corresponding limiting propagation regime is realised. From the scaling analysis, we can determine only the dimensional multipliers for the radial crack characteristics, R, w, p, in a given 'i-th' scaling. In order to approximately quantify the opening and pressure profiles, we rely on the approximations of Section 5.3.2:

$$R_i(t) = R_i^* L_i, \quad w_i(\rho, t) = \underbrace{w_i^* \epsilon_i L_i}_{(w_a)_i(R)} \left(\frac{1+\rho}{2}\right)^{\lambda_i} (1-\rho)^{\bar{\delta}_i}, \quad p_i(\rho, t) = \frac{w_i^*}{R_i^*} E' \epsilon_i \mathcal{F}(\rho, \lambda_i, \bar{\delta}_i),$$
(5.26)

where the subscript i indicates the particular limiting regime, and the function $\mathcal{F}$ is defined in equation (5.22). In order to express the prefactors values R_i^*, w_i^* through λ_i, we substitute $R_i(t)$ and $(w_a)_i(R)$ into the global fluid balance equation (5.19) (accounting the conditions inherent to the analysed regime) and the appropriate near-tip region asymptote for the crack opening. Further, the parameter λ_i can be found with the help of the accurate numerical solution (Section 5.3.1).

Before discussing different scalings and limiting propagation regimes, we introduce the relative errors in the estimation of the radius, opening, and pressure characteristics provided by the simplified approach (5.26) compared to the fully numerical

170

solution:

$$\Delta(R_i) = \left| \bar{R}_i(t) - R_i(t) \right| / \bar{R}_i(t), \tag{5.27}$$

$$\Delta(w_i^0) = \left| \bar{w}_i(0,t) - w_i(0,t) \right| / \bar{w}_i(0,t), \tag{5.28}$$

$$\Delta(w_i^\rho) = \max_\rho \left[|\bar{w}_i(\rho,t) - w_i(\rho,t)| / \bar{w}_i(0,t) \right], \tag{5.29}$$

$$\Delta(p_i^0) = \left| \bar{p}_i(0.5,t) - p_i(0.5,t) \right| / \bar{p}_i(0.5,t), \tag{5.30}$$

where $\Delta(R_i)$ is the radius error, $\Delta(w_i^0)$ is the error of width at the inlet, $\Delta(w_i^\rho)$ is the maximum relative width error, and $\Delta(p_i^0)$ is the error of pressure at the half-radius. The subscript i denotes the considered limiting regime, and the bar symbol means the fully numerical solution.

We begin with the storage-viscosity scaling and the $M-$vertex solution (subscript "m"). We set $\mathcal{G}_v = \mathcal{G}_m = 1$ and obtain the following formulas for the length scale and the small parameter:

$$L_m = \left(\frac{E'Q_0^{n+2}t^{2n+2}}{M'} \right)^{1/(3n+6)}, \qquad \epsilon_m = \frac{Q_0 t}{L_m^3}. \tag{5.31}$$

Further, we substitute L_m and ϵ_m into the remaining dimensionless groups:

$$\mathcal{C}_m = C' \left(\frac{E'^4 t^{5n+2}}{M'^4 Q_0^{2n+4}} \right)^{1/(6n+12)}, \qquad \mathcal{T}_m = \tau_0 \left(\frac{t^{2n}}{M'^2 E'^n} \right)^{1/(n+2)},$$

$$\mathcal{K}_m = K' \left(\frac{t^{4n-2}}{M'^5 E'^{6n+7} Q_0^{n+2}} \right)^{1/(6n+12)}, \tag{5.32}$$

where we reassign $\mathcal{G}_c, \mathcal{G}_t, \mathcal{G}_k$ as the dimensionless leak-off $\mathcal{C}_m$, yield stress $\mathcal{T}_m$ and toughness $\mathcal{K}_m$. After that, we obtain formulas for the prefactors R_m^*, w_m^*:

$$R_m^* = \left(2\pi\beta_m \alpha_m^{n/(n+2)} \mathcal{B}_m \right)^{-1/3}, \qquad w_m^* = \left(\frac{\beta_m^2 \alpha_m^{2n/(n+2)}}{2\pi\mathcal{B}_m} \right)^{1/3}, \tag{5.33}$$

where $\alpha_m = (2n+2)/(3n+6)$, $\mathcal{B}_m = \mathcal{B}(\lambda_m, \bar{\delta}_m)$ (see equation (5.19)), the value of β_m is provided by equation (5.21), and $\bar{\delta}_m = 2/(2+n)$ is taken from the storage-viscosity tip asymptote [Dontsov and Kresse, 2018]. The parameter λ_m is obtained

by fitting the approximate solution above (5.26) and (5.33) to the full numerical solution (Section 5.3.1) in terms of R_m and $w_m(0,t)$. We computed λ_m for different values of flow indexes $n \in [0.25, 1]$, and the obtained curve is shown in Figure 5-2(a). The relative errors defined by equations (5.27)-(5.30) are depicted in Figure 5-2(b), where $\Delta(R_m)$ is shown by the solid line, $\Delta(w_m^0)$ is shown by the dashed line, $\Delta(w_m^\rho)$ is shown by the dash-dotted line, and $\Delta(p_m^0)$ is shown by the dotted line.
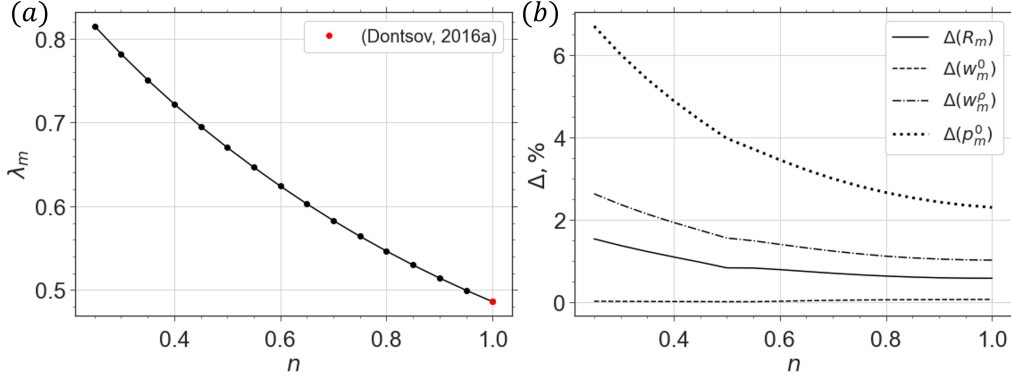
Figure 5-2: Figure (a) presents the dependence of λ_m on the flow index n. The red dot corresponds to the $\lambda_m(1)$ value obtained by Dontsov [2016a]. In Figure (b), we demonstrate the relative errors in the calculation of the radius, opening, and pressure parameters for the $M-$vertex with the help of the simplified approach (Section 5.3.2).

Figures 5-3(a) and 5-3(d) present comparison of the approximate normalised profiles of $w_m(\rho, t)$, $p_m(\rho, t)$ (dashed lines) with the corresponding properties evaluated by the fully numerical solution (solid lines) for $n = 1$ (light-blue colour) and $n = 0.3$ (blue colour). We use the normalisation of the width by $\epsilon_m(t)L_m(t)$, pressure by $\epsilon_m(t)E'$ as per (5.24) and of the radial distance from the source by $L_m(t)$ scale; these scales account for the M limiting solution dependence on time and largely on the flow behaviour index n. The characteristics for the Newtonian fluid are very close to each other, while the accurate and approximate profiles for $n = 0.3$ intersect for both opening and pressure; moreover, there is a noticeable difference for the pressure values near the fracture front.

Let us consider the case of the leak-off-viscosity scaling and the corresponding $\widetilde{M}-$vertex solution (subscript $\widetilde{m}$). This scaling corresponds to $\mathcal{G}_c = \mathcal{G}_m = 1$. Hence,

$$L_{\tilde{m}} = t^{1/4}\sqrt{\frac{Q_0}{C'}}, \qquad \epsilon_{\tilde{m}} = \left(\frac{C'^6 M'^{4/n}}{Q_0^2 t^3 E'^{4/n}}\right)^{\frac{n}{8n+8}}. \tag{5.34}$$
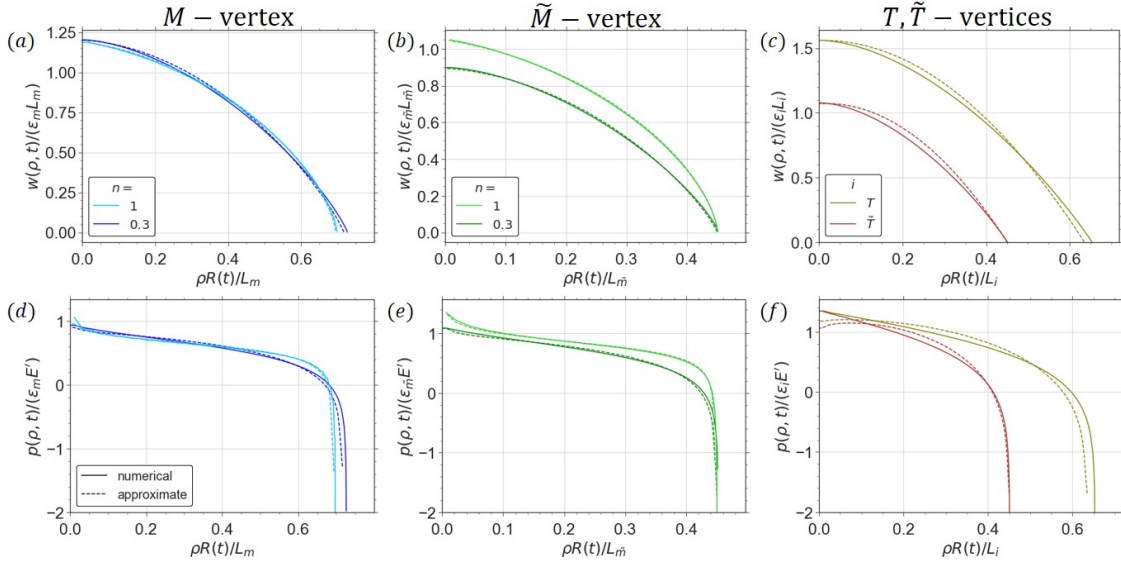
Figure 5-3: The spatial variations of the crack opening (upper line) and net fluid pressure (bottom line) in the limiting propagation regimes M (panels (a) and (d)), $\tilde{M}$ (panels (b) and (e)), T and $\tilde{T}$ (panels (c) and (f)) calculated by the fully numerical (solid lines) and approximate (dashed lines) approaches. We apply $\epsilon_i(t)L_i(t)$, $\epsilon_i(t)E'$ and $L_i(t)$ dimensional prefactors for the normalisation of $w(\rho,t)$, $p(\rho,t)$ profiles, and distance from the source, and here, the subscript i denotes the analysed regime. In the case of M and $\tilde{M}$ vertex solutions, we look at $n = 1$ or $n = 0.3$ and show the computed properties in plots (a), (d) and (b), (e) by the light-blue or light-green and blue or green colours, correspondingly. The normalisation coefficients take into account the value for the flow behaviour index. We use olive and maroon colours for the yield stress dominated regimes T and $\tilde{T}$ in the charts (c), (f).

The evolution parameters have the meaning of the dimensionless storage $\mathcal{S}_{\tilde{m}}$, yield stress $\mathcal{T}_{\tilde{m}}$ and toughness $\mathcal{K}_{\tilde{m}}$:

$$\mathcal{S}_{\tilde{m}} = \left(\frac{M'^4 Q_0^{2n+4}}{E'^4 t^{5n+2} C'^{6(n+2)}} \right)^{1/(8+8n)}, \qquad \mathcal{T}_{\tilde{m}} = \tau_0 \left(\frac{Q_0^2 t^3}{M'^{4/n} C'^6 E'^4} \right)^{n/(4+4n)},$$

$$\mathcal{K}_{\tilde{m}} = K' \left(\frac{C'^{2-4n} t^{2n-1}}{M'^4 Q_0^2 E'^{8n+4}} \right)^{1/(8+8n)}. \tag{5.35}$$

For the $\tilde{M}-$vertex, we derive the following prefactors $R_{\tilde{m}}^*, w_{\tilde{m}}^*$:

$$R_{\tilde{m}}^* = \frac{\sqrt{2}}{\pi}, \qquad w_{\tilde{m}}^* = \beta_{\tilde{m}} \left(\frac{\alpha_{\tilde{m}}^n 2^{2+3n}}{\pi^{4+2n}} \right)^{1/(4+4n)}, \tag{5.36}$$

where $\alpha_{\tilde{m}} = 1/4$, $\beta_{\tilde{m}}$ is given by equation (5.21), and we also utilise $\bar{\delta}_{\tilde{m}} = (4 + n)/(4 + 4n)$ known from the leak-off-viscosity near-tip region asymptote [Dontsov and Kresse, 2018]. The parameter $\lambda_{\tilde{m}}$ featured in the $w_{\tilde{m}}$ profile is found from the

comparison of $w_{\tilde{m}}(0,t)$ (equation (5.26) combined with (5.36)) with the numerical solution (Section 5.3.1). This approach yields to the values of $\lambda_{\tilde{m}}(n)$ presented in Figure 5-4(a). Moreover, we also estimate the relative errors of the fracture aperture $w_{\tilde{m}}(\rho,t)$ and pressure evaluated at the half-radius $p_{\tilde{m}}(0.5,t)$, provided by equations (5.17), (5.22), respectively, with $\lambda_{\tilde{m}}(n)$ (Figure 5-4(b)). We utilise equations (5.28), (5.29), (5.30) for computing $\Delta(w_{\tilde{m}}^0)$, $\Delta(w_{\tilde{m}}^\rho)$, $\Delta(p_{\tilde{m}}^0)$, correspondingly.
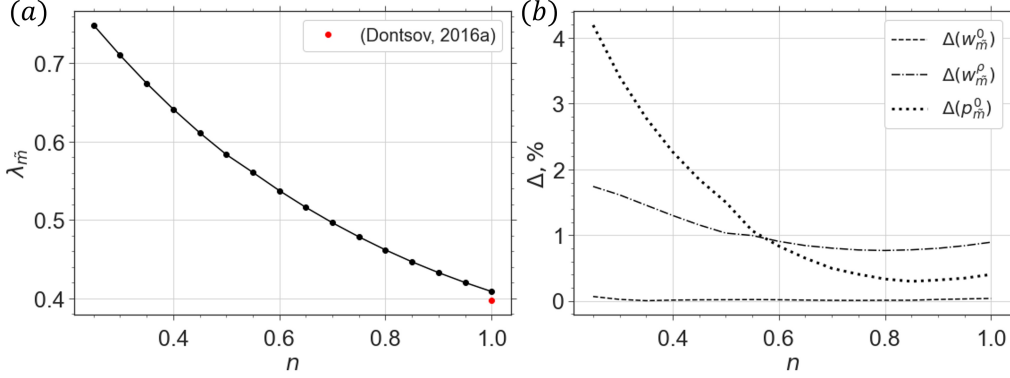
Figure 5-4: Figure (a) shows the values of the function $\lambda_{\tilde{m}}(n)$ computed numerically. Here, we mark $\lambda_{\tilde{m}}(1)$ obtained by Dontsov [2016a] by the red dot. Figure (b) presents the relative errors in the estimation of the opening profile and the pressure evaluated at the half-radius for the $\tilde{M}-$vertex via the simplified approach (Section 5.3.2).

In the panels (b), (e) of Figure 5-3, we demonstrate the spatial variations of the width and pressure calculated by the accurate solution (solid lines) and provided by the approximate approach (dashed lines), i.e., $w_{\tilde{m}}(\rho,t)$, $p_{\tilde{m}}(\rho,t)$, for two cases of the flow behaviour index $n = 1$ (light-green colour) and $n = 0.3$ (green colour). The dimensional prefactors $\epsilon_{\tilde{m}}(t)L_{\tilde{m}}(t)$, $\epsilon_{\tilde{m}}(t)E'$, $L_{\tilde{m}}(t)$ are applied for the normalisation of the aperture, pressure and distance from the source, and they include the value of the flow behaviour index. We can mention that for both analysed values of the flow index, the accurate and approximate opening and pressure profiles are very close to each other.

Next, we discuss the storage-toughness scaling that corresponds to the $K-$vertex solution (subscript "k"). Here, we require $\mathcal{G}_v = \mathcal{G}_k = 1$ leading to:

$$L_k = \left(\frac{E'Q_0 t}{K'}\right)^{2/5}, \quad \epsilon_k = \left(\frac{K'^6}{E'^6 Q_0 t}\right)^{1/5}, \tag{5.37}$$

and the evolution parameters can be interpreted as the dimensionless leak-off $\mathcal{C}_k$,

yield stress $\mathcal{T}_k$ and viscosity $\mathcal{M}_k$:

$$\mathcal{C}_k = C' \left(\frac{E'^8 t^3}{K'^8 Q_0^2} \right)^{1/10}, \quad \mathcal{T}_k = \tau_0 \left(\frac{E'^7 Q_0^2 t^2}{K'^{12}} \right)^{1/5}, \quad \mathcal{M}_k = \left(\frac{M'^5 E'^{6n+7} Q_0^{n+2} t^{2-4n}}{K'^{6(n+2)}} \right)^{1/(5n)}.$$

(5.38)

The LEFM asymptote governs the tip behaviour in the storage-toughness limiting propagation regime, i.e. $\bar{\delta}_k = 1/2$. Moreover, in this case, the crack opening profile is elliptical [Savitski and Detournay, 2002]. Consequently, the simplified form of the radius crack opening profile (5.17) allows describing it accurately by taking $\lambda_k = 1/2$. Using the global fluid balance equation (5.19) and the "square-root" asymptote [Irvin, 1957], we find out the following coefficient in the radius and opening profiles:

$$R_k^* = \left(\frac{3}{\sqrt{2\pi}} \right)^{2/5}, \quad w_k^* = \left(\frac{3}{\sqrt{2\pi}} \right)^{1/5}.$$

(5.39)

Next, we construct the leak-off-toughness scaling and focus on the $\tilde{K}-$vertex solution (subscript "$\tilde{k}$"). We put $\mathcal{G}_c = \mathcal{G}_k = 1$, and get the expressions for the length scale $L_{\tilde{k}}$ and the small parameter $\epsilon_{\tilde{k}}$:

$$L_{\tilde{k}} = t^{1/4} \sqrt{\frac{Q_0}{C'}}, \quad \epsilon_{\tilde{k}} = \left(\frac{C'^2 K'^8}{E'^8 Q_0^2 t} \right)^{1/8}.$$

(5.40)

The evolution parameters are identified as the dimensionless storage $\mathcal{S}_{\tilde{k}}$, yield stress $\mathcal{T}_{\tilde{k}}$ and viscosity $\mathcal{M}_{\tilde{k}}$:

$$\mathcal{S}_{\tilde{k}} = \frac{K' Q_0^{1/4}}{C'^{5/4} E' t^{3/8}}, \quad \mathcal{T}_{\tilde{k}} = \tau_0 \frac{E' Q_0^{1/2} t^{1/4}}{C'^{1/2} K'^2}, \quad \mathcal{M}_{\tilde{k}} = \left(\frac{M' Q_0^{1/2} E'^{1+2n} C'^{n-1/2} t^{1/4-n/2}}{K'^{2+2n}} \right)^{1/n}.$$

(5.41)

Similarly to the $K-$limiting propagation regime, the crack opening behaviour near the tip is described by the LEFM asymptote ($\bar{\delta}_{\tilde{k}} = 1/2$), while the whole profile is elliptical ($\lambda_{\tilde{k}} = 1/2$). The derivation of the prefactors for the radius and opening leads to:

$$R_{\tilde{k}}^* = \frac{\sqrt{2}}{\pi}, \quad w_{\tilde{k}}^* = \frac{2^{1/4}}{\sqrt{\pi}}.$$

(5.42)

We should highlight that the approximate solution reproduces all fracture properties (radius, opening, and pressure) precisely for both toughness dominated regimes K

and $\tilde{K}$.

Finally, next we reach the cases that correspond to dominance of yield stress. The storage-yield-stress scaling (subscript "t") corresponds to the case: $\mathcal{G}_t = \mathcal{G}_m = 1$, which results to:

$$L_t = \left(\frac{tE'^{1/2}Q_0}{\tau_0^{1/2}} \right)^{1/3}, \quad \epsilon_t = \sqrt{\frac{\tau_0}{E'}}. \tag{5.43}$$

In turn, the evolution parameters are the dimensionless leak-off, viscosity and toughness:

$$\mathcal{C}_t = C' \left(\frac{E'\sqrt{t}}{Q_0\tau_0} \right)^{1/3}, \quad \mathcal{M}_t = \frac{\sqrt{E'}M'^{1/n}}{t\tau_0^{(n+2)/(2n)}}, \quad \mathcal{K}_t = \frac{K'}{(E'^7 Q_0^2 t^2 \tau_0^5)^{1/12}}. \tag{5.44}$$

Further, we should determine the prefactors R_t^*, w_t^* from the global fluid balance (5.19) and the yield stress dominated near-tip region asymptote [Bessmertnykh and Dontsov, 2019]:

$$R_t^* = \frac{1}{2^{5/6}\sqrt{\pi}\mathcal{B}_t^{1/3}}, \quad w_t^* = \frac{2^{2/3}}{\mathcal{B}_t^{1/3}}, \tag{5.45}$$

where $\mathcal{B}_t = \mathcal{B}(\lambda_t, \bar{\delta}_t)$ and $\bar{\delta}_t = 1$. Using the radius and wellbore opening characteristics computed via the accurate numerical solution (Section 5.3.1), we find out that $\lambda_t = 1.029$ provides the most accurate approximation. This value together with equations (5.17), (5.22), (5.45) result in $\Delta(R_t) = 2.8\%$ (equation (5.27)), $\Delta(p_t^0) = 12.2\%$ (equation (5.30)), while the opening at the wellbore $w_t(0, t)$ is captured precisely. At the same time, the absolute difference between the fully numerical and approximate opening profiles $w_t(\rho, t)$ normalised by $w_t(0, t)$ can reach $\Delta(w_t^\rho) = 5\%$ (equation (5.29)), which demonstrates that the accuracy of the approximation (5.26) reduces for such values of λ.

The last case is the leak-off-yield-stress scaling and the $\tilde{T}$−vertex solution associated with it. We set $\mathcal{G}_c = \mathcal{G}_t = 1$, which results in the following parameters:

$$L_{\tilde{t}} = t^{1/4}\sqrt{\frac{Q_0}{C'}}, \quad \epsilon_{\tilde{t}} = \sqrt{\frac{\tau_0}{E'}}. \tag{5.46}$$

Here, the evolution parameters are identified as the dimensionless storage $\mathcal{S}_{\tilde{t}}$, vis-

cosity $\mathcal{M}_{\tilde{t}}$ and toughness $\mathcal{K}_{\tilde{t}}$:

$$\mathcal{S}_{\tilde{t}} = \left(\frac{Q_0\tau_0}{C'^3 E'\sqrt{t}}\right)^{1/2}, \quad \mathcal{M}_{\tilde{t}} = \frac{C'^{3/2} E' M'^{1/n}}{\sqrt{Q_0}t^{3/4}\tau_0^{(n+1)/n}}, \quad \mathcal{K}_{\tilde{t}} = K'\left(\frac{C'}{E'^2 Q_0\sqrt{t}\tau_0^2}\right)^{1/4}.$$
(5.47)

Then, we retrieve the coefficients for the radius and opening (equation (5.26)) based on the global fluid balance (5.19) and the tip asymptote [Bessmertnykh and Dontsov, 2019]:

$$R_{\tilde{t}}^* = \frac{\sqrt{2}}{\pi}, \quad w_{\tilde{t}}^* = \frac{4}{\sqrt{\pi}}.$$
(5.48)

Similarly to the $\tilde{M}-$vertex solution, we estimate $\lambda_{\tilde{t}}$ via the tuning of the simplified opening profile (5.17) to the accurate numerical solution (Section 5.3.1). We compute $\lambda_{\tilde{t}} = 1.077$, and it provides the best approximation which reproduces precisely the fracture opening at the wellbore $w_{\tilde{t}}(0,t)$ and gives the error in the spatial variation $w_{\tilde{t}}(\rho,t)$ (in relation to $w_{\tilde{t}}(0,t)$) up to $\Delta(w_{\tilde{t}}^\rho) = 6\%$ (equation (5.29)). Pressure evaluated at the half-radius is reproduced by the approximate solution with the relative error of $\Delta(p_{\tilde{t}}^0) = 11\%$ (equation (5.30)).

Figures 5-3(c) and 5-3(f) depict the aperture and pressure profiles obtained by the accurate method (solid lines) and that computed by the approximate one (dashed lines) for the yield stress dominated regimes T (olive colour) and $\tilde{T}$ (maroon colour). For both vertices, we observe the intersection between the fully numerical and simplified solutions and a noticeable difference between them, which is caused by the loss of accuracy of the width approximation utilised to construct the simplified solution (5.26). One possible mitigation of this issue is to introduce a more sophisticated expression for fracture width that captures such behaviour for the T and $\tilde{T}$ limits. The existing approximation was initially proposed for smaller values of $\bar{\delta}$ and λ that correspond to Newtonian fluids. However, for the purpose of this study, i.e., for exploring the problem parameter space, such accuracy is acceptable, especially since the boundaries of the limiting solutions vary on a logarithmic scale.

The fracture characteristics observed in the limiting propagation regimes are summarised in Appendix A.5. In addition to the dimensional form, we also present the solutions in the normalised form obtained by the application of the mk-scaling

introduced in Section 5.5.1.

5.4.2 Representation of the problem solution space

The parametric space of solutions for the discussed radial fracture model can be conceptually presented in the form of a hexahedral pyramid, and the limiting propagation regimes are located at its vertices. The sketch of the pyramid $M\tilde{M}\tilde{K}KT\tilde{T}$ is shown in Figure 5-5. Each edge of the pyramid links two vertex solutions, e.g., i
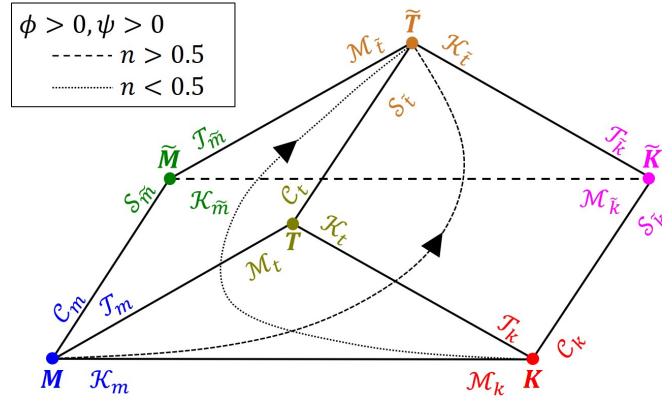
Figure 5-5: Parametric space $M\tilde{M}\tilde{K}KT\tilde{T}$ for a radial hydraulic fracture in a permeable rock driven by a fluid with Herschel-Bulkley rheology. The vertex solutions are located at its corners. The evolution parameters are specified near the edges for each propagation regime. The solution trajectories examples in the general case ($\phi > 0$, $\psi > 0$) are depicted for two values of the flow index: $n > 0.5$ (dashed line) and $n < 0.5$ (dotted line).

and j, and it is possible to introduce a characteristic transition time between them t_{ij} by solving the following equation: $\epsilon_i(t) = \epsilon_j(t) \rightarrow t = t_{ij}$. Furthermore, the evolution along the edge is controlled by a single evolution parameter, which can be expressed as a function of normalised time $\tau_{ij} = t/t_{ij}$ (two evolution parameters are related to each edge). Let us consider the MT-edge as an example. The transition time scale is $t_{mt} = \sqrt{E'}M'^{1/n}\tau_0^{-(n+2)/(2n)}$, while $\mathcal{T}_m(t)$ and $\mathcal{M}_t(t)$ are evolution parameters related to this edge. By introducing the dimensionless time $\tau_{mt} = t/t_{mt}$, we can write out the relations: $\mathcal{T}_m = \tau_{mt}^{2n/(n+2)}$, $\mathcal{M}_t = \tau_{mt}^{-1}$.

In the current problem, we have 9 transition time scales, and only 3 of them are independent, e.g., t_{mk}, $t_{m\tilde{m}}$, t_{mt}. Consequently, location of the solution inside the parametric space can be expressed as a function of the three dimensionless times $\tau_{mk} = t/t_{mk}$, $\tau_{m\tilde{m}} = t/t_{m\tilde{m}}$, $\tau_{mk} = t/t_{mt}$. Further, we introduce the parameters ϕ

and ψ as:

$$\phi = \left(\frac{t_{mk}}{t_{m\tilde{m}}}\right)^{(10n+4)/(3n+6)} = C'^4 \left(\frac{M'^3 E'^{10n+1} Q_0^{2-n}}{K'^{10n+4}}\right)^{1/(2n-1)},$$

$$\psi = \left(\frac{t_{mk}}{t_{mt}}\right)^{2n/(n+2)} = \tau_0 \left(\frac{E'^4 Q_0 M'^{1/n}}{K'^6}\right)^{n/(2n-1)}, \tag{5.49}$$

and they can be interpreted as the dimensionless leak-off and yield stress numbers. By taking the set of parameters $\{\tau = \tau_{mk}, \phi, \psi\}$, we can express $\tau_{m\tilde{m}}$ and τ_{mt} in terms of them in order to characterise the solution trajectories. Along each trajectory, the numbers ϕ and ψ are constant while τ varies.

When the flow index is greater than one-half ($n > 0.5$), all solution trajectories start from the M limiting propagation regime (early-time asymptote) since all the dimensionless groups (5.32) vanish when time tends to zero. However, their destination points (large-time asymptote) can be different: (i) $\phi = \psi = 0 - K$-vertex, (ii) $\phi > 0, \psi = 0 - \tilde{K}$-vertex, (iii) $\phi = 0, \psi > 0 - T$-vertex and (iv) $\phi > 0, \psi > 0 - \tilde{T}$-vertex. One can explain the endpoints of the solution trajectories by looking at the evolution parameters of the corresponding regimes (e.g., (5.38), (5.41), (5.44), (5.47)) which go to zero when time tends to infinity or they are identically zero due to values of ϕ, ψ. For intermediate time intervals, the solution trajectory can be attracted to either of the vertices, and its behaviour strongly depends on the values of ϕ and ψ. For example, when the yield stress is absent ($\psi = 0$), K and $\tilde{M}$ regimes can be considered in the general solution as intermediate asymptotes when the leak-off is small ($\phi \ll 1$) and large ($\phi \gg 1$), correspondingly. As another example, we can take zero leak-off case ($\phi = 0$) with the yield stress ($\psi > 0$), and K-vertex attracts the solution trajectory when $\psi \ll 1$.

The situation changes for $n < 0.5$. Here, the trajectories start at the K-vertex (see the corresponding evolution parameters (5.38) turn to zero when $t = 0$), and the final point can be: (i) $\phi = \psi = 0 - M$-vertex, (ii) $\phi > 0, \psi = 0 - \tilde{M}$-vertex, (iii) $\phi = 0, \psi > 0 - T$-vertex and (iv) $\phi > 0, \psi > 0 - \tilde{T}$-vertex (similarly to the previous discussion, it is required to draw attention to the parameters provided by equations (5.32), (5.35), (5.44), (5.47)).

We want to emphasise that in the general case when the dimensionless numbers ϕ and ψ are both non-zero, the large time asymptotic behaviour is always dominated by leak-off and yield stress, i.e., $\tilde{T}$-vertex, regardless of the value of the flow index n. The examples of the solution trajectories for $n > 0.5$ and $n < 0.5$ are shown in Figure 5-5 by dashed and dotted lines, respectively.

Finally, we should mention that the chosen set of parameters, i.e. $\{\tau = \tau_{mk},\ \phi,\ \psi\}$, is not applicable for the description of the solution trajectories behaviour for $n = 0.5$ since they are not properly defined in this case. One possibility to mediate this issue is to introduce another set of variables, e.g., $\{\tau = \tau_{m\tilde{m}},\ \phi' = (t_{mk}/t_{m\tilde{m}})^{(1-2n)/(3n+6)},\ \psi' = (t_{m\tilde{m}}/t_{mt})^{2n/(n+2)}\}$, where ϕ' is the dimensionless toughness, and ψ' is the dimensionless yield stress. Nevertheless, since the problematic region consists of solely a single point, we proceed with the chosen set of parameters $\{\tau = \tau_{mk},\ \phi,\ \psi\}$.

5.5 Results and discussion

5.5.1 Admissible ranges of the dimensionless problem parameters.

Let us start by rewriting the problem formulation in terms of the dimensionless variables. For the normalisation of the governing equations, we rely on the *mk*-scaling consisting on the following parameters [Detournay, 2016]:

$$\rho = \frac{r}{R}, \quad \tau = \frac{t}{t_{mk}}, \quad \gamma = \frac{R}{L_{mk}}, \quad \Omega = \frac{w}{\epsilon_{mk}L_{mk}}, \quad \Pi = \frac{p}{E'\epsilon_{mk}}, \tag{5.50}$$

where the dimensionless distance to the source ρ, time τ, radius γ, opening Ω, and pressure Π are introduced; t_{mk} is the transition timescale between M and K limiting regimes (Section 5.4.2), $L_{mk} = L_m(t_{mk})$ is the lengthscale, and $\epsilon_{mk} = \epsilon_m(t_{mk})$ is the

small parameter (see equation (5.31)):

$$t_{mk} = \left(\frac{M'^5 E'^{6n+7} Q_0^{n+2}}{K'^{6(n+2)}} \right)^{1/(4n-2)}, \qquad L_{mk} = \left(\frac{M' E'^{2n+1} Q_0^n}{K'^{2(n+1)}} \right)^{1/(2n-1)},$$

$$\epsilon_{mk} = \left(\frac{K'^{6n}}{M' E'^{6n-1} Q_0^n} \right)^{1/(4n-2)}. \tag{5.51}$$

The elasticity (5.5), Reynolds (5.8), (5.9), global fluid balance (5.10) equations and the propagation condition (5.11) written in terms of the dimensionless distance ρ and using (5.50) and (5.51) can be written in the normalised form as:

- *Elasticity:*

$$\Pi = -\frac{1}{2\pi\gamma} \int_0^1 G\left(\rho, s\right) \frac{\partial \Omega}{\partial s} ds;$$

- *Reynolds:*

$$\frac{\partial \Omega}{\partial \tau} - \frac{\rho \dot{\gamma}}{\gamma} \frac{\partial \Omega}{\partial \rho} + \frac{\phi^{1/4}}{\sqrt{\tau - \theta_0}} =$$

$$= \frac{1}{\gamma\rho} \frac{\partial}{\partial\rho} \left[\rho \frac{\Omega^{2+1/n}}{\gamma^{1/n}} \frac{\partial \Pi}{\partial \rho} \left| \frac{\partial \Pi}{\partial \rho} \right|^{1/n-1} \left(1 - 2\psi \frac{\gamma}{\Omega} \left| \frac{\partial \Pi}{\partial \rho} \right|^{-1} \right)^{1+1/n} \left(1 + 2\psi \frac{\gamma}{\Omega} \left| \frac{\partial p}{\partial \rho} \right|^{-1} \frac{n}{n+1} \right) \right],$$

where the dimensionless leak-off ϕ and yield stress ψ are defined in equation (5.49), and the dimensionless inverse radius function is given by $\theta_0(\rho, \tau) = t_0(r)/t_{mk}$. For completeness, we also provide the definitions of ϕ and ψ through the characteristics of the mk-scaling:

$$\phi = \left(\frac{C' \sqrt{t_{mk}}}{L_{mk} \epsilon_{mk}} \right)^4, \qquad \psi = \frac{\tau_0}{E' \epsilon_{mk}^2};$$

- *Global fluid balance:*

$$\frac{\tau}{\pi\gamma^2} = 2 \int_0^1 \rho\Omega \, d\rho + 4\phi^{1/4} \int_0^1 \rho\sqrt{\tau - \theta_0} \, d\rho;$$

- *Propagation condition:*

$$\Omega = \sqrt{\gamma}\sqrt{1-\rho}, \qquad \rho \to 1.$$

181

We can use the numerical schemes presented in Sections 5.3.1 and 5.3.2 for the solution of the normalised system of governing equations assuming $E' = K' = M' = Q_0 = 1$, $C' = \phi^{1/4}$, $\tau_0 = \psi$, and $t = \tau$.

Further, it is useful to estimate the realistic ranges of the dimensionless governing parameters ϕ and ψ. To obtain the desired ranges, some input parameters are kept fixed, while the remaining ones are altered within their own intervals. We consider the following values/spans:

- geomechanics:

  - plane-strain elastic modulus: $E' = 10 \div 50$ GPa;

  - rock toughness: $K_{Ic} = 0.5 \div 2.5$ MPa $\cdot \sqrt{\mathrm{m}}$;

  - far-field confining stress: $\sigma_o = 10 \div 30$ MPa;

- reservoir:

  - permeability: $k = 0 \div 100$ mD;

  - porosity: $\phi_r = 5 \div 25\%$;

  - ratio of far-field pore pressure and far-field confining stress: $p_o/\sigma_o = 0.4 \div 0.95$;

- Fracturing fluid:

  - flow behaviour index: $n = 0.5 \div 1$;

  - consistency index: $M = 10^{-3} \div 2$ Pa $\cdot$ s^n;

  - yield stress: $\tau_0 = 0 \div 15$ Pa;

- pore fluid:

  - viscosity: $\mu = 1 \div 5$ cP;

  - total compressibility: $c_t = 10^{-3}$ MPa^{-1};

- volumetric injection rate:

  - $Q_0 = 0.01 \div 0.1$ m^3/s.

We take three values of the flow behaviour index $n = \{0.6, \ 0.8, \ 1\}$ and compute the intervals for the governing parameters ϕ and ψ by varying each of the aforementioned dimensional input parameters independently. We illustrate the evaluated domains in Figure 5-6(a). It can be noticed that the domain for $n = 0.6$ (green
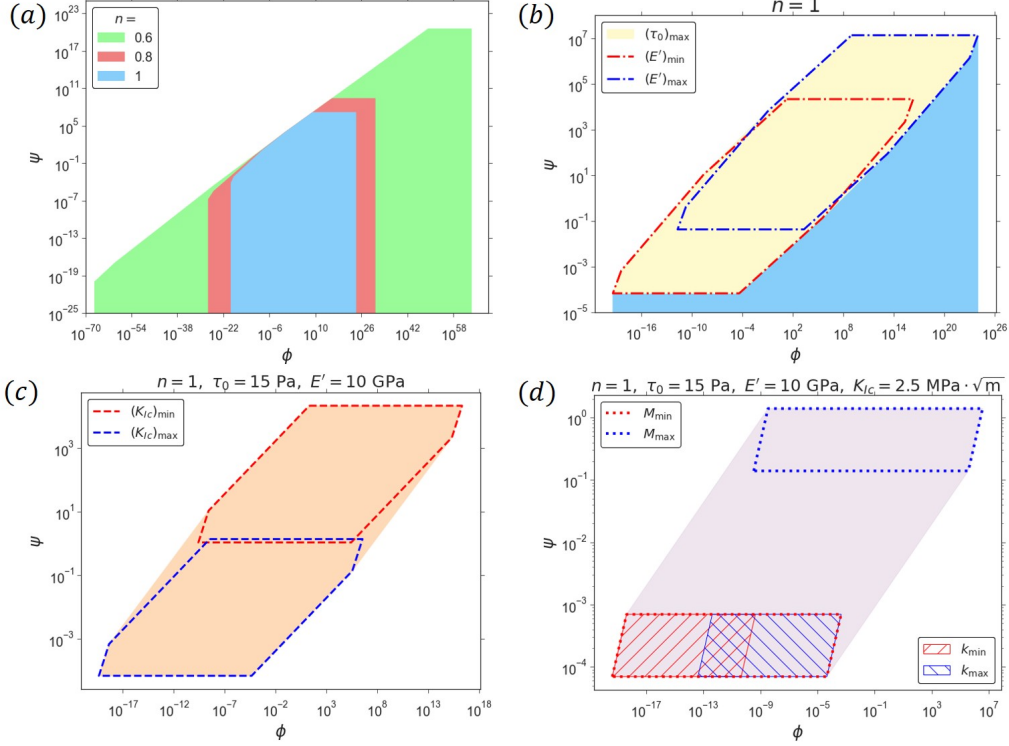
Figure 5-6: The panel (a) provides the domains in the coordinates (ϕ, ψ) corresponding to $n = \{0.6, \ 0.8, \ 1\}$ and typical field parameters by green, red, and blue colours. In the panel (b), the yellow decagon shows the locus for $n = 1$ and $\tau_0 = 15$ Pa, while the octagons framed by the red and blue dash-dotted lines are related to the minimum and maximum values of the plane-strain elastic modulus. The structure of the octagon cell is presented in the panel (c) (for $E' = 10$ GPa) where the red and blue dashed lines limit the hexagons corresponding to the minimum and maximum values of rock toughness. On the chart (d), we analyse the internal structure of the hexagon (using the case for $K_{Ic} = 2.5$ MPa $\cdot \sqrt{\mathrm{m}}$) by identifying the locations of data points belonging to the minimum and maximum values of the consistency index (red and blue dotted boundaries) and rock permeability (domains with red and blue line fill).

one) includes the analogous zone for $n = 0.8$ (red one) which, in turn, includes the region for $n = 1$ (blue one). To understand the structure of the non-dimensional parametric domain for a fixed n (how different dimensional input parameters affect the locations inside it) we look closely at the example of the Bingham fluid ($n = 1$) with the yield stress $\tau_0 = 15$ Pa (yellow decagon in Figure 5-6(b); such decagons for different $\tau_0 \in [0, 15$ Pa] fill completely the whole blue domain). We identify two

sub-domains (octagons) corresponding to the minimum and maximum values of the plane-strain elastic modulus and frame them by coloured dash-dotted lines (Figure 5-6(b)); the octagons belonging to the intermediate values of E' are located between them. Consequently, the resultant interval for the dimensionless leak-off number is controlled by the predefined range for E', while the interval for ψ is primary governed by the yield stress parameter and then by E'. Next, each octagon is limited by two hexagons corresponding to the limiting values of the rock toughness. In Figure 5-6(c), we show the octagon related to the minimum value of the plane-stain elastic modulus ($E' = 10$ GPa) by the orange colour and highlight the sub-domains for the minimum and maximum values of K_{Ic} by the coloured dashed lines. One can also examine the interior of each hexagon and reveal the parallelograms corresponding to the extreme values of the consistency index and rock permeability which we emphasise by the coloured dotted boundaries and the coloured line fill in Figure 5-6(d) using the hexagon for $K_{Ic} = 2.5$ MPa $\cdot \sqrt{\text{m}}$. Finally, we can mention that the lower and upper sides of each parallelograms (Figure 5-6(d)) are locuses of the points represented by the minimum and maximum values of the volumetric fluid injection rate, and the structure of each side includes the alterations of the remaining parameters ($\sigma_o, \phi_r, p_o/\sigma_o$).

5.5.2 Analysis of the parametric space

This section considers analysis of the parametric space for a radial crack driven by a fluid with Herschel-Bulkley rheology. We utilise the dimensionless problem formulation (Section 5.5.1) in which the crack characteristics governed by the following dimensionless variables: time (τ), distance from the source (ρ), leak-off (ϕ) and yield stress (ψ).

In this section, we focus on the results related to the following values of the flow behaviour index: $n = 1$ and $n = 0.3$, and the examination includes the following two main components. Firstly, we identify the applicability domains of the limiting propagation regimes inside the parameter space and draw them as the regime maps. The construction of such kind of maps helps to understand the crack propagation conditions for the given problem parameters. The validity zones of the vertices are

defined according to the following criterion (the same was used in Dontsov [2016a]):

$$\sqrt{\left(1 - \frac{\Omega_i(0,\tau)}{\Omega(0,\tau)}\right)^2 + \left(1 - \frac{\gamma_i(\tau)}{\gamma(\tau)}\right)^2} < 0.01, \quad i = M, \ \tilde{M}, \ K, \ \tilde{K}, \ T, \ \tilde{T}. \quad (5.52)$$

Equation (5.52) states that the combination of the relative differences of the opening at the wellbore and of the fracture radius between the numerical solution and the i-th limiting regime should be less than 1% for the solution being considered at the vertex.

It is important to highlight that for the purpose of this section we apply the simplified approach (Section 5.3.2) for calculations due to its computational efficiency. Appendix A.6 presents the validation of the approximate solution. Its predictions was compared to that provided by the accurate numerical method (Section 5.3.1). We apply criterion (5.52) to estimate the applicability boundaries of all vertex solutions numerically. Moreover, to provide quick analytic estimates, we fit the obtained points by the appropriate analytical functional dependencies that are derived from the consideration of the transition timescales between the limiting regimes. As an example, let us consider the validity boundaries of the storage-viscosity (M) and storage-yield-stress (T) regimes framing the MT transition (another interpretation of the transition is the MT-edge of the solution space outlined in Section 5.4.2). The time t normalised by the transition timescale t_{mt} has the form: $\tau_{mt} = \tau\psi^{(2+n)/(2n)}$, providing the following relation for the discussed boundaries: $\psi \propto \tau^{-2n/(2+n)}$. The prefactors are estimated numerically via the fitting procedure for M and T vertices separately. We summarise all possible relationships arising in the model as the applicability boundaries of the limiting solutions in Table 5.1.

The second element of the analysis is the examination of the variations of the main time-dependent crack characteristics such as radius $\gamma(\tau)$, opening at the wellbore $\Omega(0,\tau)$, pressure at the half-radius $\Pi(1/2,t)$, and efficiency $\eta(\tau)$ with the dimensionless leak-off and yield stress parameters.

5.5.2.1 Impermeable rock

Bingham fluid ($n = 1$)

Table 5.1: The validity boundaries of the limiting regimes obtained by setting $\tau_{\text{edge}} =$ const.

Transition	$\tau_{\text{edge}} =$
MK	τ
$M\tilde{M}$	$\tau\phi^{(3n+6)/(10n+4)}$
MT	$\tau\psi^{(2+n)/(2n)}$
$K\tilde{K}$	$\tau\phi^{5/6}$
KT	$\tau\psi^{5/2}$
$\tilde{M}\tilde{K}$	$\tau/\sqrt{\phi}$
$\tilde{M}\tilde{T}$	$\tau\psi^{(4n+4)/(3n)}/\sqrt{\phi}$
$\tilde{K}\tilde{T}$	$\psi^4\tau/\sqrt{\phi}$
$T\tilde{T}$	$\tau\phi^{3/2}/\psi^2$

We start with a radial crack driven by the Bingham fracturing fluid ($n = 1$) in an impermeable formation ($\phi = 0$). The regime map is shown in Figure 5-7(a) in the
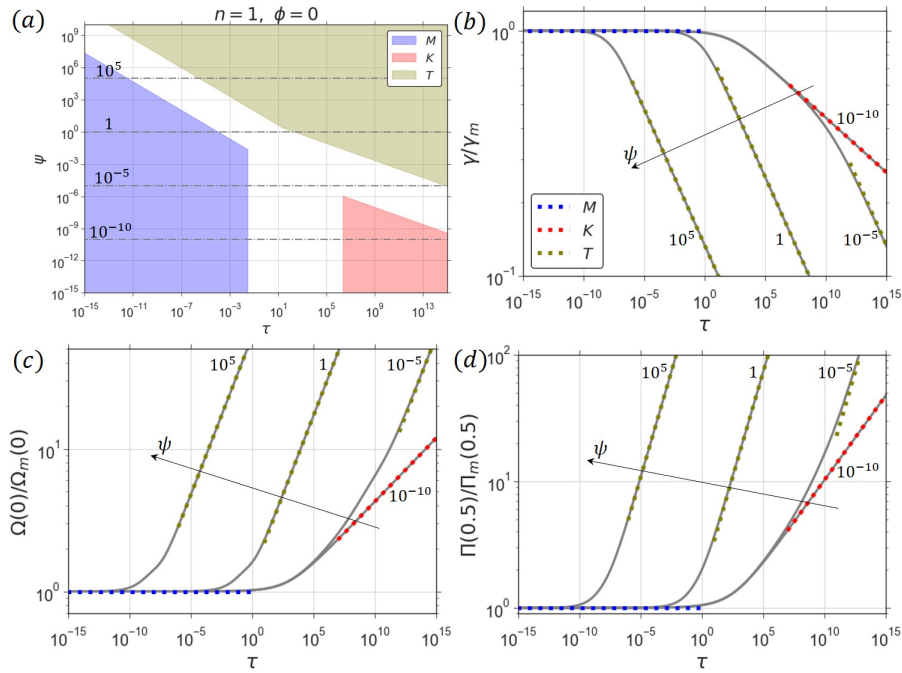
Figure 5-7: Results for a radial hydraulic fracture driven by the Bingham fluid ($n = 1$) with non-zero yield stress ($\psi > 0$) in an impermeable rock ($\phi = 0$). The regime map (a) is presented in the coordinates (τ, ψ), and the coloured regions denote the applicability domains of the limiting regimes. The time-dependent crack characteristics (radius (b), opening at the wellbore (c), and pressure at the half-radius (d)) normalised by the storage-viscosity limiting solution (M) are depicted for the yield stress number values: $\psi = \{10^{-10}, 10^{-5}, 1, 10^5\}$. In figure (a), the grey dash-dotted lines highlight the considered solution trajectories, while the coloured dotted lines in (b) – (d) correspond to the limiting solutions.

coordinates (τ, ψ). Generally, when the leak-off number $\phi = 0$, only three storage vertices can be realised: viscosity (M), toughness (K), and yield stress (T). For the flow behaviour index $n > 0.5$, the problem solution evolves from M to T $(\psi > 0)$ or to K $(\psi = 0)$ as it is confirmed by Figure 5-7(a) for $n = 1$. Moreover, for $n > 0.5$ and non-zero yield stress, the solution passes through the toughness dominated regime (K) over an intermediate time range if yield stress (ψ) is small enough. For example, the K-vertex approximates the general solution along certain time intervals when $\psi \lesssim 10^{-6}$ for $n = 1$, while the solution is dominated by dissipation in the fluid at all times, i.e., solution is given by M to T transition bypassing K-vertex, when the yield stress is large enough, e.g., $\psi \gtrsim 1$ for $n = 1$ (Figure 5-7(a)). The time domain of the storage-viscosity regime gradually shrinks with increasing $\psi \gtrsim 10^{-1}$ for $n = 1$ (Figure 5-7(a), whereas the time domain of the storage-yield-stress regime expands.

Further, we look at the solution trajectories in the parameter space for $n = 1$ and $\phi = 0$ corresponding to the following values of the dimensionless yield stress number: $\psi = \{10^{-10},\ 10^{-5},\ 1,\ 10^5\}$ (the grey dash-dotted lines in Figure 5-7(a)). We calculate evolution of the time-dependent crack parameters (radius $\gamma(\tau)$, wellbore opening $\Omega(0, \tau)$, and pressure $\Pi(1/2, \tau)$) and plot them normalised by the M-vertex solution in Figures 5-7(b) – (d). One can notice that the solutions are approximately independent of the yield stress ψ and given by the M-vertex solution during an initial time period which duration depends on the magnitude of ψ. After that initial propagation stage, the presence of the non-zero yield stress leads to a radial crack with the smaller radius (slower fracture growth), larger wellbore opening and higher pressure compared to the $\psi = 0$ case (see panels (b) – (d) in Figure 5-7 where the solution for $\psi = 10^{-10}$ coincides with the $\psi = 0$ case within the chosen time interval). Moreover, the relative differences between the computed properties for Newtonian $(\psi = 0)$ and Bingham $\psi > 0$ fluids grow with the increase of the magnitude of the dimensionless yield stress number ψ. Various asymptotic regimes of the solution as discussed above with the help of the parametric map (Figure 5-7(a)) can also be identified with corresponding M, K and T limiting solutions (Appendix A.5) shown in Figures 5-7(b) – (d) by coloured dotted lines.

Herschel–Bulkley fluid with $n = 0.3$

Now we proceed with the discussion of a radial crack driven by the Herschel–Bulkley fluid with $n = 0.3$ in an impermeable rock. The problem solution is demonstrated in Figure 5-8. For $n < 0.5$, the solution trajectories start at the storage-toughness (K)
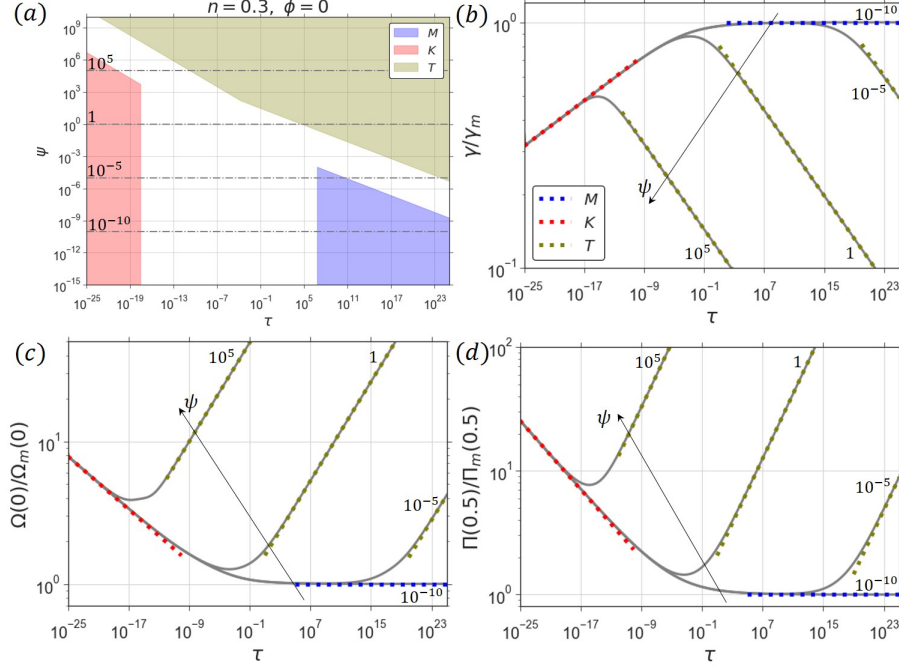
Figure 5-8: Results for a radial hydraulic fracture driven by the fluid with the flow behaviour index $n = 0.3$ and non-zero yield stress in an impermeable rock ($\phi = 0$). The regime map (a) is presented in the coordinates (τ, ψ), and the coloured regions denote the applicability domains of the limiting regimes. The time-dependent crack characteristics (radius (b), opening at the wellbore (c), and pressure at the half-radius (d)) normalised by the storage-viscosity limiting solution (M) are depicted for the yield stress number values: $\psi = \{10^{-10}, 10^{-5}, 1, 10^5\}$. In figure (a), the grey dash-dotted lines highlight the considered solution trajectories, while the coloured dotted lines in (b) – (d) mean the limiting solutions.

regime and finish at the storage-viscosity (M) regime for the power-law fluid ($\psi = 0$) or storage-yield-stress (T) regime for the Herschel–Bulkley fluid ($\psi > 0$) (panel (a) in Figure 5-8). The general solution can be approximated by the M-vertex solution during the intermediate time intervals for $\psi > 0$, e.g., it is realised along certain time ranges when $\psi \lesssim 10^{-4}$ for $n = 0.3$. The validity zone of the storage-toughness limiting solution (K) diminishes with increasing yield stress number ψ, while the T-vertex domain expands. Similarly to the Bingham fluid case, we examine four solution trajectories inside the parameter space for $n = 0.3$ and $\phi = 0$ correspond-

ing to the set of values of the yield stress number: $\psi = \{10^{-10},\ 10^{-5},\ 1,\ 10^5\}$ (the grey dash-dotted lines in Figure 5-8(a)), and plot time-dependent crack characteristics normalised by the storage-viscosity limiting solution in Figures 5-8(b) – (d). The results demonstrate that the non-zero yield stress affects radial fracture growth qualitatively similar to the Bingham fluid case: (i) the non-zero yield stress impacts the crack properties after a definite time range from the initiation which duration is governed by the yield stress number value; (ii) when the solution for the Herschel–Bulkley fluid deviates from that of for the power-law fluid, it is characterised by the reduced crack radius and increased maximum opening and pressure; (iii) the relative difference between the compared solutions, i.e., for $\psi > 0$ and $\psi = 0$, grows with increasing ψ.

5.5.2.2 Permeable rock

Next, consider the radial crack problem in a permeable reservoir ($\phi > 0$). Here, we vary both governing parameters ϕ and ψ to fully explore the problem parameter space. For each selected value of the flow behaviour index, i.e., $n = 1,\ 0.3$, we carry out calculations for the following values of the dimensionless yield stress number: $\psi = \{10^{-10},\ 10^{-5},\ 1, 10^5\}$ and construct the regime maps in the coordinates (τ, ϕ). Then, we investigate variations of the major time-dependent crack properties for $\psi = 1$ and different values of ϕ.

Bingham fluid ($n = 1$)

Figure 5-13 shows regime maps for a radial crack driven by fluid with $n = 1$ and various values of yield stress. When the flow behaviour index $n > 0.5$, the problem solution evolves from the storage-viscosity (M) to the leak-off-toughness ($\tilde{K}$) regime for the power-law fluid ($\psi = 0$) or to the leak-off-yield-stress ($\tilde{T}$) vertex for the fluid with yield stress ($\psi > 0$). The applicability domains of the limiting propagation regimes for $\psi > 0$ are shown by various colours in Figure 5-9, while the boundaries of the vertices for $\psi = 0$ are depicted by coloured dashed lines. When the yield stress is absent, the storage-toughness (K) and the leak-off-viscosity ($\tilde{M}$) regimes are realised as the intermediate asymptotes, and for $n = 1$, they emerge along the

189
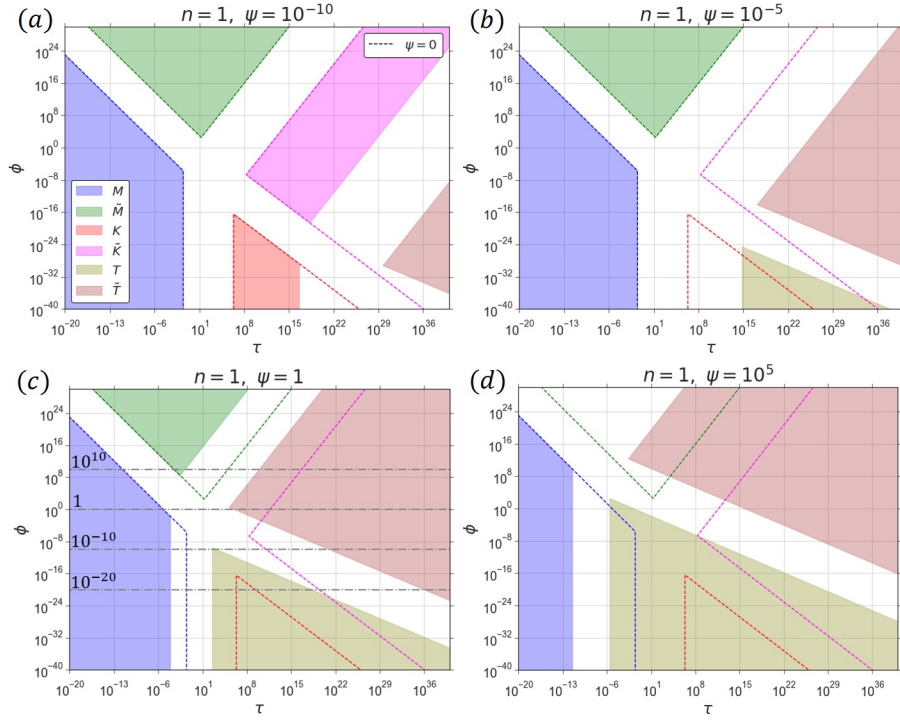
Figure 5-9: The parameter space for the problem of a radial hydraulic fracture driven by Bingham fluid ($n = 1$) in a permeable rock ($\phi > 0$). The regime maps are depicted in the coordinates (τ, ϕ) for several values of the dimensionless yield stress number: $\psi = \{10^{-10}, \ 10^{-5}, \ 1, 10^{5}\}$. The applicability domains of the limiting propagation regimes are indicated by different colours, and the boundaries corresponding to $\psi = 0$, i.e., Newtonian fluid case, are presented by the coloured dashed lines. In figure (c), the grey dash-dotted lines highlight the considered solution trajectories discussed in the current section.

intervals $\phi \lesssim 10^{-15}$ and $\phi \gtrsim 10^{3}$, respectively (see the coloured dashed lines in Figure 5-9). For a non-zero yield stress, the yield stress dominated regimes T, $\tilde{T}$ emerge earlier in the solution with an increase of ψ (see the shifting of corresponding domains from Figure 5-9(b) to (d)). In other words, the larger value of yield stress τ_0 (resulting in larger values of ψ) leads to reaching the condition $\tau_0 \gg M\dot{\gamma}^n$ quicker, if the remaining input parameters of the model remain the same. As a result, the validity zones of the toughness dominated regimes K, $\tilde{K}$ shrink with growing ψ, and eventually, they disappear completely (see Figure 5-9(a) versus (b) – (d)). The latter observation can be reformulated in the following way: for $\psi \gtrsim 10^{-5}$ and arbitrary ϕ the conditions for the realisation of the toughness dominated limiting propagation regimes $K, \tilde{K}$ can not be met since the values of evolution parameters $\mathcal{T}_k$ and $\mathcal{T}_{\tilde{k}}$ (equations (5.38), (5.41)) never tend to zero. Moreover, the domains belonging to the viscosity dominated regimes M, $\tilde{M}$ recede after a certain value

190

of the dimensionless yield stress (see Figures 5-9(c), (d) as compared to (a), (b));
however, they always exist in the model for certain values of τ and ϕ, and for all
ψ. To summarise, during the intermediate time intervals, the general solution is
approximated by K, $\tilde{K}$, $\tilde{M}$, T vertex solutions depending on the values of the
governing parameters ϕ and ψ. The boundaries between KT, $\tilde{K}\tilde{T}$, $T\tilde{T}$ transitions
do not depend on the flow behaviour index in the range $n > 0.5$ since this parameter
affects only the regions of the parameter space where the dissipation effects related
to the viscous fluid flow are significant, i.e., viscosity-toughness and viscosity-yield-
stress transitions. Further, we compared the applicability regions of the limiting
regimes for $n = 1$ and $n = 0.75$ (not shown) and found that the reduction of the
flow behaviour index within the interval $n \in (0.5, 1]$ leads to further separation of
$M, \tilde{M}, K, \tilde{K}$ regimes from the "center" of the map, i.e., the boundaries of M and
K vertices framing the MK transition move to the left (i.e., smaller times) and to
the right (i.e., larger times), respectively, while the boundaries of $\tilde{M}$ and $\tilde{K}$ regimes
framing the $\tilde{M}\tilde{K}$ transition shift up-left and down-right, correspondingly. The value
of n starts to influence locations of the boundaries of T and $\tilde{T}$ regimes related to
MT and $\tilde{M}\tilde{T}$ transitions only for large values of ψ.

Further, we take a closer look at variations of the time-dependent properties
of the radial crack driven by Bingham fluid ($n = 1$) with respect to parameters
ϕ and ψ. (At this point, we should note that the following analyses are qualita-
tively applicable to the other values of the flow behaviour index inside the interval
$0.5 < n \leq 1$.) We consider the following set of the dimensionless leak-off values
$\phi = \{10^{-20}, 10^{-10}, 1, 10^{10}\}$ and perform computations for both zero (Newtonian
fluid) and non-zero (Bingham fluid) yield stress ($\psi = 1$). The obtained results are
demonstrated in Figure 5-10. The solid black lines show the solution with $\psi = 1$,
while the case $\psi = 0$ is presented by the dashed grey lines. First, we discuss the
dependence of the solution on the leak-off number ϕ for a fixed value of the yield
stress number ($\psi = 0$ or $\psi = 1$). We observe that the solution is independent of
ϕ (and thus given by the impermeable case, $\phi = 0$) during an initial time period
of fracture propagation which duration depends on ϕ and ψ values. Outside this
initial time span, the increase of leak-off leads to smaller radius, opening at the
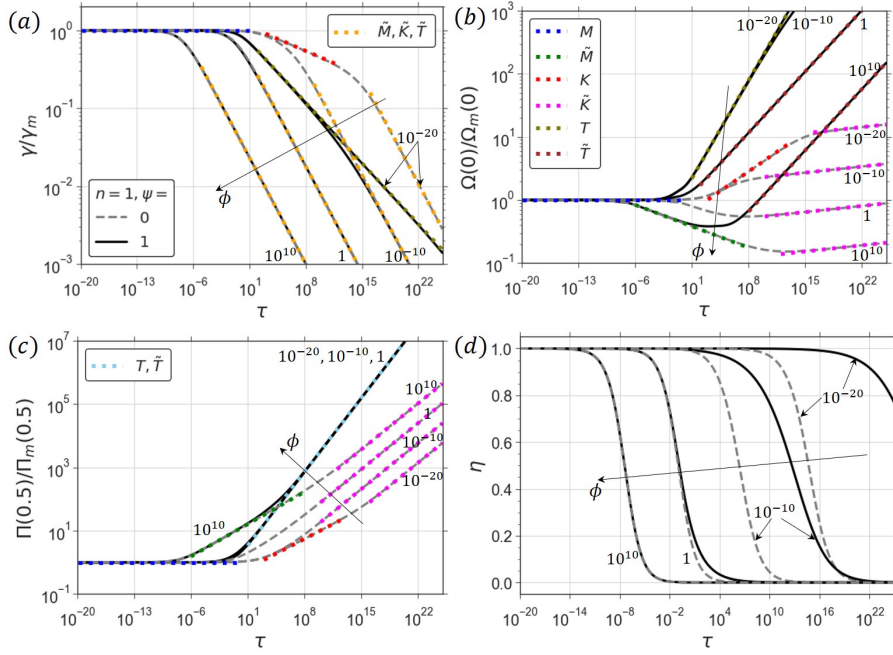
Figure 5-10: The time-dependent characteristics of a radial crack propagating in a permeable rock ($\phi > 0$) due to the injection of Bingham fluid: (a) radius $\gamma(\tau)$, (b) opening at the wellbore $\Omega(0, \tau)$, (c) pressure at the half-radius $\Pi(1/2, \tau)$, and (d) efficiency $\eta(\tau)$. The properties in charts (a) – (c) are normalised by the storage-viscosity (M) limiting solution. The profiles corresponding to $\phi = \{10^{-20}, \ 10^{-10}, \ 1, \ 10^{10}\}$ and $\psi = 1$ are shown by the solid black lines. The solutions for the same values of leak-off and zero yield stress are depicted by the dashed grey lines for comparison. The vertex solutions are presented by the dashed coloured lines. In graph (a), the asymptotic behaviour of the radius in the leak-off dominated regimes $\tilde{K}, \tilde{M}, \tilde{T}$ are represented by the orange colour due to the same functional relationships $\gamma_{\tilde{K}}(\tau)$, $\gamma_{\tilde{M}}(\tau)$, $\gamma_{\tilde{T}}(\tau)$ for all of them. Similarly, in graph (c), we apply cyan colour for the pressure behaviour in the the yield stress dominated regimes $T, \tilde{T}$ ($\Pi_T(1/2, \tau)$, $\Pi_{\tilde{T}}(1/2, \tau)$) which are very close to each other.

wellbore, and crack efficiency, whereas the pressure becomes larger (Figure 5-10). However, the pressure behaviour can differ from the description provided above for the non-zero yield stress case in which pressure for all ϕ values tends to reach the same yield stress dominated asymptote (see the cyan line in Figure 5-10(c)).

Next, we focus on the effect of the yield stress by comparing the solutions for Newtonian ($\psi = 0$) and Bingham ($\psi = 1$) fluids at a fixed value of the leak-off number (Figure 5-10). These solutions are insensitive to the fluid yield stress and thus coincide at the early stages of crack growth. Moreover, when the leak-off is very large ($\phi = 10^{10}$), two solutions match in the entire time domain for the radius and efficiency (Figures 5-10(a), (d)). At larger time the fluid yield stress ($\psi = 1$) leads to the reduced value of the radius and increased opening at the wellbore, pressure,

and efficiency compared to the Newtonian fluid case ($\psi = 0$).

The time domains where the fracture propagation is dominated by different limiting regimes can be identified in Figure 5-10 by comparing the computed fracture properties with the vertices (Appendix A.5) shown by the coloured dashed lines. We note that the limiting solutions for the radius are identical in all leak-off dominated regimes and thus shown in Figure 5-10(a) by a single (orange) colour. Similarly, the limiting solutions for pressure is all yield stress dominated regimes in Figure 5-10(c) are depicted by same colour (cyan) line.

Herschel–Bulkley fluid with $n = 0.3$

We now turn to the discussion of the parametric dependence of the solution for a radial crack propagation in a permeable rock ($\phi > 0$) due to the injection of Herschel–Bulkley fluid with the flow behaviour index $n = 0.3$. Figure 5-11 shows the computed propagation regime maps. When the flow behaviour index $n < 0.5$, the problem solution starts at the storage-toughness (K) regime and finishes at the leak-off-viscosity ($\tilde{M}$) regime for the power-law fluid ($\psi = 0$) or at the leak-off-yield-stress ($\tilde{T}$) regime for Herschel–Bulkley fluid ($\psi > 0$). The validity zones of the limiting regimes corresponding to $\psi > 0$ cases are shown by various colours in Figure 5-11, where we also plot the boundaries of the corresponding zones for the power-law fluid case $\psi = 0$ by dashed lines for comparison purposes. The general solution may approach the leak-off-toughness ($\tilde{K}$), storage-viscosity (M), leak-off-viscosity ($\tilde{M}$), and/or storage-yield-stress (T) regimes at an intermediate time depending on the values of ϕ and ψ. The behaviour of the yield stress dominated regimes with an increase of ψ is qualitatively similar to the already discussed case of the Bingham fluid, namely, T and $\tilde{T}$ domains expand towards smaller times. This shift leads to shrinking and, eventually, vanishing time domains of the viscosity dominated regimes as it can be noticed for $n = 0.3$ from Figures 5-11(a), (b) as compared to the panels (c), (d), and to the shrinking of the toughness regimes time domains (see Figure 5-11(d)). In contrast to $n > 0.5$ case, for $n < 0.5$ the change of the dimensionless yield stress does not affect the boundaries framing the $T\tilde{T}$ transition. We also should comment on the alterations of the regime map with the variation
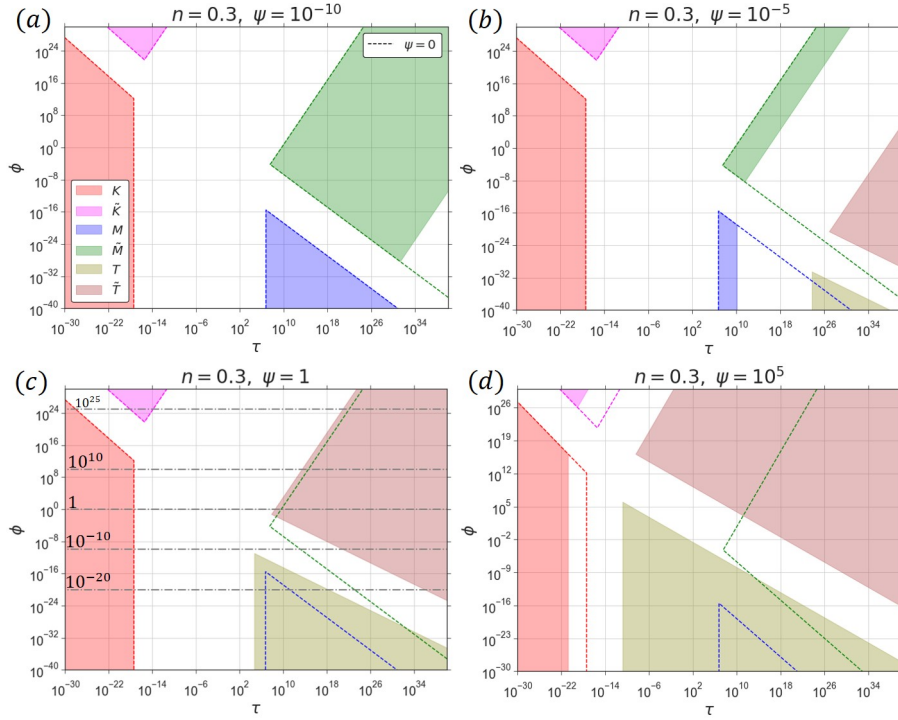
Figure 5-11: The parameter space of the model for a radial hydraulic fracture driven by Herschel–Bulkley fluid with $n = 0.3$ in a permeable rock ($\phi > 0$). The regime maps are depicted in the coordinates (τ, ϕ) for several values of the dimensionless yield stress: $\psi = \{10^{-10},\ 10^{-5},\ 1, 10^5\}$. The applicability domains of the limiting propagation regimes are filled by different colours, and the boundaries corresponding to $\psi = 0$, i.e., power-law fluid, are presented by coloured dashed lines. In figure (c), the grey dash-dotted lines highlight the considered solution trajectories discussed in the current section.

of the flow behaviour index inside the interval $n \in [0, 0.5)$ (not shown). When we increase the value of n, the boundaries of K and M vertex solutions framing the KM transition move to the left (i.e., smaller times) and to the right (i.e., larger times) respectively, whereas the boundaries of $\tilde{K}$ and $\tilde{M}$ domains framing the $\tilde{K}\tilde{M}$ transition go up-left and down-right, correspondingly. Similarly to $n > 0.5$, the flow behaviour index affect the boundaries of the yield stress dominated regimes framing KT and $\tilde{K}\tilde{T}$ transitions only for the large values of the dimensionless yield stress.

Figure 5-12 illustrates the evolution of fracture characteristics with time for the Herschel–Bulkley fluid ($n = 0.3$, $\psi = 1$) for various values of the leak-off number: $\phi = \{10^{-20},\ 10^{-10},\ 1,\ 10^{10},\ 10^{25}\}$ (see the corresponding dash-dotted trajectories in the parametric map in Figure 5-11(c)). The solutions for the power-law fluid case ($n = 0.3$, $\psi = 0$) are also shown for comparison by grey dashed lines. (Note that the solutions for the radius, maximum opening, and pressure at the half-radius in panels

(a)–(c) in Figure 5-12 are normalised by the storage-viscosity limiting solution (M).)
One can notice that the fluid yield stress impacts the problem solution qualitatively
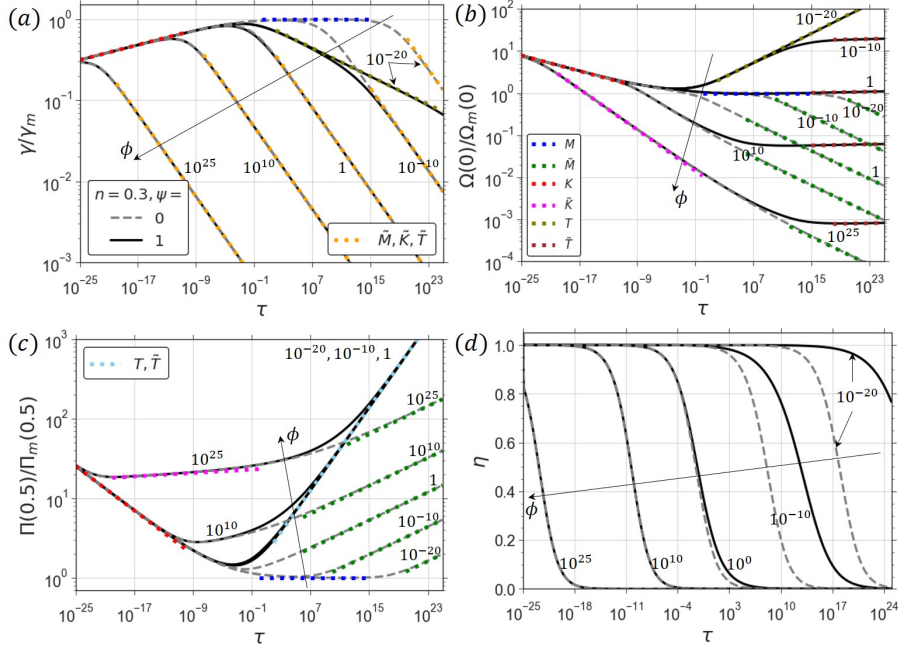
Figure 5-12: The time-dependent characteristics of a radial crack propagating in a permeable rock ($\phi > 0$) due to the injection of Herschel–Bulkley fluid with $n = 0.3$: (a) radius $\gamma(\tau)$, (b) maximum opening $\Omega(0, \tau)$, (c) pressure at the half-radius $\Pi(1/2, \tau)$, and (d) efficiency $\eta(\tau)$. The properties in charts (a) – (c) are normalised by the storage-viscosity (M) limiting solution. The profiles corresponding to $\phi = \{10^{-20}, 10^{-10}, 1, 10^{10}, 10^{25}\}$ and $\psi = 1$ are shown by the solid black lines. The solutions for the same values of leak-off and zero yield stress case are depicted by the dashed grey lines for comparison. The vertex solutions are presented by the dashed coloured lines. In graph (a), the asymptotic behaviour of radius in the leak-off dominated regimes $\tilde{K}, \tilde{M}, \tilde{T}$ are represented by the orange colour due to the same functional relationships $\gamma_{\tilde{K}}(\tau)$, $\gamma_{\tilde{M}}(\tau)$, $\gamma_{\tilde{T}}(\tau)$ for all of them. Similarly, in graph (c), we apply the cyan colour for the pressure behaviour in the yield stress dominated regimes $T, \tilde{T}$ ($\Pi_T(1/2, \tau)$, $\Pi_{\tilde{T}}(1/2, \tau)$) which are very close to each other.

similar to the Bingham fluid case: (i) for the fixed yield stress number, the increase of leak-off results in the fracture with smaller radius, maximum opening, and efficiency, but higher fluid pressure; (ii) when we fix the leak-off number and raise the yield stress number, we observe the reduction of the radius and increase of opening at the wellbore, pressure, and efficiency. The tendencies (i) and (ii) are applicable for the large enough time when the solutions for Herschel–Bulkley fluid ($\psi > 0$) and power-law fluid ($\psi = 0$) are distinct. For a better perception of the crack propagation regimes realised at different time in the demonstrated solutions, we plot the limiting (vertex) solutions (Appendix A.5) by the dashed coloured lines in Figure 5-12.

5.5.3 Quantitative estimations of the plug zone

In the current model for the hydraulic fracture driven by Herschel–Bulkley fluid, the plug zone is formed inside the regions where the shear stress τ_m is less than the yield stress τ_0, and its width is equal to $w_{\mathrm{plug}}(\rho, t) = 2y_\tau = 2\tau_0 R \left|\partial p / \partial \rho\right|^{-1}$. To track evolution of the unyielded zone, we introduce the time-dependent characteristic $\Upsilon(t)$ defined as volumetric fraction of the plug within the crack, i.e., $\Upsilon(t) = V_{\mathrm{plug}}(t)/V_{\mathrm{crack}}(t) = \int_0^1 \rho w_{\mathrm{plug}} d\rho / \left[\int_0^1 \rho w d\rho\right]$. Further, we express $\Upsilon(t)$ through the dimensionless crack properties (5.50) and the governing parameters ϕ, ψ (5.49) as:

$$\Upsilon(\tau, \phi, \psi) = 2\psi\gamma \frac{\int_0^1 \rho \left|\frac{\partial \Pi}{\partial \rho}\right|^{-1} d\rho}{\int_0^1 \rho \Omega d\rho}. \tag{5.53}$$

Equation (5.53) can be also simplified for the impermeable rock case as follows:

$$\Upsilon(\tau, 0, \psi) = \frac{4\pi\psi\gamma^3}{\tau} \int_0^1 \rho \left|\frac{\partial \Pi}{\partial \rho}\right|^{-1} d\rho.$$

The fully numerical solution (Section 5.3.1) is utilised for calculating $\Upsilon(\tau, \phi, \psi)$ time histories for various ϕ, ψ since the approximate approach (Section 5.3.2) provides the pressure gradient profiles with a reduced accuracy. The results are shown in Figure 5-13 in the form of the isolines (the dashed black lines) $\Upsilon(\tau, \phi, \psi) = \mathrm{const}$ where the constant can be varied within the segment $[0, 1]$ and, in our case, takes values $0.1, 0.5$, and 0.9. The plug fraction isolines are shown for two values of the flow behaviour index $n = 1$ (the left column) and $n = 0.3$ (the right column) for both impermeable (the top row) and permeable (the bottom row) formation cases. We demonstrate the results in the parameter space (τ, ψ) when $\phi = 0$ and in the space (τ, ϕ) for the fixed yield stress of $\psi = 1$ for non-zero leak-off $\phi > 0$. To better understand positions of the isolines relatively to the limiting regimes, we add their validity zones using the same colour palette as in the regime maps in Figures 5-7, 5-8, 5-9, 5-11.

The selected isolines $\Upsilon(\tau, \phi, \psi) = \mathrm{const}$ are predominantly located in the transition regions between the limiting propagation regimes. For a crack driven by
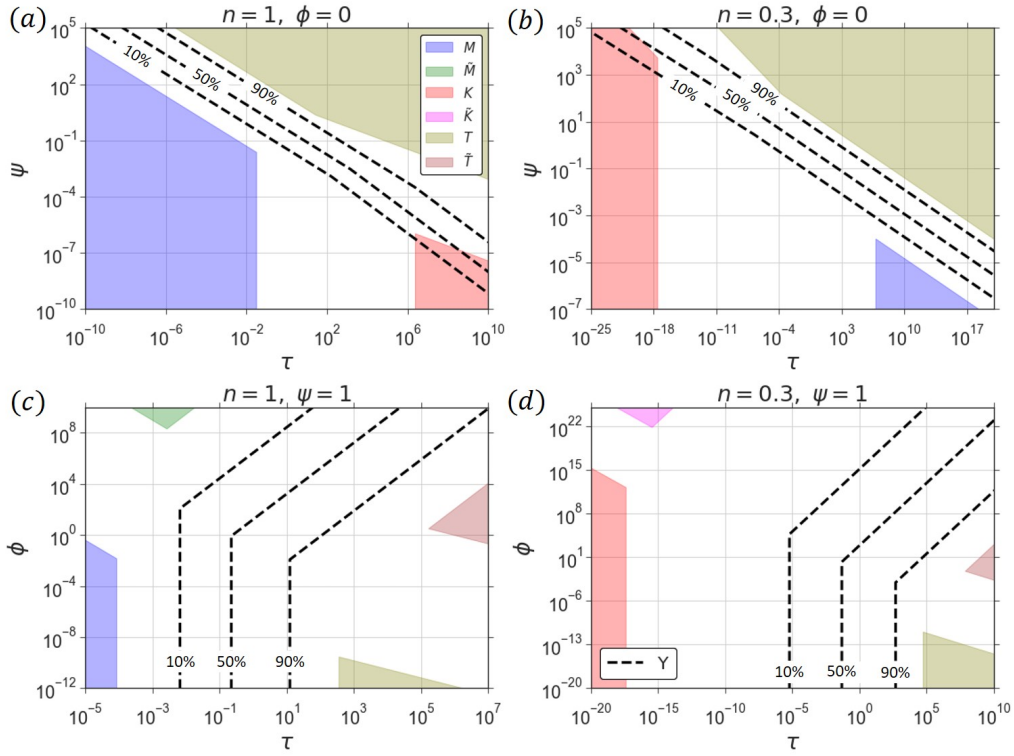
Figure 5-13: The charts present the isolines for $\Upsilon(\tau, \phi, \psi) = V_{\mathrm{plug}}/V_{\mathrm{crack}}$ (the dashed black lines) corresponding to the quantities 10%, 50%, and 90%. Two cases of the flow behaviour index are analysed: $n = 1$ (panels (a) and (c)) and $n = 0.3$ (panels (b) and (d)). The top row reflects the impermeable reservoir case, while the bottom figures correspond to simulations with leak-off and for the yield stress number $\psi = 1$. The regime maps demonstrated in Figures 5-7, 5-8, 5-9, 5-11 are applied as background in the diagrams.

Bingham fluid in an impermeable rock (panel (a) in Figure 5-13), MT and KT transitions contain the contour lines within the time intervals $\tau \lesssim 10^{-2}$ and $\tau \gtrsim 10^{6}$, respectively. The reversed situation is observed for the Herschel–Bulkley fluid with $n = 0.3$ (panel (b) in Figure 5-13) in which the isolines are located inside the KT and MT transition zones for $\tau \lesssim 10^{-18}$ and $\tau \gtrsim 10^{7}$, correspondingly. The isoline $\Upsilon = 0.1$ passes closely to the applicability domains of the storage limiting regimes, i.e., viscosity M and toughness K, in which $\Upsilon = 0$. In turn, the level $\Upsilon = 0.9$ lies near the validity region of the T vertex associated with $\Upsilon = 1$.

Generally, the function $\Upsilon(\tau, \phi, \psi)$ for the fixed values of the governing parameters ϕ and ψ grows smoothly with time from 0 to 1 evolving from the viscosity $M, \tilde{M}$ or toughness $K, \tilde{K}$ limiting regimes to the yield-stress $T, \tilde{T}$ vertices. In the model with the non-zero leak-off (panels (c) and (d) in Figure 5-13), we observe that the isolines belong to MT (KT) and $\tilde{M}\tilde{T}$ ($\tilde{K}\tilde{T}$) transitions when the leak-off number

$\phi \ll 1$ and $\phi \gg 1$, respectively, and $n = 1$ ($n = 0.3$). Moreover, one can notice that the contour lines are parallel to the boundaries of the applicability domains of the vertex solutions framing the transition zones enclosing the isolines.

Finally, we focus on the behaviour of the isolines near the toughness dominated limiting regimes when the leak-off number ϕ is fixed, and the yield stress number ψ is small (for $n > 0.5$) or large (for $n < 0.5$). Using the panels (a) and (b) in Figure 5-13 for $\phi = 0$ cases, it is possible to observe that the contour lines for $\Upsilon = 0.1, 0.5$ penetrate into the validity zone of the storage-toughness regime. This phenomenon can be explained in the following way: the unyielded region starts to form when the crack geometry (radius and aperture) corresponds to the K vertex solution in which the energy is spent primarily on the brittle rock failure and is independent of the fluid flow process inside the crack channel where the coexistence of both liquid and solid (plug) states can occur.

5.5.4   Simulations of the crack growth for typical field cases

This subsection outlines results of the radial crack propagation in terms of the dimensional variables. We choose the values of the input parameters representative of typical field applications, and they consist of the geomechanical and filtration-storage properties of the porous rock, fluids (pore and hydraulic fracturing) characteristics, and the injection rate. The main aim of the analysis is to examine the impact of non-zero yield stress on the problem solution quantitatively for particular cases relevant to the field.

We consider fracture propagation during the first $6 \cdot 10^3$ seconds of injection with the volumetric rate of $Q_0 = 0.01$ m^3/s. The set of the geomechanical parameters is: plane-strain elastic modulus $E' = 30$ GPa, rock toughness $K_{Ic} = 1$ MPa $\cdot \sqrt{\text{m}}$, far-field confining stress $\sigma_o = 10$ MPa. We take the fracturing fluid with the flow behaviour index $n = 0.7$, consistency index $M = 1$ Pa $\cdot$ s$^\text{n}$ providing $M' = 7.7$ Pa $\cdot$ s$^\text{n}$, and the yield stress value is $\tau_0 = 10$ Pa (since we estimate the yield stress influence, the reference solution corresponds to the power-law fluid with the same n and M but $\tau_0 = 0$). We analyse the crack propagation in both impermeable and permeable formations. In the latter case, we consider the pore fluid and formation characteris-

tics to be the following: far-field pore pressure $p_o = 6$ MPa, permeability $k = 1$ mD, porosity $\phi_r = 20$ %, viscosity $\mu = 5$ cP (Newtonian fluid), total compressibility $c_t = 10^{-4}$ atm^{-1}. For simplicity, it is assumed that the filtrate of the fracturing fluid has the same properties as the pore fluid. Consequently, the leak-off parameter is equal to $C' = 2.9 \cdot 10^{-5}$ m/$\sqrt{\text{s}}$ in the permeable reservoir case. In terms of the dimensionless governing parameters (τ, ϕ, ψ) introduced in Section 5.4.2, the analysed cases can be written as: $\tau \in (0, \ 1.04 \cdot 10^{-10})$, $\phi = 0$ (impermeable rock) or $\phi = 1.2 \cdot 10^7$ (permeable rock), $\psi = 5.8 \cdot 10^4$ (Herschel–Bulkley fluid) or $\psi = 0$ (power-law fluid).

Figure 5-14 shows evolution in time of the fracture radius $R(t)$, opening at the wellbore $w(0,t)$, net pressure at the half-radius $p(R(t)/2,t)$, and efficiency $\eta(t)$ calculated using fully numerical solution (see Section 5.3.1). The results for a radial
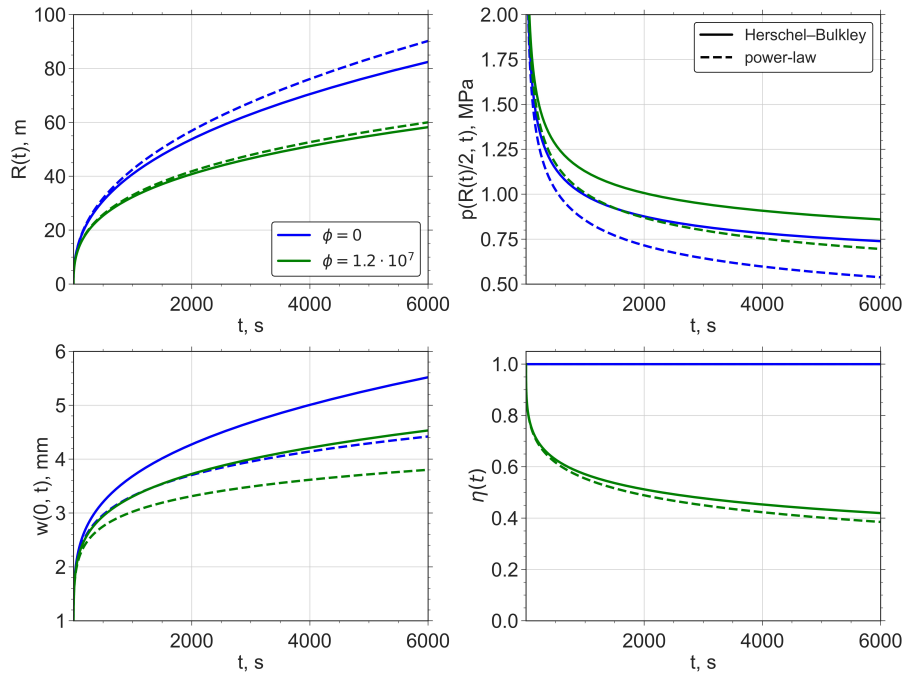
Figure 5-14: The figure illustrates various time-dependent radial crack parameters computed using fully numerical solution (Section 5.3.1). The left column shows the radius $R(t)$ and aperture near the wellbore $w(0,t)$ evolutions, while the right column shows the net pressure $p(R(t)/2,t)$ and the efficiency $\eta(t)$ variations. The solid lines correspond to the cases of the crack driven by the Herschel–Bulkley fluid, and the dashed lines are utilised for the solutions corresponding to the fluid with power-law rheology. The blue and green colours denote the impermeable and permeable formation cases, respectively.

crack driven by the Herschel–Bulkley fluid are depicted by the solid lines, for a crack

driven by power-law fluid by the dashed lines. We utilise the blue colour for the zero leak-off case and the green one for when the rock formation is permeable.

We observe that the non-zero yield stress $\tau_0 = 10$ Pa leads to the reduction of the crack radius, increase of the opening at the wellbore, pressure, and efficiency (there is no alteration in efficiency for the impermeable formation case) (see the solid lines versus the dashed ones of the same colour in Figure 5-14). Therefore, these findings are in the agreement with the analyses stated in Section 5.5.2. To characterise the discrepancies between two compared solutions, i.e., for Herschel–Bulkley ("hb") and power-law ("pl") fluids, quantitatively, we calculate the relative differences between the crack properties for the time moment $t = 6000$ s using the following formula: $\delta_A = |A_{\mathrm{hb}} - A_{\mathrm{pl}}|/A_{\mathrm{hb}}$, where A is an analysed parameter. The obtained metrics are summarised in Table 5.2.

Table 5.2: The relative differences (δ_A) between various radial fracture parameters (A) corresponding to the fracturing fluids with the Herschel–Bulkley ("hb") and power-law ("pl") rheologies that are calculated at $t = 6000$ s.

$\delta_A = |A_{\mathrm{hb}} - A_{\mathrm{pl}}|/A_{\mathrm{hb}}$ (in %)		
Parameter (A)	$\phi = 0$	$\phi = 5.8 \cdot 10^4$
$R(t)$	9.4	3.1
$w(0,t)$	19.9	16.1
$p(R(t)/2, t)$	27.2	19.1
$\eta(t)$	0	8.2

One can notice that the variations between the two compared solutions are more substantial during the fracture propagation in an impermeable rock. Here, δ_A for the radius and maximum aperture parameters is approximately 9 % and 20%, correspondingly. When leak-off is introduced into the model, the radius values in Herschel–Bulkley fluid case are close to that of in power-law fluid fracturing (3% difference), while the opening at the wellbore and crack efficiency are higher for Herschel–Bulkley fluid by 16.1 % and 8.2 %, respectively. Finally, δ_A for the net pressure at the half-radius reaches approximately 27 % and 19 % for $\phi = 0$ and $\phi > 0$. All these clearly demonstrate the importance of yield stress for modelling practical cases of hydraulic fracturing.

Chapter 6

Conclusions

In the present thesis, we investigated the influence of various fluid mechanics phenomena on the evolution of a fluid-driven fracture. Within this work, we considered three different effects:

1. pressure-dependent fluid exchange between the fracture and ambient permeable formation,

2. turbulent-laminar flow of water-based liquid with friction reducing agents inside the crack channel,

3. fracturing fluid rheology characterised by a non-zero yield stress and non-linearity of the shear stress.

We carried out the analysis applying two crack geometries: semi-infinite and radial. The first one accurately describes the near-tip region of a finite fracture and helps resolve the contribution of physical processes realising in the vicinity of the crack front to its movement. The second one is a model of a finite hydraulic fracture that occurs in nature and allows one to observe the influence of the considered hydro-dynamical phenomenon on the crack propagation and evolution of its properties in time.

Chapter 3 examined the effect of pressure-dependent leak-off (PDL) on the propagation of a hydraulic fracture in a permeable reservoir. Carter's leak-off law governs a pressure-independent fluid exchange process in most of existing models. In the

current study, we refine the fluid exchange mechanism by utilising the actual fluid pressure inside the crack channel. In our modelling framework, the leak-off intensity becomes (i) less than Carter's value in the near-tip region ($p_f < \sigma_o$) leading to a leak-in process and (ii) more than Carter's value away from the fracture tip ($p_f > \sigma_o$). The distinguishing feature of the hydraulic fracture model with the PDL is the presence of a circulation zone adjacent to the front filled by the pore fluid. We performed the asymptotic analysis of the limiting propagation regimes for the fracture tip framing the general structure of the solution (opening and pressure profiles) and its parametric dependence within the space of two non-dimensional parameters: leak-off χ and leak-in ζ numbers. We observed that the tip solution differs significantly from Carter's one ($\zeta = 0$) with an increase of the leak-in number. The full numerical solution provides a practical framework to understand the coupling of the physical processes near the fracture tip and its evolution with the crack tip velocity. The constructed maps allow one to assess the propagation regime of a finite hydraulic fracture by contrasting the asymptotic domain boundaries to the length of a finite fracture. Further, we constructed a penny-shaped hydraulic fracture model with the PDL and embedded into it the fracture tip model for an accurate description of the near-tip region. We demonstrated that the PDL effect can change the problem solution (radius, opening, pressure, efficiency) by more than 10% compared to Carter's leak-off case for realistic values of parameters corresponding to field applications. In the PDL case, a radial fracture is smaller in terms of aperture and radius as compared to Carter's case since the PDL increases the total leaked-off volume along the major part of the fracture. Next, we converted the problem formulation into a dimensionless form in which the solution depends on Carter's leak-off number ϕ and PDL number ψ apart from time and distance to the source. The PDL number ψ describes the magnitude of the PDL. To quantify the PDL effect, we compared the radial crack properties computed with the PDL and with simplified Carter's leak-off law for various cases inside the parametric space (ϕ, ψ). The results demonstrated that relatively small PDL numbers influence the high-efficiency cases, while the large PDL numbers are required to provide a noticeable influence for the cases of small fracture efficiencies.

Chapter 4 analysed how the turbulent-laminar flow inside the fracture channel impacts the propagation of either semi-infinite or radial hydraulic fracture in a permeable formation. We accounted for the flow regime transformation from the laminar to turbulent moving away from the fracture tip. The fluid exchange process between the fracture and ambient rock is modelled using Carter's leak-off law. The hydraulic fracturing fluid is slickwater, i.e., a water-based fluid including polymeric additives increasing the solvent viscosity and significantly modifying the turbulent flow frictional behaviour. The latter is modelled by the phenomenological maximum drag reduction (Virk's) asymptote. We found the general solution (opening and pressure profiles) for the fracture tip and explored its behaviour in the problem parametric space of two dimensionless parameters: leak-off number χ and characteristic Reynolds number $\mathcal{R}$. We enumerated limiting regimes realised in the tip model and plotted regime maps with their applicability domains. We paid attention to the transition boundary between the flow regimes and concluded that the laminar domain shrinks towards the tip with an increase of the leak-off number χ (while $\mathcal{R}$ is fixed) as compared to the zero leak-off case. Consequently, turbulence has a greater impact on the fracture tip solution when leak-off exits (while the rest of the problem parameters and the propagation velocity are kept the same). Next, we developed a numerical model for a radial hydraulic fracture. Simulations of a radial crack growth for the values of the model parameters corresponding to typical field cases demonstrated that turbulence changes the crack characteristics near the wellbore zone during the initial propagation period. E.g., in the slickwater fracturing, the turbulent-laminar solution differs significantly from the fully-laminar one during a couple of seconds, tens of seconds, and several minutes in terms of the radius, opening at the wellbore, and pressure, respectively. We revealed that the leak-off process prolongs the turbulence effects. Although the fracture geometries in the models with and without turbulent flow are practically the same after several minutes of the propagation, the pressure near the wellbore has larger values in the turbulent-laminar case during tens of minutes, meaning a greater amount of power is required for the fluid pumping than the laminar model predicts. We performed the exploration of the problem solution inside the non-dimensional problem parameter

space of the leak-off number ϕ and characteristic Reynolds number $\mathcal{R}$. We derived the limiting propagation regimes, determined their applicability domains, identified how the fracture properties vary with the change of the values of the governing parameters.

In Chapter 5, we constructed a numerical model for a radial hydraulic fracture driven by a Herschel–Bulkley fluid in a permeable rock and carried out extensive analysis of the combined impact of the fluid yield stress and leak-off on the crack propagation. In most existing models, the fracturing fluid is taken as Newtonian or power-law; however, certain fracturing fluids, such as gels and foams, demonstrate shear-thinning rheology with the yield stress that Herschel–Bulkley rheological model can describe. The system of governing equations is formulated in dimensional and non-dimensional forms, and, for the latter, all crack characteristics are governed by two dimensionless parameters: the leak-off number ϕ and the yield stress number ψ. Two different approaches are used to obtain the problem solution: accurate and simplified algorithms. We investigated the problem parametric space using the dimensionless formulation by looking at the validity domains of the limiting propagation regimes and variations of different time-dependent crack characteristics versus the dimensionless problem parameters. The regime maps allow us to rapidly detect the dominance of various physical processes in a hydraulic fracture for certain values of the governing parameters without running numerical simulations. Using the obtained results, we concluded that the non-zero yield stress leads to a radial crack with a smaller radius, larger crack opening at the wellbore, pressure, and efficiency (for a permeable rock case) as compared to the power-law fluid case. Further, we simulated the growth of a radial fracture by taking the input parameters close to typical field applications and revealed that the yield stress could potentially result in notable deviations of the fracture parameters from the outcomes of the zero yield stress model. For example, in the impermeable rock case, we obtained 9% relative difference between the crack radius values at the end of injection period in the case of Herschel–Bulkley fluid and power-law fluid; this metric for the maximum opening property equals 20%. When the leak-off with Carter's coefficient $C' = 3 \cdot 10^{-5}$ m/$\sqrt{s}$ was introduced into the model, the deviation for radius comprises 3%, while for the

fracture opening near the wellbore, it is about 16%.

The developed fracture tip models (Section 3.2, Section 4.2) allows one to accurately describe the interplay between the physical processes in the vicinity of the crack front and their combined impact on the transient propagation of a finite hydraulic fracture, e.g., in the context of the penny-shaped fracture model, KGD model, enhanced PKN model or more complex planar crack models using the Pseudo3D and Planar3D approached. In doing so, the proposed near-tip solutions may be numerically implemented into a module for the growth of a finite fracture in the form of a so-called tip element, used to match the fracture opening in the near-tip zone between the global numerical solution and the local near-tip asymptote and invert for the local fracture front velocity. Actually, we carried out this procedure in Section 3.3 constructing a radial crack model with the PDL. In turn, the proposed penny-shaped hydraulic fracture models (Section 3.3, Section 4.3, Chapter 5) can be used as a benchmark solution for the numerical simulators of more realistic (complex) fracturing problems including the same physics, i.e., PDL / laminar-turbulent flow / fracturing fluid with Herschel-Bulkley rheology.

Constructed radial crack models can be verified using laboratory experiments. In lab conditions, mechanical experiment can be organised in such a way that a penny-shaped hydraulic fracture is formed. During the experiment, one can measure fluid pressure at the source, track the fracture footprint via acoustic signal, and measure rock deformations within time which can be used for calculating the crack aperture. As a result, it is possible to compare the measured radius, maximum opening, and pressure near the source with the corresponding properties provided by the numerical model. For the verification of the radial fracture model with the pressure-dependent fluid exchange, we should be able to create a hydraulic fracture in a permeable rock sample. Regarding the radial crack model driven by turbulent-laminar flow, we should inject fluid at large rate leading to the turbulent flow regime realisation during the initial period of the propagation. The third model, i.e., penny-shaped crack driven by Hershel-Bulkley fluid, requires a laboratory experiment with viscoplastic fluid. It is required to highlight that the laboratory experiment should be a model [Bunger and Detournay, 2008], i.e., we should create the conditions at

which various physical processes neglected in the numerical model do not realize, e.g., presence of the cohesion zone, lag saturated by vapour, damage zone ahead of the fracture. In other words, if some physical effect dominates in the lab experiment but is not accounted for in the model, we cannot obtain similar fracture properties provided experimentally and numerically. However, sometimes, the physical processes which dominate in lab conditions are not manifested in the field conditions where the fracture size is considerably large. In turn, field data can be used for model calibration, e.g., determination of Carter's coefficient via interpretation of the leak-off test. Thereafter, the estimated value is utilised for the design of a hydraulic fracture which can be created in the same rock formation. It is crucial to apply the model whose assumptions are close to real field conditions; otherwise, the interpretation outcomes will be incorrect. E.g., in the work [Ames et al., 2015], the authors performed PKN crack model calibration on the field data, and they highlighted that using the fully laminar model, one can estimate Carter's coefficient incorrectly if the fracture was created by fully turbulent flow. It happened because the laminar model overpredicts crack radius and underpredicts pressure.

Finally, we would like to provide possible directions for future research in the numerical modelling of hydraulic fracture growth related to the topics discussed in the thesis. In recent times, examination of a hydraulic fracture arrest and closure in a permeable formation after injection shutdown has become popular. E.g., in the work [Möri and Lecampion, 2021], the authors considered the arrest of a radial crack, while Peirce [2022] investigated not only the arrest but also the recession dynamics of a deflating radial fracture. Moreover, the arrest and recession of the fracture with KGD geometry, i.e., a state of plane strain, is presented in [Peirce and Detournay, 2022a], and [Peirce and Detournay, 2022b] derived various approximate similarity solutions for KDG and radial cracks close to the point of closure. In these studies, the fluid exchange process between the fracture and ambient permeable formation is taken in the form of Carter's leak-off law. However, fluid exchange plays an important role after injection stopping and has a significant impact on hydraulic fracture dynamics during the arrest and recession stages. That is why the consideration of a hydraulic fracture arrest and closure after shut-in accounting for more sophisti-

cated pressure-dependent mechanism of the fluid exchange is of interest. Next, one can mention the problem in which natural hydraulic fractures are formed inside the subducting oceanic slab due to metamorphic dehydration reactions [Audet et al., 2009, 2010]. Dehydration can lead to pore fluid pressure buildup over the minimum principal stress and result in natural hydraulic fracturing. In this case, the fracture driving mechanism is the influx of pore fluid into the fracture channel from the surrounding porous media until the buoyancy force influence becomes significant. The influx should be described by the pressure-dependent leak-in mechanism in the numerical models. Further, in Section 3.2.4.3, we enumerated several limitations of the constructed fracture tip model with pressure-dependent leak-off (limitations are also related to a radial crack model presented in Section 3.3), e.g., application of 1D mechanism for the fluid-exchange description and sameness of fracturing and pore fluids. We suppose that in the future research, it is possible to remove these restrictions and analyse how 2D pressure-dependent leak-off and presence of fracturing and pore fluids with different properties influence on the propagation of hydraulic fractures with semi-infinite and finite (e.g., radial, KGD, PKN) geometries. Let us move on to the topics related to the fluid flow inside the fracture channel, namely, non-laminar flow and non-Newtonian fracturing fluid rheology. We can propose that it will be interesting to analyse a hydraulic fracture driven by turbulent-laminar slickwater flow accounting for the roughness of the crack channel surface. It can be done via an approximation of Virk's experiments on slickwater flow in a rough pipe [Virk, 1971, 1975]. Next, we should mention the problem of waterless hydraulic fracturing which requires careful examination. In this reservoir treatment the utilised fracturing fluid is either foam or supercritical CO_2 or liquefied N_2, i.e., compressible liquid with complex rheology [Fu and Liu, 2019]. The last proposition is the study of a hydraulic fracture propagation accounting for the proppant transport inside the fracture channel, i.e., the flow of slurry governing by non-Newtonian rheological model [Lecampion and Garagash, 2014].

Appendix

A.1 Derivation of the pressure-dependent fluid exchange rate

The present section is devoted to the derivation of the pressure-dependent fluid exchange rate $g(X, t)$. For the description of the fluid exchange process we use the following assumptions:

- we assume a one-dimensional diffusion perpendicular to fracture surface, so that the flow rate $g(X, t)$ is governed by the history of fluid pressure values at the considered point X along the fracture, $p_f(X, t)$;

- a single fluid model is used, so that it is assumed that the hydraulic fracturing and pore fluids have the same properties (viscosity μ and total compressibility c_t).

As a result, the fluid exchange rate depends on the fluid pressure $p_f(X, t)$, fluid properties (μ, c_t) and the reservoir characteristics such as permeability k, porosity ϕ and the far-field pore fluid pressure p_o.

Let us consider a one-dimensional filtration problem in the semi-infinite space. It consists of filtration equation formulated for the pressure distribution in the reservoir, initial condition and two boundary conditions: on the fracture face and at infinity. The problem statement has the following form:

$$\frac{\partial p_r}{\partial t} = c \frac{\partial^2 p_r}{\partial Y^2}, \quad p_r(t = 0) = p_o, \quad p_r(Y = 0) = p_f(X, t), \quad p_r(Y \to \infty) = p_o,$$

where $c = k/(\mu\phi_r c_t)$ is the diffusivity coefficient, and Y is the coordinate perpendicular to the fracture.

The solution to this problem is found by Carslaw and Jaeger [1959] and has the following form:

$$p_r(X, Y, t) = p_o + \int_{-\infty}^{t} \frac{\partial}{\partial s} [H(s) \cdot (p_f(X, s) - p_o)] \cdot \operatorname{erfc}\left(\frac{Y}{2\sqrt{c(t-s)}}\right) ds,$$

where $H(x)$ is Heaviside step function, and $\operatorname{erfc}(x) = 1 - \operatorname{erf}(x)$ is the complementary error function.

Then, we calculate filtration velocity via Darcy's law. We also take into account that the fluid exchange process occurs through two fracture faces:

$$g(X, t) = -2 \cdot \frac{k}{\mu} \frac{\partial p_r}{\partial Y}\bigg|_{Y=0} = \frac{2k}{\mu\sqrt{\pi c}} \int_{-\infty}^{t} \frac{\partial}{\partial s} [H(s) \cdot (p_f(X, s) - p_o)] \frac{ds}{\sqrt{t-s}}.$$

The fluid exchange process at the considered point X starts when the fracture front reaches this point. That is why it is necessary to replace t by the exposure time $\Delta t = t - t_0(X)$ ($t_0(X)$ is the time instant at which the fracture front reaches position X) in the previous equation:

$$g(X, \Delta t) = \frac{2k}{\mu\sqrt{\pi c}} \int_{-\infty}^{\Delta t} \frac{\partial}{\partial s} [H(s) \cdot (p_f(X, s + t_0(X)) - p_o)] \frac{ds}{\sqrt{\Delta t - s}}.$$

Further, we change the limits of integration and utilise definition of the effective pressure $(p(X, t) = p_f(X, t) - \sigma_o)$ to obtain:

$$g(X, t) = \frac{C'}{\sqrt{t - t_0(X)}} + Q' \int_{-\infty}^{t} \frac{\partial}{\partial s} [H(s - t_0(X)) \cdot p(X, s)] \frac{ds}{\sqrt{t - s}}, \qquad \text{(A.1)}$$

where Carter's leak-off parameter C' and PDL number Q' are defined in (3.20).

In order to compute the fluid exchange rate for the near-tip region model $g_a(x)$, we apply the coordinate transformation $x = Vt - X$ and take the crack propagation law in the form $t_0(X) = X/V$, which leads to

$$g_a(x) = \frac{C'\sqrt{V}}{\sqrt{x}} + Q'\sqrt{V} \int_{-\infty}^{x} \frac{\partial}{\partial s} [H(s) \cdot p_a(s)] \frac{ds}{\sqrt{x - s}}. \qquad \text{(A.2)}$$

The above expression for $g_a(x)$ can be integrated from the crack front to distance x to obtain:

$$q_\perp(x) = 2C'\sqrt{Vx} + Q'\sqrt{V} \int_0^x \frac{p_a(s)ds}{\sqrt{x-s}}. \tag{A.3}$$

The obtained cumulative fluid exchange rate $q_\perp$ is also utilised in the numerical algorithm.

A.2   Discretisation of Reynolds equation

This section is devoted to the detailed derivation of the discretised Reynolds equation (3.31). Firstly, we integrate the differential equation over the time segment $[t_{i-1}, t_i]$, and after that, we carry out averaging across the circle with the radius ρ_j and width $\Delta\rho$ according to equation (3.33). It is important to highlight that the averaging procedure of the fluid exchange terms in the case of the tip element should be considered separately from the other spatial segments.

Let us consider Reynolds equation (3.31), integrated over time:

$$\underbrace{w^i - w^{i-1}}_{(I)} = \underbrace{\frac{\Delta t_i V_i}{R_i} \rho \frac{\partial w^i}{\partial \rho}}_{(II)} + \underbrace{\frac{\Delta t_i}{M'R_i^2} \frac{1}{\rho} \frac{\partial}{\partial \rho} \left(\rho (w^i)^3 \frac{\partial p^i}{\partial \rho} \right)}_{(III)} -$$

$$- \underbrace{2C' \left(\sqrt{t_i - t_0(\rho R_i)} - \sqrt{t_{i-1} - t_0(\rho R_i)} \right)}_{(IV)} -$$

$$- \underbrace{Q' \int_{t_{i-1}}^{t_i} dt' \int_{-\infty}^{t'} \frac{\partial}{\partial s} [H(s - t_0(\rho R_i)) p(\rho, s)] \frac{ds}{\sqrt{t' - s}}}_{(V)} +$$

$$+ \underbrace{Q' \int_{t_{i-1}}^{t_i} dt' \int_{-\infty}^{t'} \frac{\rho V(s)}{R(s)} \frac{\partial [H(s - t_0(\rho R_i)) p(\rho, s)]}{\partial \rho} \cdot \frac{ds}{\sqrt{t' - s}}}_{(VI)},$$

where $\Delta t_i = t_i - t_{i-1}$ is the step of the time interval i, and we also utilise notations: $w^i = w(\rho, t_i)$ and $p^i = p(\rho, t_i)$.

In the previous equation, each term was enumerated $(I) - (VI)$ in order to consider the averaging procedure across the circle ρ_j and simplification of the resultant equations for each term individually.

Term (I)

$$\frac{1}{2\pi\rho_j\Delta\rho}\int_{\mathcal{A}_\rho}(w^i - w^{i-1})d\mathcal{A} = w^i_j - w^{i-1}_j, \; j = 1, \ldots, N.$$

Term (II) In equations below, we drop the prefactor $\Delta t_i V_i/R_i$ for simplicity.

$$\frac{1}{2\pi\rho_j\Delta\rho}\int_{\rho_{j-1/2}}^{\rho_{j+1/2}} 2\pi\rho^2\frac{\partial w^i}{\partial\rho}d\rho \approx \frac{\rho_j}{\Delta\rho}(w^i_{j+1/2} - w^i_{j-1/2}) = \rho_j\frac{w^i_{j+1} - w^i_{j-1}}{2\Delta\rho}, \; j = 2, \ldots, N-1.$$

For the first segment $(j = 1)$ we utilise the fact that $w(\rho = 0) = w_1$ to obtain:

$$j = 1: \quad \frac{\rho_1}{\Delta\rho}(w^i_{3/2} - w^i_1) = \rho_1\frac{w^i_2 - w^i_1}{2\Delta\rho}.$$

For the tip element $(j = N)$ the boundary condition for the crack opening at the tip is used, namely, $w(\rho = 1) = 0$:

$$j = N: \quad \frac{\rho_N}{\Delta\rho}(-w^i_{N-1/2}) = -\rho_N\frac{w^i_N + w^i_{N-1}}{2\Delta\rho}.$$

The whole term (II) can be written in the matrix form as follows: $\mathbf{B}\mathbf{w}^i$, where $\mathbf{w}^i$ is the vector of fracture widths for all spatial points.

Term (III) For simplicity, we omit the prefactor $\Delta t_i/(M'R_i^2)$ in the derivations below.

$$\frac{1}{2\pi\rho_j\Delta\rho}\int_{\rho_{j-1/2}}^{\rho_{j+1/2}} 2\pi\frac{\partial}{\partial\rho}\left(\rho(w^i)^3\frac{\partial p^i}{\partial\rho}\right)d\rho = \frac{1}{\rho_j\Delta\rho}\left[\rho_{j+1/2}(w^i_{j+1/2})^3\left(\frac{\partial p^i}{\partial\rho}\right)_{j+1/2} - \right.$$
$$\left. - \rho_{j-1/2}(w^i_{j-1/2})^3\left(\frac{\partial p^i}{\partial\rho}\right)_{j-1/2}\right] = \frac{1}{\rho_j\Delta\rho}\left[\rho_{j+1/2}(w^i_{j+1/2})^3\frac{p^i_{j+1} - p^i_j}{\Delta\rho} - \right.$$
$$\left. - \rho_{j-1/2}(w^i_{j-1/2})^3\frac{p^i_j - p^i_{j-1}}{\Delta\rho}\right], \; j = 2, \ldots, N - 1.$$

We also should consider the first and the last segments separately. In the case of the first segment, we utilise the boundary condition at the wellbore:

$$j = 1: \quad \frac{1}{\rho_1\Delta\rho}\rho_{3/2}(w^i_{3/2})^3\frac{p^i_2 - p^i_1}{\Delta\rho} + \frac{Q_0 M'}{\pi\Delta\rho^2}.$$

For the fracture tip element, we utilise the zero flux boundary condition:

$$j = N: \quad -\frac{1}{\rho_N \Delta \rho} \rho_{N-1/2} (w_{N-1/2}^i)^3 \frac{p_N^i - p_{N-1}^i}{\Delta \rho}.$$

The third term can be also written in the matrix form as: $\mathbf{A}(\mathbf{w}^i)\mathbf{p}^i + \delta^{1j} Q_0 \Delta t_i / (\pi \Delta \rho^2 R_i^2)$ where δ^{1j} is Kronecker delta.

We proceed with the examination of the fluid exchange terms $(IV) - (VI)$, and firstly, we carry out derivations for all segments apart from the tip: $j = 1, \ldots, N - 1$. We do not perform averaging for the tip segment together with the remaining fracture because of the calculating procedure in this case has specific features related to the tip asymptotic solution.

Term (IV) For Carter's leak-off term we utilise the midpoint rule in order to carry out integration over the circle $\mathcal{A}_\rho$:

$$-\frac{2C'}{2\pi \rho_j \Delta \rho} \int_{\mathcal{A}_\rho} \left(\sqrt{t_i - t_0(\rho R_i)} - \sqrt{t_{i-1} - t_0(\rho R_i)} \right) d\mathcal{A} \approx$$

$$\approx -2C' \left(\sqrt{t_i - t_0(\rho_j R_i)} - \sqrt{t_{i-1} - t_0(\rho_j R_i)} \right), \, j = 1, \ldots, N - 1.$$

In the matrix form, we denote term (IV) as a column $[\mathbf{F}^i]_j$, $j = 1, \ldots, N - 1$.

Term (V)

Similarly to the term (IV), we also apply the midpoint rule for averaging term (V) across the circle $\mathcal{A}_\rho$:

$$-\frac{Q'}{2\pi \rho_j \Delta \rho} \int_{\mathcal{A}_\rho} \int_{t_{i-1}}^{t_i} dt' \int_{-\infty}^{t'} \frac{d[H(s - t_0(\rho R_i))p(\rho, s)]}{\sqrt{t' - s}} d\mathcal{A} \approx$$

$$- Q' \int_{t_{i-1}}^{t_i} dt' \int_{-\infty}^{t'} \frac{d[H(s - t_0(\rho_j R_i))p_j]}{\sqrt{t' - s}}.$$

Further, let us simplify the double integration with respect to time by changing the

order of integration:

$$\int_{t_{i-1}}^{t_i} dt' \int_{-\infty}^{t'} \frac{\partial[H(s - t_0(\rho_j R_i))p_j]}{\partial s} \cdot \frac{ds}{\sqrt{t' - s}} = \int_{-\infty}^{t_{i-1}} \frac{\partial[H(s - t_0(\rho_j R_i))p_j]}{\partial s} ds \int_{t_{i-1}}^{t_i} \frac{dt'}{\sqrt{t' - s}} +$$

$$+ \int_{t_{i-1}}^{t_i} \frac{\partial[H(s - t_0(\rho_j R_i))p_j]}{\partial s} ds \int_s^{t_i} \frac{dt'}{\sqrt{t' - s}} = 2 \int_{-\infty}^{t_i} \frac{\partial[H(s - t_0(\rho_j R_i))p_j]}{\partial s} \sqrt{t_i - s} ds -$$

$$- 2 \int_{-\infty}^{t_{i-1}} \frac{\partial[H(s - t_0(\rho_j R_i))p_j]}{\partial s} \sqrt{t_{i-1} - s} ds = \int_{t_0(\rho_j R_i)}^{t_i} \frac{p_j}{\sqrt{t_i - s}} ds - \int_{t_0(\rho_j R_i)}^{t_{i-1}} \frac{p_j}{\sqrt{t_{i-1} - s}} ds,$$

$j = 1, \ldots, N - 1.$

The prefactor $-Q'$ is omitted for brevity. The simplified form of term (V) is discretised as:

$$\int_{t_0(\rho_j R_i)}^{t_i} \frac{p_j}{\sqrt{t_i - s}} ds = p_j^l \int_{t_0(\rho_j R_i)}^{t_l} \frac{ds}{\sqrt{t_i - s}} + \sum_{k=l}^{k=i-1} p_j^{k+1} \int_{t_k}^{t_{k+1}} \frac{ds}{\sqrt{t_i - s}} =$$

$$= 2p_j^l \left(\sqrt{t_i - t_0(\rho_j R_i)} - \sqrt{t_i - t_l} \right) + 2 \sum_{k=l}^{k=i-2} p_j^{k+1} \left(\sqrt{t_i - t_k} - \sqrt{t_i - t_{k+1}} \right) +$$

$$+ 2p_j^i \sqrt{\Delta t_i}, \ j = 1, \ldots, N - 1;$$

$$\int_{t_0(\rho_j R_i)}^{t_{i-1}} \frac{p_j}{\sqrt{t_{i-1} - s}} ds = p_j^l \int_{t_0(\rho_j R_i)}^{t_l} \frac{ds}{\sqrt{t_{i-1} - s}} + \sum_{k=l}^{k=i-2} p_j^{k+1} \int_{t_k}^{t_{k+1}} \frac{ds}{\sqrt{t_{i-1} - s}} =$$

$$= 2p_j^l \left(\sqrt{t_{i-1} - t_0(\rho_j R_i)} - \sqrt{t_{i-1} - t_l} \right) + 2 \sum_{k=l}^{k=i-2} p_j^{k+1} \left(\sqrt{t_{i-1} - t_k} - \sqrt{t_{i-1} - t_{k+1}} \right),$$

$j = 1, \ldots, N - 1,$

where l is the sequence number of the first time moment for which $t > t_0(\rho_j R_i)$. The matrix form of the presented discretisation can be conveniently written as follows: $[\mathbf{H}^i - 2Q'\sqrt{\Delta t_i}\mathbf{p}^i]_j$, $j = 1, \ldots, N - 1$, where $[\mathbf{H}^i]_j$ is the sum of all integrals independent of p_j^i in the equation for the segment j.

Term (VI) Let us consider averaging of the second pressure-dependent term. For

calculations we utilise the following formula:

$$\frac{1}{2\pi\rho_j\Delta\rho}\int_{\rho_{j-1/2}}^{\rho_{j+1/2}} 2\pi\rho^2 \frac{\partial}{\partial\rho}\left[H(s-t_0(\rho R_i))p(\rho,s)\right]d\rho \approx \frac{\rho_j}{\Delta\rho}(p_{j+1/2}-p_{j-1/2})H(s-t_0(\rho_j R_i)) =$$

$$= \rho_j \frac{p_{j+1}-p_{j-1}}{2\Delta\rho}H(s-t_0(\rho_j R_i)), \; j=2,\ldots,N-1.$$

In the case of $j=1$ the averaged equation has the following form (we utilise the assumption $p(\rho=0)=p_1$):

$$\frac{\rho_1}{\Delta\rho}(p_{3/2}-p_1)H(s-t_0(\rho_1 R_i)) = \rho_1 \frac{(p_2-p_1)}{2\Delta\rho}H(s-t_0(\rho_1 R_i)).$$

To deal with the double time integral, we firstly introduce the following notation: $\widetilde{p}_j = p_{j+1}-p_{j-1}$ (for $j=1$: $\widetilde{p}_1 = p_2 - p_1$). For brevity, we omit the prefactor $Q'\rho_j/(2\Delta\rho)$ and account the presence of Heaviside function $H(s-t_0(\rho_j R_i))$ through the lower limit of integration:

$$\int_{t_{i-1}}^{t_i} dt' \int_{t_0(\rho_j R_i)}^{t'} \frac{V(s)}{R(s)}\frac{\widetilde{p}_j}{\sqrt{t'-s}}ds = \int_{t_0(\rho_j R_i)}^{t_{i-1}} \frac{V(s)}{R(s)}\widetilde{p}_j ds \int_{t_{i-1}}^{t_i} \frac{dt'}{\sqrt{t'-s}}+$$

$$\int_{t_{i-1}}^{t_i} \frac{V(s)}{R(s)}\widetilde{p}_j ds \int_s^{t_i} \frac{1}{\sqrt{t'-s}}dt' = 2\int_{t_0(\rho_j R_i)}^{t_i} \frac{V(s)}{R(s)}\widetilde{p}_j \sqrt{t_i-s}ds-$$

$$- 2\int_{t_0(\rho_j R_i)}^{t_{i-1}} \frac{V(s)}{R(s)}\widetilde{p}_j \sqrt{t_{i-1}-s}ds, \; j=1,\ldots,N-1.$$

The above integrals can be computed in the following way:

$$\int_{t_0(\rho_j R_i)}^{t_i} \frac{V(s)}{R(s)}\widetilde{p}_j \sqrt{t_i-s}ds = \frac{V_l}{R_l}\widetilde{p}_j^l \int_{t_0(\rho_j R_i)}^{t_l} \sqrt{t_i-s}ds + \sum_{k=l}^{k=i-1} \frac{V_{k+1}}{R_{k+1}}\widetilde{p}_j^{k+1} \int_{t_k}^{t_{k+1}} \sqrt{t_i-s}ds =$$

$$= \frac{2}{3}\frac{V_l}{R_l}\widetilde{p}_j^l \left((t_i-t_0(\rho_j R_i))^{3/2} - (t_i-t_l)^{3/2}\right) + \frac{2}{3}\sum_{k=l}^{k=i-2} \frac{V_{k+1}}{R_{k+1}}\widetilde{p}_j^{k+1} \left((t_i-t_k)^{3/2} - (t_i-t_{k+1})^{3/2}\right) +$$

$$\frac{2}{3}\frac{V_i}{R_i}\Delta t_i^{3/2}\widetilde{p}_j^i,$$

$$\int_{t_0(\rho_j R_i)}^{t_{i-1}} \frac{V(s)}{R(s)} \widetilde{p}_j \sqrt{t_{i-1}-s} ds = \frac{V_l}{R_l} \widetilde{p}_j^l \int_{t_0(\rho_j R_i)}^{t_l} \sqrt{t_{i-1}-s} ds +$$

$$\sum_{k=l}^{k=i-1} \frac{V_{k+1}}{R_{k+1}} \widetilde{p}_j^{k+1} \int_{t_k}^{t_{k+1}} \sqrt{t_{i-1}-s} ds =$$

$$= \frac{2}{3} \frac{V_l}{R_l} \widetilde{p}_j^l \left((t_{i-1}-t_0(\rho_j R_i))^{3/2} - (t_{i-1}-t_l)^{3/2} \right) +$$

$$\frac{2}{3} \sum_{k=l}^{k=i-2} \frac{V_{k+1}}{R_{k+1}} \widetilde{p}_j^{k+1} \left((t_{i-1}-t_k)^{3/2} - (t_{i-1}-t_{k+1})^{3/2} \right).$$

The term (VI) can be conveniently written in the matrix form as: $[\mathbf{G}_1^i + \mathbf{G}_2^i \mathbf{p}^i]_j$, $j = 1, \ldots, N-1$. Here we introduce the column $\mathbf{G}_1^i$ consisting of the sums of all integrals independent of $\mathbf{p}^i$, and matrix $\mathbf{G}_2^i$ is required for the representation of the equation part including $\widetilde{p}_j^i$ in the matrix multiplication form.

As was noted previously, the discretised equations for the tip element should be considered separately. Firstly, it is noted that the expressions for the terms (I)−(III) for the tip segment are provided earlier. As a result, we need to focus only on the remaining terms, namely:

$$j = N: \quad (IV) + (V) + (VI) = -\frac{\Delta t}{2\pi \rho_N \Delta \rho R_i} \int_{R_i(1-\Delta\rho)}^{R_i} 2\pi s g_a(R_i - s) ds \approx$$

$$-\frac{\Delta t}{\Delta \rho R_i} q_\perp(\Delta \rho R_i) = -\frac{\Delta t}{\Delta \rho R_i} \cdot \frac{K'^4}{E'^3 M'} \cdot \Upsilon \left(\frac{\Delta \rho R_i}{\ell_{mk}}, \chi_i, \zeta_i \right), \tag{A.4}$$

where the function $\Upsilon(\xi, \chi, \zeta)$ is introduced by equation (3.28), ℓ_{mk} is the characteristic length in the mk-scaling (3.25).

It is known that the net fluid pressure computed using the asymptotic solution $p_a(R-r, V, \mathcal{Q})$ is defined up to a constant σ_o^a, which is the far-field confining pressure in the near-tip region model: $p_a = p_a^f - \sigma_o^a$ where p_a^f is the absolute pressure. In the general case, the near-tip net fluid pressure profile does not match the corresponding profile along the remaining part of the crack. In order to compensate for this discrepancy, we carry out the tuning of σ_o^a by introducing the correction δp^i that equals to the difference between pressure values at the second-to-last segment $(j = N - 1)$ calculated through the elasticity equation (3.30) and the asymptotic solution:

$$\delta p^i = p^i_{N-1} - p_a \left(\frac{3}{2} \Delta\rho R_i, V_i, \mathcal{Q} \right) = p^i_{N-1} - \frac{E'^2 V_i M'}{K'^2} \cdot \Pi_a \left(\frac{3}{2} \frac{\Delta\rho R_i}{\ell_{mk}}, \chi_i, \zeta_i \right). \quad \text{(A.5)}$$

As a result, it is necessary to introduce a new term $\{\delta\mathrm{p}\}$ associated with the pressure shift δp^i into equation (A.4):

$$\{\delta\mathrm{p}\} = -2Q'\Delta t \sqrt{\frac{V_i}{\Delta\rho R_i}} \delta p^i \quad \text{(A.6)}$$

By using equations (A.4), (A.6) together with the derivations for terms $(\mathrm{I}) - (\mathrm{III})$ presented at the beginning of this section, it is possible to write the discretised form of the Reynolds equation (3.31) for the tip element $(j = N)$ as:

$$w^i_N - w^{i-1}_N = -\frac{\Delta t V_i}{R_i} \rho_N \frac{w^i_N + w^i_{N-1}}{2\Delta\rho} - \frac{\Delta t}{M' R_i^2} \frac{\rho_{N-1/2}}{\rho_N \Delta\rho} (w^i_{N-1/2})^3 \frac{p^i_N - p^i_{N-1}}{\Delta\rho} -$$
$$- \frac{\Delta t}{\Delta\rho R_i} \cdot \frac{K'^4}{E'^3 M'} \cdot \Upsilon \left(\frac{\Delta\rho R_i}{\ell_{mk}}, \chi_i, \zeta_i \right) - 2Q'\Delta t \sqrt{\frac{V_i}{\Delta\rho R_i}} \cdot \left(p^i_{N-1} - \frac{E'^2 V_i M'}{K'^2} \Pi_a \left(\frac{3}{2} \frac{\Delta\rho R_i}{\ell_{mk}}, \chi_i, \zeta_i \right) \right).$$
$$\text{(A.7)}$$

Finally, combination of all of the above leads to

$$\mathbf{w}^i - \mathbf{w}^{i-1} = \mathbf{B}\mathbf{w}^i + \left(\mathbf{A}(\mathbf{w}^i) + \hat{\mathbf{S}}^i \right) \mathbf{p}^i + \mathbf{S}^i,$$

where the matrices $\mathbf{A}$ and $\mathbf{B}$ are defined at the beginning of this section, while the source/leak-off terms can be summarised as

$$[\mathbf{S}^i]_j = \delta^{1j} Q_0 \Delta t_i / (\pi \Delta\rho^2 R_i^2) + [\mathbf{H}^i]_j + [\mathbf{G}^i_1]_j, \ j = 1, \dots, N-1;$$

$$[\mathbf{S}^i]_N = -\frac{\Delta t}{\Delta\rho R_i} \cdot \frac{K'^4}{E'^3 M'} \cdot \Upsilon \left(\frac{\Delta\rho R_i}{\ell_{mk}}, \chi_i, \zeta_i \right) - 2Q'\Delta t \sqrt{\frac{V_i}{\Delta\rho R_i}} \cdot \frac{E'^2 V_i M'}{K'^2} \cdot \Pi_a \left(\frac{3}{2} \frac{\Delta\rho R_i}{\ell_{mk}}, \chi_i, \zeta_i \right);$$

$$[\hat{\mathbf{S}}^i \mathbf{p}^i]_j = -2Q'\sqrt{\Delta t_i} + [\mathbf{G}^i_2 \mathbf{p}^i]_j, \quad j = 1, \dots, N-1;$$

$$[\hat{\mathbf{S}}^i \mathbf{p}^i]_N = -2\Delta t \sqrt{\frac{V_i}{\Delta\rho R_i}} Q' p^i_{N-1}.$$

where the source term $\mathbf{S}^i$ does not depend on the pressure at the considered time

step ($\mathbf{p}^i$) and the term $\hat{\mathbf{S}}^i$ captures the fluid exchange part that depends on $\mathbf{p}^i$.

A.3 Verification of the numerical solver based on Gauss-Chebyshev quadrature and Barycentric Lagrange interpolation techniques

In Chapters 4 and 5, we apply the algorithm based on Gauss-Chebyshev quadrature and Barycentric Lagrange interpolation techniques (let us call it "GC-algorithm" for brevity) for calculation of the radial crack properties during its propagation. We rely on the approach initially proposed by Liu et al. [2019] and modify it to account for laminar-turbulent flow inside the fracture channel (Section 4.3.2) and Herschel–Bulkley rheology of the fracturing fluid (Section 5.3.1). However, before application of this approach to the solution of new problems, we should check that our implementation of the algorithm provides correct results for a radial crack driven by laminar flow of Newtonian fluid in a permeable formation (classic formulation outlined in Section 2.2).

We consider the problem formulation in the normalised form obtained via application of mk-scaling (Section 4.3.5). Solution is calculated for the following set of the leak-off number values: $\phi = \{10^{-20}, 10^{-10}, 10^{-5}, 1, 10^5, 10^{10}\}$. We look at the time dependent crack properties: radius $\gamma(\tau)$, maximum opening $\Omega(0, \tau)$, pressure at the half radius $\Pi(0.5, \tau)$, and efficiency $\eta(\tau)$. Figure A-1 shows the comparison of the enumerated characteristics obtained with the help of the GC-algorithm and reference approach. The latter is the numerical algorithm described in [Dontsov, 2016a] relied on the "tip-logic". We utilise this approach in Section 3.3 with the modifications linked with the pressure-dependent leak-off. Using the results provided in Figure A-1, one can notice the acceptable match between the outcome of GC-algorithm and reference solution.

Further, we compare the numerical solution with several semi-analytical solutions corresponding to the limiting propagation regimes of a radial hydraulic fracture (Section 4.3.4, laminar regimes) in terms of the spatial distribution of the fracture
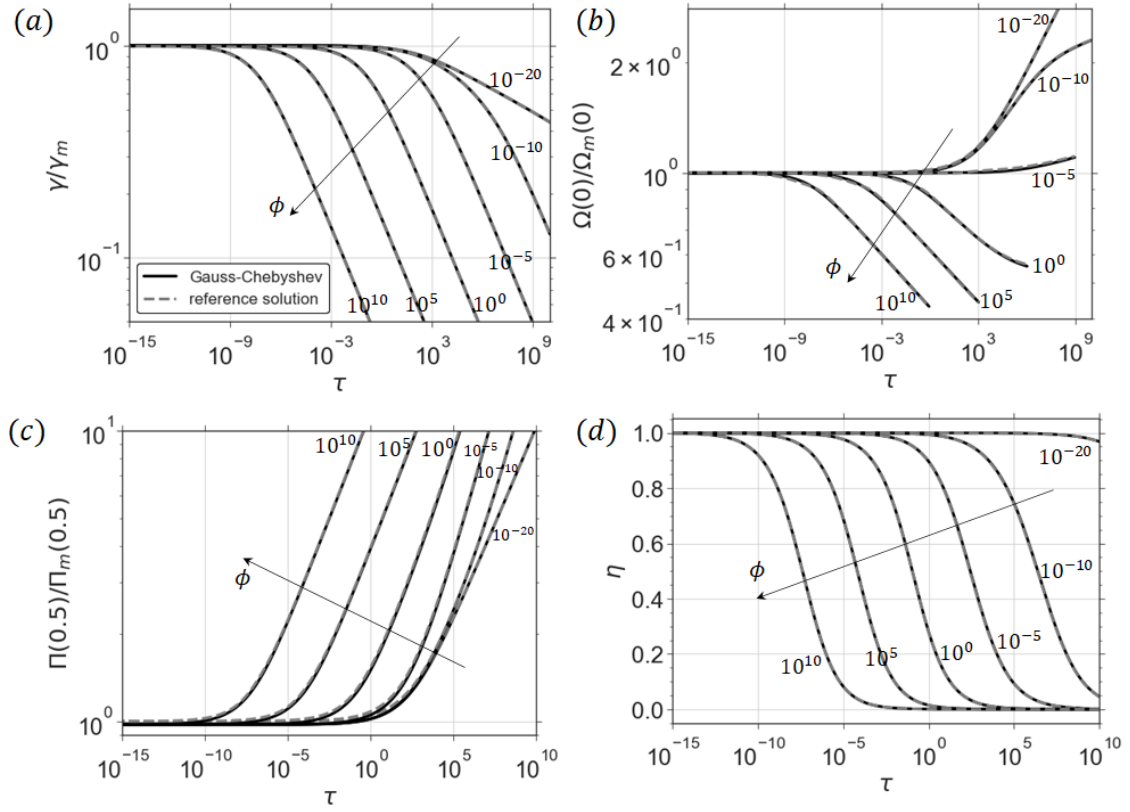
Figure A-1: The comparison between the numerical solution obtained via application of the algorithm based on Gauss-Chebyshev quadrature and Barycentric Lagrange interpolation techniques (the solid black lines) and the outcome provided by the approach based on the tip-logic (the dashed grey lines). Solutions correspond to the set of the leak-off number values $\phi = \{10^{-20}, 10^{-10}, 10^{-5}, 1, 10^5, 10^{10}\}$. Four time-dependent crack parameters are considered: radius (a), maximum opening (b), pressure at the half-radius (c), and efficiency (d). The solution profiles in panels (a)-(c) are normalised by the storage-viscosity limiting solution.

aperture. We choose the values of the leak-off number ϕ and time moments τ when the conditions of the vertex solutions realisation are satisfied. Opening profile in each case is plotted as a function of the dimensionless spatial coordinate, i.e., $\Omega = \Omega(\xi), \xi = r/R$, by grey solid line. In the charts, we also show the limiting solutions given in [Savitski and Detournay, 2002, Madyarova, 2004, Bunger et al., 2005] by coloured dashed lines. Figure A-2 presents the obtained results demonstrating the good match between the numerical and semi-analytical solutions in the limiting cases.

As it is mentioned in Sections 4.3.2 and 5.3.1, GC-algorithm does not require explicit implementation of the full tip asymptotic solution due to fine resolution near
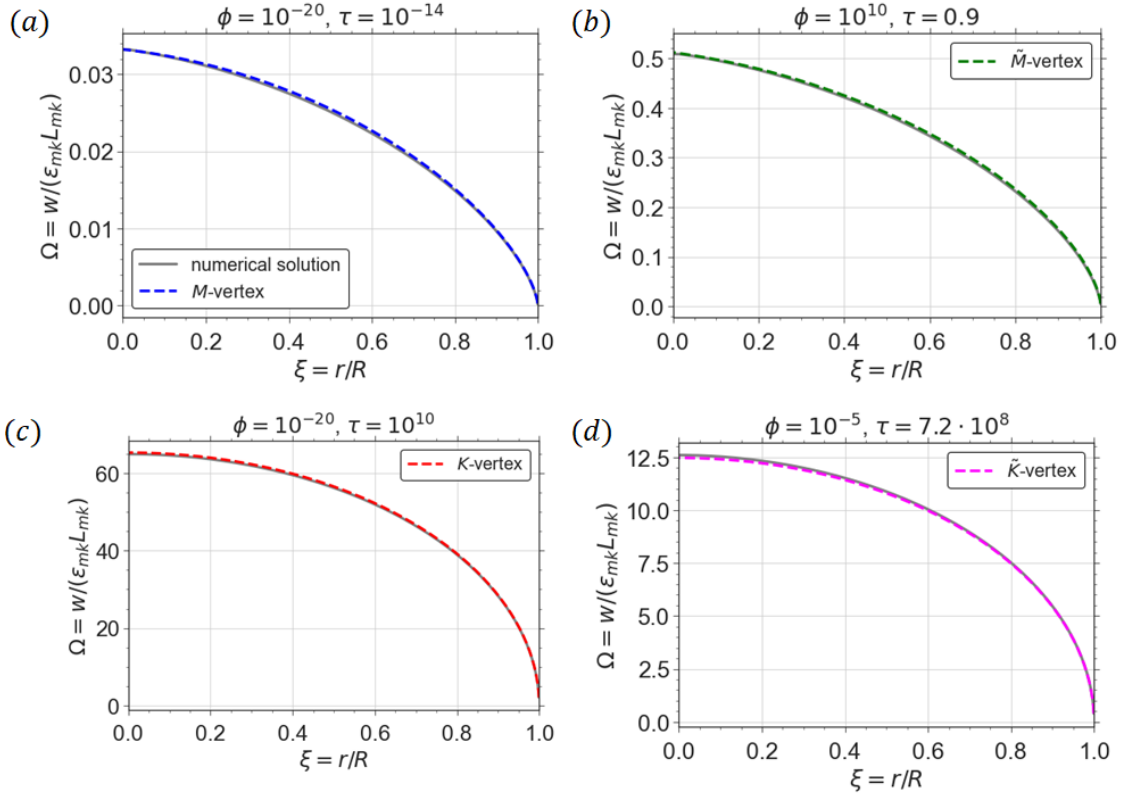
Figure A-2:   The comparison between the numerical solution obtained via application of the algorithm based on Gauss-Chebyshev quadrature and Barycentric Lagrange interpolation techniques (the solid black lines) and the semi-analytical solutions for the limiting propagation regimes of a radial fracture (the coloured dashed lines): M-vertex (a), $\tilde{M}$-vertex (b), K-vertex (c), $\tilde{K}$-vertex (d).

the tip. That is why, we would like to verify that the crack opening behaviour near the fracture tip is reproduced accurately by the numerical solver. In each limiting propagation regime of a radial fracture, i.e., M, K, $\tilde{M}$, and $\tilde{K}$, we compare the aperture behaviour near the moving front with the analytical fracture tip solutions (Section 3.2.2.1, asymptotes corresponding to Carter's leak-off case). Figure A-3 depicts the obtained results. Opening profiles computed numerically are the same as given in Figure A-2, and in Figure A-3, we zoom in the spatial domain located in the vicinity of the fracture front, $\xi \in [0.9, 1]$, and draw the analytical fracture tip solutions by coloured dashed lines. Using Figure A-3(a), one can notice that storage-viscosity asymptote (m-vertex) covers the numerical solution along the domain $\xi \in [0.98, 1]$. Similar zone is shorter in the case of the leak-off-viscosity asymptote ($\tilde{m}$-vertex) in Figure A-3(b), and it is a consequence of the fact that the radial crack solution is close to the $\tilde{M}$ regime, but it is not inside it (it is impossible to compute

219

the solution deeper inside the $\tilde{M}$-regime via GC-algorithm due to the convergence issues). Finally, from panels (c) and (d) in Figure A-3, one can find out that the toughness asymptote is valid along the region $\xi \in [0.96, 1]$.
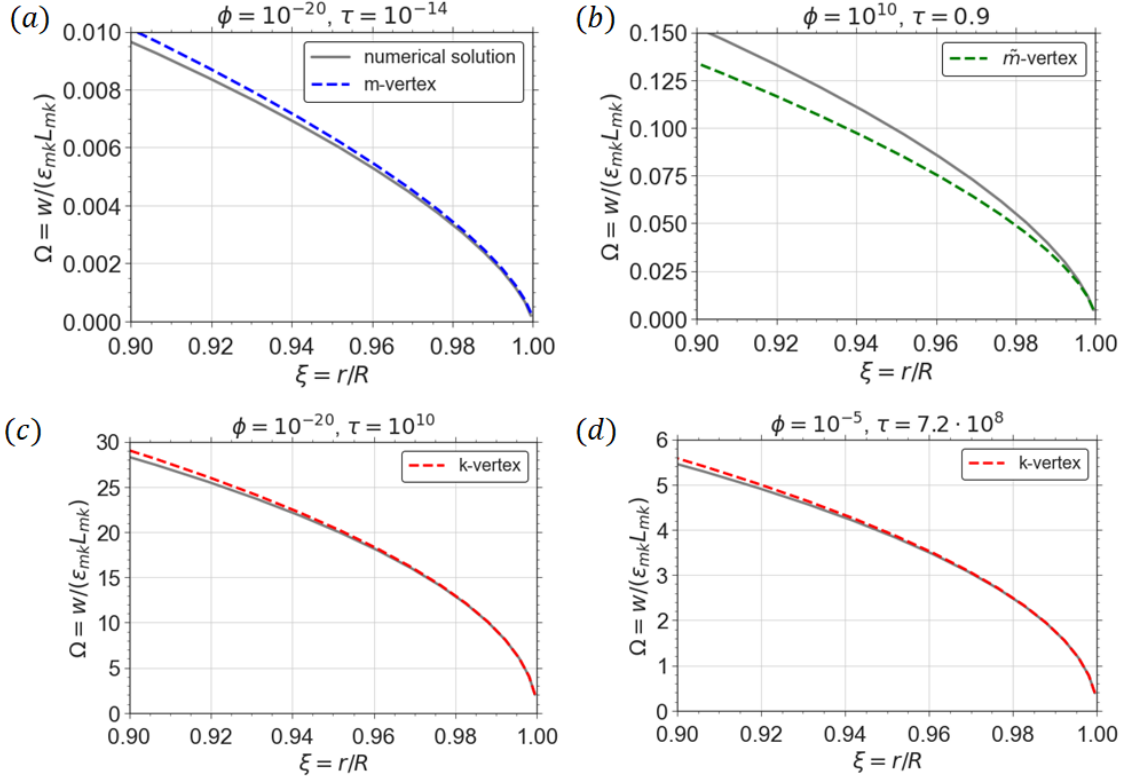
Figure A-3: The comparison between the numerical solution obtained via application of the algorithm based on Gauss-Chebyshev quadrature and Barycentric Lagrange interpolation techniques (the solid black lines) and the analytical fracture tip solutions (the coloured dashed lines): m-vertex (a), $\tilde{m}$-vertex (b), k-vertex (c) and (d).

A.4 Calculation of λ for the approximate numerical solution (Section 5.3.2)

In Section 5.4.1, we outline the values of λ for all limiting propagation regimes realised in the model: $\lambda_m = \lambda_m(n)$ (see Figure 5-2(a)), $\lambda_{\tilde{m}} = \lambda_{\tilde{m}}(n)$ (see Figure 5-4(a)), $\lambda_k = \lambda_{\tilde{k}} = 0.5$, $\lambda_t = 1.029$, and $\lambda_{\tilde{t}} = 1.077$. As it was demonstrated in Section 5.5.2, the validity regions of the vertex solutions strongly depend on time and the governing parameters. Consequently, based on the values of λ for the vertices, it is necessary to construct an interpolation scheme allowing one to determine λ for all

possible values of input parameters.

Let us define the auxiliary set of parameters:

$$\Xi_i = w_i(0,t)/R_i(t), \qquad \eta_{\mathrm{pl}} = \frac{2\pi R^2 w_a(R)\mathcal{B}(0.5,\bar{\delta})}{Q_0 t}, \qquad \eta_{\tau_0} = \frac{2\pi R^2 w_a(R)\mathcal{B}(1.05,\bar{\delta})}{Q_0 t},$$
(A.8)

where the subscript i denotes the considered limiting regime, and it can take values $i = \left\{m, \tilde{m}, k, \tilde{k}, t, \tilde{t}\right\}$. The radius $R_i(t)$ and wellbore opening $w_i(0,t)$ evolution in the vertex solutions are defined by the equations (5.26), and the function $\mathcal{B}(\lambda, \bar{\delta})$ given by equation (5.19). The parameter η_{pl} can be interpreted as the approximate efficiency for the crack filled by the power-law fluid, and the similar interpretation can be done for η_{τ_0} which is more suitable for the yield-stress dominated regimes $T, \tilde{T}$.

Using the variables (A.8), we can construct the following interpolation function for λ:

$$\lambda = \frac{\lambda_m(\Xi_m\eta_{\mathrm{pl}})^\kappa + \lambda_k(\Xi_k\eta_{\mathrm{pl}})^\kappa + \lambda_{\tilde{m}}[\Xi_{\tilde{m}}(1-\eta_{\mathrm{pl}})]^\kappa + \lambda_{\tilde{k}}[\Xi_{\tilde{k}}(1-\eta_{\mathrm{pl}})]^\kappa + \lambda_t(\Xi_t\eta_{\tau_0})^\kappa + \lambda_{\tilde{t}}[\Xi_{\tilde{t}}(1-\eta_{\tau_0})]^\kappa}{(\Xi_m\eta_{\mathrm{pl}})^\kappa + (\Xi_k\eta_{\mathrm{pl}})^\kappa + [\Xi_{\tilde{m}}(1-\eta_{\mathrm{pl}})]^\kappa + [\Xi_{\tilde{k}}(1-\eta_{\mathrm{pl}})]^\kappa + (\Xi_t\eta_{\tau_0})^\kappa + [\Xi_{\tilde{t}}(1-\eta_{\tau_0})]^\kappa},$$
(A.9)

where κ is a fitting parameter which is the current study is set 3. We also should mention that for the zero leak-off case $\Xi_{\tilde{m}} = \Xi_{\tilde{k}} = \Xi_{\tilde{t}} = 0$. Similarly, when we simulate the radial crack driven by the power-law fluid, we set $\Xi_t = \Xi_{\tilde{t}} = 0$.

A.5 Limiting propagation regimes (summary of Section 5.4.1)

M-vertex

Dimensional form:

$$R_m(t) = R_m^* \left(\frac{E'Q_0^{n+2}t^{2n+2}}{M'}\right)^{1/(3n+6)},$$

$$w_m(\rho,t) = w_m^{**}\left(\frac{M'^2 Q_0^{n+2}t^{2-n}}{E'^2}\right)^{1/(3n+6)}(1+\rho)^{\lambda_m}(1-\rho)^{\bar{\delta}_m},$$

$$p_m(\rho,t) = p_m^*\left(\frac{M'E'^{n+1}}{t^n}\right)^{1/(2+n)}\mathcal{F}(\rho,\lambda_m,\bar{\delta}_m).$$

221

Normalised form:

$$\gamma_m(\tau) = R_m^* \tau^{(2n+2)/(3n+6)}, \qquad \Omega_m(\rho, \tau) = w_m^{**} \tau^{(2-n)/(3n+6)},$$

$$\Pi_m(\rho, \tau) = p_m^* \tau^{-n/(2+n)}.$$

Parameters:

$$R_m^* = \left(2\pi \beta_m \alpha_m^{n/(n+2)} \mathcal{B}_m\right)^{-1/3}, \qquad w_m^{**} = \left(\frac{\beta_m^2 \alpha_m^{2n/(n+2)}}{2\pi \mathcal{B}_m}\right)^{1/3} 2^{-\lambda_m}, \qquad p_m^* = \beta_m \alpha_m^{\frac{n}{n+2}},$$

$$\beta_m = \left[\frac{2(2+n)^2}{n} \tan\left(\frac{\pi n}{2+n}\right)\right]^{1/(2+n)}, \qquad \bar{\delta}_m = \frac{2}{2+n}, \qquad \alpha_m = \frac{2n+2}{3n+6},$$

$$\mathcal{B}_m = \mathcal{B}(\lambda_m, \bar{\delta}_m) \text{ (equation (5.19))}, \qquad \lambda_m = \lambda_m(n) \text{ is shown in Figure 5-2(a)}.$$

$\tilde{M}$-vertex

Dimensional form:

$$R_{\tilde{m}}(t) = 0.4502 t^{1/4} \sqrt{\frac{Q_0}{C'}}, \qquad w_{\tilde{m}}(\rho, t) = w_{\tilde{m}}^{**} \left(\frac{M'^4 Q_0^{2n+4} t^{2-n}}{E'^4 C'^{4-2n}}\right)^{1/(8+8n)} (1+\rho)^{\lambda_{\tilde{m}}} (1-\rho)^{\bar{\delta}_{\tilde{m}}},$$

$$p_{\tilde{m}}(\rho, t) = p_{\tilde{m}}^* \left(\frac{M'^4 C'^{6n} E'^{8n+4}}{Q_0^{2n} t^{3n}}\right)^{1/(8+8n)} \mathcal{F}(\rho, \lambda_{\tilde{m}}, \bar{\delta}_{\tilde{m}}).$$

Normalised form:

$$\gamma_{\tilde{m}}(\tau) = 0.4502 \tau^{1/4} \phi^{-1/8}, \qquad \Omega_{\tilde{m}}(\rho, \tau) = w_{\tilde{m}}^{**} \left(\tau \phi^{-1/2}\right)^{(2-n)/(8+8n)} (1+\rho)^{\lambda_{\tilde{m}}} (1-\rho)^{\bar{\delta}_{\tilde{m}}},$$

$$\Pi_{\tilde{m}}(\rho, \tau) = p_{\tilde{m}}^* \left(\phi^{1/2}/\tau\right)^{3n/(8+8n)} \mathcal{F}(\rho, \lambda_{\tilde{m}}, \bar{\delta}_{\tilde{m}}).$$

Parameters:

$$w_{\tilde{m}}^{**} = \beta_{\tilde{m}} \left(\frac{2}{\pi^2}\right)^{(n+2)/(4n+4)} 2^{-\lambda_{\tilde{m}}}, \qquad p_{\tilde{m}}^* = \beta_{\tilde{m}} \left(\frac{\pi^2}{2}\right)^{n/(4n+4)},$$

$$\beta_{\tilde{m}} = \left[\frac{64(1+n)^2}{3n(4+n)} \tan\left(\frac{3\pi n}{4+4n}\right)\right]^{1/(2+2n)}, \qquad \bar{\delta}_{\tilde{m}} = \frac{4+n}{4+4n},$$

$$\lambda_{\tilde{m}} = \lambda_{\tilde{m}}(n) \text{ is shown in Figure 5-4(a)}.$$

K-vertex

Dimensional form:

$$R_k(t) = 0.8546 \left(\frac{E'Q_0 t}{K'} \right)^{2/5}, \quad w_k(\rho, t) = 0.6537 \left(\frac{K'^4 Q_0 t}{E'^4} \right)^{1/5} \sqrt{1 - \rho^2},$$

$$p_k(t) = 0.3004 \left(\frac{K'^6}{E'Q_0 t} \right)^{1/5}.$$

Normalised form:

$$\gamma_k(\tau) = 0.8546 \tau^{2/5}, \quad \Omega_k(\rho, \tau) = 0.6537 \tau^{1/5} \sqrt{1 - \rho^2},$$

$$\Pi_k(\tau) = 0.3004 \tau^{1/5}.$$

$\tilde{K}$-vertex

Dimensional form:

$$R_{\tilde{k}}(t) = 0.4502 t^{1/4} \sqrt{\frac{Q_0}{C'}}, \quad w_{\tilde{k}}(\rho, t) = 0.4744 \left(\frac{K'^8 Q_0^2 t}{C'^2 E'^8} \right)^{1/8} \sqrt{1 - \rho^2},$$

$$p_{\tilde{k}}(t) = 0.4139 \left(\frac{C'^2 K'^8}{Q_0^2 t} \right)^{1/8}.$$

Normalised form:

$$\gamma_{\tilde{k}}(\tau) = 0.4502 \tau^{1/4} \phi^{-1/8}, \quad \Omega_{\tilde{k}}(\rho, \tau) = 0.4744 \tau^{1/8} \phi^{-1/16} \sqrt{1 - \rho^2},$$

$$\Pi_{\tilde{k}}(\tau) = 0.4139 \tau^{-1/8} \phi^{1/16}.$$

T-vertex

Dimensional form:

$$R_t(t) = 0.6349 \left(\frac{t E'^{1/2} Q_0}{\tau_0^{1/2}} \right)^{1/3}, \quad w_t(\rho, t) = 1.5598 \left(\frac{Q_0 \tau_0 t}{E'} \right)^{1/3} (1 + \rho)^{1.029} (1 - \rho),$$

$$p_t(\rho, t) = 5.0133 \sqrt{\tau_0 E'} \mathcal{F}(\rho, 1.029, 1).$$

Normalised form:

$$\gamma_t(\tau) = 0.6349\tau^{1/3}\psi^{-1/6}, \qquad \Omega_t(\rho,\tau) = 1.5598\tau^{1/3}\psi^{1/3}\left(1+\rho\right)^{1.029}\left(1-\rho\right),$$

$$\Pi_t(\rho,\tau) = 5.0133\sqrt{\psi}\mathcal{F}(\rho,1.029,1).$$

<div align="center">

$\tilde{T}$-**vertex**

</div>

Dimensional form:

$$R_{\tilde{t}}(t) = 0.4502t^{1/4}\sqrt{\frac{Q_0}{C'}}, \qquad w_{\tilde{t}}(\rho,t) = 1.0697\left(\frac{Q_0\sqrt{t}\tau_0}{C'E'}\right)^{1/2}\left(1+\rho\right)^{1.077}\left(1-\rho\right),$$

$$p_{\tilde{t}}(\rho,t) = 5.0128\sqrt{E'\tau_0}\mathcal{F}(\rho,1.077,1).$$

Normalised form:

$$\gamma_{\tilde{t}}(\tau) = 0.4502\tau^{1/4}\phi^{-1/8}, \qquad \Omega_{\tilde{t}}(\rho,\tau) = 1.0697\tau^{1/4}\phi^{-1/8}\psi^{1/2}\left(1+\rho\right)^{1.077}\left(1-\rho\right),$$

$$\Pi_{\tilde{t}}(\rho,\tau) = 5.0128\psi^{1/2}\mathcal{F}(\rho,1.077,1).$$

A.6 Validation of the approximate solution

This section presents the validation procedure for the constructed approximate numerical solution (Subsection 5.3.2) with the help of the accurate approach (Subsection 5.3.1). We check its accuracy in terms of the radius, opening at the wellbore, pressure at the half-radius, and efficiency time histories carrying out simulations for different values of the governing parameters ϕ, ψ and the flow behaviour index n. In Section 5.4.1, we have already looked at the accuracy of the approximate method in the limiting propagation regimes, and here, the main focus is aimed at the transitions between them.

For the impermeable formation case, we analyse the set $n = \{1,\ 0.75,\ 0.3\}$ and for each value of the flow behaviour index, the computations are performed for $\psi = \{10^{-10}, 10^{-5}, 10^0, 10^5\}$. Figure A-4 shows the crack properties related to $n = 1$, and they are normalised by the storage-viscosity limiting solution. We estimate the relative differences between the fracture characteristics in the fully numerical and

Figure A-4: The comparison between the fully numerical (the solid black lines) and approximate (the dashed grey lines) numerical solutions corresponding to $n = 1$ flow behaviour index, an impermeable rock ($\phi = 0$), and the set of the yield stress number values: $\psi = \{10^{-10}, 10^{-5}, 10^0, 10^5\}$. Three time-dependent crack parameters are considered: radius (a), opening at the wellbore (b), and pressure at the half-radius (c), and all properties are normalised by the storage-viscosity limiting solution.

approximate solutions according to the relation: $\delta_A = |A_{\text{numer}} - A_{\text{appr}}|/|A_{\text{numer}}|$, $A = \{\gamma, \Omega(0), \Pi(0.5)\}$, find the maximum and average quantities of δ_A across the time domain $[\tau_{\min}, \tau_{\max}]$. We summarise the calculations in Table A.1 together with $\tau_{\min}$ and $\tau_{\max}$ values.

Using the metrics from Table A.1 in combination with Figure A-4, we conclude that the approximate methodology provides reasonably accurate predictions of the radius evolution. The average error in the wellbore opening calculations is relatively small (the peak value among the considered cases is 2%); however, the maximum difference can reach 16% in the transition zone between M and T vertex solutions. The pressure profiles are computed with the average error lying within the interval $(2, 11)\%$, and there is a tendency of the difference growth with an increase of the yield stress number. Similarly to the wellbore opening, the maximum error for $\Pi(0.5)$ is reached between the viscosity and yield-stress regimes, and it is up to 16%. Note that $\tau_{\max}$ is not constant for all these cases, and it is linked with the ability of the fully numerical solution to perform calculations inside the yield-stress dominated regime where almost the whole fracture is occupied by the plug zone, and the fluid flow velocity approaches zero.

Let us move on to the validation of the approximate solution for crack propagation in a permeable rock. Both power-law ($\psi = 0$) and Herschel–Bulkley ($\psi = 1$) rheologies are analysed for $n = \{1, 0.75, 0.3\}$, and we apply the following set of the leak-off number values: $\phi = \{10^{-20}, 10^{-10}, 10^{-5}, 10^0, 10^5, 10^{10}\}$. Figure A-

Table A.1: Table contains the values (in %) of the relative differences δ_A between the fully numerical and approximate numerical solutions in terms of radius γ, aperture at the wellbore $\Omega(0)$, and pressure at the half-radius $\Pi(0.5)$. Two values of δ_A are written in each cell corresponding to the aforementioned parameters: maximum and average across the considered time span $\tau \in [\tau_{\min}, \tau_{\max}]$. We analyse solutions for $n = \{0.3, 0.75, 1\}$ and the set of the yield stress number values $\psi = \{10^{-10}, 10^{-5}, 10^0, 10^5\}$.

Average | Maximum $\delta_A = \|A_{\mathrm{numer}} - A_{\mathrm{appr}}\|/\|A_{\mathrm{numer}}\|$ (in %) across time interval $[\tau_{\min}, \tau_{\max}]$				
	$\phi = 0$			
Parameter (A) \ ψ	10^{-10}	10^{-5}	10^0	10^5
	$n = 1, \ \tau_{\min} = 10^{-15}$			
$\tau_{\max}$	10^{20}	10^{20}	$2.5 \cdot 10^{16}$	10^9
γ	0.3 | 0.7	1.0 | 2.8	1.7 | 2.8	2.2 | 2.8
$\Omega(0)$	0.6 | 9.3	2.1 | 15.8	1.1 | 13.0	1.3 | 12.7
$\Pi(0.5)$	1.7 | 7.0	6.3 | 15.5	8.1 | 12.3	9.8 | 12.3
	$n = 0.75, \ \tau_{\min} = 10^{-15}$			
$\tau_{\max}$	10^{20}	10^{20}	$2.4 \cdot 10^{14}$	$1.8 \cdot 10^5$
γ	0.4 | 0.7	1.0 | 2.8	1.6 | 2.8	2.2 | 2.8
$\Omega(0)$	0.9 | 7.9	1.8 | 12.4	1.0 | 9.7	1.3 | 9.5
$\Pi(0.5)$	2.4 | 5.4	6.3 | 12.7	8.0 | 12.2	10.2 | 12.1
	$n = 0.3, \ \tau_{\min} = 10^{-20}$			
$\tau_{\max}$	10^{20}	10^{20}	10^{20}	$9.5 \cdot 10^7$
γ	0.8 | 1.5	0.9 | 2.3	1.5 | 2.9	2.2 | 2.9
$\Omega(0)$	1.8 | 6.2	2.2 | 6.2	2.1 | 7.0	1.8 | 12.5
$\Pi(0.5)$	5.5 | 7.8	6.1 | 10.1	8.4 | 12.1	10.7 | 12.1

5 shows the comparison for $n = 1$, $\psi = 1$ (the radius, opening, and pressure profiles are normalised by the M vertex solution), while the relative differences δ_A, $A = \{\gamma, \Omega(0), \Pi(0.5), \eta\}$ (average and maximum values over the time span $[\tau_{\min}, \tau_{\max}]$) are summarised in Table A.2. We also note that the upper boundary of the time interval is limited now by the ability of the fully numerical approach to handle the crack propagation with almost zero efficiency (apart from the obstacle connected with the plug zone mentioned before for $\phi = 0$ investigations).
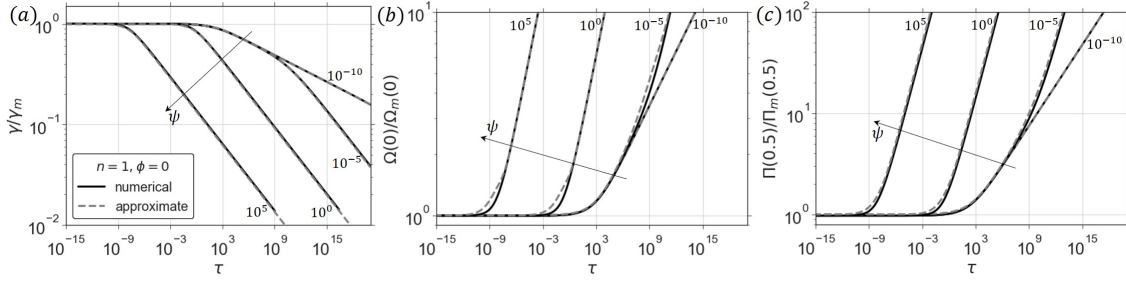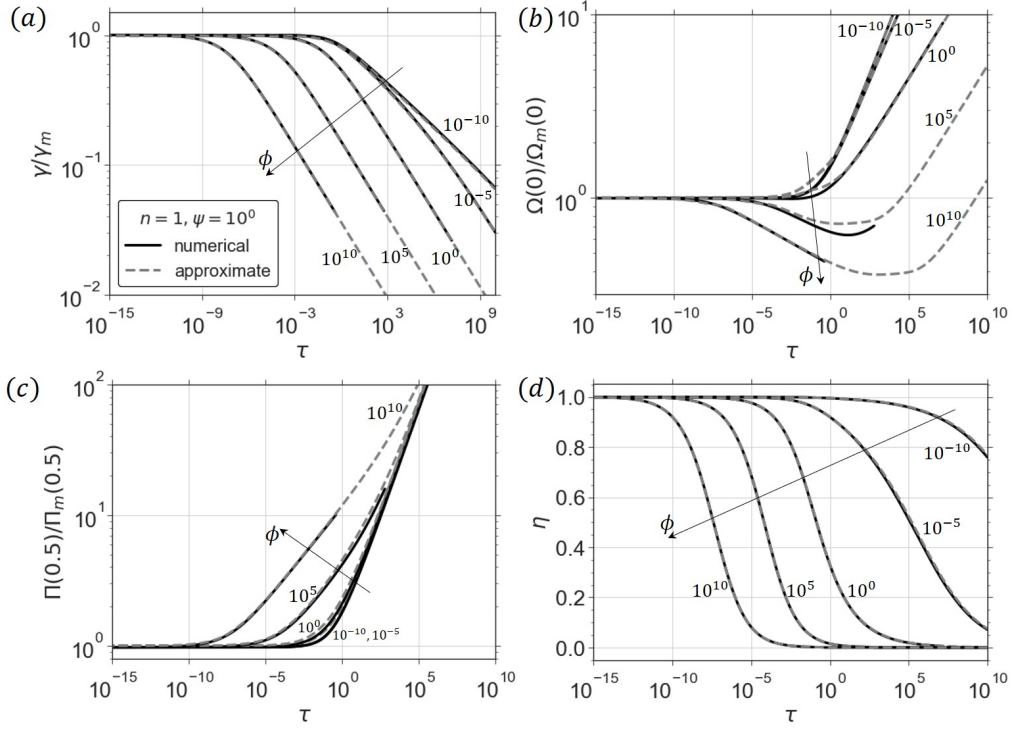
Figure A-5: The comparison between the fully numerical (the solid black lines) and approximate (the dashed grey lines) numerical solutions corresponding to $n = 1$ flow behaviour index, the set of the leak-off number values $\phi = \{10^{-10}, 10^{-5}, 10^0, 10^5, 10^{10}\}$, and $\psi = 1$ yield stress number. Four time-dependent crack parameters are considered: radius (a), opening at the wellbore (b), pressure at the half-radius (c), and efficiency (d). The solution profiles in panels (a)-(c) are normalised by the storage-viscosity limiting solution.

By looking at the results shown in Table A.2(a) for the power-law fluid, we find out that the approximate approach estimates the radius and efficiency evolution accurately with the average and maximum errors no more than 1% and 3%, respectively. Approximately the same scores are noticed for $\Omega(0)$ when $n = 1$ and 0.75. In contrast, the quality of estimations degrades for $n = 0.3$ where the average and maximum differences are approximately 3% and 6%. The approximate methodology provides values of the pressure at the half-radius with the average relative error less than 5%.

Further, we turn to the case $\psi = 1$ (see metrics in Table A.2 and Figure A-5 for $n = 1$), and here, the main trends are similar to the analysis for the power-law fluid. The average errors of the radius and efficiency computations are smaller than 1.5%, and the maximum differences reach 3% and 6%, correspondingly. The approximate

Table A.2: Tables contain the values (in %) of the relative differences δ_A between the fully numerical and approximate solutions in terms of radius γ, aperture at the wellbore $\Omega(0)$, pressure at the half-radius $\Pi(0.5)$, and efficiency η. Two values of δ_A are written in each cell corresponding to the aforementioned parameters: maximum and average across the considered time span $\tau \in [\tau_{\min}, \tau_{\max}]$. We analyse solutions for $n = \{0.3, 0.75, 1\}$, and for each value of the flow behaviour index, both power-law ($\psi = 0$, table (a)) and Herschel–Bulkley ($\psi = 10^0$, table (b)) rheologies are examined. In turn, the set of the leak-off number values $\phi = \{10^{-20}, 10^{-10}, 10^{-5}, 10^0, 10^5, 10^{10}\}$ is applied for calculations for each n and ψ.

(a) $\psi = 0$

Average | Maximum $\delta_A = \lvert A_{\mathrm{numer}} - A_{\mathrm{appr}}\rvert/\lvert A_{\mathrm{numer}}\rvert$ (in %) across time interval $[\tau_{\min}, \tau_{\max}]$						
Parameter (A) \ ϕ	10^{-20}	10^{-10}	10^{-5}	10^0	10^5	10^{10}
	$n = 1,\ \tau_{\min} = 10^{-15}$					
$\tau_{\max}$	10^{10}	10^{10}	$9.5 \cdot 10^8$	$1.1 \cdot 10^6$	$1.1 \cdot 10^3$	$9.1 \cdot 10^{-1}$
γ	0.4 | 0.7	0.5 | 0.7	0.5 | 0.7	0.6 | 0.8	0.6 | 0.8	0.5 | 0.8
$\Omega(0)$	0.3 | 0.8	0.3 | 0.7	0.4 | 1.2	0.4 | 1.6	0.4 | 1.5	0.4 | 1.6
$\Pi(0.5)$	2.0 | 3.1	2.0 | 3.1	2.2 | 2.8	2.4 | 2.8	1.9 | 2.4	1.6 | 2.4
η	0.0 | 0.0	0.2 | 1.2	0.3 | 1.4	0.2 | 1.0	0.2 | 0.6	0.2 | 0.6
	$n = 0.75,\ \tau_{\min} = 10^{-15}$					
$\tau_{\max}$	10^{10}	10^{10}	10^{10}	$2.2 \cdot 10^6$	$8.1 \cdot 10^2$	$1.9 \cdot 10^{-1}$
γ	0.5 | 0.7	0.5 | 0.7	0.5 | 0.7	0.6 | 0.7	0.6 | 0.8	0.5 | 0.7
$\Omega(0)$	0.7 | 1.5	0.6 | 1.6	0.6 | 2.3	0.6 | 2.1	0.5 | 1.7	0.5 | 1.6
$\Pi(0.5)$	3.0 | 3.8	3.0 | 3.8	3.1 | 3.9	2.9 | 3.4	2.4 | 2.9	1.9 | 2.8
η	0.0 | 0.0	0.3 | 1.7	0.6 | 2.0	0.3 | 1.6	0.1 | 0.4	0.1 | 0.4
	$n = 0.3,\ \tau_{\min} = 10^{-20}$					
$\tau_{\max}$	10^{10}	10^{10}	10^{10}	$6.2 \cdot 10^6$	$1.2 \cdot 10^2$	$4.5 \cdot 10^{-3}$
γ	0.6 | 1.4	0.5 | 0.9	0.3 | 0.9	0.3 | 0.9	0.2 | 0.9	0.1 | 0.8
$\Omega(0)$	2.4 | 6.2	2.5 | 6.2	2.6 | 6.2	3.0 | 6.2	3.4 | 5.6	3.0 | 4.6
$\Pi(0.5)$	5.3 | 7.8	5.1 | 7.8	4.9 | 7.7	4.8 | 7.8	4.4 | 7.2	3.4 | 6.4
η	0.0 | 0.0	0.2 | 2.4	0.5 | 3.0	0.5 | 2.5	0.5 | 1.8	0.8 | 1.8

(b) $\psi = 10^0$

Average | Maximum $\delta_A = \lvert A_{\mathrm{numer}} - A_{\mathrm{appr}}\rvert/\lvert A_{\mathrm{numer}}\rvert$ (in %) across time interval $[\tau_{\min}, \tau_{\max}]$						
Parameter (A) \ ϕ	10^{-20}	10^{-10}	10^{-5}	10^0	10^5	10^{10}
	$n = 1,\ \tau_{\min} = 10^{-15}$					
$\tau_{\max}$	10^{10}	10^{10}	10^{10}	$1.5 \cdot 10^7$	$6.1 \cdot 10^2$	$4 \cdot 10^{-1}$
γ	1.5 | 2.8	1.4 | 2.7	1.1 | 2.1	0.7 | 1.1	0.6 | 0.9	0.5 | 0.8
$\Omega(0)$	1.3 | 13.0	1.4 | 12.9	1.5 | 12.7	1.4 | 8.5	3.4 | 15.7	0.5 | 2.0
$\Pi(0.5)$	7.1 | 12.3	7.1 | 12.3	6.9 | 12.2	5.9 | 11.1	4.2 | 12.8	1.8 | 2.4
η	0.0 | 0.0	0.1 | 1.1	1.0 | 5.3	1.2 | 6.2	1.0 | 4.5	0.3 | 1.1
	$n = 0.75,\ \tau_{\min} = 10^{-15}$					
$\tau_{\max}$	10^{10}	10^{10}	10^{10}	$2.4 \cdot 10^8$	$4 \cdot 10^2$	10^{-1}
γ	1.4 | 2.8	1.4 | 2.7	1.0 | 2.0	0.6 | 0.9	0.6 | 0.8	0.5 | 0.7
$\Omega(0)$	1.2 | 9.7	1.3 | 9.7	1.4 | 9.5	1.3 | 6.4	3.1 | 12.3	0.7 | 2.0
$\Pi(0.5)$	7.3 | 12.2	7.3 | 12.2	7.1 | 11.9	6.4 | 11.0	4.4 | 11.1	2.0 | 2.8
η	0.0 | 0.0	0.1 | 1.1	0.9 | 5.3	1.3 | 6.3	0.7 | 3.2	0.2 | 0.7
	$n = 0.3,\ \tau_{\min} = 10^{-20}$					
$\tau_{\max}$	10^{10}	10^{10}	10^{10}	$1.3 \cdot 10^9$	$3.5 \cdot 10^2$	$4.5 \cdot 10^{-3}$
γ	1.0 | 2.8	1.0 | 2.6	0.7 | 1.9	0.3 | 0.9	0.2 | 0.9	0.1 | 0.8
$\Omega(0)$	2.8 | 7.0	2.8 | 7.0	2.9 | 7.0	2.8 | 6.9	4.2 | 7.2	3.3 | 6.1
$\Pi(0.5)$	7.1 | 12.1	7.1 | 12.1	6.9 | 11.4	6.5 | 10.9	5.3 | 9.9	3.5 | 7.5
η	0.0 | 0.0	0.1 | 1.3	0.9 | 6.2	1.6 | 7.5	0.5 | 2.2	0.8 | 1.9

approach gives the wellbore opening with the average accuracy less than 4%, while the peak differences are noticed between $\tilde{M}$ and $\tilde{T}$ regimes and comprise values up to 16%. The average precision of the pressure calculations is approximately 7%, and the difference between the fully numerical and approximate solutions for this parameter can achieve 13%.

Nomenclature

Fracture characteristics

η efficiency

γ dimensionless radius

$\mathcal{V}$ dimensionless fluid flow velocity

Ω dimensionless opening (aperture, width)

Π dimensionless net pressure

θ_0 dimensionless inverse fracture radius

g leak-off rate

p_f, p fluid pressure, net pressure

R fracture radius

t_0 inverse fracture radius

v, q fluid velocity and flow rate inside the fracture channel

V crack tip velocity

w fracture opening (aperture, width)

y_τ half-width of the plug zone

Rock and fluid properties

μ viscosity of fracturing fluid (Sections 2, 3, 4), viscosity of fracturing fluid filtrate (Section 5), pore fluid viscosity

ϕ_r, k formation porosity and permeability

σ_o, σ_o' far-field confining stress, effective confining stress

τ_0 yield stress

c diffusivity coefficient

c_t total compressibility

E, ν, E' Young's modulus, Poisson's ratio, plane strain elastic modulus

$f, \tilde{f}$ friction factor, normalised friction factor

K_{Ic}, K' rock toughness, toughness parameter

M, n, M' consistency index, flow behaviour index, viscosity parameter

p_o far-field pore pressure

Re, Re_d Reynolds number for a fluid flow in a plane channel, round section pipe

Other parameters, variables, and symbols

α parameter of the approximate radius evolution

$\bar{\delta}$ parameter of the approximate opening profile

χ, ζ dimensionless leak-off number, dimensionless leak-in number in a fracture tip model

ϵ dimensionless small parameter

λ circulation cell length (Section 3), laminar flow domain length (Section 4), parameter of the approximate opening profile (Section 5)

$\mathcal{R}$ characteristic Reynolds number

ϕ dimensionless leak-off number in a radial fracture model

ψ dimensionless leak-in number (Section 3), dimensionless yield stress number (Section 5) in a radial fracture model

ρ dimensionless distance to the source (Sections 3, 5), density (Section 4)

τ dimensionless time

ξ dimensionless distance to the fracture front in a fracture tip model (Sections 3, 4), dimensionless distance to the source in a radial fracture model (Section 4)

C_L, C', Q' Carter's leak-off coefficient, leak-off parameter, leak-in parameter

L length scale

Q_0 volumetric rate of fluid injection

r distance to the source

t time

$t_{mk}, L_{mk}, \epsilon_{mk}$ time scale, length scale, and small parameter corresponding to the mk-scaling

$V_{\mathrm{inj}}, V_{\mathrm{crack}}, V_{\mathrm{leak-off}}, V_{\mathrm{fluid-exchange}}, V_{\mathrm{C}}, V_{\mathrm{PDL}}$ injected volume, fracture volume, leaked into the formation volume, fluid volume participated in the fluid exchange process, Carter's cumulative leaked volume, pressure-dependent leak-off volume correction

Limiting propagation regimes, scalings

$\mathcal{G}_m, \mathcal{G}_t, \mathcal{G}_k$ dimensionless parameters quantifying the distribution of the dissipated energy between the fluid flow inside the fracture channel (m for liquid state and t for solid state) and brittle rock failure (k)

$\mathcal{G}_v, \mathcal{G}_c$ dimensionless parameters quantifying the distribution of the injected volume between the fracture (v) and ambient rock (c)

$\mathcal{P}$ dimensionless evolution parameters

$\tilde{K}$−vertex leak-off-toughness regime for a radial fracture

$\tilde{M}$−vertex leak-off-viscosity regime for a radial fracture

$\tilde{m}$−vertex leak-off-viscosity regime for a fracture tip

$\tilde{o}$−vertex storage-leak-in-viscosity regime for a fracture tip

$\tilde{T}$−vertex leak-off-viscosity-turbulent (Section 4), leak-off-yield-stress (Section 5) regime for a radial fracture

$\tilde{t}$−vertex leak-off-viscosity-turbulent regime for a fracture tip

K−vertex storage-toughness regime for a radial fracture

k−vertex toughness regime for a fracture tip

M−vertex storage-viscosity regime for a radial fracture

m−vertex storage-viscosity regime for a fracture tip

T−vertex storage-viscosity-turbulent(Section 4), storage-yield-stress (Section 5) regime for a radial fracture

t−vertex storage-viscosity-turbulent regime for a fracture tip

Bibliography

H Abe, LM Keer, and T Mura. Growth rate of a penny-shaped crack in hydraulic fracturing of rocks, 2. *Journal of Geophysical Research*, 81(35):6292–6298, 1976.

J Adachi, E Siebrits, A Peirce, and J Desroches. Computer simulation of hydraulic fractures. *International Journal of Rock Mechanics and Mining Sciences*, 44(5): 739–757, 2007.

JI Adachi and E Detournay. Self-similar solution of a plane-strain fracture driven by a power-law fluid. *International Journal for Numerical and Analytical Methods in Geomechanics*, 26(6):579–604, 2002.

José I Adachi and Emmanuel Detournay. Plane strain propagation of a hydraulic fracture in a permeable rock. *Engineering Fracture Mechanics*, 75(16):4666–4694, 2008.

José I Adachi, Emmanuel Detournay, and Anthony P Peirce. Analysis of the classical pseudo-3d model for hydraulic fracture with equilibrium height growth across stress barriers. *International Journal of Rock Mechanics and Mining Sciences*, 47 (4):625–639, 2010.

Brandon Carter Ames, Andrew Bunger, et al. Role of turbulent flow in generating short hydraulic fractures with high net pressure in slickwater treatments. In *SPE Hydraulic Fracturing Technology Conference*. Society of Petroleum Engineers, 2015.

K Arin and F Erdogan. Penny-shaped crack in an elastic layer bonded to dissimilar half spaces. *International Journal of Engineering Science*, 9(2):213–232, 1971.

Pascal Audet, Michael G Bostock, Nikolas I Christensen, and Simon M Peacock. Seismic evidence for overpressured subducted oceanic crust and megathrust fault sealing. *Nature*, 457(7225):76–78, 2009.

Pascal Audet, Michael G Bostock, Devin C Boyarko, Michael R Brudzinski, and Richard M Allen. Slab morphology in the cascadia fore arc and its relation to episodic tremor and slip. *Journal of Geophysical Research: Solid Earth*, 115(B4), 2010.

Reza Barati and Jenn-Tai Liang. A review of fracturing fluid systems used for hydraulic fracturing of oil and gas wells. *Journal of Applied Polymer Science*, 131 (16), 2014.

Alexander C Barbati, Jean Desroches, Agathe Robisson, and Gareth H McKinley. Complex fluids and hydraulic fracturing. *Annual review of chemical and biomolecular engineering*, 7:415–453, 2016.

G. K. Batchelor. *An Introduction to Fluid Dynamics*. Cambridge University Press, Cambridge UK, 1967.

Kamel Ben Naceur, Marc Thiercelin, and Eric Touboul. Simulation off fluid flow in hydraulic fracturing: Implications for 3d propagation. *SPE Production Engineering*, 5(02):133–141, 1990.

Alena Bessmertnykh, Egor Dontsov, and Roberto Ballarini. The effects of proppant on the near-front behavior of a hydraulic fracture. *Engineering Fracture Mechanics*, page 107110, 2020.

Alena Bessmertnykh, Egor Dontsov, and Roberto Ballarini. Semi-infinite hydraulic fracture driven by a sequence of power-law fluids. *Journal of Engineering Mechanics*, 147(10):04021064, 2021.

Alena O Bessmertnykh and Egor V Dontsov. A semi-infinite hydraulic fracture driven by a herschel–bulkley fluid. *Journal of Applied Mechanics*, 86(12), 2019.

B.A. Bilby and J.D. Eshelby. Dislocations and the theory of fracture. In H. Liebowitz, editor, *Fracture, an Advanced Treatise*, volume I, chapter 2, pages 99–182. Academic Press, New York NY, 1968.

Eugene Cook Bingham. *Fluidity and plasticity*, volume 2. McGraw-Hill, 1922.

Robert Byron Bird, Robert Calvin Armstrong, and Ole Hassager. Dynamics of polymeric liquids. vol. 1: Fluid mechanics. 1987.

Heinrich Blasius. Das aehnlichkeitsgesetz bei reibungsvorgängen in flüssigkeiten. In *Mitteilungen über Forschungsarbeiten auf dem Gebiete des Ingenieurwesens*, pages 1–41. Springer, 1913.

James P Brill and Hemant Kumar Mukherjee. *Multiphase flow in wells*, volume 17. Society of Petroleum Engineers, 1999.

Robert S Brodkey and Brodkey. The phenomena of fluid motions. 1967.

Andrew P Bunger and Emmanuel Detournay. Early-time solution for a radial hydraulic fracture. *Journal of engineering mechanics*, 133(5):534–540, 2007.

Andrew P Bunger and Emmanuel Detournay. Experimental validation of the tip asymptotics for a fluid-driven crack. *Journal of the Mechanics and Physics of Solids*, 56(11):3101–3115, 2008.

Andrew P Bunger, Emmanuel Detournay, and Dmitry I Garagash. Toughness-dominated hydraulic fracture with leak-off. *International journal of fracture*, 134 (2):175–190, 2005.

Pierre J Carreau. Rheological equations from molecular network theories. *Transactions of the Society of Rheology*, 16(1):99–127, 1972.

Benoit Carrier and Sylvie Granet. Numerical modeling of hydraulic fracture problem in permeable medium using cohesive zone model. *Engineering fracture mechanics*, 79:312–328, 2012.

Horatio Scott Carslaw and John Conrad Jaeger. Conduction of heat in solids. *Oxford: Clarendon Press, 1959, 2nd ed.*, 1959.

BJ Carter, J Desroches, AR Ingraffea, and PA Wawrzynek. Simulating fully 3d hydraulic fracturing. *Modeling in geomechanics*, 200:525–557, 2000a.

BJ Carter, AR Ingraffea, and T Engelder. Modeling ithaca's natural hydraulic fractures, 2000b.

E.D. Carter. Optimum fluid characteristics for fracture extension. In G. C. Howard and C. R. Fast, editors, *Drilling and Production Practices*, pages 261–270, 1957.

M. R. Chandler, P. G.Meredith, N. Brantut, and B. R. Crawford. Fracture toughness anisotropy in shale. *J. Geophys. Res.*, 121(3):1706–1729, 2016.

MP Cleary and SK Wong. Numerical simulation of unsteady fluid flow and propagation of a circular hydraulic fracture. *International Journal for Numerical and Analytical Methods in Geomechanics*, 9(1):1–14, 1985.

Royal Eugene Collins. Flow of fluids through porous materials. 1976.

Malcolm M Cross. Rheology of non-newtonian fluids: a new flow equation for pseudoplastic systems. *Journal of colloid science*, 20(5):417–437, 1965.

J Desroches, E Detournay, B Lenoach, P Papanastasiou, John Richard Anthony Pearson, M Thiercelin, and Ailan Cheng. The crack tip region in hydraulic fracturing. *Proceedings of the Royal Society of London. Series A: Mathematical and Physical Sciences*, 447(1929):39–48, 1994.

E Detournay and DI Garagash. The near-tip region of a fluid-driven fracture propagating in a permeable elastic solid. *Journal of Fluid Mechanics*, 494:1–32, 2003.

Emmanuel Detournay. Propagation regimes of fluid-driven fractures in impermeable rocks. *International Journal of Geomechanics*, 4(1):35–45, 2004.

Emmanuel Detournay. Mechanics of hydraulic fractures. *Annual Review of Fluid Mechanics*, 48:311–339, 2016.

E. Dontsov, A. Bunger, B. Abell, and R. Suarez-Rivera. Ultrafast hydraulic fracturing model for optimizing cube development. In *Proceedings of the Unconventional Resources Technology Conference, doi:10.15530/urtec-2019-884*, 2019a.

E. Dontsov, A. Bunger, B. Abell, and R. Suarez-Rivera. Ultrafast hydraulic fracturing model for optimizing cube development. In *Proceedings of the Unconventional Resources Technology Conference, doi:10.15530/urtec-2019-884*, 2019b.

E. V. Dontsov. Scaling laws for hydraulic fractures driven by a power-law fluid in homogeneous anisotropic rocks. *International Journal for Numerical and Analytical Methods in Geomechanics*, 43(2):519–529, 2019.

EV Dontsov. An approximate solution for a penny-shaped hydraulic fracture that accounts for fracture toughness, fluid viscosity and leak-off. *Royal Society open science*, 3(12):160737, 2016a.

EV Dontsov. Propagation regimes of buoyancy-driven hydraulic fractures with solidification. *Journal of Fluid Mechanics*, 797:1–28, 2016b.

EV Dontsov. Tip region of a hydraulic fracture driven by a laminar-to-turbulent fluid flow. *Journal of Fluid Mechanics*, 797, 2016c.

EV Dontsov. An approximate solution for a plane strain hydraulic fracture that accounts for fracture toughness, fluid viscosity, and leak-off. *International Journal of Fracture*, 205(2):221–237, 2017.

EV Dontsov and O Kresse. A semi-infinite hydraulic fracture with leak-off driven by a power-law fluid. *Journal of Fluid Mechanics*, 837:210–229, 2018.

EV Dontsov and AP Peirce. An enhanced pseudo-3d model for hydraulic fracturing accounting for viscous height growth, non-local elasticity, and lateral toughness. *Engineering Fracture Mechanics*, 142:116–139, 2015a.

EV Dontsov and AP Peirce. A non-singular integral equation formulation to analyse multiscale behaviour in semi-infinite hydraulic fractures. *Journal of Fluid Mechanics*, 781, 2015b.

E.V. Dontsov and A.P. Peirce. Modeling planar hydraulic fractures driven by laminar-to-turbulent fluid flow. *International Journal of Solids and Structures*, 128:73 – 84, 2017a.

EV Dontsov and AP Peirce. Modeling planar hydraulic fractures driven by laminar-to-turbulent fluid flow. *International Journal of Solids and Structures*, 128:73–84, 2017b.

EV Dontsov and AP Peirce. A multiscale implicit level set algorithm (ilsa) to model hydraulic fracture propagation incorporating combined viscous, toughness, and leak-off asymptotics. *Computer Methods in Applied Mechanics and Engineering*, 313:53–84, 2017c.

Michael Economides, Ronald Oligney, and Peter Valkó. *Unified fracture design: bridging the gap between theory and practice*. Orsa Press, 2002.

Michael J Economides. *Petroleum production systems*. Pearson Education, 2013.

Michael J Economides, Kenneth G Nolte, et al. *Reservoir stimulation*, volume 2. Prentice Hall Englewood Cliffs, NJ, 1989.

Steven H Emerman, DL Turcotte, and DA Spence. Transport of magma and hydrothermal solutions by laminar and turbulent fluid fracture. *Physics of the earth and planetary interiors*, 41(4):249–259, 1986.

Terry Engelder, Alfred Lacazette, N Barton, and O Stephansson. Natural hydraulic fracturing. In *Proceedings of the International Symposium on Rock Joints, 4-6 June at Loen, Norway*, pages 35–43, 1990.

Salah Aldin Faroughi, Antoine Jean-Claude Jacques Pruvot, and James McAndrew. The rheological behavior of energized fluids and foams with application to hydraulic fracturing. *Journal of Petroleum Science and Engineering*, 163:243–263, 2018.

Chunkai Fu and Ning Liu. Waterless fluids in hydraulic fracturing–a review. *Journal of Natural Gas Science and Engineering*, 67:214–224, 2019.

D Garagash and E Detournay. The tip region of a fluid-driven fracture in an elastic medium. *J. Appl. Mech.*, 67(1):183–192, 2000.

D. I. Garagash. Hydraulic fracture propagation in elastic rock with large toughness. In J. Girard, M. Liebman, C. Breeds, and T. Doe, editors, *Pacific Rocks 2000 – Proc. 4th North American Rock Mechanics Symp.*, pages 221–228, Rotterdam, 2000. Balkema.

DI Garagash. Transient solution for a plane-strain fracture driven by a shear-thinning, power-law fluid. *International journal for numerical and analytical methods in geomechanics*, 30(14):1439–1475, 2006a.

Dmitry I Garagash. Plane-strain propagation of a fluid-driven fracture during injection and shut-in: Asymptotics of large toughness. *Engineering fracture mechanics*, 73(4):456–481, 2006b.

Dmitry I Garagash. Propagation of a plane-strain hydraulic fracture with a fluid lag: Early-time solution. *International journal of solids and structures*, 43(18-19): 5811–5835, 2006c.

Dmitry I Garagash. Plane-strain propagation of a fluid-driven fracture during injection and shut-in: Asymptotics of large toughness. *Engineering fracture mechanics*, 73(4):456–481, 2006d.

Dmitry I Garagash. Cohesive-zone effects in hydraulic fracture propagation. *Journal of the Mechanics and Physics of Solids*, 133:103727, 2019.

Dmitry I Garagash and Erfan Sarvaramini. Equilibrium of a pressurized plastic fluid in a wellbore crack. *International journal of solids and structures*, 49(1):197–212, 2012.

Dmitry I Garagash, Emmanuel Detournay, and Jose I Adachi. Multiscale tip asymptotics in hydraulic fracture with leak-off. *Journal of Fluid Mechanics*, 669:260–297, 2011.

Igor A Garagash, Andrei A Osiptsov, and Sergei A Boronin. Dynamic bridging of proppant particles in a hydraulic fracture. *International Journal of Engineering Science*, 135:86–101, 2019.

J Geertsma, F De Klerk, et al. A rapid method of predicting width and extent of hydraulically induced fractures. *Journal of Petroleum Technology*, 21(12):1–571, 1969.

Sergey V Golovin and Alexey N Baykin. Influence of pore pressure on the development of a hydraulic fracture in poroelastic medium. *International Journal of Rock Mechanics and Mining Sciences*, 108:198–208, 2018.

M Gu and KK Mohanty. Rheology of polymer-free foam fracturing fluids. *Journal of Petroleum Science and Engineering*, 134:87–96, 2015.

WH Herschel and Ronald Bulkley. Measurement of consistency as applied to rubber-benzene solutions. In *Am. Soc. Test Proc*, volume 26, pages 621–633, 1926.

J Hu and DI Garagash. Plane-strain propagation of a fluid-driven crack in a permeable rock with fracture toughness. *Journal of Engineering Mechanics*, 136(9): 1152–1166, 2010.

G. R. Irvin. Analysis of stresses and strains near the end of a crack traversing a plate. *ASME J. Appl. Mech.*, 24:361–364, 1957.

Abubakar Isah, Moaz Hiba, Khaled Al-Azani, Murtada Saleh Aljawad, and Mohamed Mahmoud. A comprehensive review of proppant transport in fractured reservoirs: Experimental, numerical, and field aspects. *Journal of Natural Gas Science and Engineering*, page 103832, 2021.

E Kanin, E Dontsov, D Garagash, and A Osiptsov. The impact of fluid yield stress on hydraulic fracture propagation. In *82nd EAGE Annual Conference & Exhibition*, volume 2021, pages 1–5. European Association of Geoscientists & Engineers, 2021a.

EA Kanin, EV Dontsov, DI Garagash, and AA Osiptsov. A radial hydraulic fracture driven by a herschel–bulkley fluid. *Journal of Non-Newtonian Fluid Mechanics*, 295:104620, 2021b.

Evgenii Kanin, Dmitry Garagash, and Andrei Osiptsov. The near-tip region of a hydraulic fracture with pressure-dependent fluid exchange between the fracture and permeable rock. In *AGU Fall Meeting 2019*. AGU, 2019.

Evgenii Kanin, Dmitry Garagash, and Andrei Osiptsov. Radial fracture in permeable rock driven by turbulent-laminar flow. In *AGU Fall Meeting 2020*. AGU, 2020a.

Evgenii Kanin, Dmitry Garagash, and Andrei Osiptsov. Turbulent flow effects in a slickwater fracture propagation in permeable rock. In *ECMOR XVII*, volume 2020, pages 1–18. European Association of Geoscientists & Engineers, 2020b.

Evgenii Kanin, Dmitry Garagash, and Andrei Osiptsov. Turbulent flow effects in hydraulic fracture propagation in permeable rock. 2021c.

Evgenii A Kanin, Egor V Dontsov, Dmitry I Garagash, and Andrei A Osiptsov. A radial hydraulic fracture with pressure-dependent leak-off. *Journal of the Mechanics and Physics of Solids*, 143:104062, 2020c.

Evgenii A Kanin, Dmitry I Garagash, and Andrei A Osiptsov. The near-tip region of a hydraulic fracture with pressure-dependent leak-off and leak-in. *Journal of Fluid Mechanics*, 892, 2020d.

Melvin F Kanninen and Carl L Popelar. Advanced fracture mechanics. 1985.

M Kano, N Zolfaghari, BC Ames, and AP Bunger. Solution for a pkn hydraulic fracture driven by turbulent fluid with large leakoff. *Hydraulic Fracturing Journal*, 2(1):34–38, 2015.

S Khristianovic and Y Zheltov. Formation of vertical fractures by means of highly viscous fluids. In *Proc. 4th world petroleum congress, Rome*, volume 2, pages 579–586, 1955.

Y. Kovalyshen. *Fluid-Driven Fracture in Poroelastic Medium*. PhD thesis, University of Minnesota, 2010.

Yevhen Kovalyshen, Emmanuel Detournay, et al. Fluid-driven fracture in a poroelastic rock. In *ISRM International Conference for Effective and Sustainable Hydraulic Fracturing*. International Society for Rock Mechanics and Rock Engineering, 2013.

Alexandre Lavrov. Flow of truncated power-law fluid between parallel walls for hydraulic fracturing applications. *Journal of Non-Newtonian Fluid Mechanics*, 223:141–146, 2015.

Brice Lecampion and Jean Desroches. Simultaneous initiation and growth of multiple radial hydraulic fractures from a horizontal wellbore. *Journal of the Mechanics and Physics of Solids*, 82:235–258, 2015.

Brice Lecampion and Dmitry I Garagash. Confined flow of suspensions modelled by a frictional rheology. *Journal of Fluid Mechanics*, 759:197–235, 2014.

Brice Lecampion and Haseeb Zia. Slickwater hydraulic fracture propagation: near-tip and radial geometry solutions. *Journal of Fluid Mechanics*, 880:514–550, 2019.

Brice Lecampion, Andrew Bunger, and Xi Zhang. Numerical methods for hydraulic fracture propagation: a review of recent trends. *Journal of natural gas science and engineering*, 49:66–83, 2018.

S. H. Advaniand T.S. Lee and J.K. Lee. Three-dimensional modeling of hydraulic fractures in layered media: Part I–finite element formulations. *J. Energy Resour. Technol.*, 112:1–9, 1990.

B Lenoach. The crack tip solution for hydraulic fracturing in a permeable solid. *Journal of the Mechanics and Physics of Solids*, 43(7):1025–1043, 1995.

A. Li, W. Ding, J. He, P. Dai, S. Yin, and F. Xie. Investigation of pore structure and fractal characteristics of organic-rich shale reservoirs: A case study of lower cambrian qiongzhusi formation in malong block of eastern yunnan province, south china. *Marine and Petroleum Geology*, 70:46–57, 2016.

John R Lister. Buoyancy-driven fluid fracture: the effects of material toughness and of low-viscosity precursors. *Journal of Fluid Mechanics*, 210:263–280, 1990.

John R Lister and Ross C Kerr. Fluid-mechanical models of crack propagation and their application to magma transport in dykes. *Journal of Geophysical Research: Solid Earth*, 96(B6):10049–10077, 1991.

Dong Liu and Brice Lecampion. Propagation of a plane-strain hydraulic fracture accounting for a rough cohesive zone. *Journal of the Mechanics and Physics of Solids*, 149:104322, 2021.

Dong Liu, Brice Lecampion, and Dmitry I Garagash. Propagation of a fluid-driven fracture with fracture length dependent apparent toughness. *Engineering Fracture Mechanics*, 220:106616, 2019.

M Madyarova. *Propagation of a penny-shaped hydraulic fracture in elastic rock*. PhD thesis, Master's thesis, University of Minnesota, Minneapolis, 2004.

K. Magara. Comparison of porosity-depth relationships of shale and sandstone. *J. Petroleum Geol.*, 3(2):175–185, 1980.

G. E. Manger. Porosity and bulk density of sedimentary rocks. Technical Report 1144, USGS, 1963.

Andreas Möri and Brice Lecampion. Arrest of a radial hydraulic fracture upon shut-in of the injection. *International Journal of Solids and Structures*, 219:151–165, 2021.

Fatima-Ezzahra Moukhtari and Brice Lecampion. A semi-infinite hydraulic fracture driven by a shear-thinning fluid. *Journal of Fluid Mechanics*, 838:573–605, 2018.

Hai T Nguyen, Jang Hyun Lee, and Khaled A Elraies. A review of pkn-type modeling of hydraulic fractures. *Journal of Petroleum Science and Engineering*, page 107607, 2020.

Frans TM Nieuwstadt, Jerry Westerweel, and Bendiks J Boersma. *Turbulence: introduction to theory and applications of turbulent flows*. Springer, 2016.

RH Nilson. Gas-driven fracture propagation. 1981.

RP Nordgren et al. Propagation of a vertical hydraulic fracture. *Society of Petroleum Engineers Journal*, 12(04):306–314, 1972.

AA Osiptsov, IA Garagash, SA Boronin, KI Tolmacheva, KE Lezhnev, and GV Paderin. Impact of flowback dynamics on fracture conductivity. *Journal of Petroleum Science and Engineering*, page 106822, 2019.

Andrei A Osiptsov. Fluid mechanics of hydraulic fracturing: a review. *Journal of petroleum science and engineering*, 156:513–535, 2017.

Daniel Peck, Michal Wrobel, Monika Perkowska, and Gennady Mishuris. Fluid velocity based simulation of hydraulic fracture: a penny shaped model—part i: the numerical algorithm. *Meccanica*, 53(15):3615–3635, 2018a.

Daniel Peck, Michal Wrobel, Monika Perkowska, and Gennady Mishuris. Fluid velocity based simulation of hydraulic fracture—a penny shaped model. part ii: new, accurate semi-analytical benchmarks for an impermeable solid. *Meccanica*, 53(15):3637–3650, 2018b.

A Peirce. Modeling multi-scale processes in hydraulic fracture propagation using the implicit level set algorithm. *Computer Methods in Applied Mechanics and Engineering*, 283:881–908, 2015.

Anthony Peirce. The arrest and recession dynamics of a deflating radial hydraulic fracture in a permeable elastic medium. *Journal of the Mechanics and Physics of Solids*, page 104926, 2022.

Anthony Peirce and Emmanuel Detournay. An implicit level set method for modeling hydraulically driven fractures. *Computer Methods in Applied Mechanics and Engineering*, 197(33-40):2858–2885, 2008.

Anthony Peirce and Emmanuel Detournay. The arrest and recession dynamics of a deflating hydraulic fracture in a permeable elastic medium in a state of plane strain. *International Journal of Solids and Structures*, page 111906, 2022a.

Anthony Peirce and Emmanuel Detournay. Sunset similarity solution for a receding hydraulic fracture. *Journal of Fluid Mechanics*, 944, 2022b.

Lucas Pereira and Brice Lecampion. A plane-strain hydraulic fracture driven by a shear-thinning carreau fluid. *International Journal for Numerical and Analytical Methods in Geomechanics*, 2021.

TK Perkins, LR Kern, et al. Widths of hydraulic fractures. *Journal of Petroleum Technology*, 13(09):937–949, 1961.

James R Rice et al. Mathematical analysis in the mechanics of fracture. *Fracture: an advanced treatise*, 2:191–311, 1968.

E Rivalta, B Taisne, AP Bunger, and RF Katz. A review of mechanical models of dike propagation: Schools of thought, results and future directions. *Tectonophysics*, 638:1–42, 2015.

Allan M Rubin. Tensile fracture of rock at high confining pressure: implications for dike propagation. *Journal of Geophysical Research: Solid Earth*, 98(B9):15919–15935, 1993.

Allan M Rubin. Propagation of magma-filled cracks. *Annual Review of Earth and Planetary Sciences*, 23(1):287–336, 1995.

E Sarris and P Papanastasiou. The influence of the cohesive process zone in hydraulic fracturing modelling. *International Journal of Fracture*, 167(1):33–45, 2011.

AA Savitski and E Detournay. Propagation of a penny-shaped fluid-driven fracture in an impermeable rock: asymptotic solutions. *International journal of solids and structures*, 39(26):6311–6337, 2002.

Antonin Settari, Michael P Cleary, et al. Development and testing of a pseudo-three-dimensional model of hydraulic fracture geometry. *SPE Production Engineering*, 1(06):449–466, 1986.

JL Sousa, BJ Carter, and AR Ingraffea. Numerical simulation of 3d hydraulic fracture using newtonian and power-law fluids. In *International journal of rock mechanics and mining sciences & geomechanics abstracts*, volume 30, pages 1265–1271. Elsevier, 1993.

DA Spence and DL Turcotte. Magma-driven propagation of cracks. *Journal of Geophysical Research: Solid Earth*, 90(B1):575–580, 1985.

Jonathan J Stickel and Robert L Powell. Fluid mechanics and rheology of dense suspensions. *Annu. Rev. Fluid Mech.*, 37:129–149, 2005.

R. Suarez-Rivera, E. Dontsov, and B. Abell. Quantifying the induced stresses during stacked, multi-stage, multi- well completions, to define stimulation sequencing and optimize pad productivity. In *Proceedings of the Unconventional Resources Technology Conference, doi:10.15530/urtec-2019-892*, 2019.

Victor C Tsai and James R Rice. A model for turbulent hydraulic fracture and application to crack propagation at glacier beds. *Journal of Geophysical Research: Earth Surface*, 115(F3), 2010.

Victor C Tsai and James R Rice. Modeling turbulent hydraulic fracture near a free surface. *Journal of applied mechanics*, 79(3), 2012.

Cornelis J van der Veen. Fracture propagation as means of rapidly transferring surface meltwater to the base of glaciers. *Geophysical Research Letters*, 34(1), 2007.

L. Vandamme and J.H. Curran. A three-dimensional hydraulic fracturing simulator. *Int. J. Numer. Meth. Eng.*, 28:909–927, 1989.

Robert C Viesca and Dmitry I Garagash. Numerical methods for coupled fracture problems. *Journal of the Mechanics and Physics of Solids*, 113:13–34, 2018.

Preetinder S Virk. Drag reduction fundamentals. *AIChE Journal*, 21(4):625–656, 1975.

PS Virk. Drag reduction in rough pipes. *Journal of fluid mechanics*, 45(2):225–246, 1971.

Pauli Virtanen, Ralf Gommers, Travis E Oliphant, Matt Haberland, Tyler Reddy, David Cournapeau, Evgeni Burovski, Pearu Peterson, Warren Weckesser, Jonathan Bright, et al. Scipy 1.0: fundamental algorithms for scientific computing in python. *Nature methods*, 17(3):261–272, 2020.

Mahta Vishkai and Ian Gates. On multistage hydraulic fracturing in tight gas reservoirs: Montney formation, alberta, canada. *Journal of Petroleum Science and Engineering*, 174:1127–1141, 2019.

J. B. Walsh. Effect of pore pressure and confining pressure on fracture permeability. *Int. J. Rock Mech. Min. Sci. & Geomech. Abstr.*, 18(5):429–435, 1981.

Michal Wrobel. On the application of simplified rheological models of fluid in the hydraulic fracture problems. *International Journal of Engineering Science*, 150: 103275, 2020.

Michal Wrobel, Gennady Mishuris, and Panos Papanastasiou. On the influence of fluid rheology on the hydraulic fracture evolution. *arXiv preprint arXiv:2007.04208*, 2020.

Bo Yang, Jinzhou Zhao, Jincheng Mao, Hongzhong Tan, Yang Zhang, and Zhifeng Song. Review of friction reducers used in slickwater fracturing fluids for shale gas reservoirs. *Journal of Natural Gas Science and Engineering*, 62:302–313, 2019.

Haseeb Zia and Brice Lecampion. Propagation of a height contained hydraulic fracture in turbulent flow regimes. *International Journal of Solids and Structures*, 110:265–278, 2017.

Haseeb Zia and Brice Lecampion. Pyfrac: A planar 3d hydraulic fracture simulator. *Computer Physics Communications*, page 107368, 2020.

N Zolfaghari and AP Bunger. Approximate semi-analytical solution for a penny-shaped rough-walled hydraulic fracture driven by turbulent fluid in an impermeable rock. *International Journal of Solids and Structures*, 143:144–154, 2018.

N Zolfaghari and AP Bunger. Numerical model for a penny-shaped hydraulic fracture driven by laminar/turbulent fluid in an impermeable rock. *International Journal of Solids and Structures*, 158:128–140, 2019.

N Zolfaghari, E Dontsov, and AP Bunger. Solution for a plane strain rough-walled hydraulic fracture driven by turbulent fluid through impermeable rock. *International Journal for Numerical and Analytical Methods in Geomechanics*, 42(4): 587–617, 2018.

Navid Zolfaghari, Colin R Meyer, and Andrew P Bunger. Blade-shaped hydraulic
    fracture driven by a turbulent fluid in an impermeable rock. *Journal of Engineer-
    ing Mechanics*, 143(11):04017130, 2017.